**Coventry University**

## DOCTOR OF PHILOSOPHY

# Investigation of physico-chemical properties of Ni-based catalysts produced by solution combustion synthesis and their catalytic activity in liquid phase hydrogenation

Thoda, Olga

*Award date:*
2020

*Awarding institution:*
Coventry University

Link to publication

# Investigation of physico-chemical properties of Ni-based catalysts produced by solution combustion synthesis and their catalytic activity in liquid phase hydrogenation

By

**Olga Thoda**

**Doctor of Philosophy**

**March 2019**

***A thesis submitted in partial fulfilment of the University's requirements for the Degree of Doctor of Philosophy***

Content removed on data protection grounds

Content removed on data protection grounds

# Certificate of Ethical Approval

Applicant:

Olga Thoda

Project Title:

Investigation of physic-chemical properties of Ni-based nano- and micro-structured catalysts produced by combustion synthesis and their catalytic activity in liquid phase hydrogenation.

This is to certify that the above named applicant has completed the Coventry University Ethical Approval process and their project has been confirmed and approved as Low Risk

Date of approval:

23 July 2018

Project Reference Number: P72980

Content removed on data protection grounds

## Acknowledgements

I would like to express my graditude to my supervisor Prof. G. Xanthopoulou and my Director of Studies Prof. A. Chroneos for their constant support, help and guidance. The knowledge that they provided as well as their encouragement and motivation were priceless. I consider myself very lucky that I had the opportunity to work close to those great people and scientists.

I am also very grateful to Dr. G. Vekinis, Head of the Advanced Ceramics and Composites Laboratory in NCSR “Demokritos”, for providing the working space and the materials required for this research project. He also gave me countless tips and advice during my studies, being an inspiration for me.

Furtheromore, I would like to say thanks to all the people working in the laboratory with me for the amazing cooperation all these years. A very special gratitude goes out to Dr. A. Marinou. She provided such a valuable help and she played a major role in our research on in-flight SCS process.

Lat but not least I would like to express my graditude to all the scientists who performed various measurements that were included in my thesis. Dr. N. Boukos from “NCSR Demokritos” perfomed TEM measuremnts (pp.79, 165), Dr. A. Steinman and S. Roslyakov from National University of Science and Technology “MISIS” conducted the TGA (pp.100, 151-152, 188) and the IR-camera measurements (pp.114, 134, 148-149) respectively. Also, the RF-IGC measurements and data analysis (pp.130-132) conducted in collaboration with Dr. E. Metaxa in School of Chemical Engineering, NTUA and Dr. V. Prokof’ev model the effect of preheating temperature on the combustion temperature during SCS (pp.101-102). Finally, Dr. D. Kovalev from the Institute of Structural Macrokinetics and Materials Science in Russia performed the TRXRD analysis (pp.95, 157).

Thank you all for your help! It was a great honor working with you all!

# Table of Contents

## List of Figures and Tables

# Abstract

Solution Combustion Synthesis is a versatile method for the production of various materials directly at the nanoscale. The main source of heat comes for the exothermic combustion reactions that take place once the water in the solution has evaporated, so it is a self-sustaining thermal synthesis process. It is already widely used to prepare catalysts for laboratory and industrial purposes, due to the advantages it offers. This research project has been designed to study and enable the clarification of the mechanisms of reactions that take place during the production of Solution Combustion Synthesis catalysts based on nickel. Furthermore, the hydrogenation of maleic acid toward the as-synthesized catalysts was investigated to outline the catalysts properties and behaviour during catalysis.

However, SCS is a very sensitive synthesis approach and in this work an effort was made to investigate the main parameters that influence the final products' composition and properties.

Nickel nitrate hexahydrate ($Ni(NO_3)_2{\cdot}6H_2O$) and aluminium nitrate nonahydrate ($Al(NO_3)_3{\cdot}9H_2O$) were used as oxidizers and glycine as the reducer. In most cases distilled water was added to the initial gel mixture to facilitate mixing prior to SCS. The parameters that were investigated during this work were:

- water quantity in the initial SCS mixture
- pre-treatment of water used in the initial SCS mixture
- duration of heated stirring as a pre-treatment for SCS initial solution
- fuel (reducer) to oxidizer ratio and total fuel concentration in the initial SCS mixture
- preheating temperature in correlation to a computational model
- heating mode during SCS and
- time in furnace after SCS was completed.

This research work targeted in the investigation of the role of water in producing Ni-based nanopowders using SCS. More specifically, nanopowders were produced using $Ni(NO_3)_2$, glycine as a fuel and distilled water as a diluter. Different amounts of distilled water were added in that initial batch, in order to find the influence of the degree of dilution on the composition of the final products. In this work it was found for the first time that the initial concentration of nitrates in the aqueous solution affects the characteristics and properties of Ni-based catalysts including their final composition, crystallite size and parameters of crystal

lattice, pores size distribution and surface area. In addition, the relative amount of water in the initial aqueous solution appears to have a substantial effect on their catalytic activity in maleic acid liquid phase hydrogenation. The underlying mechanism for this effect appears to be the prolonged persistence and delayed decomposition of hydrates that form during the early preheating stages of SCS. This is especially significant for structure-sensitive catalytic reactions, such as catalysis in the liquid-phase.

The structure, composition, surface area and catalytic activity of Solution Combustion Synthesis (SCS) catalysts are all influenced by the conditions of preparation and in particular, the glycine concentration in the initial SCS solution. Regular three-dimensional (3D) flowerlike Ni-NiO hierarchical architectures were synthesized by SCS. The results have revealed a three-dimensional percolation network with hierarchical structure on the basis of nano-structured metal oxides and metals synthesized during SCS. Such hierarchically nanoporous catalysts have versatile structural properties such as increased surface area and large overall pore volume that can alleviate diffusional limitations of conventional nanocatalysts with solely microporous frameworks. The three-dimensional percolation-like network and hierarchical structure of nano-composites on the basis of metal oxides and metals obtained by combustion in solutions provides a distinct possibility of increasing the selectivity and activity of such catalysts.

Some of the as-synthesized catalysts were tested for catalytic liquid-phase hydrogenation of unsaturated hydrocarbons in order to investigate the effect of the synthesis parameters on the catalysts' catalytic behaviour. It was concluded that all the parameters above influence the SCS process in a complex way and subsequently the final products' composition and activity in the hydrogenation process. The results revealed that the presence of Ni-Al alloys in the final SCS catalytic structure enhances significantly their catalytic performance. Moreover, in the $Ni(NO_3)_2$-glycine system the presence of NiO in the final product composition is crucial, as it acts as a carrier for the metallic nickel, and in its absence the catalysts is almost inactive.

The results of this extensive research of various parameters that were investigated enlightened the underlying mechanisms of SCS and exhibited its complex nature. In conclusion, SCS can be used to synthesize nano-catalysts with specific properties and offers notable advantages over other methods of producing catalysts.

# Part A

# 1. Catalysis

## 1.1. Introduction

Catalysis is of crucial importance for the chemical industry. This is demonstrated by the fact that approximately 85–90% of all chemical products require a catalytic step during the course of production.[1] Figure 1.1 represents applications of catalysis in industry. In the last few years, there is a growth of catalytic applications concerning the environment.

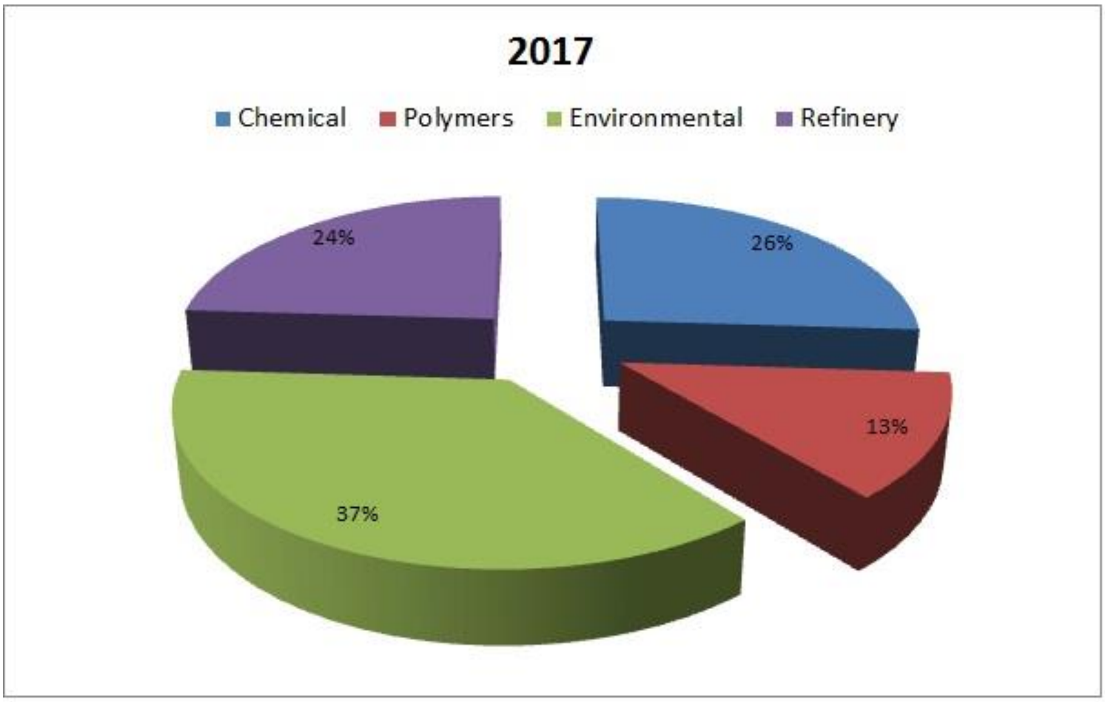

Figure 1.1. Global catalyst market (adapted from [2]).

Catalysis is the process of increasing the rate of a chemical reaction due to the participation of an additional substance called a catalyst. The catalyst is not consumed in the catalytic reaction and can be used repeatedly.

Depending upon whether a catalyst exists in the same phase as the substrate catalysts can be classified as heterogeneous and homogenous catalysts, while biocatalysts (enzymes) are often considered as a separate group. There is a vast variety of catalysts applied in industry, which come in various forms, from heterogeneous catalysts in the form of porous solids to homogeneous catalysts dissolved in the liquid reaction mixture to biological catalysts in the form of enzymes. Figure 1.2 shows a schematic representation of a catalytic reaction between two molecules A and B with the involvement of a catalyst. [1]

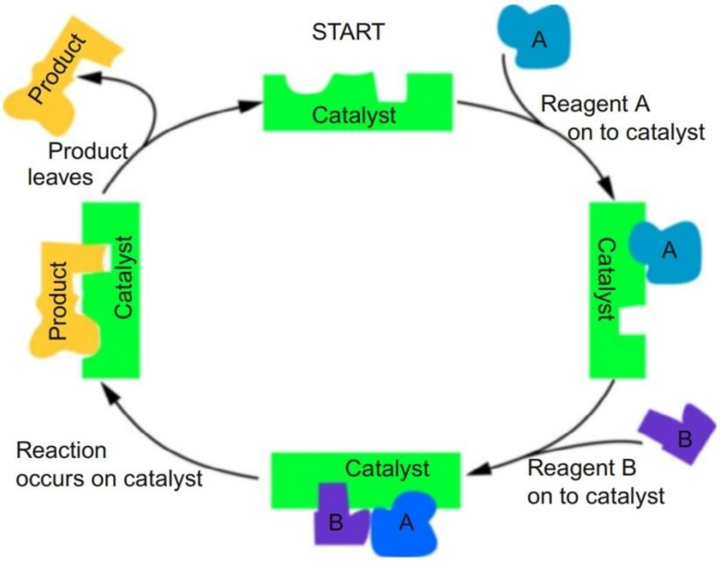

Figure 1.2. Catalytic circle. [1]

## 1.2. The modes of catalysis

### *1.2.1. Homogeneous catalysis*

In case of homogeneous catalysis, a catalyst is in the same phase as the reactants. Three types of homogeneous catalysis are usually considered: gas phase, acid-base, and by transition metals. One common example of catalysis in the gas phase is the decomposition of ozone ($O_3$) into oxygen ($O_2$), which is catalyzed by chloroflourocarbons (CFCs), Volatile organic compounds (VOCs), or nitric oxide (NO).[3]

Figure 1.3 demonstrates a catalytic cycle containing Cl and ClO; thus, formally ozone destruction has a chlorine catalytic cycle. For gas-phase catalytic reactions, usually the catalyst should have a radical nature with a relatively low value of activation energy in order the catalytic complex to form. [1]

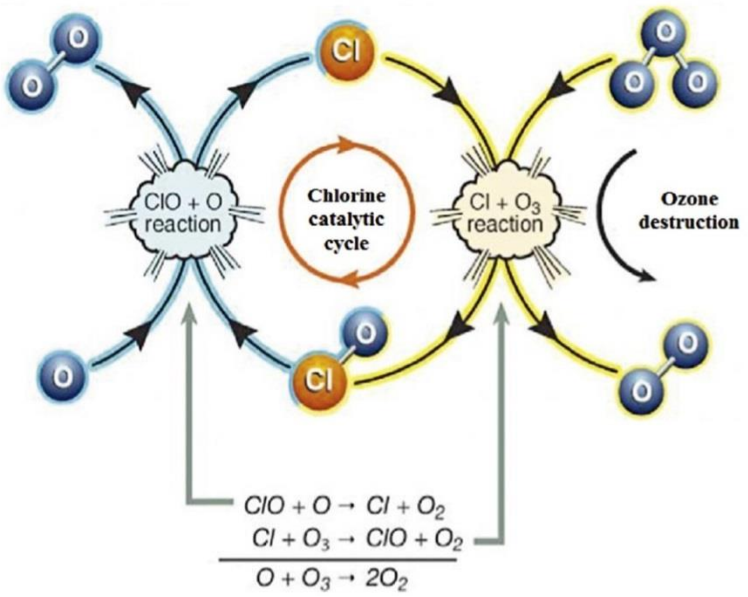

Figure 1.3. Desruction of ozone layer by CFCs. [1]

### *1.2.2. Heterogeneous catalysis*

Roughly 90% of all catalytic processes in chemical industry are heterogeneous catalytic reactions. Various types of solid materials are employed to catalyze a variety of reactions in the gas or liquid phase.

In heterogeneous catalysis, the phase of the catalyst differs from the phase of the reactants. Heterogeneous catalysis typically involves solid catalysts and gaseous reactants. Heterogeneous catalytic processes involve three stages: (i) adsorption of the substrate on the catalyst, (ii) the catalytic reaction (itself often a sequence of catalytic steps), and (iii) desorption of the products. The catalyst after desorption should be found in the same state as it was before adsorption and ready to be employed in the next catalytic reaction. Ideally, it can catalyze thousands of subsequent reactions, called catalytic cycles. Mechanisms in which the catalyst is not recycled are not considered catalytic.[4]

The catalytic properties of activity, selectivity and stability are closely related to the catalyst composition. Most catalysts have multiple components and have a complex composition (Fig. 1.4). Beside the active agent itself, catalyst components could possibly include a support, a promoter, and an inhibitor. The active agent causes the main catalytic action and without it, the catalyst has no effect. The promoter is added into the catalyst to enhance the activity, selectivity or stability for the extension of the catalyst life. On the other hand, an inhibitor is the opposite of a promoter. When added in small amounts, it diminishes activity, selectivity or stability and is used for the reduction of the catalyst activity for an undesirable side reaction.[5]

Moreover, metal catalysts are not usually used in their bulk form, but dispersed on a substrate (support) with high specific surface area, such as $Al_2O_3$ or $SiO_2$. Occasionally, the metal and the support both exhibit catalytic activity (referred to as bi-functional catalysts). An example is platinum dispersed on alumina support employed in gasoline reforming.[1]

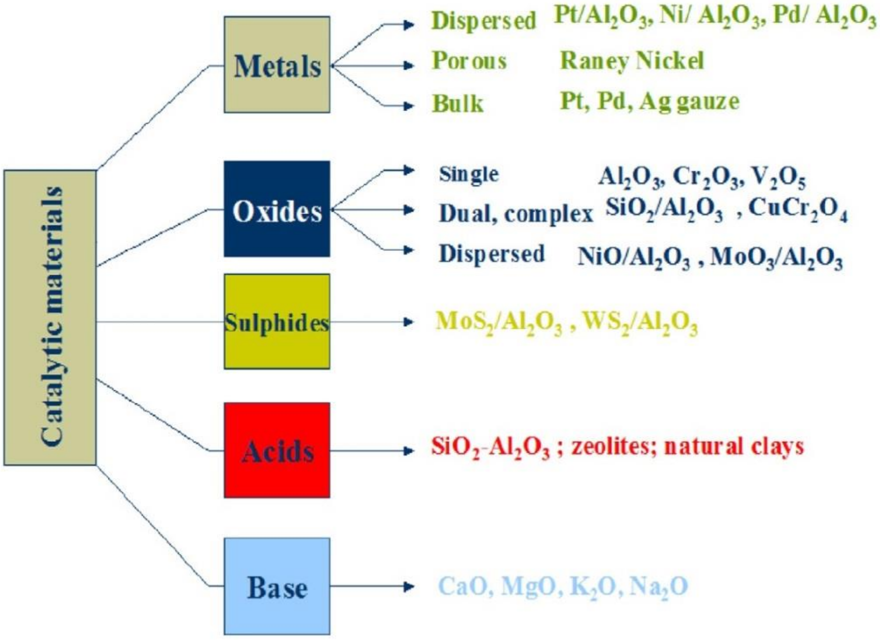

Figure 1.4. Classification of catalytic materials. [1]

In all heterogeneously catalyzed processes, in order for the catalytic reaction to proceed, at least one of the reactants must be attached for a significant period of time to the exterior surface of the solid catalyst. Thus, two distinct mechanisms can arise in the surface-catalyzed transformation of gas-phase species A and B to a product C, as shown on Figure 1.5.[6]

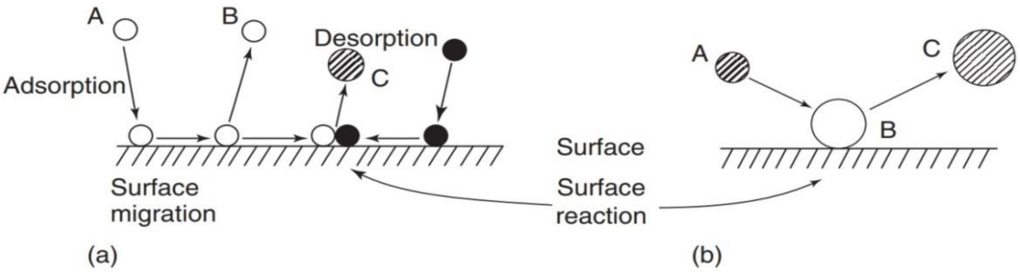

Figure 1.5. Two possible ways in which heterogeneous catalysis proceeds at a surface: the Langmuir–Hinshelwood mechanism (a) and the Eley–Rideal mechanism (b). [6]

In the first case (a), both species are bound to the surface and atomic reorganization takes place in the resulting adsorbed layer (the so-called Langmuir–Hinshelwood mechanism of heterogeneous catalysis). The other case (b) involves the attachment of only one of them on the catalytic surface, which is converted into product when the other impinges upon it from the gas phase (the Eley–Rideal mechanism). In the literature it is highlighted that the first of these mechanisms is more frequent than the second and that the distinction between them is sometimes blurred. [6]

To summarize, both heterogeneous and homogeneous catalysts play important roles in the chemical industry. Heterogeneous catalysts are more widely used in industrial processes than homogeneous catalysts due to their wider scope, the higher lifetime and the easy recycling. There are no homogeneous catalysts as yet for cracking, reformation, ammonia synthesis, etc. Nevertheless, homogeneous catalysts, due to their high selectivity, are becoming increasingly significant for the manufacture of tailor-made plastics, fine chemicals, pharmaceutical intermediates, etc.[3]

## 1.3. Mechanism of Catalysis

The following theories are proposed to explain the mechanism of catalysis:

*Adsorption theory:*

According to the adsorption theory of catalysis, the reactants (in gaseous state or dissolved in a solution) are adsorbed on the solid catalytic surface. The increase of the reactants concentration on the surface of the catalyst results in the increase of availability and probability of the occurrence of a reaction between two species, and thus increasing the reaction rate. Also, as the reactants abide to the catalyst surface, an amount of energy is released due to the exothermic nature of the process. The released heat is used in the reaction between the two species, thus enhancing the reaction rate.[7]

*Intermediate compound theory*:

As per the intermediate compound theory of catalysis, the reaction that is desirable is accomplished with the formation of an intermediate compound and the following decomposition of that compound into the final products. [7]

*Modern adsorption theory*:

The modern adsorption theory combines the old theory of adsorption to the intermediate theory of compound formation. According to this theory, the process of heterogeneous catalysis occurs in the following steps:

- The reactants diffuse to the catalyst surface. In this process, the reactants, at first, get in contact with the external surface, out of which some of them cross the barrier and enter the interior exposed surface that includes paths and cracks on the external surface.
- These molecules then become attached to the suitable sites available for adsorption.
- The reactants, when adsorbed to the surface have a higher probability of reacting with each other, forming an intermediate compound, after the reaction.
- After this process, the intermediate compound gets desorbed from the surface, which becomes available again for other molecules to adsorb.
- The intermediate compound then disintegrates to form the final products, which then diffuse out of the internal pores and the external surface of the catalyst.[7]

*Energy activation theory:*

According to this theory, catalyst changes the value of activation energy which can be crossed by the reactants easily and consequently products are formed. Arrhenius suggested that reactions should overcome a certain barrier in order to proceed. The change in the Gibbs free energy between the reactants and the products $\Delta G$ does not change in case of a catalytic reaction; however, the catalyst provides an alternative path for the reaction.

Moreover, the catalyst (heterogeneous, homogeneous, or enzymatic) affects only the reaction rate; it changes neither the thermodynamics of the reaction (Gibbs energy) nor the equilibrium composition. Thus, a catalyst can change kinetics but not thermodynamics of a reaction.[8]

## 1.4. Catalyst deactivation

Catalyst deactivation is a problem of continuous and increasing concern in the industrial catalytic processes. It involves the loss over time of catalytic activity and/or selectivity. The time scales for catalyst deactivation vary considerably; for instance, in the case of cracking catalysts, catalyst deactivation may occur in the order of seconds, while the iron catalyst used in the synthesis of ammonia may last for 5–10 years. Nevertheless, it is inevitable that all catalysts will decay.[9]

Typically, the loss of activity in a well-controlled process occurs slowly. However, process upsets or poorly designed hardware can bring about catastrophic failure. For example, operation of the reactor at extremely high temperatures must be avoided in steam reforming of methane or naphtha but the reactor should operate above a critical value of temperature at steam to hydrocarbon ratios.[9]

There are many mechanisms of catalyst deactivation; nevertheless, they can be classified into six distinct categories, which are briefly defined in Table 1.1.

Table 1.1. Mechanisms of catalyst deactivation [9]

| Mechanism | Type | Brief definition/description |
|---|---|---|
| **Poisoning** | Chemical | Strong chemisorption of species on catalytic sites, thereby blocking sites for catalytic reaction |
| **Fouling** | Mechanical | Physical deposition of species from fluid phase onto the catalytic surface and in catalyst pores |
| **Thermal degradation** | Thermal | Thermally induced loss of catalytic surface area, support area, and active phase–support reactions |
| **Vapor formation** | Chemical | Reaction of gas with catalyst phase to produce volatile compound |
| **Vapor–solid and solid–solid reactions** | Chemical | Reaction of fluid, support, or promoter with catalytic phase to produce inactive phase |
| **Attrition/crushing** | Mechanical | Loss of catalytic material due to abrasion<br>Loss of internal surface area due to mechanical-induced crushing of the catalyst particle |

## 1.5. Nickel catalysts

The nickel catalyst is employed in many chemical processes in industry and in organic synthesis because of its stability and high catalytic activity even at room temperature. The key characteristics of nickel used in hydrogen generation by steam reforming, in hydrotreating and hydrocracking, as well as in the hydrogenation of oils and fats, is its ability to absorb large quantities of hydrogen, which therefore increases the efficiency of the catalytic reaction. In addition, nickel is a costly-efficient catalyst compared to competing materials of the platinum group, while nickel is more abundant than platinum. Nickel-based catalysts set out competition for major industries such as food and oil refining.[10]

Despite palladium's standing as the premier amongst transition metals, nickel has long found application in organometallic chemistry with Sabatier awarded the 1912 Nobel Prize in Chemistry for the nickel-mediated hydrogenation of ethylene. In the last decade, there is an increasing interest to investigate the advantages of nickel catalysts as compared to palladium. Whereas palladium catalysis typically cycles in even, two-electron manifolds Pd(0)/Pd(II) and Pd(II)/Pd(IV), the corresponding nickel(I) and (III) oxidation states are more easily accessed, creating a plethora of catalytic opportunities. Notably, nickel catalysts have found widespread application in tandem with stoichiometric organometallic reagents allowing reactivity manifolds such as asymmetric cross coupling of alkylelectrophiles to be realised. [10]

The key advantages of nickel catalysts include: [11]

- High performance in reactions for which other metals were not efficient;
- Large variability of electronic states – Ni(0)/Ni(I)/Ni(II)/Ni(III);
- New reactions and transformation beyond the known limits of other metals;
- Facile activation and transformation of molecules that are chemically less reactive;
- Excellent perspective in photocatalytic and hybrid catalytic cycles. [11]

## 1.5. Hydrogenation processes

Catalytic hydrogenation is among the most useful and widely applicable process for the reduction of chemical substances and is being widely employed in organic synthesis both in research laboratories and industrial applications.[12]The catalytic hydrogenation of multi-functional molecules is alluring in many aspects. Hydrogenation is the main process in organic chemistry that the heterogeneous catalysts are applied and it is also used for the industrial synthesis of the so-called "fine chemicals". The exhibited selectivity if the catalyst towards various functional groups provides significant information about the catalyst properties and the successive steps of the reaction mechanism.[13] In most industrial processes the hydrogenation takes place in the gas phase, while many countries such as China, liquid-phase hydrogenation is also frequently applied.[14]

The main parameters that have a significant influence on the hydrogenation reaction and its products are:[15]

- The type of metal
- The catalyst support
- The metal concentration in the catalyst
- The catalyst prereduction
- The reaction temperature
- The type of solvent (only for liquid-phase hydrogenation)

Catalytic hydrogenation is used in the large-scale production of many chemicals, a very important example being ammonia, which is prepared via the Haber process of hydrogenation of nitrogen.[16] In food processing, one of the best-known catalytic applications is the hydrogenation of fats using nickel catalysts to produce margarine.[17][18]

### *1.5.1. Hydrogenation catalysts and applications*

There are two distinct types of hydrogenation catalysts, homogeneous and heterogeneous. Homogeneous catalysts are dissolved in a liquid media, forming one single phase. On the other hand, heterogeneous catalysts are categorized into two different types: those which are used in fixed-bed processing and those employed in slurry or fluidized-bed processing. In the first case, the catalyst is stationary and the reactants pass over it upward or downward. The employed catalysts are large particles in the form of cylinders, spheres, or granules. The second type of catalysts is fine powders which can be suspended readily in a liquid or gas. Fixed-bed processes are reported to be highly applicable for production in large scale, and indeed many bulk chemicals were synthesized by this approach. However, the vast majority of catalytic hydrogenations take place using slurry processing, since fixed-bed processing requires a dedicated unit, continuous production, invariant feed, large capital investment, and lengthy development to establish optimum conditions and adequate catalyst life. On the contrary, slurry processing allows variations in the substrate, multiuse equipment, easily changed reaction conditions, intermittent operation, and relatively quick development time. Moreover, the experiments in the laboratory scale are efficiently upgraded into industrial scale. [15]

The vast majority of catalytic hydrogenations have been undertaken using heterogeneous catalysts since the earliest stages. They were further developed and widened the scope of catalytic hydrogenation, especially for highly selective transformations. Nevertheless, heterogeneous catalysts have many advantages over homogeneous catalysts such as stability, easy separation from the product, ample variety of applicable reaction conditions, better catalytic performance toward the hydrogenation of hard-to-reduce functional groups such as aromatic nuclei and sterically hindered unsaturations and for the hydrogenolyses of carbon–carbon bonds.[12]

In many reports, group VIII metals (Fe, Ru, Os, Co, Rh, Ir, Ni, Pd, Pt) have been used to produce hydrogenation catalysts [19]. For the hydrogenation of aromatic compounds, nitriles and organic acids have been reported, including polymer-stabilized colloidal noble metal clusters [20-21], supported noble metal catalysts [22-25], Raney nickel [26], nickel alloys [22] and amorphous alloys [27-28]. Ziegler-Natta type of catalysts is a more complicated group of hydrogenation catalysts. Their catalytic reactivity follows the sequence: Ni >> Co ≥ Cu >> Fe ≥ Cr > V for transition metal compounds combined with organometallic reducing agents [19].

A broad variety of catalysts, such as Raney-nickel, so-called "amorphous Ni–B alloys" or Fe based catalysts are reported to exhibit exquisite catalytic characteristics for the liquid-phase hydrogenation of alkyne, although commonly harsh conditions are necessary, i.e., high temperature and pressure. Particularly in fine chemical production industry, mild conditions are preferred and thus, Pd is mostly the selected metal for alkyne hydrogenation.[29]

*Nickel-based catalysts*

Nickel-based catalysts are known to be active for a wide range of chemical reactions in various industrial processes. Reactions occurring in petroleum refining are particularly significant and include hydro-treating, hydro-cracking and hydro-processing [30]. Hydrogen production from ethanol (decomposition, steam reforming and oxidative steam reforming) is another important industrial process [31-33]. T. Wang *et al.* [34] studied a nanoporous nickel catalyst which exhibited remarkable catalytic activity in the reduction of a wide range of carbonates to produce formic acid in excellent yields with high selectivity. Ni-$Al_2O_3$ catalysts with metallic Ni loading were used for slurry phase CO methanation [35], while another study of the hydrodeoxygenation of eugenol demonstrated the efficacy of nickel-based catalysts [36]. J. Xiong *et al.* [22] tested different supports on nickel catalysts toward the hydrogenation of o-chloronitrobenzene, suggesting that titania was the most suitable in terms of activity and selectivity to o-chloroaniline. Furthermore, attempts have been made to replace platinum partially or completely by transition metal compositions as anodes for alkaline fuel cells that would retain performance in fuel cell electrodes without being too expensive. For example, N. Borchtchoukova *et al.*[37] found that Ni-based catalysts were suitable for replacing platinum. Finally, nickel-based catalysts proved to be useful in selective hydrogenation of medium or low distillate oil, in particular during the first-stage selective hydrogenation process of pyrolysis gasoline distillation [38].

The use of nickel as a hydrogenation catalyst is apparent if one considers nature.The hydrogenase enzymes employ of the widely available transition metals nickel and iron as catalysts toward the activation of dihydrogen or the protons reduction. The hydrogenase enzyme that contains nickel is not able to perform the hydrogenation of organic substrates, but it can activate dihydrogen at atmospheric pressure and ambient temperature.[39]

It is commonly established that the selective hydrogenation of C=C, C=O, and C=N bonds is feasible using Ni or Co metals. Kalyon *et al.* [40] investigated the liquid-phase hydrogenation of citral in n-hexane at different temperatures using the nanoscale borides $Co_2B$ $Ni_7B_3$. They concluded that the cobalt boride preferentially hydrogenates C=O bonds, while the nickel boride is selective for C=C double bonds.

It is widely acknowledged that alloys exhibit superior activity, selectivity and higher resistance to both sulfur and amine poisoning during numerous hydrogenation processes.[41-44] H. Li *et al.*[27] found that Ni-B amorphous alloy possessed comparable activity to that of Raney Ni but increased selectivity to ethylamine. Furthermore, their research revealed that Co-B amorphous alloy exhibited even higher selectivity to ethylamine despite its poor activity. Based on these findings, they manufactured a Ni-Co-B amorphous alloy with various Co/(Co+Ni) molar ratios, achieving higher activity and selectivity, when the molar ratio was equal and above 0.5. Moreover, X. Yan *et al.*[45] prepared a Fe-promoted Ni-P amorphous alloy catalyst and compared its catalytic performance to those of Ni-P, Fe-P and Raney Ni catalysts. They reported that the Ni-Fe-P catalyst showed superior catalytic activity and selectivity toward liquid-phase hydrogenation of m-chloronitrobenzene and p-chloronitrobenzene to corresponding chloroaniline. Another example of the alloys superior catalytic behavior in hydrogenation was provided by X. Chen *et al*.[46] They employed Ni-Al intermetallic compounds with different phases as catalysts for the hydrogenation of naphthalene to tetralin. It was suggested that NiAl is a highly active and selective catalyst with long-term stability and resistance to coking.

Generally, there are various catalysts employed in the ample variety of hydrogenation processes. Specifically, nickel and nickel-based catalysts are widely used in various hydrogenation reactions due to their high reactivity, easy availability and lower price.

### *1.5.2. Liquid phase hydrogenation*

Liquid-phase hydrogenation mainly used for comparison of catalyst activity for gas-phase high temperature hydrogenation industrial processes, but there are some compounds, which can be produced at low temperature liquid phase hydrogenation in industry. Hydrogenations in the aqueous phase of C–C triple bonds are extensively applied in the industrial manufacture of fine chemicals [47] and pharmaceuticals, for example for the production of Vitamin K or as final step in the Linalool synthesis.[48] After C–C-coupling by alkynylation of an organohalide or ketone, the occurred alkyne is semi-hydrogenated to the analogous alkene, although the complete hydrogenation to the alkane is undesirable.[29] Selective hydrogenation of aromatic ketones into the corresponding alcohols is of interest as the reaction products are broadly used as flavors and fragrances, as well as intermediates for the production of useful organic particles.[49]

Moreover, liquid-phase hydrogenation is one of the most promising and often-used techniques in environmental applications, such as nitrate removal from drinking water without the production of waste water. Pintar *et al.*[50] studied an ample range of reactant concentrations and reaction conditions using Pd/Cu catalyst toward liquid-phase reduction. They also investigated the influence of the catalyst loading and the initial nitrate concentration on the reaction rate. The catalyst with 4.7 wt.-% of Pd and 1.4 wt.-% of Cu supported by γ-$Al_2O_3$ showed very high efficiency for nitrate removal and high chemical stability at the experimental conditions tested. The catalyst concentration and the initial reactant concentration appeared to have no influenceon the nitrate removal rate.

Weerachawanasak *et al.* [51] conducted a comparative study for the interaction between Pd catalysts and micron-/nano-sized titania. The catalytic performance of the as-synthesized supported catalysts was evaluated during liquid-phase hydrogenation of phenylacetylene. The microstructural analysis revealed that the metal–support interaction was strong only for the nano-sized $TiO_2$ supported Pd catalyst, but not in the case of the micro-sized $TiO_2$. This strongly established interaction played a key role in the high catalytic performance of the supported Pd catalysts toward phenyl acetylene hydrogenation to styrene.

### *1.5.2.1. Kinetics of liquid-phase hydrogenation*

The kinetics of liquid-phase hydrogenation reactions were reviewed by U. K. Singh and M. A. Vannice with special emphasis on hydrogenation of α,β-unsaturated aldehydes [52]. The following aspects were highlighted by their research.

- It is critical to ensure the absence of all transfer limitations.
- The way that the solvent influences the heterogeneously catalyzed hydrogenation reactions is not well understood, but it was concluded that these effects can affect reaction kinetics through bulk fluid-phase interactions as well as by competitive adsorption with the reactants. Nonetheless, it was indicated that in the case of quasi-equilibrium between $H_2$ in the gas phase, the liquid phase and the adsorbed state, solvent effects can affect the surface coverage with hydrogen at a constant partial pressure of $H_2$. When the solvent effects are absent, the surface coverage of hydrogen does not depend on the liquid-phase $H_2$ concentration and is only influenced by the $H_2$ partial pressure in the gas phase.
- Liquid-phase hydrogenation reactions can be complex and affected but not limited by various factors such as process parameters, side reactions, metal–support interactions, and metal specificity. The high importance of the reaction dynamics study is underlined in order to properly understand these effects due to the major alterations in activity and product distribution that occur during reaction.
- Hydrogenation reactions are generally considered to be structure insensitive; yet, cases are reported in which hydrogenation reactions depend on crystallite size and exposed crystal plane.

### *1.5.2.2. Hydrogenation of maleic acid*

Succinic acid, the main product of maleic acid hydrogenation [53], is a product of considerable commercial importance and is used in the production of lacquers, dyes, surfactants, biodegradable plastics, green solvents, photographic chemicals, perfumery, esters and many other products [54]. One of its major commercial applications is in the production of 1,4-butanediol. It mainly manufactured from the hydrogenation of maleic acid, although a fermentation pathway is also feasible in which succinic acid is obtained as a byproduct.[53]

Aqueous-phase catalytic hydrogenation of maleic acid has been widely studied and it has been found that noble metal catalysts in combination with Pd, Re or Sn and supported by alumina, titania or carbon are the most promising for hydrogenation of 1,4 butanediol, γ-butyrolactone, tetrahydrofuran and their mixtures[53, 55-56]. The catalytic hydrogenation of maleic to succinic acid in the liquid phase has been also studied over Pd or Pt supported catalysts [57-58]. Ruiz *et al.*[57] and Vertes *et al.*[58] studied the influence of the different supports on Pt or Pd catalysts in a trickle bed type reactor, while P. D. Vaidya and V. V. Mahajani investigated the kinetics of the catalytic hydrogenation of maleic acid in a slurry reactor over $Ru/Al_2O_3$ catalyst.[53] The effect of the support nature on a palladium catalyst was thoroughly studied by M. A. Kulagina *et al*.[59] Various oxides, salts and carbon supports with extremely high low or high porosity were tested in both water and ethanol solutions. It was found that in the case of the non-porous supports the catalytic aqueous hydrogenation depends only on the support identity and the metal particle population on the catalyst surface. On the other hand, when ethanol was employed these factors were not operative, since ethanol is a much less polar solvent.

However, there is little information in the literature on the hydrogenation of maleic acid over Ni or Ni-based catalysts even though they exhibit particularly low tendency to isomerize alkenes during the hydrogenation [60].

# 2. Solution Combustion Synthesis

Part of the results presented here has been published in the *Advanced Engineering Materials Journal, 2018, 20, 1800047, in the Special Section: Exothermic and Non-Isothermal Processing of Advanced Materials*

## 2.1. Introduction

Combustion synthesis (CS) is a widely used process for the synthesis and processing of advanced structural and functional ceramics, catalysts, composites, alloys, intermetallics and nanomaterials.[61-62]The term 'combustion' covers flaming (gas-phase), smouldering (heterogeneous) as well as explosive reactions. The exothermicity of the reduction-oxidation or electron transfer chemical reaction is exploited to synthesize useful materials.[61] Up to 2008, combustion synthesis has been utilized in order to fabricate more than 1000 kinds of oxides powders[63] in more than 65 countries [64].

Combustion synthesis is characterized by some features which make it a very attractive method for the manufacture of technologically useful materials at lower costs, compared to conventional ceramic methods. Some of the noteworthy advantages of CS are:[65]

- high reaction temperatures with relatively low preheating temperature
- quick heating rates
- short duration of reactions
- relatively simple equipment
- products with high-purity
- stabilization of metastable phases and
- products with any size and shape

Depending on the nature of reactants (elements or compounds; solid, liquid or gas) and the exothermicity (adiabatic temperature, $T_{ad}$), combustion synthesis can be categorized as: self-propagating high temperature synthesis (SHS); low-temperature combustion synthesis, solution combustion synthesis (SCS), gel-combustion, sol–gel combustion, emulsion combustion, volume combustion (thermal explosion) and others.[65]

**Solid state synthesis**

In solid state combustion all of the initial reactants as well as the intermediates and the final products are in solid state and Merzhanov *et al.*[66] started working on it in 1967. Solid state combustion can occur in two different modes: Linear or self-propagating high temperature synthesis (SHS) and bulk or volume combustion synthesis (VCS). In both cases, the reactants are pressed into a, usually cylindrical, pellet. Then, an external source is usually used to ignite the pellet locally (SHS) or uniformly (VCS), which initiates an exothermic reaction, but there are also cases of self-ignited reactions. In SHS, the hot combustion wave (2000-4000K) passes through the pellet yielding the products, whilst in VCS, it is heated uniformly until the simultaneous reaction takes place throughout the volume.

The high scale of heterogeneity in conjunction with the high reaction temperatures complicates the composition of nano structured materials. However, several methods have been suggested to prepare nanomaterials using SHS:

- SHS synthesis followed by intensive milling
- SHS synthesis with mechanical activation
- Chemical dispersion (SHS synthesis is followed by chemical treatment)
- Alkali metal molten salt assisted combustion (SHS synthesis with additives)
- Carbon combustion synthesis

SHS offers a good possibility for the preparation of a wide range of advanced materials such as refractory materials, intermetallics and alloys. Those are used in aerospace materials, as cutting tools, as abrasives, as high temperature lubricants, for hydrogen storage, as parts of ceramic engine, in fuel cells, as semiconductors and as catalysts.[65, 67]

## 2.2. Solution Combustion Synthesis (SCS)

A combination of combustion synthesis and reactive solution methods leads to SCS.[52] SCS, which was firstly proposed by Patil *et al.*[61], is being used widely to prepare oxide materials for numerous applications. In the specific case of Solution Combustion Synthesis (SCS), the exothermicity of the redox (reduction–oxidation or electron transfer) chemical reaction is employed to manufacture advantageous materials. According to the Web of Science, more than 5000 articles related to SCS have been published over the last 20 years. This growth of interest can be attributed to the method simplicity and its abundance of applications. [68]

Solution combustion synthesis is sometimes reported in the literature as gel combustion synthesis, auto-combustion, aqueous/wet combustion synthesis, solution combustion method (SCM), one-pot combustion synthesis, glycine-nitrate based solution combustion synthesis, urea nitrate combustion synthesis, auto-ignition synthesis, etc.

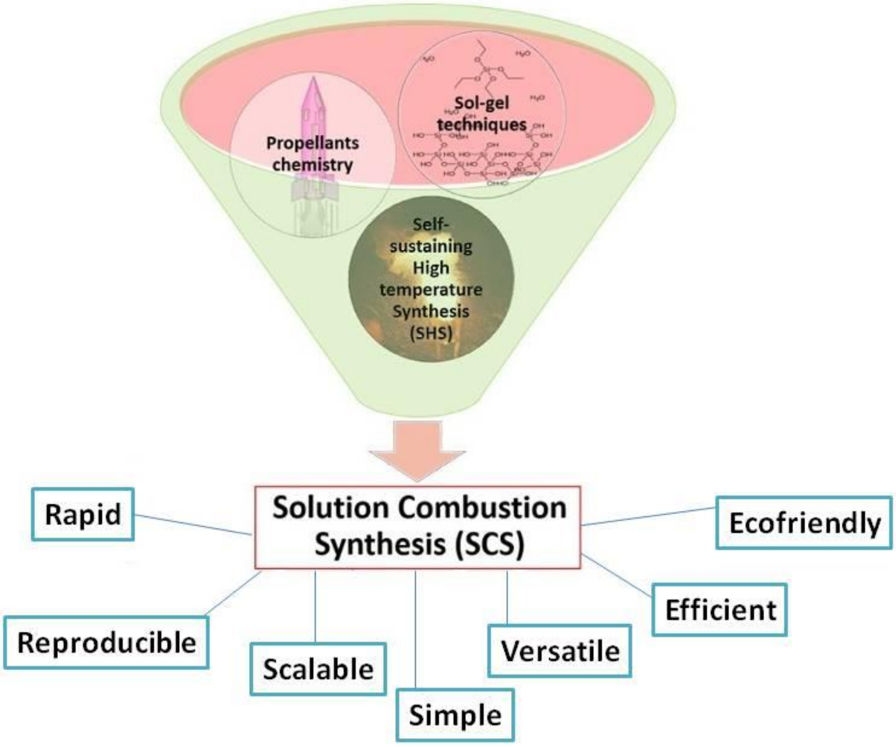

Figure 2.1. Groundwork and features of SCS.[69]

SCS comes from sol-gel chemistry [70] and propellant chemistry [71], despite the fact that it employs a quicker process than sol-gel synthesis [72] and it is recommended for multicomponent oxides [73]. Between 1985 and 1993, Patil and co-workers combined for the first time propellant chemistry with the production of nanomaterials in solution, studying the formation of complexes between propellants and metal cations.[74-75] This research provided a huge impulse to the following studies regarding Solution Combustion Synthesis and signified the start of using SCS for the effective and fast synthesis of inorganic substances.[69]

Typically, SCS incorporates a cascade of self-sustaining redox reactions in a homogeneous aqueous solution of reagents containing metal nitrates (oxidizers) and various fuels. The prevalence of this class of oxidizers is possibly justified by their good solubility in water and the relatively low decomposition temperature that leads to the formation of active oxygen. For example, the onset decomposition temperature of aluminium nitrate nonahydrate [$Al(NO_3)_3\cdot 9H_2O$] is ~130°C, while aluminium sulfate [$Al(SO_4)_3$] decomposes at ~600°C. The employed fuels can be classified in correspondence to their chemical structure, i.e. the type of reactive groups (e.g. amino, hydroxyl, and carboxyl) bonded to the hydrocarbon chain. The reaction between fuel and oxygen- containing species, which are formed during the nitrates decomposition, provides high-temperature rapid interaction. Typically, an initial liquid solution of reactants is preheated to a temperature range between 150–200°C, where the water is rapidly evaporated and the remaining reacting solution dries up and its temperatures further increases. Within a short period of time (a few seconds up to few minutes), it ignites and rapid exothermic reaction (Fig.2.2) produces powder forms directly in the nanoscale with composition depending on initial reactants. This process not only yields nanosized oxide materials but also trace amounts of rare-earth impurity ions are allowed to be doped homogeneously in a single step. [76]

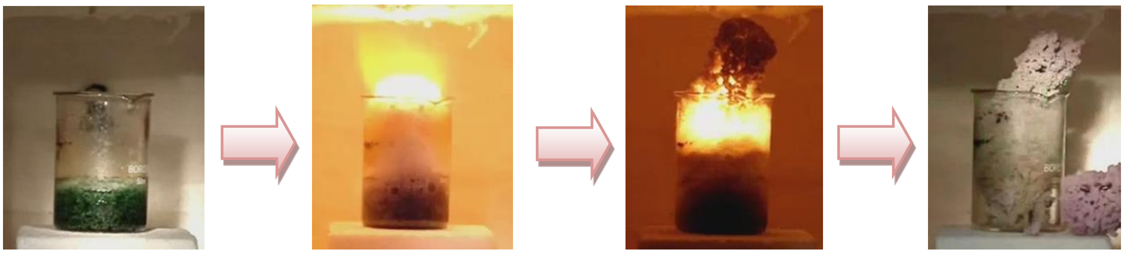

Figure 2.2. Structure of SCS-derived product as it emerges during SCS.*

However, a disadvantage of the SCS is the possibility of $NO_x$ emission during the reaction. Metal nitrates can be subjected to a partial thermal oxidation before the reaction takes place, as long as fuels containing nitrogen atoms can decompose producing $NO_x$. Though, $NO_x$ emissions are easy to trap, using scrubers. [77]

### *2.2.1. SCS modes*

Depending upon the nature of precursors and the process conditions, SCS may occur as either volume or self-propagating combustion modes. Both modes are employed for catalyst manufacture. In the first mode, which is called *volume combustion mode or thermal explosion* (Fig.2.3), the entire volume of the reacting mixture is heated uniformly to the boiling point of the solvent (stage I). In stage II, there is a relatively long constant temperature, where the free

---

* https://www.youtube.com/watch?v=u3IDWm3XZxI

and portion of bound water is evaporated. This stage is followed by a higher heating rate (stage III) and then, at the ignition temperature ($T_{ig}$) it increases to a maximum value ($T_m$, stage IV), while cooling stage (stage V) succeeds it.[78-80]

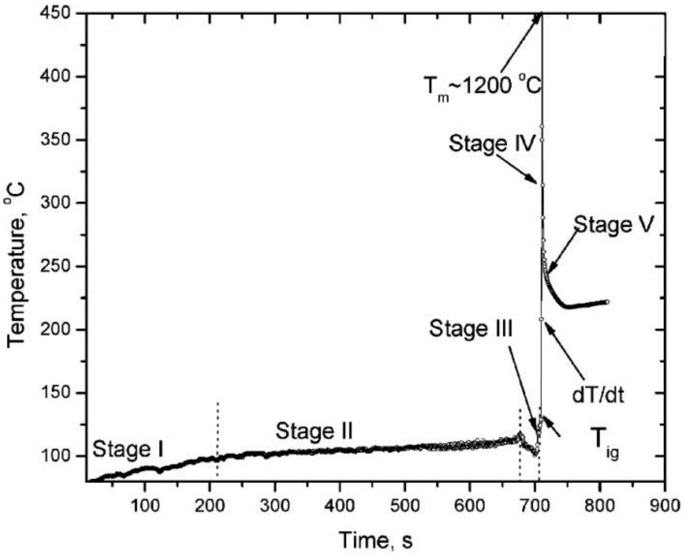

Figure 2.3. Time – temperature profile of $Fe_2O_3$ synthesis in $Fe(NO_3)_3$+glycine system in volume combustion mode. [80]

In case of the, as called, *self-propagating combustion mode* [81] (Fig.2.4a), a small volume (~1mm$^3$) of the precursor mixture is heated locally for the combustion initiation and then it is propagated along the remaining reactive mixture in the form of a combustion wave. The time – temperature profile on Figure 2.4b, as reported by K. V. Manukyan *et al.* [82], suggests that the preheating stage in this mode is shorter, in comparison with the volume combustion mode.

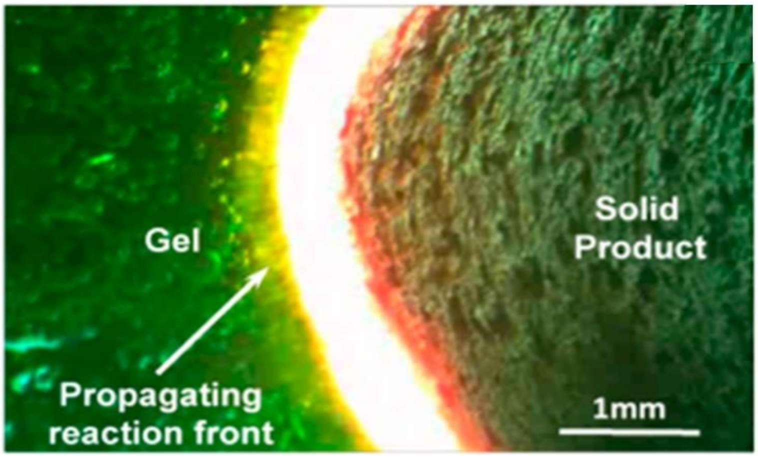

a

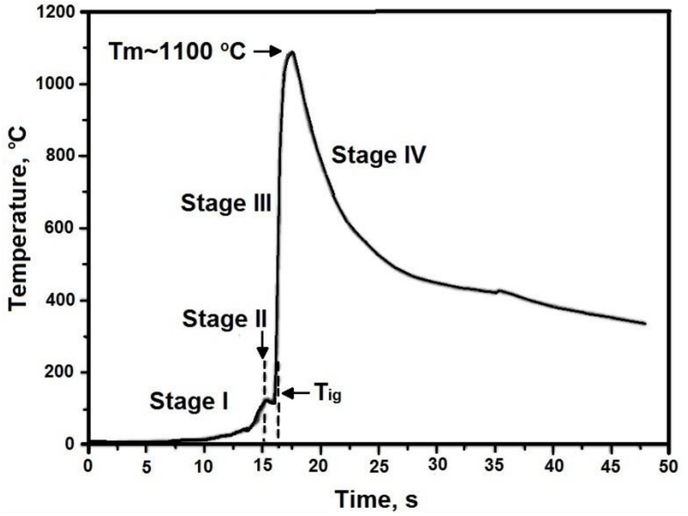

b

Figure 2.4. Reaction in nickel nitrate+glycine system in self-propagating combustion mode (a) andtime – temperature profile of the process (b). [82]

### *2.2.2. SCS heating routes*

Various methods have been reported for heating the precursor solution and a specific SCS route is created for each method. The simplest method is placing a glass or ceramic container with the initial reactive mixture on a hot plate [83] or inside a preheated furnace [84]. In most cases, the employed temperature range is between 500-1500°C. Heating, solvent evaporation, gel formation and decomposition, self-ignition, combustion and final products formation proceed in one technological step. This approach is the most ordinarily operated heating method for SCS of catalysts.[68]

Another commonly employed SCS route is the so-called sol-gel combustion synthesis [85], also mentioned as gel CS [86-87]. In this approach, the precursor, reactive aqueous solution is dried at a temperature below the boiling point of the solvent, where the unbound water evaporates and a gel-type media forms. Benefiting from the low viscosity of the gel, the impregnation of the solution in a broad range of porous materials is feasible, facilitating the synthesis of catalysts on carriers. Various studies have shown that the accomplishment of the SCS reactions is possible in those impregnated layers, resulting in the synthesis of desired compounds and this route is called impregnated layer CS.[63, 78, 88] The employed layers can be inert or active from the reactivity point of view, and thus CS in porous inert media [89-90] or CS in porous active media [91-92] may be outlined. Typically, inert layers are used to manufacture supported catalysts, while the active media are used to synthesize materials that have relatively low heats of reaction and hence, the combustion of the active layer expedites the propagation of the combustion front. In the case of use a porous media, such as silica or alumina, in order to control the particles size of the products, the route is called template-assisted SCS.[93-95]The porous material is removed (dissolved) after synthesis and nanoparticles with a narrow particle size distribution or nanotubes are obtained.[68]

Microwaves are a relatively novel heating method of the precursor solution up to the self-ignition temperature and this approach is called microwave-assisted SCS [96-97]. It has fundamental differences with the conventional heating routes; heating is directly generated in the materials as the electromagnetic field interacts with electric and magnetic dipoles, which are responsible for the materials' dielectric, electric and magnetic properties [68]. As an example, Ajamein *et al.* reported the synthesis of CuO/ZnO/$Al_2O_3$ catalysts using microwave-assisted solution combustion synthesis for hydrogen generation through steam methanol reforming reaction. The influence of fuel/nitrates ratio and microwave irradiation was evaluated and the results revealed that application of microwave oven instead of conventional furnace led to higher crystallinity of CuO and ZnO species, homogeneously smaller particles, respectively and higher specific surface area of the catalysts. Moreover, increased fuels/nitrates ratio led also to the enhancement of surface area and to better dispersion of different species. [98]

Many features of SCS are common with the liquid aerosol flame synthesis. In many modifications of this method, such as spray pyrolisis [99], emulsion evaporation (emulsion CS) [100] the initial precursor medium is an aqueous solution containing fuel(s) and oxidizer(s). However, usually the reactions take place in the external gaseous flame. The aerosol SCS was established, where the production of hollow metal spheres takes place in the flux of inert gas solely because of the - fuel - oxidizer reaction.[101]

Recently, a new SCS-based route was reported for the synthesis of high-quality thin films for electronic devices and solar cell applications.[87, 102-103] In this approach the initial reactive solution is deposited on a substrate using spin coating or spraying techniques. Combustion of thin precursor layers results in uniform high-qualitative oxide films.[68]

### *2.2.3. Thermodynamic aspects*

Generally, SCS involves self-sustained redox reactions between metal nitrate(s) and reducer(s), which are mixed at the molecular level and possess all the features of other combustible systems. The driving force for such redox reactions is the system's tendency to minimize Gibbs free energy by converting chemical potential into heat. By definition when Gibbs free energy is minimum, the system is in the equilibrium state. Thus, the initial state of SCS system can be characterized as a nonequilibrium quasi-stationary state. It is indeed nonequilibrium due to the fact that Gibbs free energy is not minimal and it is quasi-stationary as there are not significant changes for a reasonably long period of time. During combustion, the system's state is moved to an equilibrium state that will last indefinitely (thus be stationary) if there is no interaction between the sample and the surrounding atmosphere. On the long time scales though, the sample exchanges energy with the environment. The large difference in temperature between the sample and the environment that is caused by the combustion reaction, results in alteration of the sample's temperature. After the cooling period to ambient temperature, the sample reaches a new equilibrium steady state.[68]

A widely accepted scheme that describes the stoichiometric equilibrium combustion reaction (using metal nitrite as an oxidizer and glycine as a fuel) is the following:

$$M^v(NO_3)_v + (\frac{5}{9}v\varphi)CH_2NH_2COOH + v\frac{5}{4}(\varphi - 1)O_2$$
$$\rightarrow M^vO_{\frac{v}{2}}(s) + (\frac{10}{9}v\varphi)CO_2(g) + \frac{25}{18}\varphi H_2O(g) + v(\frac{5\varphi + 9}{18})N_2(g)$$

where $M^v$ is a v-valent metal and $\varphi$ is the fuel/oxidizer ratio; $\varphi$ =1 implies that the initial mixture does not require atmospheric oxygen for complete oxidation of the fuel, whereas $\varphi$>1 (<1) signifies fuel-rich (lean) conditions. [64]

It has thus been suggested that SCS reactions may be characterized by the following four parameters:

*Initial temperature ($T_o$)* is the average temperature of the reagent solution before the reaction is ignited;

*Ignition temperature ($T_{ig}$)* represents the point at which the combustion reaction is spontaneous without an additional supply of external heat;

*Adiabatic combustion temperature ($T_{ad}$)* is the maximum combustion temperature achieved under adiabatic conditions;

*Maximum combustion temperature ($T_m$)* is the maximum temperature reached in the actual configuration, i.e., under conditions that are not adiabatic.

As a general rule, the ignition process is obtained with a small, but significant amount of reagent solution. When this solution is rapidly heated above the temperature where the chemical reaction rate is high enough, the heat release rate is higher than the dissipation of heat.[104] A value of $T_{ig}$ is defined not only by thermal properties of the system but also by a type of reductant, acidity of solution, etc. In most cases $T_{ig}$ is determined experimentally.[105] The combustion temperature measurements are almost always much smaller than the calculated adiabatic values. Irradiated losses, incomplete combustion and air heating contribute to a decrease in the actual combustion temperature. However, $T_m$ depends on a number of factors such as the type and amount of reactants, ambient pressure, temperature, humidity, etc.[104]

Calculation of $T_{ad}$ is often impossible due to the lack of data on standard enthalpy of formation, the heat capacity of compounds, and the ignition temperature.[63] Measurements of $T_m$ are often difficult due to high rates of SCS processes. For SCS reactions with glycine yielding oxides and hydroxides, the formation of calcium carbonate is also reported.[105]

### *2.2.4. Influence of various parameters on the SCS-derived products*

There are certain features of SCS that provide the unique characteristics of the derived products. First of all, the initial reaction takes place in the aqueous phase allowing the mix of the reactants on a molecular level, thus permitting narrow and consistent formation of the desired composition on the nano scale. In addition, the high reaction temperature ($T_c$) establishes high purity with no residual carbon and the crystallinity of the produced foams is governed by the cooling rate. This characteristic plays a key role in skipping high-temperature product calcinations which is an additional step and usually follows the conventional approaches, to achieve the desired phase composition. Last but not least, the short process duration and the generation of many gaseous products during SC inhibit the particles' growth benefiting the synthesis of nanocrystalline powders with high specific surface area, a very important feature for catalysts synthesis. [61, 63, 80, 106]

#### 2.2.4.1. Type of reducer

The nature, the type of the fuel as well as the fuel to oxidizer ratio are important factors that significantly influence the structural and surface properties of the final SCS products. Patil *et al.*[61] have concluded that the combustion can fluctuate from flaming to non-flaming mode. Flaming reactions are attributed to the generation of gaseous byproducts such as NO, $NO_2$, $NH_3$, CO, $CO_2$ etc. The nature of the organic reducer seems to be explicit for the metal employed for SCS and/or the type of mixed metal oxide formed.[107] The organic substance that is used as fuel for the synthesis of SCS catalysts should have the following characteristics:

- Water solubility; however, organic solvent can also be employed in order to improve fuel solubility.
- Compatible with metal nitrates, as reaction should not lead to explosion.
- Operation as metal dispersing agent; in some cases facilitates complexes formation between fuel and metal species.
- Melting point should be below 250 °C and its ignition temperature below 500 °C.
- To be fully decomposable; during reducer decomposition large amounts of gases are formed that can improve catalyst textural properties. [108]

Urea and glycine are known to be among the most popular fuels for synthesizing highly uniform oxide ceramic powders.[107] Hadke *et al.* [109] who produced NiO nanopowders using urea or glycine, suggested that glycine exhibited better interaction with the metal cations, caused a more intense combustion, while the final product had a branched cotton wool structure with softer agglomerates and lower residual carbon. Additionally, when glycine was used, the as-burnt nanopowders possessed larger crystal size and lower densification ability. On the contrary, the urea-nitrate system's products had spherical shape with hard agglomerates and small crystallite size, resulting in better sintering ability of the as-produced nanopowders. Fathi *et al.* [110] also compared glycine and urea in their studies for the synthesis of $Fe_3O_4$ oxide and they suggested a potential scheme of what happens to the powder microstructure in both cases, as presented on Figure 2.5. In this case, glycine had a smoldering combustion with intensive gas generation and high temperature, resulting in spongy powders with bigger crystallite size and higher porosity than urea. Conversely, when urea was employed, the precipitation of the metal cations inside the combustion gel was favored, leading to particles nucleation and extended agglomeration when combustion ended.

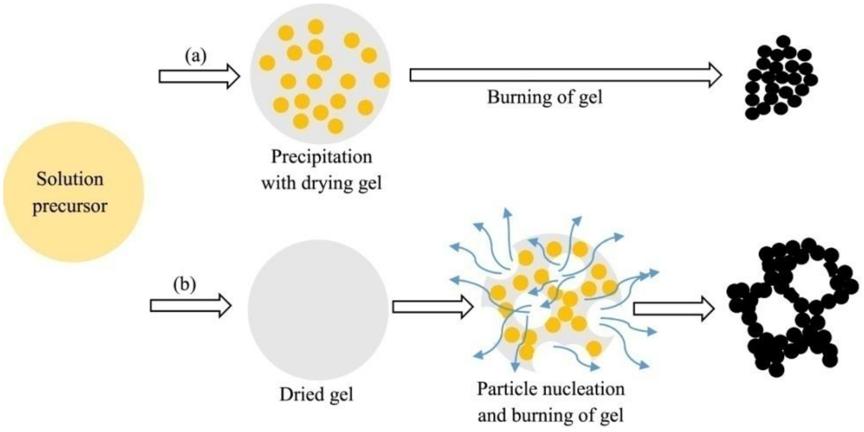

Figure 2.5. A potential microstructural evolution scheme during combustion using a) urea and b) glycine as reducer.[110]

Furthermore, the employment of various organic compounds as reducers like alanine, asparagines, serine, methyl cellulose, ammonium acetate, ammonium citrate and ammonium tartarate was explored. Using a combination of different fuels such as citric and succinic acid, citric acid and glycine, urea, monoethiloamine and alanine, etc was also investigated as an option. Despite the fact that complex fuels favor the formation of nanosize particles, a further calcinations treatment is sometimes required in order to remove organic residuals.[64] It is very interesting though, that some of the fuels were found to be specific for a particular process and also that, recent studies have been focused on the role of fuel in controlling the particle size and the microstructure of the yielded products.[110-111] All these fuels are the source of carbon and hydrogen, which during the combustion form $CO_2$ and $H_2O$, releasing heat. Moreover, they act as complexing agents with metal ions and that facilitates the solution's cations' mixing homogeneously.[107] The influence of the reducing agent on the structural and textural properties of various materials and catalysts prepared by SCS are listed in Table 2.1.

Table 2.1: Various SCS-derived catalysts and materials using different fuels [107]

| Catalyst/material | Fuel | Fuel effect |
|---|---|---|
| **$Co_3O_4$/γ-$Al_2O_3$** | Urea, citric acid, glycine or glycerine | Glycine-prepared catalyst showed the highest velocity of combustion, lower combustion temperature and higher methane conversion [112] |
| **$LaFeO_3$and$LaMnO_3$** | Glycine or ethylene glycol | Nature of the fuel markedly affected the surface area and crystalline size of La-based perovskite oxides because of combustion characteristics [113] |
| **$LaMnO_3$-MeO (Me=Mg, Ce, Zn, Zr)** | Glycine, alanine or glycerol | Glycine-prepared mixed metal oxides showed higher surface area and activity for methane combustion [114] |
| **$CoCr_2O_4$, $CuCo_2O_4$and spinel/$CeO_2$ (ή$ZrO_2$)** | Glycine or glycerol | Glycerol-prepared mixed metal oxides showed lower crystalline size, higher surface area and activity for n-hexane combustion[115] |
| **CuO-ZnO-ZrO2** | Glycine or urea | Higher surface area, $CO_2$ conversion and methanol yield a lower fuel amount were achieved [116-117] |
| **5mol.% Mn/$CeO_2$** | Urea, glycine or polyethylene glycol | Amount and nature of fuel affect not only Mn dispersion but also its oxidation state. Lower glycine or higher urea concentrations facilitated higher flame temperature [118] |

In summary, the type and the amount of fuel are very important parameters that severely influence the nature of the combustion process, the phase composition, the microstructure and the morphology of the final powders. They can also affect the strain, the surface properties, the oxidation vacancies as well as the oxidation state of metal cations in the resulting material.

### 2.2.4.2. Fuel-to-oxidizer ratio

The main parameter that controls the amount of fuel added in the initial SCS mixture is the fuel-to-oxidizer ratio, generally known as $\varphi$. The original definition of this ratio was given by Jain *et al.*[71], according to the concepts of propellant chemistry. The overall SCS reaction by using for example a metal nitrate as oxidizer and glycine as fuel can be written as follow:

$$M^{v}(NO_3)_v + (\frac{5}{9}v\varphi)CH_2NH_2COOH + v\frac{5}{4}(\varphi - 1)O_2$$
$$\rightarrow M^{v}O_{\frac{v}{2}}(s) + (\frac{10}{9}v\varphi)CO_2(g) + \frac{25}{18}\varphi H_2O(g) + v(\frac{5\varphi + 9}{18})N_2(g)$$

where $M_v$ is a v-valent metal and $\varphi$ is the so-called "elemental stoichiometric coefficient" or fuel-to-oxidizer ratio. This parameter indicates the amount of fuel with respect to oxidants and it is not representative of the combustion mixture, because reducers can be the fuels as well as metal cations and some counter anions. Moreover, $\varphi = 1$ represents a stoichiometric ratio, $\varphi > 1$ corresponds to fuel rich mixture and $\varphi < 1$ means fuel lean mixture. It is worth noting that $\varphi$ is only a sufficient approximation and not the real fuels-to-oxidizers content due to the potential mistakes concerning the elements' oxidation state in the final product, as concluded by Zhang *et al*.[119]

Solution combustion synthesis is not an adiabatic process and the measured temperature is always lower than the theoretical one since there are heat losses that are further enhanced by the massive gas generation.[120] The theoretical temperature for an adiabatic process and the experimental trend of temperature as a function to $\varphi$ parameter is demonstrated on Figure 2.6. However, it should be highlighted that the observation would be altered in case of another system depending upon the complexities of the cations involved and the precursor SCS mixture.[69]

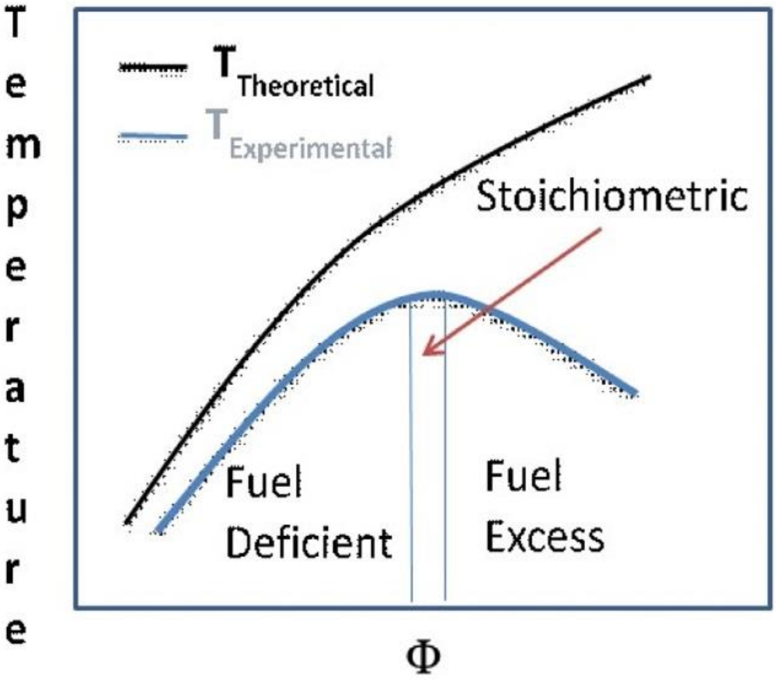

Figure 2.6. Theoretical and experimental temperature curves vs $\varphi$ ratio.[69]

Generally, the combustion process can take place from fuel-lean to fuel-rich conditions, although the nature of combustion and especially the reaction's exothermicity are strongly controlled by the fuel-to-oxidizer ratio.[82, 92, 121] Taking that into consideration, the combustion reaction can be categorized into the following cases:

- *Extremely fuel-deficient combustion*. Flameless smoldered reaction is yielded accompanied with high generation of gases. The majority of these gases are toxic $NO_x$, [111] so it is not considered to be a preferable pathway.
- *Fuel deficient combustion*. The combustion that takes place is sluggish, but highly porous materials with soft agglomerates and better powder properties are produced, since there is large emission of gases.[69]
- *Stoichiometric combustion*. A self-propagating auto-ignited violent reaction happens, accompanied with flame that appears for 3-5 sec. The combustion exothermicity is very high and up to 1800°C can be achieved during combustion. The products consist of hard agglomerates due to the localized partial sintering. [69]
- *Fuel excess combustion*. The reaction is similar to the stoichiometric combustion. It is recommended when the possibility of explosive combustion occurs for safety reasons.[73]

- *Extremely fuel-rich combustion*. In this case, the reaction undergoes the gel decomposition resulting in charring of the product, without the existence of flame during combustion.[69] The as-burnt materials are usually amorphous with high concentration of residual carbon that requires a longer calcination period in the air for its removal. Most of the emitted gases are involving toxic CO, making this an unattractive option.[122]

The importance of fuel to oxidizer for the production of $TiO_2$ with SCS and its influence on photocatalysis was recently investigated by S. Challagulla and S. Roy.[123] Nano $TiO_2$ was synthesized using glycine, urea, and oxalyldihydrazide as reducers. The oxidizer to fuel ratio from lean to rich conditions also found to have a crucial impact in determining the polymorphic percentage concentration in the synthesized $TiO_2$ powders. However, diffuse reflectance spectroscopy and photoluminescence spectroscopy studies did not reveal any critical differences in the products electronic properties. The presence of various $TiO_2$ polymorphs resulting from difference in fuels during combustion affected the exhibited photocatalytic activity toward methylene blue degradation and hydrogen production. In materials science, polymorphism is the ability of a solid material to exist in more than one form or crystal structure. Polymorphism can potentially be found in any crystalline material including polymers, minerals, and metals, and is related to allotropy, which refers to chemical elements. The three existing polymorphs of titania ($TiO_2$) are anatase, rutile and brookite, with the first two being the most popular. They are all different structures of an octahedron and their structural differences offer them different macroscopic properties.

Zhou *et al.*[120] calculated the adiabatic combustion temperature as well as the quantity of the generated gaseous products and compared the results with experimentally measured temperatures (Fig.2.7). They used lithium nitrate, titanyl nitrate and citric acid as model system, which can be described by the following overall reaction:

$$2LiNO_3 + TiO(NO_3)_2 + 1.11\varphi C_6H_8O_7 + (5\varphi - 5)O_2 \rightarrow Li_2TiO_3 + 6.67\varphi CO_2 + 2N_2 + 4.44\varphi H_2O$$

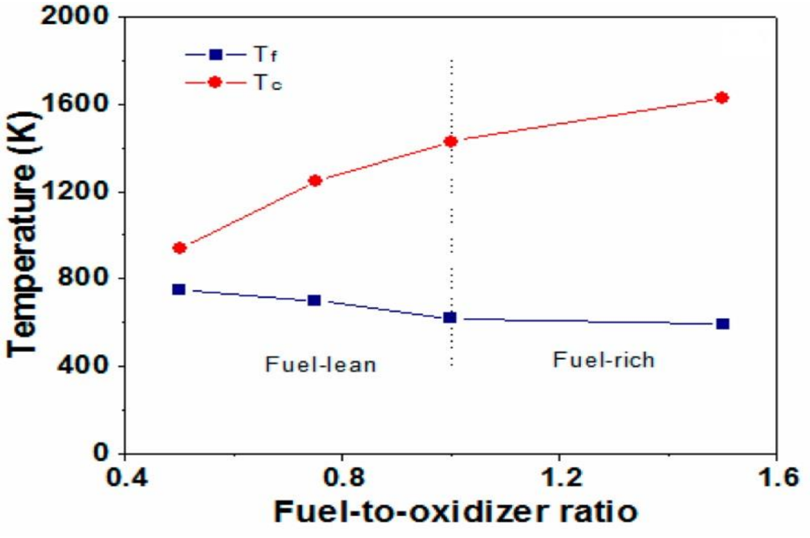

a

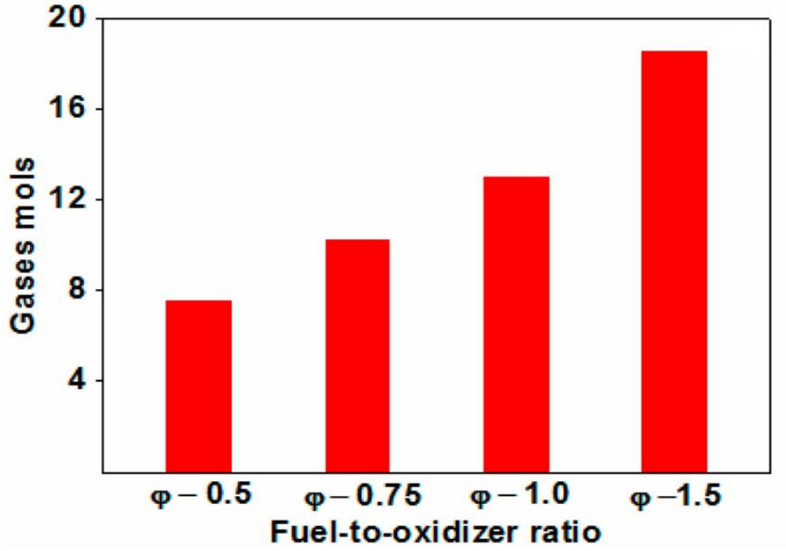

b

Figure 2.7. Calculated ($T_f$) and measured ($T_c$) maximum temperatures as a function to $\varphi$ (a), as well as calculated volumes of gases produced at room temperature and ambient pressure at different $\varphi$ (b). [68, 120]

Figure 2.7a illustrates the measured combustion temperatures in contrast with the thermodynamically calculated results. The observed significant deviation of the experimental results from the calculated data was attempted to be explained by two factors: i) the experimental condition were not adiabatic ii) for fuel-rich conditions, the fuel does not completely react with the atmospheric oxygen due to infiltration limitations. Although, Varma *et al.*[68] pointed out in their review that the utilization of an incorrect assumed reaction route and the inaccurate measurement of the combustion temperature could also possibly lead to such large discrepancy. This signifies that the reactions that are responsible for the product formation could be different from the reactions accountable for the self-sustained combustion process. Hence, the maximum combustion temperature may occur in the gas phase and not in the condensed phase that it is typically located.

As discussed before, the flame temperature of combustion can vary by changing the fuel-to-oxidizer ratio ($\varphi$). Bedekar *et al.*[124] exploited this fact and stabilized $YCrO_3$ and $YCrO_4$ preparation. They used glycine and meal nitrates as precursors and they found that in stoichiometric conditions $YCrO_3$ yielded, while in fuel lean conditions $YCrO_4$ was synthesized.

Moreover, Zhou *et al.*[120] concluded that the amount of the generated gases increases by increasing of the $\varphi$ parameter. The emitted gases in the combustion process influence the temperature to a large extent, due to the great amount of heat that may be taken away by the gas flow. In the fuel-rich conditions, the volume of the generated gases is two times more than that in the fuel-lean conditions. For the reasons mentioned above, the maximum measured temperature of the fuel-lean system is much higher than that of the fuel-rich system.

On Table 2.2, various catalysts are listed as well as the fuel that was used for each catalyst. Furthermore, the effect of the different fuels on the catalysts' properties is also mentioned.

Table 2.2: Various SCS-derived catalysts and materials using different fuels. [107]

| Catalyst/material | Fuel | Fuel effect |
|---|---|---|
| **$LaMnO_3$** | Urea + $NH_4NO_3$ | Perovskite crystallinity and carbonaceous residue formation are dependent on urea to oxidizer ratios. $NH_4NO_3$ increased surface area and methane combustion[114] |
| **$NiO\text{-}MoO_3/\gamma\text{-}Al_2O_3$** | Urea | Increase of urea to oxidizer ratio improved the combustion reaction. No significant changes in the HDS catalyst performance were observed [115] |
| **(La, Sr, Ce, Ba) (Ce, Fe, Y)$O_{3-\lambda}$** | Citric acid | The combustion intensity increased as metal-citrate complex stability decreased. Low citrate/oxidant ratios decreased particle size [116] |

To sum up, the fuel-to-oxidizer ratio is a parameter to control the fuel amount in the initial SCS mixture. It has found to influence the structure and the phase composition of the final powders as well as the nature of combustion. In general, stoichiometry is preferred in order to maximize the reaction's exothermicity, while there are some cases that under-stoichiometric or over-stoichiometric conditions are more convenient.

#### 2.2.4.3. Metal cations precursors, oxidants and additional oxidants

A metal precursor is a substance added in the initial combustion mixture that contains the metal cations and it is used to introduce the metallic elements in the final products. In case of redox and combustion reactions, an oxidant is employed to provide oxygen for the reducer. Usually, metal precursors contain themselves the oxidizing moieties as counter anions. The most common metal precursors that are used are the commercial nitrates, as they are water-soluble and low-cost. There are other metal precursors used such as oxy-nitrates [128], chlorides [129] and oxychlorides [130], although chlorides are not recommended due to the possibility of adsorbing of incorporating onto the powder and contaminating it.[69] Moreover, oxalates[131], acetates[132], hydroxides[133], acetylacetonates[134] or alkoxides[135] are employed in the initial mixture as metal precursors. However, the use of these substances requires the use of an additional oxidant, as the net valence of the counter anions is positive, making them reducer and not oxidant.[69] Kaur *et al.*[133] highlighted that the use of metal precursors other that metal nitrates has some advantages. They produced ferrite at lower temperature using iron hydroxides as metal precursors. They suggested that Fe-O bond is more polar and more easily breakable in the case of hydroxides, thus permitting the formation of ferrite at lower temperature.

It is worth noting that natural or waste-derived inorganic substances have been employed as metal precursors in the SCS. For example, Gabal *et al.* extracted Mn and Zn metal precursors from waste batteries and achieved the synthesis of Mn-Zn-Fe spinel nanoparticles deposited onto carbon nanotubes, using them as metal precursors.[136] In addition, Choudhary *et al.* reported the extraction of calcium metal precursor from chicken eggshells wastes and their use for the SCS preparation of calcium magnesium silicates with citric acid as reducer.[137]

The chemical composition of the final product is evidently influenced by the choice of the metal precursor (cation), while the metal cation acts as reducer (positive charge) and the counter anion (negative charge, i.e. $NO_3^-$) as oxidizer.[71] The type of the metal precursor may affect the combustion process, the phase composition and the microstructure/morphology of the final product.[129, 138] Interestingly, Kang *et al.* [139] investigated the influence of metal precursor in correlation to its interaction with the fuel, by comparing the cerium nitrate and the cerium ammonium nitrate in combination with reducers like glycine and hydrazide. Thy concluded that these parameters severely affect the combustion characteristics, including combustion temperature and amount of gas emitted during combustion, and, in turn, the properties of formed $CeO_2$ powders.

Oxidants are the counter anion from metal precursors, such as nitrates [73] and dichromates[140], but not phosphates, since they are only used as a source of elements for the final product [141]. Additional oxidants are in some cases necessary for the regulation of the combustion process and the fuel-to-oxidizer ratio.[142-143] Its addition is also required for the compensation of the excess of fuel to maintain the $\phi$ratio at its stoichiometric value when:

- The metal cations require higher amount of fuel than that required by the combustion equation [144]
- The counter anions are reducers and enhance excessively the amount of reducers [145]
- Chloride or oxide precursors are employed that do not possess any oxidizing ability in the examined system [146]
- Mixed fuel mixtures are used [142]

$NH_4NO_3$ and $HNO_3$ are the most frequently employed additional oxidants [73, 93, 127], while other additional oxidants contain ammonium perchlorate, which is also used as solid oxidizer in rocket and missiles [147]. Furthermore, $HNO_3$ is a quite convenient additional oxidant as it facilitates dissolving of some insoluble (in some diluters) metal compounds [120], despite the fact that its use severely affects the precursor mixture's pH value and it is considered to be less effective than $NH_4NO_3$ [69, 135].

#### 2.2.4.4. Influence of preheating rate on SCS and its products

Depending upon the initiation type of the combustion process, two distinct approaches can be identified provided that the sample is uniformly heated:

❖ *Uncontrolled thermal treatment (uncontrolled SCS)*: According to this approach, the sample temperature is rapidly raised up to the combustion temperature, which is in most cases higher than the ignition temperature of the redox mixture. This results in a violent chemical reaction as a result of the large amount of gases in a very short period of reaction (usually less than 60 s) that generate during combustion. This preheating mode appears to be appropriate for the production of nano-sized metal and mixed-metal oxides powders,[74]as well as bulk [125, 148]and supported catalysts.[149]

- *Controlled thermal treatment (controlled SCS)*: In this means of synthesis the sample temperature is gradually increased with relatively low heating rate (1-25 °C $min^{-1}$) up to the mixture’s ignition temperature or higher temperatures. In this mode, the fuel and metal precursors are melting, dehydrating and finally decomposed through a reaction casquade. This approach is found to be applicable for the preparation of supported catalysts [63, 150] as it can considerably reduce the formation of fine particles upon the combustion reaction due to the regulated exothermic effects.[107] In the presence of a carrier in the solution combined with slow heating result in controlled SCS as the heating mode changes to mild and the reactions take place on the inert surface with heat exchange; additionally, those conditions eliminate the possibility of explosive type of combustion.

#### 2.2.4.5. Effect of pH

The pH plays an important role for the determination of the fuels dissociation degree with basic/acid moieties indicating their chelation ability to the metal cations.[151] The influence of pH is strictly associated with the mixture’s chemical composition and the fuel-to-metal cations ratio.[152] High fuel-to-metal values appear to have low effectiveness in regards to the fuel’s tendency of forming complexes, in case its molecules are not fully dissociated. For instance, Pourgolmohammad *et al.*[153] concluded that the high fuel-to-metal ratio (1.25) and high pH is the optimum combination for the obtaining $CoFe_2O_4$ spinel nanopowders. Furthermore, Junliang *et al.*[152] found that the pH value has to exceed 7 and the fuel-to-metal ratio 1.25, in order to receive single phase barium hexaferrite powders through SCS using citric acid as reducer.

One more role of the pH was underlined by Lwin *et al.*[154], who demonstrated that higher pH values facilitate the formation of metal hydrates that can be transformed into crystals more easily. The quicker rate of solidification influences decreases the grain size, affecting the microstructure and morphology. However, the particle size increases, as a result of the crystals agglomerating due to the strong magnetic interaction between the ferrite crystallites.

The pH of the precursor solution was proved to affect the microstructure and morphology of the final products, the intensity of the combustion [127] and in some cases cause slight distortion in the structure, particularly at high values.[155] In the literature, ammonia was found to play a key role in the formation of the combustion gel network. Kim *et al.*[156] highlighted that the addition of ammonia alters the sol, and results in increase of its gelation and polymerization. Moreover, Komova *et al.*[157] suggested that the addition of ammonia increases the intensity of the combustion process in the glycine- metal nitrates system and influences the powder properties in a profitable manner. Their analysis revealed that ammonia was fixed in the gel network as $NH_4NO_3$, not crystallized but interacting with the other components.

Generally, the pH level in the solution should be kept in the slight acidic range because it prevents metal hydroxides or other salts' precipitation, as any form of precipitation is considered to be disadvantageous in the combustion process. In all cases, the solution's acidity plays a significant role, as the acid/basic moieties on the surface of the insoluble compound are affected by the pH of the solution that they are in contact with.[69]

#### 2.2.4.6. Addition of salts

Chen *et al.* [158] is the first to introduce salts in the SCS precursor solution, which severely increases the specific surface area of the resulting products. The salts appear to play a double role: decrease of the combustion temperature as the salts additives absorb the reaction heat and in situ coating of the newly formed nanoparticles, protecting them from sintering and agglomeration.[159-160] The salts are not expensive and they can be easily removed from the final product by water washing. W. Wen *et al.* [161] suggested that NaF is more suitable than NaCl for specific surface area enhancement in the nickel nitrate – citric acid system. It is worth mentioning that the addition of a specific amount of salt altered the combustion mode and the so-called eruption mode occurred. In the eruption combustion process, a great amount of powders were lifted off and naturally fall down around the vessel, leaving highly fluffy products with a relatively high volume. The as-burnt powder had smaller particles, high dispersity and notably increased specific surface area. NiO/Ni nanocomposites that he synthesized are important materials for Li-ion batteries.[162]

#### 2.2.4.7. External template

In the typical SCS process the fuel acts as microstructural template, but in the literature there are some cases in which external microstructural templates (EMTs) were further employed during synthesis.[94-95] The most commonly used EMTs reported are silica, colloidal silica, alumina, inorganic salts and carbon.[69] The EMTs does not fully participate in the reaction, although it may inhibit the combustion wave propagation or it may change the oxidation states of the mixed valence metal cations in the as-burnt powder. After the completion of its action as a template, the EMT might be eliminated [93] or it can be preserved in the final product creating a metal oxide/EMT or metal/EMT composite [163]. All the hard templates that are used in the hard templating synthesis can be suitably used as EMTS in SCS as well. [164-165] Another possibility is to create a highly dispersed metal oxide on a support, preparing the nanocomposite using an in situ SCS approach. In this process the alumina support is not introduced in the mixture as formed oxide powder. Instead, aluminium nitrate is introduced as precursor in the initial SCS mixture and then it is transformed in its oxide form.[146]

Consequently, for the preparation of SCS porous materials for catalytic application there are two approaches to be considered. The first one is to adjust the type and amount of fuel bringing into action its ability to act as a template. The other option is to introduce an external hard template to obtain supported oxides with high surface area or oxides with high porosity.[69]

### *2.2.5. Structure of the SCS products*

SCS is widely used for the preparation of abundant inorganic nanopowders with high reactivity and tailored defects, as it is a time and energy saving process. The final SCS-derived materials have high phase purity with superior powder characteristics, such as high specific surface area, narrow particle size distribution, optimum agglomeration and better sintering properties.[127]

Generally, it is suggested that a lower combustion temperature results in finer particles in all mechanisms of product formation. This temperature may be controlled by changing the composition of the precursor reactive solution or the surrounding atmosphere (inert or reacting gas, gas pressure) that the reaction takes place. However, the specific morphology of the products depends on the mechanism of the structure formation that is strongly affected by the characteristic temperatures (melting, dissociation, sublimation, etc.) of the precursors. Another controlling parameter is the quantity of the generated gases and defines the size and the phase composition of the products.[68]

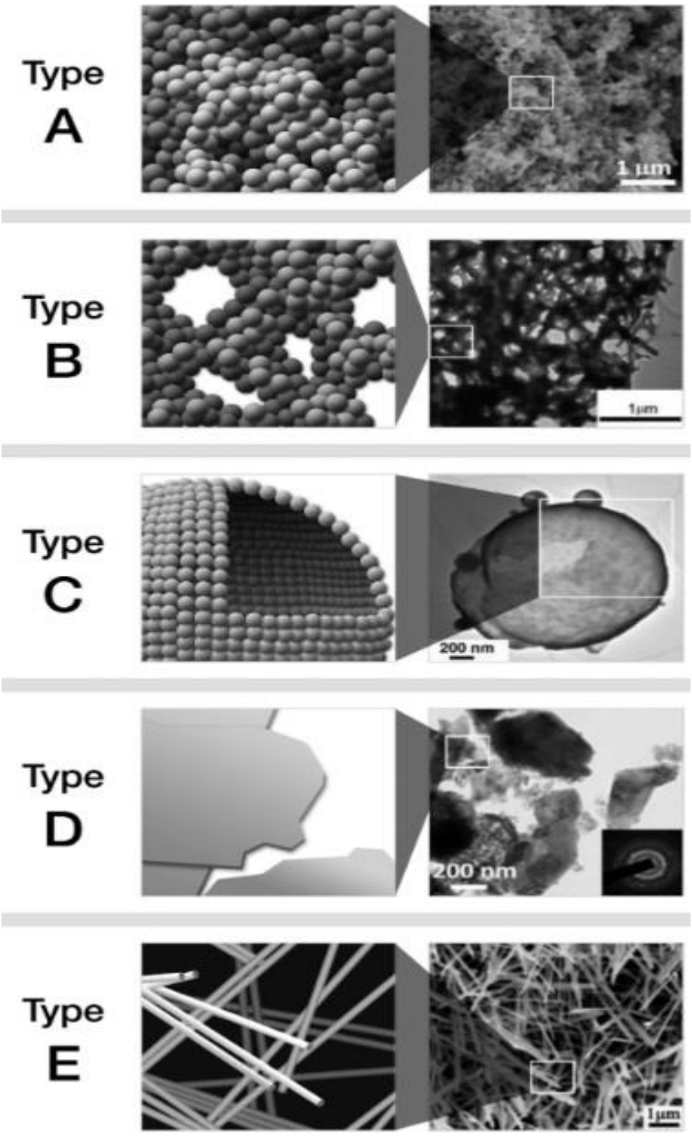

Figure 2.8. Classes of microstructures in SCS-derived materials: ZnO (type A), NiO−Ni (type B), $CeO_2$ (type C), CuO (type D), and $W_{18}O_{49}$ (type E). [68]

The variety of the SCS derived products microstructure can be classified in five different types, as presented on Figure 2.8. Isotropic nanograins such as spherical, polyhedral, irregular-shaped, etc. form the types A, B, and C that are associated in various nano-, micro-, and macrostructures. Type D represents the thin films, flakes and sheets which are characterized as two-dimensional nanostructures. Finally, anisotropic structures with two dimensions notably smaller than the third are type E, including rods, whiskers and fibers. [68]

Porous materials appear to have advantageous applications in numerous fields of gas sensors, catalysis, energy storage and conversion.[166-168] Many of the approaches employed to synthesize porous materials require the use of external templates. The adoption of SCS for the production of porous materials is appealing, since it is a simple, rapid, energy and cost efficient process, without the demand of an external template. In some cases, the porous structure can be achieved by the gas emission during the combustion. However, the pores are usually inhomogeneous in terms of shape and size. It is critical to obtain homogeneous porous materials with nano- and micro- sized pores, which is advantageous for gas or liquid diffusion and results in a relatively high specific surface area. [169]

The careful selection of fuel and a high fuel-to-oxidizer ratio can result in the production of an organic-rich and amorphous precursor that can be further decomposed resulting in porous metal oxide by a subsequent calcinations due to gas generation. The employment of this approach led to the synthesis of homogeneous, largesize porous ZnO flakes, which exhibited high response for detecting acetone and ethanol. Their unique two-dimensional structure shortens efficiently the diffusion distance of the gas and provides highly accessible open channels and active surfaces for the target gas.[170] The same approach was employed for the synthesis of porous $Co_3O_4$ networks, as reported by W. Wen *et al*.[171] They suggested that by increasing the calcinations temperature, the grain growth was enhanced and as a result the particle size and the pore size increased as well.

SCS is usually employed to synthesize materials in powder form. Many precursors used in SCS are in some ways similar to analogous compounds used in sol-gel routes.[138] Consequently, it is feasible to fabricate metal oxide thin films by SCS. Kim *et al.*[103] utilized combustion processing as a novel route to obtain metal oxide thin film electronics at temperatures as low as 200°C.

### *2.2.6. Metal nanoparticles produced by SCS*

As illustrated, SCS has been adopted worldwide to produce various materials with different morphology and phase composition. Numerous nanomaterials and especially simple and complex oxides are manufactured by SCS, due to its simplicity, time and cost efficiency. Besides the numerous oxides, the development of metals, alloys and metal sulfides are now possible through controlling the reaction parameters (fuel type, fuel to oxidizer ratio, etc.). The metals or alloys are considered to be produced by the reduce of the corresponding pre-formed metal oxides in reducing atmosphere that results from either the excessive reducing fuel or the gas formation during combustion in fuel-rich conditions. In most cases, the SCS products are aggregates of nano-particles with relatively low specific surface area. [169]

#### 2.2.6.1. Synthesis of Ni nanoparticles using SCS

When SCS is used for the synthesis of Ni-based materials, the decomposition of nickel nitrate hexahydrate includes several stages as well [172], as it is shown on Figure 2.9. During the first stage, at 37-77 °C, the water evaporates, the second stage (147-187°C) involves the partial decomposition of the nitrate which forms $Ni(NiO_3)(OH)_{0.25}{\cdot}H_2O$, which decomposes during the third stage (257-297 °C) producing $Ni_2O_3$, $HNO_3$ and $H_2O$. Further analysis of the above results indicates that both decomposition and combustion reactions occur at the same temperature range of 237-347 °C. It was also noted that the oxidizer and fuel simultaneously supply the gaseous products $HNO_3$ and $NH_3$ respectively, which is a highly exothermic mixture that yields high temperatures and $H_2O$, $N_2$ and $H_2$ as the main equilibrium products. [76]

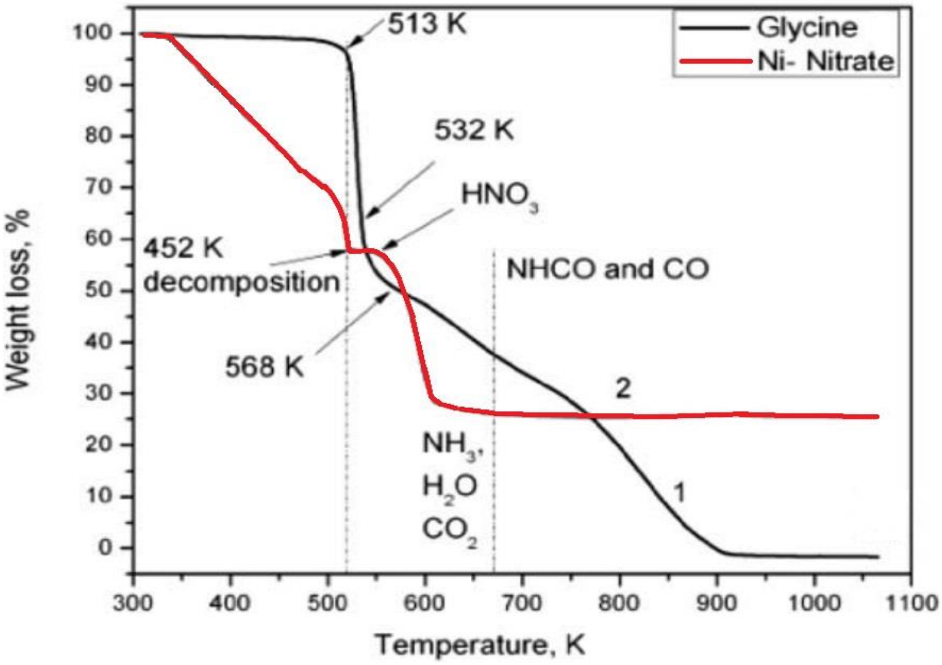

a

Figure 2.9. (a) Typical TGA profile during thermal decompositions in air of (1) glycine and (2) nickel nitrate hexahydrate.[76]

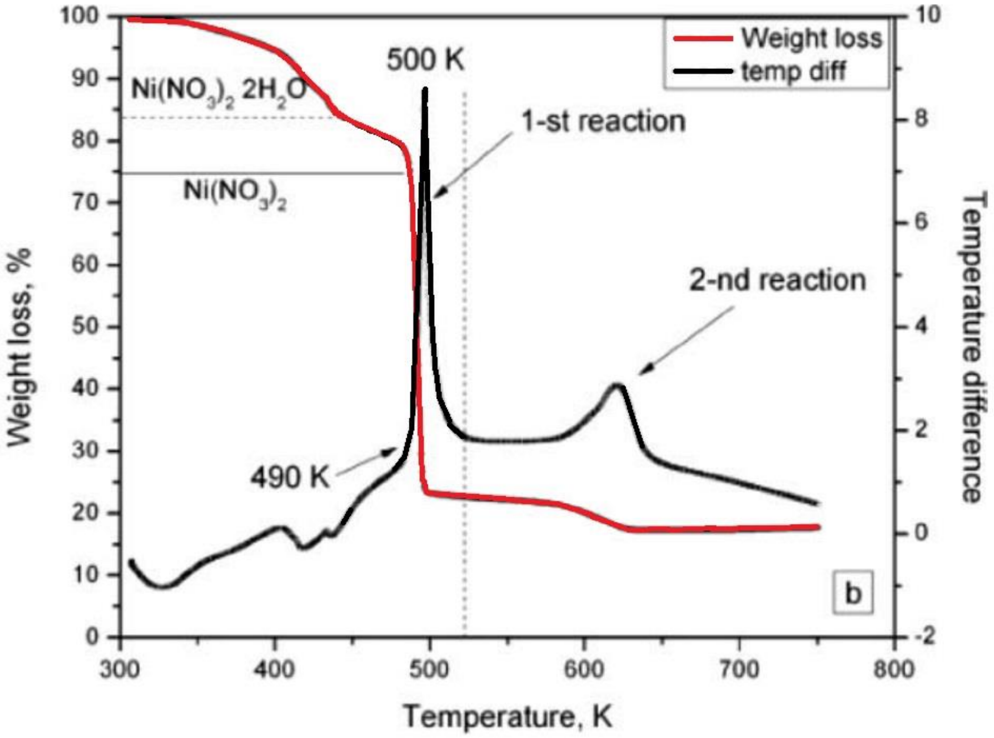

b

Figure 2.9. (b) DTA–TGA data during reaction in glycine–nickel nitrate hexahydrate (ϕ=1.75) aqueous solution. [76]

The main driving force of the combustion process in the nickel nitrate-glycine system is the highly exothermic reaction between gases $HNO_3$ and $NH_3$. $N_2O$ forms during the decomposition of nickel nitrate hexahydrate at 250°C, while $NH_3$ is yielded as one of the main products of glycine's decomposition. It was thus concluded that the combustion reaction is triggered by an exothermic reaction between $HNO_3$ and $NH_3$. However, there are two endothermic steps that are responsible for the formation of the metallic phase in the SCS solid products. In the first step, the decomposition of nickel nitrate at ~250°C that forms NiO nanoparticles. The second step takes place in higher temperatures (above 450°C) in which the reduction of NiO occurs by excess of $NH_3$ to metallic nickel. [68]

Kumar *et al.* [68] investigated the reaction pathways of SCS using nickel nitrate as oxidizer and glycine as fuel. They concluded that the glycine's decomposition starts at approximately 242°C and that the main product of that decomposition stage is $NH_3$, while CO and HNCO are formed in the temperature range of 312-457°C [173].

A. Kumar and co-authors suggested that excess glycine (fuel) provides a hydrogen reduction atmosphere in the reaction front, resulting in pure metal in the post-combustion zone. In addition, it was illustrated that the necessary condition for the synthesis of pure metals in oxidizer–glycine system through SCS pathway is the oxidizer's property (e.g., metal nitrate) to decompose and the nitric acid ($HNO_3$) generation from nitrates decomposition.[76]

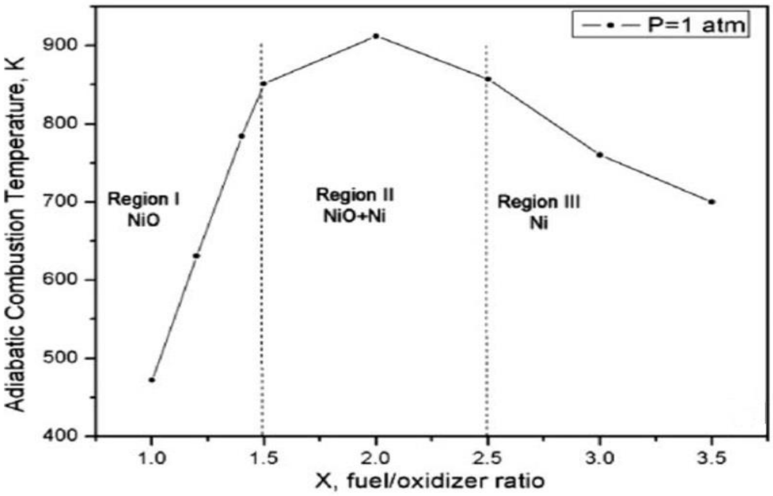

a

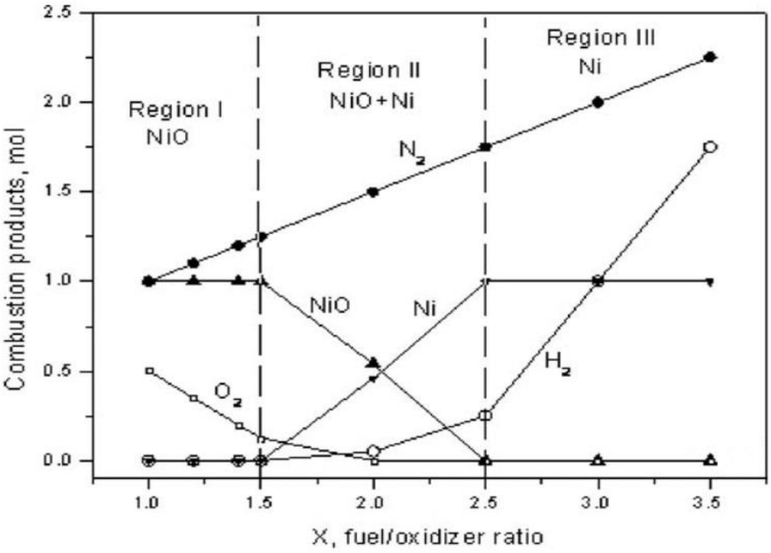

b

Figure 2.10. Thermodynamic characteristics of $HNO_3$: x-$NH_3$:5.5-$H_2O$: NiO system: (a) adiabatic combustion temperature; (b) equilibrium products. [76]

The obtained results revealed that the glycine-nickel nitrate system is characterized by a reasonably high adiabatic temperature (427-627°C) and there are three distinct regions of products depending on the concentration of $NH_3$ (Fig.2.10). At low $NH_3$ amounts, NiO remains unreduced, whilst increase of $NH_3$ content results in the formation of NiO-Ni or Ni phases. As hydrogen concentration increases with the increase of $NH_3$, this leads to the conclusion that increasing the amount of glycine in the initial solution leads to the formation of reductive gases, such as $NH_3$ and $H_2$, in the first stage of combustion. Such variation of the gaseous species composition results in a change in the process of solid products from NiO to NiO-Ni mixture to pure Ni. [68]

It is worth noting that, at the first stage of glycine's decomposition the main product of pyrolisis is ammonia. Li *et al.* [76] studies demonstrated that at higher temperatures the main gaseous products from glycine decomposition are HNC, CO and HCN. These carbon-containing species act as reducing agents for nickel oxide for the formation of metallic nickel. When there is enough amount of fuel added in the precursor mixture, which provides sufficient quantity of hydrogen for the reduction of NiO during the first combustion stage, CO may inhibit the secondary oxidation of nickel to nickel oxide through interaction with oxygen in air in postcombustion zone.

In conclusion, the self-ignition temperature, which is a basic characteristic for the volume combustion synthesis mode, is associated to the temperatures that the reactants of the precursor mixture decompose, in the range of 237-242$^{o}$C. It is also proposed that the self-sustained nature of the process is mainly attributed to the highly exothermic phenomenon that takes place between the products of glycine and nitrates decomposition (i.e. $NH_3 + HNO_3$).

## 2.3. SC synthesized materials and their applications

SCS is a very quick and low-cost process that allows the effective production of nano-size materials with the desired composition and microstructure. It yields a wide range of technologically useful oxides with different magnetic, mechanical, electrical, dielectric, catalytic, optical and luminescent properties.[65] Furthermore, ferrites, perovskites, spinels, garnets, phosphates, metals and alloys are also synthesized by SCS and have a broad range of applications. The various properties and microstructure of all of the above SCS-derived materials resulting from the controllability of the products' shape, texture and structure that SCS provides, make it an alluring route for their synthesis.

Many papers have been published focusing on producing SC synthesized materials for solid oxide fuel cells (SOFC) [174-177] and direct methanol fuel cells (DMFC) [178-179] as well as for supercapacitors [180], batteries [181] and dye-sensitized solar cells [182]. Furthermore, various phosphor-based materials have been produced by SCS and they have a big range of applications such as detection of ionizing radiation and dense scintillators [183], long lasting phosphorescence materials [184], red phosphors [185], fluorescent lamps, colored lightning for advertising industries and other optoelectronic devices [186], long persistent luminescent materials [187], magneto optical films and materials for solid state lasers [188], and red emitting phosphor used in CRT screens, plasma displays and fluorescent lamps [189]. They have also application as pigments, oxygen storage capacitors, magnetic ad dielectric materials, oxygen sensors, for catalysts support and catalysts.

Nanomaterials of diverse nature have attracted major research interest due to their unique size-dependent properties that are not typically found in the corresponding bulk material. Importantly, nanomaterials demonstrate a high specific surface area to volume ratio, which is the basis of their novel physical-chemical properties and fundamental characteristic for catalysts' preparation.[190]

Among the nanomaterials, metal nanoparticles gather great scientific interest in modern materials chemistry and physics, as they find a wide range of application in such fields as nanoelectronics, optics, photochemistry, catalysis, etc. Podbolotov *et al.* [191], who investigated the influence of fuel nature on copper nanopowders, employed a novel approach of SCS (Fig.2.11) as an efficient alternative for fine metal nanopowder synthesis. Furthermore, it was illustrated that the microwave-assisted foam preparation accelerates water removal, decomposition of fuels, copper oxide nucleation, and its reduction during the combustion process due to promotion of reducing the mixture of gases access to whole volume of reaction mixture.[191]

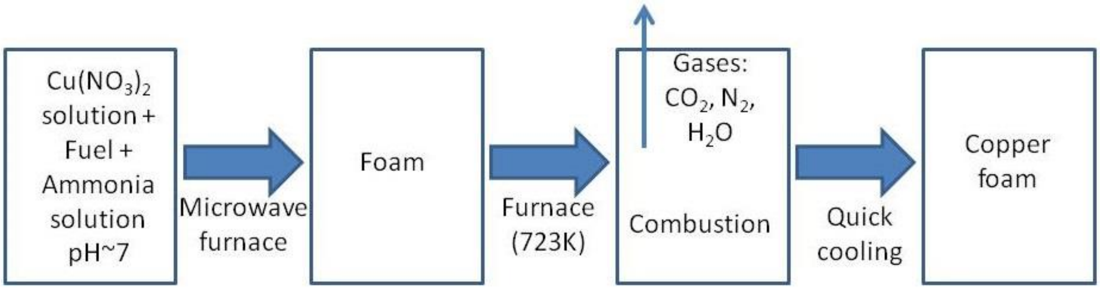

Figure 2.11. Schematic representation of Cu nanopowders synthesis procedure. [191]

# 3. Catalysts derived by solution combustion synthesis

Part of the results presented here has been published in the *Advanced Engineering Materials Journal, 2018, 20,* 1800047, *in the Special Section: Exothermic and Non - Isothermal Processing of Advanced Materials*

There are currently various synthesis approaches for the preparation bulk and supported catalysts, such as sol–gel, impregnation and deposition–precipitation.[192-194] Expensive raw material or long thermal treatment or the use of separation methods is demanded in these approaches, in order to obtain the final product, resulting in severe raise of production costs. Conversely, SCS is an approach that involves moderately rapid development of novel materials with intriguing catalytic properties at relatively low costs.[107] It is a relatively new approach for catalysts manufacturing and it involves elements of conventional techniques combined with its own unique methods.[68] A wide range of catalysts derived by SCS is listed in Table 3.1., including the employed fuel and their application.

Table 3.1: SCS prepared catalysts, used fuel, and their application. [64, 107]

| Catalyst | Fuel used | Application |
|---|---|---|
| **$LaBO_3$ B=Cr, Mn, Fe, Co** | Urea | Decomposition of $N_2O$ to $N_2$ and $O_2$[195] |
| **$Cu/CeO_2$** | Urea | De-$NO_x$ catalyst [196] |
| **$Ce_{0.98}Pd_{0.02}O_{2-\delta}$** | Oxalyl dihydrazide | Selective CO oxidation [197] |
| **$Cu/ZnO/ZrO_2/Pd$** | Glycine | Oxidative hydrogen production from methanol [198] |
| **Ni** | Glycine | Partial oxidation of methane to syn-gas [199] |
| **$WO_3$-$ZrO_2$** | Urea | Solvent-free synthesis of coumarins [200] |
| **$WO_3$** | Glycine, urea, thiourea | Removal of organic dye from water [201] |
| **$TiO_2$** | Glycine | Carcinogenic hexavalent chromium reduction [202] |
| **MgO** | Glycine | Fluoride removal from drinking water [203] |
| **$Ce_xZr_{1-x}O_2$** | Polyvinyl alcohol | Oxidation of carbon monoxide [107] |
| **$La_{1-x}K_xFeO_3$** | Iron | Soot combustion [204] |
| **$Cu_xCr_yO_z$** | Glycine and citric acid | Burn of solid propellants [205] |

Assuming a catalytic process is not controlled by transport limitations, the activity of solid catalysts is generally proportional to their surface area per catalytically active volume. This implies that, for high catalytic activity, small catalytic particles are necessary.[206] However, small particles are thermodynamically unstable and are known to grow during heat treatment, sometimes uncontrollably, at temperatures where the pretreatment and the catalytic reaction are studied. As a result, the size of catalytic crystallites needs to be optimized to ensure both high thermal stability and satisfactory catalytic activity. Thus, to obtain a solid tailored catalyst with specific properties such as shape, density, porosity, phase stability, mechanical strength, activity and selectivity, two approaches are possible:

1. The production of active *bulk catalysts*, which are then combined with suitable materials to meet the criteria of shape and mechanical stability. For the accomplishment of conversion and product specifications, mild conditions during combustion (such as low temperature, low reaction pressure, high space velocities, etc.) are applied in bulk catalysts.[107] The as-prepared porous foam-like aggregates or powders are ready to be used directly as catalysts. [68] In this group, simple and complex oxides as well as alloys are included. An example of bulk SCS-derived catalyst is cerium- or nickel substituted $LaFeO_3$ perovskites, as reported by Erri *et al.*[207] after calcinations they exhibited high activity and stability for autothermal reforming of hydrocarbon mixtures (JP-8).

2. The synthesis of *supported catalysts*, where the active phase is deposited onto a solid support employing a quick reaction at high temperatures.[68] The support is usually thermostable and provides the desired shape, mechanical strength and porosity to the synthesized catalyst. However, the supported active species can achieve the product specifications under mild and severe reaction conditions.[107] For example, Piumetti *et al.* synthesized manganese oxides onto pore-free cordierte ($2MgO·2Al_2O_3·5SiO_2$) monolith filters. They immersed the filters into a manganese nitrate and glycine containing reactive solution and placed them in a preheated furnace for the combustion initiation. The synthesized $Mn_3O_4$ evenly coated the support and the thickness of layer appeared to be controlled by regulating the concentration of reactants in the precursor solution.[68, 208]

## 3.1. Hydrogen production processes on SCS catalysts

Hydrogen is a fuel of high importance, as it is widely considered as the next-generation energy carrier because of its special characteristics. It is clean fuel as it is environmentally friendly and can be produced in a renewable manner for a huge prospective transportation market, for backup power, and for domestic gas grids.[209] The steam reforming of methanol, partial oxidation of methanol or ethanol, natural gas conversion and biogas oxy-steam-reforming are considered the most popular ways to efficiently produce large amounts of hydrogen. Catalysts reported in literature for hydrogen production include mostly noble (e.g. Pt) as well as non-noble metals (e.g. Ni), several bimetallic compositions and variety of support materials such as ceria and γ-alumina. The hydrogen generation over SCS catalysts was studied by various researchers during the last few years.

In the available literature, metals of groups 8–10 of the periodic table, and particularly nickel, are employed as catalysts for the partial oxidation reactions preferred for industrial applications.[210] However, investigations on partial oxidation of ethanol, were performed over copper-based catalysts.[211] Copper exhibited high activity and selectivity for the production of mainly acetaldehyde and hydrogen from ethanol, but promoters and supports are crucial to inhibit both metal sintering and surface contamination due to the acetaldehyde adsorption and the formation of coke. Typically, the products of partial oxidation of ethanol are hydrogen, acetaldehyde, methane, ethylene, CO and $CO_2$.[212-216]

Methanol steam reforming (MSR) reaction has been characterized as a highly appealing and prospective process for hydrogen synthesis and it can be described by the following chemical reactions: $CH_3OH+H_2O \rightarrow CO_2+3H_2$, $CO+H_2O \rightarrow CO_2+H_2$, $CH_3OH \rightarrow CO+2H_2$. Steam reforming of methanol has been widely investigated and the most ordinary catalysts are based on copper, such as $Cu/ZnO/Al_2O_3$, working in a temperature range of 240–260 °C.[219-222] The steam reforming of methanol generation over SCS catalysts was studied by various researchers during the last few years.[223-229]

Nowadays, the United States has the highest hydrogen production which is yielded mainly via steam reforming of methane ($CH_4+H_2O \rightarrow CO+3H_2$). The production process involves a high-temperature steam (700°C–1000°C) which is used to generate hydrogen from a methane source, such as natural gas. In steam reforming of methane, steam reacts with methane under 3–25 bar pressure over a catalyst in order to synthesize hydrogen, carbon monoxide, and a rather small volume of carbon dioxide. [230-232]

Biomass is derived from various organic raw materials in different sectors ranging from zootechnical to agro-industrial. Biogas, which is considered to be among the most common renewable fuels, is obtained from biomass, [233-234] and it consists of 50-75% $CH_4$, 25-45% $CO_2$, 2-7% $H_2O$ (at 20-40 °C), 2% $N_2$, less than 1% $H_2/H_2S$ and traces of $O_2$, $NH_3$, halides and siloxanes.[235] The biogas employment for syngas/hydrogen production by reforming processes [236] to feed fuel cells is illustrated as an alternative direction to avert the conventional use of this renewable fuel in less adept and polluting engines to yield energy and heat. Among the attainable reforming reactions, steam reforming (SR) is widely employed for hydrogen generation ($CH_4+CO_2 \rightarrow 2CO+2H_2$), since it is the widest and typically most cost-effective way specifically for applications in industry.[237-244]

## 3.2 Oxidation reactions on SCS catalysts

PROX is an acronym for PReferential OXidation, while CO-PROX refers to the preferential oxidation of carbon monoxide over a catalyst. The catalysts that are usually employed include metals such as platinum, iron, ruthenium, gold and copper based catalysts. The CO-PROX reaction ($CO + H_2O \rightarrow H_2 + CO_2$) is an important research area in association to the design of fuel cells. However, the extensive presence of hydrogen results in, occasionally, the yield of the competing undesired reaction $2H_2 + O_2 \rightarrow 2H_2O$.[245-247]

Catalytic oxidation of CO is a known and commonly used process in the industry: clearing of exhaust gases of internal combustion engines, gaseous waste of petrochemical and metallurgical manufactures, generation of pure gases, CO oxidation for production of pure (without CO) hydrogen for proton-exchange membrane fuel cells. CO oxidation is an elementary step in many important industrial processes such as the production of methanol and the water-gas shift reaction. End-of-pipe-technology that employs noble metal catalytic converters is recommended in order to restrain vehicular exhaust pollution. The CO oxidation reaction over late transition metals has been the most widely studied surface catalyzed reaction, while the development of active and stable catalysts for this process under an ambient atmosphere remains a intriguing challenge.[248-252]

Catalytic oxidation is recognized among the most efficient techniques for removing Volatile Organic Compounds (VOC), due to the fact that the diluted fuel oxidation occurs at relatively low temperatures resulting in low emissions of $NO_x$ and unburned fuels.[253-254] This approach is highly versatile, and provides the option of treating waste streams with various concentrations of VOC and effluent flow rates.[255-259]

The solid carbon (soot) is responsible for diesel exhaust particulates formation and can be burnt off above 600 °C, despite the fact that the exhaust temperatures of diesel engines typically range between 200–500 °C.[260] Consequently, oxidation catalysts can be employed to enhance the oxidation rate of filter traps at lower temperatures. Typically, among the most active soot oxidation catalysts are materials based on ceria under either $O_2$ or in a $NO_x/O_2$ atmosphere. Ceria alone, or in combination with other metal oxides, is possible to exhibit promising activity during soot oxidation.[261-265]

The oxidation of alcohols is among the principal reactions in organic chemistry [266] and are alluring for the evolution of environmentally friendly processes, [267] synthesis of original materials [268] and energy sources.[269-270] There are two oxidative routes available for the primary alcohols (R-$CH_2$-OH) that yield either aldehydes (R-CHO) or carboxylic acids (R-$CO_2H$), while the oxidation of secondary alcohols ($R^1R^2$CH-OH) typically finishes at the stage of ketone ($R^1R^2$C=O) and notably, tertiary alcohols ($R^1R^2R^3$C-OH) are resistant to oxidation.[271]A recent environmentally compatible and sustainable approach induces aerobic oxidations over transition-metal catalysts (based on Pd, Ru, Fe, Cu, Pt, Au, Ir, Rh, etc.,) and dioxygen or hydrogen peroxide as oxidants.[270] Various SCS-derived catalysts such as spinels and hexaluminates were employed to catalyze this process.[271-277]

## 3.3. Methanation reaction on SCS catalysts

Relatively complete combustion and satisfactory calorific value makes natural gas a highly efficient and comparatively greener-than coal fuel.[278] Synthetic natural gas is often produced from coal or biomass by catalytic reactions.[279-280] A well developed technology to synthesize natural gas from syngas ($H_2$ + CO) is methanation which has attracted a lot attention in the community in the past few years.[281-282] In 1902, Sabatier and Senderens first demonstrated that reaction of CO with $H_2$ over a nickel catalyst generates methane.[283] Ruthenium, nickel and copper based catalysts are widely used for the CO methanation reaction, while nickel, in particular, is perpetually preferred in industry for the broad availability and relatively low-cost.[284] Especially, Ni-based catalysts supported on $Al_2O_3$ have been extensively employed as a result of its high performance-cost ratio.[285]

Selective CO methanation ($CO + 3H_2 \rightarrow CH_4 + H_2O$) is an investigated process with relatively high potential to reduce the trace of CO in $H_2$-rich reformate gas mixture, which is a fuel for the proton exchange membrane fuel cell. During this operation, all the required reactants (CO and $H_2$) are already present in the reformate gas created via the steam-reforming and water-gas-shift reactions.[286] It should be considered, however, that the side reactions - e.g. $CO_2$ methanation ($CO_2 + 4H_2 \rightarrow CH_4 + 2H_2O$) and water-gas-shift reaction ($CO_2 + H_2 \leftrightarrow CO + H_2O$) - may also occur simultaneously and they inevitably exhaust a large quantity of hydrogen. Therefore, it is a challenging subject to investigate.[287-291]

### 3.4. Liquid phase hydrogenation on SCS catalysts

The liquid-phase hydrogenation reaction is primarily employed in order to compare the catalytic activity of tested catalysts in order for them to be used in gas-phase high temperature hydrogenation industrial processes. However, there are some compounds, which can be produced at low temperature by liquid phase hydrogenation in industry.

Mistri *et al.*[292] delivered for the first time nano-sized bimetal-ion-substituted ceria, $Pd_{0.01}Ru_{0.01}Ce_{0.98}O_{2-\delta}$ (PdRuC2) by SCS towards liquid-phase hydrogenation of p-chloronitrobenzene. PdRuC2 has been evaluated as more active and selective than the monometal ion substituted counterpart $Pd_{0.02}Ce_{0.98}O_{2-\delta}$ (PdC2). It is worth noting that $Ru_{0.02}Ce_{0.98}O_{2-\delta}$ (RuC2) was not active in the hydrogenation of p-chloronitrobenzene to p-chloroaniline under ambient conditions in the aqueous phase. The enhanced activity and selectivity of the PdRu bimetal catalyst has been associated to the involvement of $Ru^{4+}$-promotion in PdRuC2, while it exhibited high catalytic activity towards the hydrogenation of o-, m-chloronitrobenzene and nitrobenzene.[68]

### 3.5. Further applications of SCS catalysts in various processes

The generation of methanol from CO and $H_2$ has acquired more importance since methanol is one of the materials that can substitute the petroleum as a fuel. In terms of industrial manufacturing, methanol is synthesized on copper-based catalysts such as $Cu/ZnO/Al_2O_3$ and $Cu/ZnO/Cr_2O_3$ from synthesis gas consisting of carbon monoxide, carbon dioxide and hydrogen in a gas-phase procedure at high pressures and temperatures.[293-297]

Dye degradation with photocatalysis takes place through photosensitization (self-dye degradation) and/or photooxidation (by reactive species produced). Both mechanisms depend on the electronic structures, especially the band structure, of the catalyst and the dye. Synthetic dyes used for clothes, leather accessories, and furniture production, up to 12% of these dyes are wasted during the dying process and approximately 20% of this wastage infiltrates into the environment and particularly into water supply. Heterogeneous photocatalysis is a well-recognized approach for environmental purification. [298-299]

SCS-derived catalysts were also employed in other processes such as the photodegradation of methylene blue [300-302], in processes for bacterial protection [303], in a single cylinder diesel engine [304], in transesterification process (that converts triglycerides, like vegetable oil, into fatty acid methyl esters, commonly known as biodiesel) [305] as well as in low temperature selective catalytic reduction of ammonia [306]. Moreover, “incipient wetness” approach and “glycine nitrate” method were compared for the synthesis of Ni-based SCS catalyst, where it was concluded that glycine nitrate process offered enhancement of the catalysts’ stability and, on the basis of the de-coking mechanism, its reducibility over n-dodecane pre-reforming.[307]

Last but not least, hydrogen storage is one of the most crucial challenges that the hydrogen based economy faces. Recently, metal hydrides, and especially sodium borohydride ($NaBH_4$), have been receiving increased attention as a possible alternative storage method to compressed gas systems. Pfeil *et al.* [308] reported the fabrication of a SCS nanostructured cobalt oxide ($Co_3O_4$) as catalyst precursor for the hydrolysis of $NaBH_4$ and concluded that the CS cobalt oxide outperformed the commercially available cobalt oxide. Its supremacy is ascribed to its nano-foam morphology and crystallinity, as during the hydrolysis it is in situ converted to an amorphous catalyst with high specific surface area and honeycomb type morphology.

In conclusion, SCS has exponential distribution all over the world because of the major advantages that offers and it is a very prospective approach for synthesis of catalysts. As it has been already mentioned, combustion approach employed in numerous types of reactions, as it provides catalysts with various structures and properties. Moreover, SCS offers the possibility of synthesizing nickel nanocatalysts and impregnated catalysts with low cost in a short period of time. It allows the regulation of catalysts activity and selectivity as a function to the composition of the precursor mixture, the additives and the parameters of reaction that will be adopted.

## Aim of work

Solution combustion synthesis meets the demands of material science and engineering in tailoring and producing a plethora of novel materials with desired composition, structure and properties which is a very important issue for synthesis of selective catalysts. It is possible to produce nanocatalysts with high specific surface area and tailored properties by SCS. This clearly explains and justifies our choice of this method for the catalysts synthesis. Moreover, the lack of studies of SCS catalytic behavior in the liquid-phase hydrogenation as well as its suitability for catalytic tests in the laboratory scale led us to test the as-synthesized catalysts activity with this reaction.

This research project is aiming to identify a range of active catalysts made by combustion synthesis, for the hydrogenation of unsaturated hydrocarbons, in the example of maleic acid liquid-phase hydrogenation. In addition to the technical applicability of such catalysts in industry, the project will enable a deeper understanding of the mechanisms during SCS reactions as well as elucidation of the parameters that affect the SCS final products properties enabling a measure of predictability in producing new active catalysts.

# Part B

# 4. Methodology

## 4.1. Materials

In Table 4.1 that follows, the materials that have been used for catalysts production using Solution Combustion Synthesis (SCS) are listed. Also, the manufacturers and their assay are included.

Table 4.1. Materials used for SCS catalysts production and the hydrogenation reaction.

| Material | Manufacturer | Assay/Purity |
|---|---|---|
| Nickel (II) nitrate hexahydrate for analysis [$Ni(NO_3)_2 \cdot 6H_2O$] | Merck | 99.0-102.0 % |
| Aluminium nitrate nonahydrate for analysis [$Al(NO_3)_3 \cdot 9H_2O$] | Carlo Erba | ≥99.0 % |
| Glycine for synthesis [$CH_2NH_2COOH$] | PanReacAppliChem | 99.0 % |
| Maleic acid [HOOCCH=CHCOOH] | Riedel-de Haën | 99.0 % |
| Isopropyl alcohol [$CH_3CH(OH)CH_3$] | Sigma Aldrich | ≥99.8 % |
| Urea [$CH_4N_2O$] | Sigma Aldrich | ≥99.5 % |
| Carbohydrazide [$CH_6N_4O$] | Sigma Aldrich | 98% |
| Hydrogen [$H_2$] | Air liquide | 99.999% |

## 4.2. Catalysts produced by Solution Combustion Synthesis (SCS)

The initial solution used for SCS contained the oxidizers and the reducer. Distilled water has been used to facilitate the mixing of reactants and in most cases the initial SCS mixture was pre-heated in a borosilicate glass beaker on a hot plate with mild magnetic stirring until the temperature reached 70°C. Then, it was placed in a pre-heated furnace at 500°C to enable SCS reactions, thereby yielding different nano-and micro- structured powdered catalysts. Once SCS is completed, the beaker is left to cool inside the furnace or removed and allowed to cool at room temperature.

The oxidizers that used as reactants are nickel (II) nitrate hexahydrate [$Ni(NO_3)_2{\cdot}6H_2O$], aluminium nitrate nonahydrate [$Al(NO_3)_3{\cdot}9H_2O$], and glycine as fuel. All produced catalysts are consequently Ni-based, as Ni is widely used as catalyst in industrial processes.

It was observed that Solution Combustion Synthesis is a very sensitive technique and its products are influenced by many different parameters. There are not many reports that examine these parameters and for those reasons, it was found necessary to investigate them. The parameters that studied here are the following:

☐ *Quantity of initial SCS solid mixture*

The quantity of initial mixture affects immediately the combustion temperature as well as the exothermic reaction's energy. The quantities that were studied are 3, 6, 9, 12 g nickel nitrate hexahydrate, 50% glycine with 10ml distilled water placed in a pre-heated furnace at 500°C after the end of combustion the beaker was removed from the furnace and left to cool in room temperature.

☐ *Time in furnace after SCS ended*

After the combustion ended, the samples [with initial composition: 9g nickel nitrate hexahydrate, 50% glycine and 10ml distilled water for a total solid mass of 14g] were placed in the pre-heated furnace at 500°C.Once, the reaction ended they were left in the heated furnace for 0, 2, 7, 10 minutes.

☐ *Preheating temperature*

The initial SCS mixture consisted of 66.7%wt. nickel nitrate hexahydrate with 33.3%wt. glycine as a fuel (for a total solid mass of 14g) and it was placed in the pre-heated furnace at four different temperatures (500, 600, 650, 700°C). After combustion synthesis ended the beaker was removed from the furnace and left to cool down in room temperature.

☐ *Heated stirring as pre-treatment for SCS initial solution*

Various quantities of water (25, 50, 75, 100ml) were mixed with 66.7%wt. of nickel nitrate hexahydrate and 33.3%wt. glycine (for a total solid mass of 14g) and 8 solutions were prepared – 2 with each quantity of water. One solution from each water quantity was pre-heated in a borosilicate glass beaker on a hot plate with mild magnetic stirring until the temperature reached 70°C. At that point the beaker is placed in a pre-heated furnace at 500°C in air atmosphere for the SCS to take place. The other four solutions (with 25, 50, 75 and 100ml of water) were placed directly in the furnace without any pretreatment. In all experiments, after the completion of the SCS cascade of reactions, the beaker was removed from the furnace and left to cool down in room temperature.

❑ *Water quantity in the initial SCS solution*

The initial solution used consists of 66.7%wt. nickel nitrate hexahydrate [$Ni(NO_3)_2{\cdot}6H_2O$] as the oxidizer with 33.3%wt. glycine as the reducer for a total solid mass of 14g.The solid mixture was then dissolved in 25, 50, 75 or 100ml of distilled water and placed on a hot plate with mild magnetic stirring up to 70$^{o}$C. The beaker was then placed in the pre-heated furnace at 500$^{o}$C to enable SCS.

❑ *Initial SCS mixture composition*

Different proportions between nickel nitrate hexahydrate (20, 40, 60, 80%wt.) and aluminium nitrate nonahydrate (80, 60, 40, 20%wt. correspondingly) with 60% of the total reactants’ mass glycine and 75 ml distilled water were studied. The four samples were pre-heated on a hot plate with mild magnetic stirring until the solution’s temperature reached 70$^{o}$C. Then, they were placed in the furnace which was in room temperature with target temperature 500$^{o}$C and heating rate 7-7.5$^{o}$C/min.

The same proportions were investigated by using 40%wt. of the total reactants’ mass glycine and the mixture was placed in a pre-heated furnace at 500$^{o}$C after pre-treatment.

❑ *Type of reducer*

Three different fuels (glycine, urea and carbohydrazide) were added in the precursor mixture with initial concentration: 40%wt. nickel nitrate hexahydrate, 60%wt. aluminium nitrate nonahydrate and 75ml of water. The total mass of the employed nitrates was 10g and the quantity of the added fuel was 4g. The four samples were pre-heated on a hot plate with mild magnetic stirring until the solution’s temperature reached 70$^{o}$C. Then, they were placed in the furnace which was in room temperature with target temperature 500$^{o}$C and heating rate 7-7.5$^{o}$C/min.

☐ *Fuel concentration in the initial solution*

Four different quantities of glycine (40, 50, 60, 80%wt.) with standard quantity of nickel nitrate hexahydrate (9,34g) were mixed with 75ml of distilled water. The mixture was placed on a hot plate with mild magnetic stirring until the temperature reached 70°C and then placed in the pre-heated furnace at 500°C.

☐ *Heating mode*

The same four experiments (with the four different quantities of glycine) were repeated but the way to heat the mixture was changed. The initial SCS mixture was placed in the furnace which was in room temperature and its target temperature was 500°C. The furnace's heating rate is 7-7.5°C/min.

☐ *Fuel to oxidizer ratio*

The ratios between the fuel-glycine and the oxidizer-nickel nitrate hexahydrate that were investigated are 0.5, 0.75, 1 and 1.25. The initial quantity of nickel nitrate hexahydrate added in the SCS solution was 9.34g and kept constant. 100ml of distilled water was also added and the beaker containing the initial SCS solution was placed on a hot plate with mild magnetic stirring until the temperature reached 70°C. The beaker was then placed in the pre-heated furnace at 500°C and once the combustion was over it was removed from the furnace and left to cool down in room temperature.

## 4.3. In-flight SCS

Combustion-assisted flame spraying ("CAFSY") was recently developed to produce catalytically active nickel aluminide coatings on ceramic substrates.[309] The CAFSY process showed that combustion synthesis occurs both in-flight as well as on the substrate. Marinou *et al.* reported on Ni-based catalysts produced by in-flight SCS during flame spraying, a novel method which combines conventional flame spraying and solution combustion synthesis into a single step. A fine spray of the aqueous SCS solution is inserted into the flame wherein the water is evaporated and the SCS catalyst is synthesized rapidly in the flame. The fine particles of nano-structured catalysts are then applied as coating on a Mg-Al-O spinel carrier and penetrate very efficiently into all the surface pores. Figure 4.1 shows the schematic diagram of the in-flight SCS during flame spraying and presents the main parts of the novel arrangement.

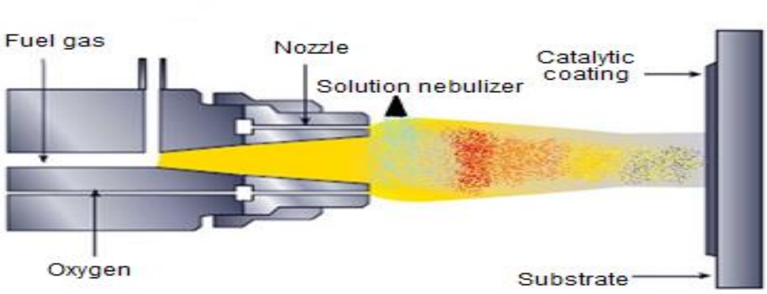

Figure 4.1. Schematic diagram of in-flight SCS during flame spraying.[37]

In this attempt nickel-based nano-catalyst was synthesized by in flight Solution Combustion Synthesis (SCS) from starting solutions of nickel nitrate $Ni(NO_3)_2 \cdot 6H_2O$ with glycine as fuel in the ratio of 2:1. In order to facilitate the homogenization 100ml distilled water was added to the initial SCS mixture. Flame spraying was carried out by a Sulzer's Metco Thermospray Gun (5P-II) and the solution was introduced into the flame using an adjustable nebuliser. The synthesized SCS nano-catalysts were deposited as thin coatings on a ceramic Mg-Al-O carrier previously made by SHS from an initial mixture of 7.41% Al + 8.33% Mg + 39.63% $Mg(NO_3)_2$ + 32.41% $Al_2O_3$+ 4.81% MgO + 7.41% $H_2BO_3$.

The spraying parameters that were applied are:

- $O_2/C_2H_2$=1.18 (oxidizing flame)
- Additional air in the flame=1bar
- Distance (between the gun and the substrate)=10cm
- Spraying duration=2min
- Carrier gas (the air that flows through the nebulizer)=4bar

## 4.4. Catalytic studies

The activity of the SCS catalysts synthesised was studied in liquid-phase hydrogenation of unsaturated hydrocarbons(H/C).The installation, as illustrated in Figure 4.2, consists of a shaker-reactor in a water bath kept stable the selected temperature for reaction. An amount of catalyst is added in the catalytic reactor with 30 ml of distilled water. After this, the unsaturated hydrocarbon is added in calculated quantity for reaction with 50ml of hydrogen at atmospheric pressure. Both catalyst saturation with hydrogen and hydrogenation are carried out under continuous mechanical stirring (360-380 rpm). Measurements of the amount of reacted hydrogen are taken every minute at atmospheric pressure. To check reproducibility, each hydrogenation test was repeated at least three times. The reproducibility was found to be within ±5%.

A platinum/calomel electrode is used in the reactor in order to monitor hydrogen adsorption and the saturation of the powdered catalysts is monitored over one hour. Calomel electrode is a reference electrode based on the reaction between elemental mercury and mercury (I) chloride. The aqueous phase in contact with the mercury and the mercury (I) chloride ($Hg_2Cl_2$, "calomel") is a saturated solution of potassium chloride in water. The electrode is linked via a porous frit to the solution in which the other electrode is immersed. This porous frit is a salt bridge.

It is well-known that the hydrogen region on the charging curve of platinum is an isotherm of hydrogen adosprion. The measurement of the differences in the potential during hydrogenation permits to evaluate the concentration ratio of the reactive substances on the catalytic surface and approximately estimate the degree of surface coating with hydrogen. It estimates the energy of the hydrogen bonding which participates in the catalytic reaction. It is also mentioned that a higher degree of hydrogen coating (~ 90-99%) is required in the case of the double bond hydrogenation. On the contrary, when the aim is the saturation of the triple bond a significantly lower degree of hydrogen coating is desired (~ 30-40%), as the surface has to be available for the various reactive molecules to be able to adsorb. [310]

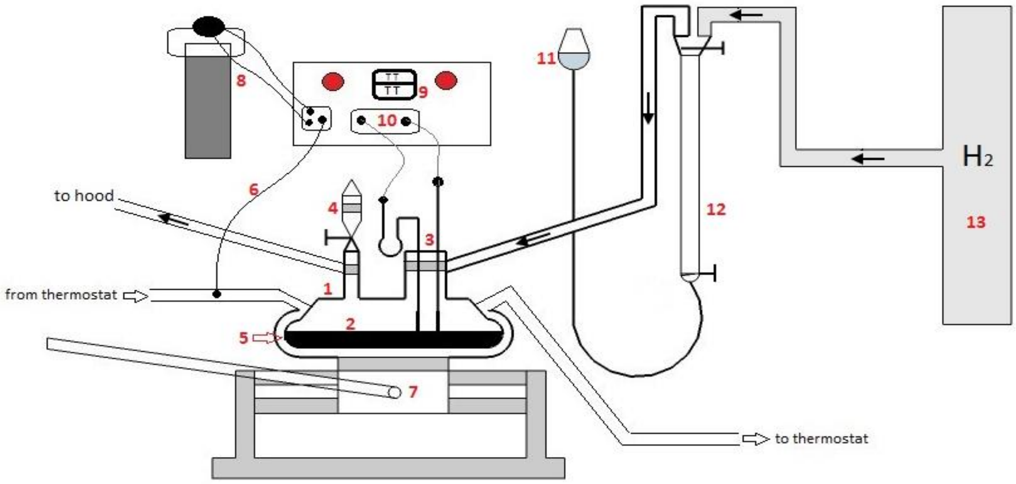

Figure 4.2. Schematic representation of the catalytic hydrogenation installation. The main parts are: 1.reactor 2.solvent with catalyst 3.Calomel electrode/Pt electrode 4.unsaturated hydrocarbon inlet 5.reactor’s water bath for temperature control 6.thermocouple for control of reactor’s heating 7.shaking mechanism 8.heater 9.temperature controller 10.signal buffer 11.vessel for pressure adjustment 12.burette 13.$H_2$ bottle

Liquid-phase hydrogenation is a very sensitive technique and allows the study of parameters that influence it. Its sensitivity is because of the reactions as well as the adsorption phenomena take place in liquid phase and reaction’s temperature is very low. The parameters that have been studied in this work are described below.

❑ *Reaction temperature*

This factor is one of the most important in catalytic studies, as it can affect the rate of the hydrogenation reaction. The temperatures that have been tested are 70, 80, 90, 95$^{o}$C. In these tests, 0.26g maleic acid were used (calculated for 50ml of hydrogen) as the unsaturated hydrocarbon and a SCS catalyst with initial mixture 66.7%wt. $Ni(NO_3)_2$, 33.3%wt. glycine, 100ml distilled water.

❑ *Quantity of catalyst*

The quantity of catalyst plays also a significant role in the yield of catalytic reaction as it is directly linked to the surface of reaction. 0.5, 1, 1.5 and 2g of Ni-based catalyst [initial SCS mixture: 66.7%wt. $Ni(NO_3)_2$, 33.3%wt. glycine, 100ml distilled water] were tested in liquid-phase hydrogenation of maleic acid (0.26g – calculated for 50ml of hydrogen) at 80$^{o}$C.

❑ *Diluter’s nature*

By changing the diluter used in liquid-phase hydrogenation the capability of substances to dilute changes as well as the adsorption of hydrogen and reactants on the catalyst. Water, and isopropyl alcohol were looked into for maleic acid’s hydrogenation on Ni-based SCS catalysts [SCS initial mixture: 66.7%wt. $Ni(NO_3)_2$, 33.3%wt. glycine, 100ml distilled water] at 80$^{o}$C.

Table 4.2: Table of the investigated parameters for Solution Combustion Synthesis (SCS) of catalysts and liquid-phase hydrogenation of maleic acid.

| | Changing parameter | Materials and processing conditions | Experiments | | | |
|---|---|---|---|---|---|---|
| SCS: $Ni(NO_3)_2$ – glycine system | Concentration of $Ni(NO_3)_2$ | $Ni(NO_3)_2$<br>50%wt glycine<br>75ml $H_2O$<br>T=500°C | 3g | 6g | 9g | 12g |
| | Quantity of glycine | 9.3g $Ni(NO_3)_2$<br>glycine<br>100ml $H_2O$<br>T=500°C | 50% | 75% | 100% | 125% |
| | Heating mode | 9.34g $Ni(NO_3)_2$<br>glycine<br>75ml $H_2O$ | Slow heating (25 $\rightarrow$ 500°C) | | Preheated furnace (500°C) | |
| | Time in furnace after SCS | 66.7%wt $Ni(NO_3)_2$<br>33.3%wt glycine<br>75ml $H_2O$<br>T=500°C | 0min | 2min | 7min | 10min |
| | Preheating temperature | 66.7%wt $Ni(NO_3)_2$<br>33.3%wt glycine | 500°C | 600°C | 650°C | 700°C |
| | Reactants concentration in the aqueous solution | 66.7%wt $Ni(NO_3)_2$<br>33.3%wt glycine<br>T=500°C | 25ml $H_2O$ | 50ml $H_2O$ | 75ml $H_2O$ | 100ml $H_2O$ |
| | Pretreatment of the precursor solution | 66.7%wt $Ni(NO_3)_2$<br>33.3%wt glycine<br>75ml $H_2O$<br>T=500°C | Pretreated samples | | No-pretreated samples | |
| | Fuel-to-oxidizer ratio ($\phi$) | 9.34g $Ni(NO_3)_2$<br>glycine<br>75ml $H_2O$<br>T=500°C | $\phi=1.4$ | $\phi=1.74$ | $\phi=2.08$ | $\phi=2.78$ |
| SCS: $Ni(NO_3)_2$ – $Al(NO_3)_3$ – glycine system | Nature of fuel | 40%wt $Ni(NO_3)_2$<br>60%wt $Al(NO_3)_3$<br>4g fuel<br>75ml $H_2O$<br>T=500°C | Carbohydrazide | Urea | Glycine | |
| | Ratio of oxidizers $Ni(NO_3)_2$ – $Al(NO_3)_3$ | 40%wt $Ni(NO_3)_2$<br>60%wt $Al(NO_3)_3$<br>4g glycine<br>75ml $H_2O$<br>T=500°C | 20% $Ni(NO_3)_2$ | 40% $Ni(NO_3)_2$ | 60% $Ni(NO_3)_2$ | 80% $Ni(NO_3)_2$ |
| Parameters of hydrogenation | Reaction temperature | - | 70°C | 80°C | 90°C | 95°C |
| | Quantity of catalyst | - | 0.5g | 1g | 1.5g | 2g |
| | Type of diluter | - | Distilled water | | Isopropyl alcohol | |

## 4.5. Characterisation of the SCS catalysts

### *4.5.1. X-Ray Diffraction (XRD)*

The crystal structure and microstructure of the synthesised catalysts were determined by several methods. Crystal structure was determined by X-ray diffraction measurements on a Siemens Spellman DF3 spectrometer with Cu-$K_\alpha$ radiation. XRD patterns were recorded in an angle range ($2\theta$) between 5 and 100 degrees and with step $0.03^{\circ}$/sec. The peaks were identified by using the Joint Committee on Powder Diffraction Standards (JCPDS) database and Crystallographica software.

The substrate employed for the XRD measurements provided the following X-ray diffraction pattern (Fig.4.3), when it was examined without any sample on. Depending on the thickness of the tested sample, any of two major peaks ($2\theta \sim 14.1, 17$) occasionally appear on the diffraction patterns of the examined nanopowders. These peaks were not in conflict with any sample peaks.

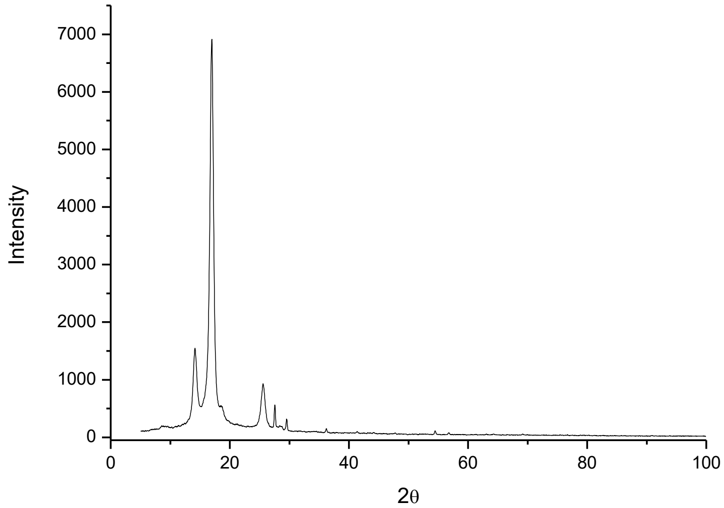

Figure 4.3. XRD pattern of the employed substrate for the XRD measurements.

For semi-quantitative XRD analysis, 10%wt. KCl was added in all samples as an internal standard. By normalising the XRD results against the 10% KCl internal standard and calculating the peak ratio of intensities of particular peaks (making sure that they are unique for each phase) it is possible to determine the relative content of each phase in the material. The hkl of the peaks selected for each phase were: for nickel 111, for nickel oxide 101 and for potassium chloride 100.

*Bragg's law*

An X-ray which reflects from the surface of a substance has travelled less distance than an X-ray which reflects from a plane of atoms inside the crystal. The penetrating X-ray travels down to the internal layer, reflects, and travels back over the same distance before being back at the surface. The distance travelled depends on the separation of the layers and the angle at which the X-ray entered the material. For this wave to be in phase with the wave which reflected from the surface it needs to have travelled a whole number of wavelengths while inside the material. Bragg expressed this in an equation now known as Bragg's Law: [311]

$$2 \cdot d \cdot sin\vartheta = n \cdot \lambda$$

$\lambda$: wavelength of the rays
$\vartheta$: the angle between the incident rays and the surface of the crystal
*d*: the spacing between layers of atoms
*n*: order (constructive interference occurs when *n* is an integer)

When "n" is an integer (1, 2, 3 etc.) the reflected waves from different layers are perfectly in phase with each other and produce a bright point on a piece of photographic film. Otherwise the waves are not in phase, and will either be missing or feint.
For the calculation of crystal lattice spacing (d), the order was kept constant and equal to 1 and the wavelength equal to 1.5406nm, as the XRD spectrometer used has Cu-$K_\alpha$ radiation.

*Scherrer's equation*

$$L = \frac{K \cdot \lambda}{\beta \cdot \cos\vartheta}$$

Scherrer formula [312] was developed in 1918, to calculate the nano-crystallite size (L) by XRD radiation of wavelength λ (1.5406Å for Cu target, $K_\alpha$ radiation) from measuring full width at half maximum of peaks (β) in radian located at any 2θ in the pattern. Shape factor of K (Scherrer constant) varies from 0.62 to 2.08, whilst the most common values for K are:

- 0.94 for full width at half maximum of spherical crystals with cubic symmetry
- 0.89 for integral breadth of spherical crystals w/ cubic symmetry
- 1, because 0.94 and 0.89 both round up to 1

### *4.5.2. Scanning Electron Microscopy (SEM)*

Prior to viewing in the SEM, the samples were sputter coated in the Polaron E5100 sputter coater. Samples are sputter coated with gold in order to make their surfaces more conductive and therefore less susceptible to the accumulation of surface charge. The samples were then attached to the appropriate SEM stages using double-side carbon tape.

SEM uses high voltage electron beam instead of light, in order to examine objects in a detailed scale. Electrons are able to be focused, due to their wave nature, on a very small area. The electron beam scans the sample's surface with which it interacts. Information related to the atoms of the elements composing the sample is obtained from the sample's interaction to the electrons. Secondary and backscattered electrons as well as X-rays are mainly transmitted from the atoms. The intensity of secondary electrons is influenced by the surface characteristics, thus SEM provides information concerning mostly the surface morphology and composition. By applying a detecting system for the dispersion of the X-Ray energies that are created on the surface from the incident beam, a semi-quantitive elemental analysis is possible. Energy Dispersive Spectroscopy (EDS) provides elemental information about the composition of the structure of the surface of a sample and it is performed in conjunction with SEM.

A FEI Quanta Inspect Scanning Electron Microscope (SEM) with W (Tungsten) filament 25kV and 3.5nm resolution equipped with an EDAX EDS system was employed for the study of specimens.

### *4.5.3. Transmission Electron Microscope (TEM)*

The transmission electron microscope (TEM) is a microscopy technique in which a beam of electrons is transmitted through a specimen to form an image. It operates on the same basic principles as the light microscope but uses electrons instead of light. TEM uses electrons as "light source" and a resolution a thousand times better than with a light microscope is achieved, owing to the smaller de Broglie wavelength of electrons. An image is formed from the interaction of the electrons with the sample as the beam is transmitted through the specimen. The image is then magnified and focused onto an imaging device, such as a fluorescent screen. Objects can be observed to the order of a few angstroms ($10^{-10}$ m). The possibility for high magnifications has made the TEM a valuable tool in materials research.

An FEI CM 20 analytical High Resolution Transmission Electron Microscope (TEM) equipped with an EDAX Electron Dispersive X-ray Spectroscopy (EDS) system and a GIF200 Gatan energy filter was utilized for TEM studies.

### *4.5.4. Surface area measurements*

The BET (Brunauer, Emmett, Teller) theory [313] applies to systems of multilayer adsorption and usually utilizes probing gases that do not chemically react with material surfaces as adsorbates to quantify specific surface area. Nitrogen is the most commonly employed gaseous adsorbate used for surface probing by BET methods. BET analysis provides precise specific surface area evaluation of materials by nitrogen multilayer adsorption measured as a function of relative pressure using a fully automated analyzer.

The concept of the theory is an extension of the Langmuir theory, which is a theory for monolayer molecular adsorption, to multilayer adsorption. The resulting BET equation is:

$$\frac{1}{V[\left(\frac{p_o}{p}\right)-1]} = \frac{c-1}{V_m c}\left(\frac{p}{p_o}\right) + \frac{1}{V_m c} \quad (1)$$

where $p$ and $p_o$ are the equilibrium and the saturation pressure of adsorbates at the temperature of adsorption, $V$ is the adsorbed gas quantity, $V_m$ is the monolayer adsorbed gas quantity and $c$ is the BET constant.

Equation (1) is an adsorption isotherm and can be plotted as a straight line with $\frac{1}{V[\left(\frac{p_o}{p}\right)-1]}$ on the y-axis and $\varphi = \frac{p}{p_o}$ on the x-axis. This plot is called a BET plot, as shown on Figure 4.4.

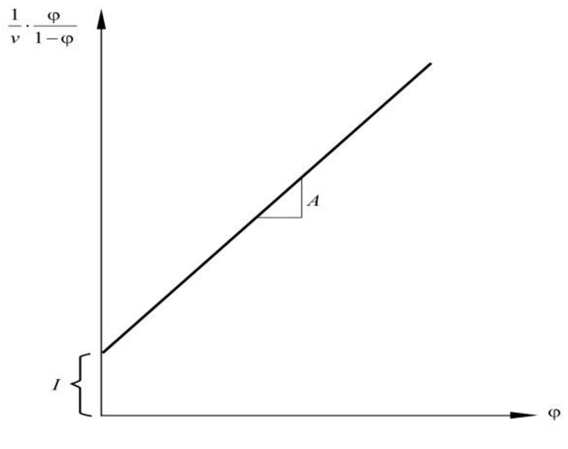

Figure 4.4. BET linear plot.

The linear relationship of this equation is maintained only in the range of $0.05 < p/p_o < 0.35$. The value of the slope $A$ and the y-intercept $I$ of the line are used to calculate the monolayer adsorbed gas quantity $V_m$ and the BET constant $c$. The following equations can be used:

$$V_m = \frac{1}{A+I} \text{ (2)} \qquad\qquad c = 1 + \frac{A}{I} \text{ (3)}$$

The BET method is widely used in materials science for the calculation of surface areas of solids by physical adsorption of gas molecules. The total surface area ($S_{total}$) and the specific surface area ($S_{BET}$) are given by:

$$S_{total} = \frac{V_m \cdot N \cdot s}{V} \text{ (4)} \qquad\qquad S_{BET} = \frac{V_{total}}{a} \text{ (5)}$$

where $V_m$ is in units of volume which are also the units of the monolayer volume of the adsorbate gas, $N$ is Avogadro's number, $s$ the adsorption cross section of the adsorbing species, $V$ the molar volume of the adsorbate gas, and $a$ the mass of the solid sample or adsorbent.

*Pore analysis*

The method of Barrett-Joyner-Halenda (BJH), proposed in 1951, was originally designed for relatively wide-pore adsorbents with a wide pore size distribution. However, it was repeatedly demonstrated that it can be successfully applied to virtually all types of porous materials. The model is based on the assumption that pores have a cylindrical shape and that pore radius is equal to the sum of the Kelvin radius and the thickness of the film adsorbed on the pore wall. BJH analysis can also be employed to determine pore area and specific pore volume using adsorption and desorption techniques. This technique characterizes pore size distribution independent of external area due to particle size of the sample.

- Rapid single point and multipoint specific BET surface area determinations.
- Full BET surface area characterization of disperse, nonporous or macroporous materials pore diameter >50nm (type b isotherms) and mesoporous materials with pore diameter between 2 nm and 50 nm (type d isotherms).
- BET surface area characterization of microporous materials (<2 nm, type a isotherms).
- Pore volume and pore area distributions in the mesopore and macropore ranges using BJH analysis with a full complement of adsorbate thickness models.
- BJH adsorption and desorption average pore diameter (4V/A) determinations.

The classification of adsorption isotherms and their correlation to the material's pore shape is presented on Figure 4.5. The two well-recognized classifications to evaluate the type of isotherms and the hysteresis loop that they exhibit are the de-Boer classification (Fig.4.5a) and the IUPAC classification (Fig.4.5b).[313-315]

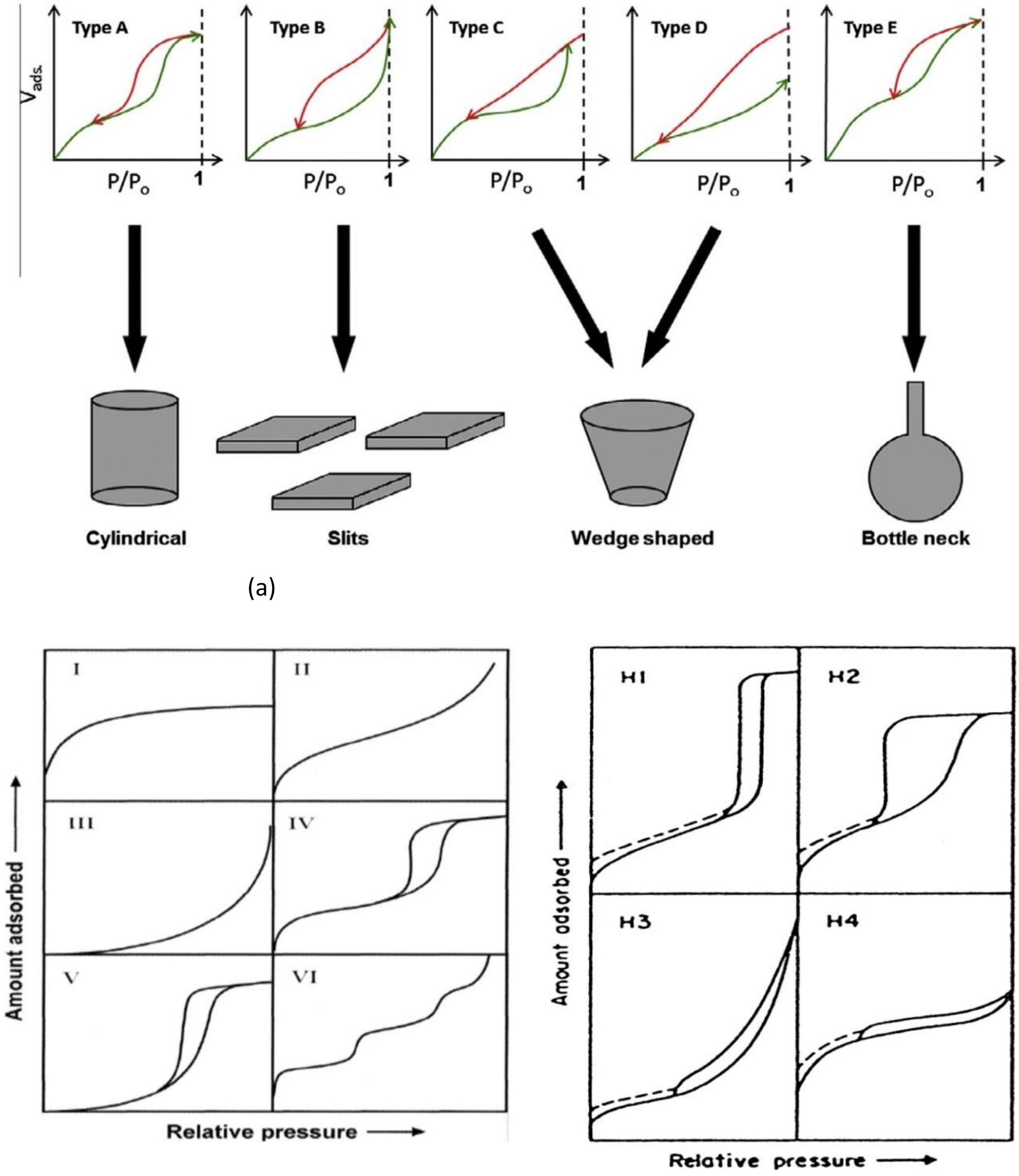

(a)

(b)

Figure 4.5. a) Correlation between the type of hysterisis and pore shape, according to de Boer and b) IUPAC classification of physisorption isotherm types and hysteresis loops.[314-315]

Five types of isotherms were identified and correlated with various pore shapes by De Boer, as shown on Figure 4.5a. Type A corresponds to cylindrical pores; type B is related to slit-shaped pores; type C and D isotherms are attributed to wedge-shaped pores, and type E is produced by bottle neck pores.[315] The shape of pores is a very important factor to evaluate the catalytic performance, as it influences the absorption/desorption phenomena on the catalytic surface.

Furthermore, according to the IUPAC classification (Fig4.5b), Type I isotherms are given by microporous solids having relatively small external surfaces, while the reversible Type II isotherm is the normal form of isotherm obtained with a non porous or macroporous adsorbent. The reversible Type III isotherm is convex to the x axis over its entire range and it is indicative of an unrestricted multilayer formation process. Finally, adsorption on mesoporous solids that proceeds via multilayer adsorption followed by capillary condensation result in Type IV and V isotherms.[314]

Concerning the hysteresis loop IUPAC classification (Fig4.5b), type H1 is often associated with porous materials showing a narrow distribution of relatively uniform (cylindrical-like) pores. Materials that give rise to H2 hysteresis have a more complicated pore structure in which network effects (e.g., pore blocking/percolation) play an important role. Isotherms with type H3 hysteresis do not exhibit any limiting adsorption at high $P/P_0$ that can be caused, for example, by the existence of non-rigid aggregates of plate-like particles or assemblages of slit-shaped pores. H4 hysteresis loops are mainly obtained by complex materials containing both micropores and mesopores. Both, types H3 and H4 hysteresis contain a characteristic step-down in the desorption branch associated with the hysteresis loop closure.[314]

Specific surface area (BET) and BJH pore size distribution measurements were carried out on GAPP V-Sorb 2800 Analyser using nitrogen and helium as carrier gas. The technique encompasses external area and pore area evaluations to determine the total specific surface area, yielding important information in studying the effects of surface porosity and particle size in many applications. In this project, the specific surface area measurements as well as the BJH pore size distribution are employed for the evaluation of the synthesized catalysts. Also, the obtained isotherms were employed to shed light on the pore shape of the examined catalysts.

B.E.T. specific surface area and pore distribution measurements were carried out on a GAPP V-Sorb 2800 Analyser using nitrogen (99.9%) with helium (99.999%) as carrier gas. All samples were subjected to degassing under vacuum ($3\cdot10^{-4}$ Torr) in two stages during pretreatment. During the first stage the samples were heated up to 80°C for 45min, while in the second stage they are heated up to 150°C for another 45min.

### *4.5.5. Reversed Flow-Inverse Gas Chromatography (RF-IGC)*

Hydrogen adsorption phenomena were studied by Reversed Flow-Inverse Gas Chromatography (Fig.4.6). By using Reversed-Flow Inverse Gas Chromatography (RF-IGC), which is a time-resolved flow perturbation version of IGC, being introduced in 1980 by N. A. Katsanos *et al.*[316] and extensively used since as a tool to study various physicochemical processes. The physicochemical characterization of solid adsorbents and catalysts is achieved through the determination of various kinetic and energetic parameters over an extended period of time [316-318].

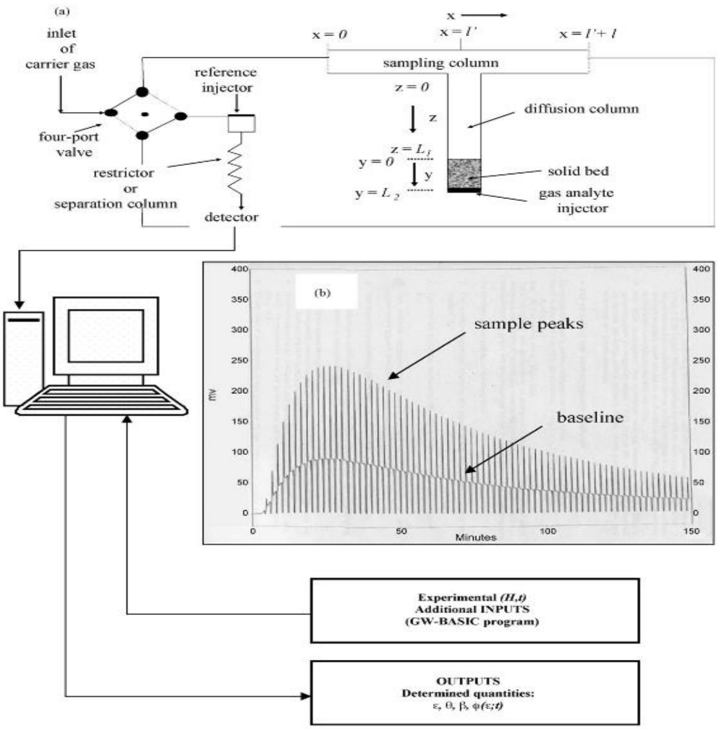

Figure 4.6. Schematic representation of the RF-IGC set-up for surface characterization through the diffusion of gases (a) and a typical chromatogram (b). [319]

RF-IGC method substitutes the role of carrier-gas in classical chromatography with gaseous diffusion currents inside a new diffusion column vertical to chromatographic current (sampling column). The latter is placed a little far from the solid bed where all the physicochemical phenomena that take place in the absence of gas running. In addition, the direction of carrier-gas flow is reversed for short time intervals by using a four or six port valve. As a result, the chromatographic peaks taken are extra narrow and deposit onto the conventional chromatographic signal (Fig.4.6a & b). Based on these modifications, the carrier gas flow has no interference with the measurement of physicochemical quantities, which describe all physicochemical phenomena that take place inside the diffusion column where there is no flow of carrier gas but only a static pressure that it creates.

The extra chromatographic peaks (Fig.4.6b) obtained by repeatedly reversing the carrier gas direction for short time intervals are called sample peaks. They have different heights depending on the duration of each flow reversal and the experimental parameters that affect those reversals are mentioned in Figure 4.6b. The fact that flow reversals occur regularly, suggests that it is a time-resolved experiment similar to those in chemical kinetics. Further details including the theoretical prediction of the sample peaks and the general principles of this method's mathematical model are described in the book "Air pollution and cultural heritage searching for the relation between cause and effect" [319].

In this work, helium was used as carrier gas with a constant volumetric flow rate of 24 $cm^3$/min, 0.5ml of hydrogen is used as the injected reactant at atmospheric pressure and 5 $cm^3$ of catalyst is placed in the diffusion column. The direction of the carrier gas flow was reversed once every minute, which is a shorter time than the gas hold-up, in order to double the chromatographic signals.

### *4.5.6. Temperature profile analysis*

The temperature profile analyzer that was employed has been manufactured in the Advanced Ceramics & Composite Materials Laboratory of NCSR "Demokritos". The pyrex beaker containing the initial SCS mixture is placed in the preheated furnace at 500$^{o}$C. There are three 100 μm type K (chromel/alumel) thermocouples connected to a multiple input thermometer for temperature measurement, mounted in the lid and they are placed in and above the solution. Thermocouples were situated at a distance of 0.4, 2 and 3.5cm measured from the beaker's bottom. The thermocouple system is connected on a temperature recorder and its data are processed by computer software (PicoLog & Microsoft Excel) in order to obtain temperature-time graphs. A PICO TC-08 data logger was used to record the temperature signals at a rate of 0.5ms.

#### 4.5.7. Infra-red camera

Infrared Camera enables the observation and the accurate quantification of heat patterns, leakage, dissipation, and other heat related factors in equipment, products, and processes in real time. In this study, the temperature of the combustion wave was also measured in-situ using a high-speed infrared camera (FLIR Systems, model A655SC). The camera features a 640x480 pixel microbolometer that detects temperature differences down to <30 mK, for accuracy at longer distances and the time constant is less than 8ms. The speed of the combustion wave was calculated by analysis of the data obtained from the high-speed infrared camera.

#### 4.5.8. Dynamic X-Ray diffraction

For in-situ observation of the combustion process and study of the dynamics of phase formation in the reaction front of the combustion, wave time-resolved (dynamic) X-ray diffraction (DXRD) was used. This method is a powerful tool for studying the mechanism of phase formation, since it can monitor a sample’s phase compositional changes in real time during the propagation of the reaction wave. For this purpose, the samples are placed in a small PTFE container of dimensions 20x10x2mm inside a furnace equipped with an X-ray source with a copper anode. A monochromator made of pyrolytic graphite was attached to the X-ray tube. The window of the chamber is made of a beryllium plate to ensure minimum possible X-ray absorption. Diffracted X-rays from the sample are recorded in the horizontal plane by using a 1-dimensional position-sensitive detector which can receive data over a range of 2θ of 30° to 75°. The detector control, synchronization of measurements and data capture and processing were all carried out by means of a computer.

#### 4.5.9. Thermogravimetric analysis

Thermogravimetric analysis (TGA) and differential thermal analysis (DTA) were used to monitor the change in sample weight and any endothermic and exothermic thermal transformations occurring during SCS. For these studies, an STA 449F1 instrument from NETZSCH-Gerätebau GmbH, Germany was employed. Heating rate for all samples (weight of 17-21 mg) was 30°C/min between 40°C and 500°C and all experiments were conducted under Ar with a flow rate of 80 ml/min in an alumina crucible.

# 5. Parameters that influence the liquid-phase hydrogenation of maleic acid

## 5.1. Temperature of reaction

### *5.1.1. Catalyst preparation*

The initial solution used for the employed catalyst consists of 66.7%wt. nickel nitrate hexahydrate [$Ni(NO_3)_2 \cdot 6H_2O$] as the oxidizer with 33.3%wt. glycine as the reducer for a total solid mass of 14g which gives 3g of Ni in the final catalyst. The solid mixture was then dissolved in 100ml of distilled water and the solution was pre-heated in a borosilicate glass beaker on a hot plate with mild magnetic stirring until the temperature reached 70$^{o}$C and then placed in a pre-heated furnace at 500$^{o}$C to enable SCS. Once SCS is completed, the beaker is removed from the furnace and allowed to cool at room temperature.

### *5.1.2. Results and discussion*

The catalytic reactor was programmed in four different temperatures (70, 80, 90, 95°C) for the hydrogenation reaction to take place. In these tests, 0.26g maleic acid were used (calculated for 50ml of hydrogen) as the unsaturated hydrocarbon and a SCS catalyst. The obtained results are presented on Figure 5.1, below. In the experiments 1g of the Ni-based SCS catalyst was added.

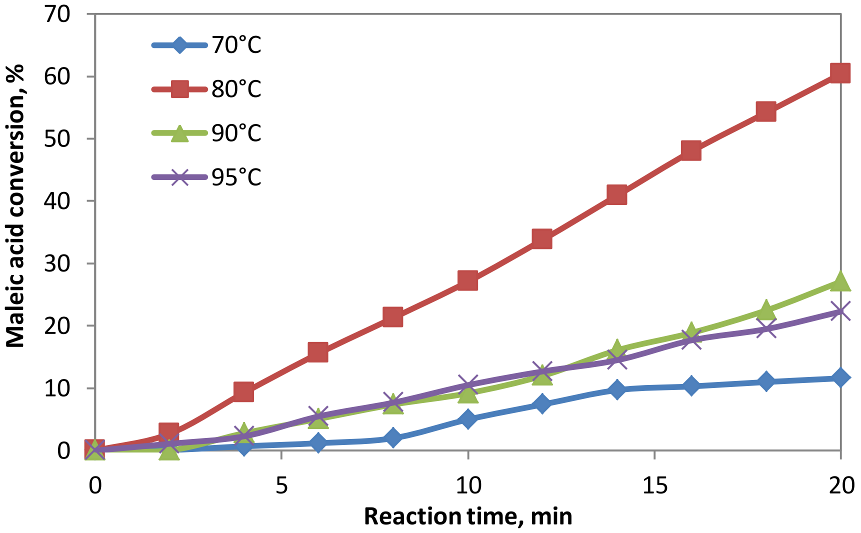

Figure 5.1. The dependence of maleic acid conversion on the temperature of the reaction, calculated from the quantity of absorbed hydrogen.

It was concluded that 80°C is the optimum temperature for the selected reaction. At lower temperature (70°C) the observed catalytic activity was lower, as the temperature decrease resulted in a decrease of the adsorption and the reaction velocity, due to the decrease of the molecules' velocity. As the temperature of the reaction increases above 80°C (90 and 95°C), the temperature of reaction is not the limiting stage but adsorption is. In other words, when the temperature of reaction is above the 80°C, the adsorption rate alters due to the enhanced water evaporation. At 90 and 95°C the solvent evaporation increases and because of the reduced quantity of the solvent, the dissolution of the reaction components is reduced and consequently the adsorption rate and activity are decreased too.

## 5.2. Quantity of catalyst

### *5.2.1. Catalysts preparation*

The initial solution used for the employed catalyst consists of 66.7%wt. nickel nitrate hexahydrate [$Ni(NO_3)_2 \cdot 6H_2O$] as the oxidizer with 33.3%wt. glycine as the reducer for a total solid mass of 14g which gives 3g of Ni in the final catalyst. The solid mixture was then dissolved in 100ml of distilled water and the solution was pre-heated in a borosilicate glass beaker on a hot plate with mild magnetic stirring until the temperature reached 70°C and then placed in a pre-heated furnace at 500°C to enable SCS. Once SCS is completed, the beaker is removed from the furnace and allowed to cool at room temperature.

### *5.2.2. Results and discussion*

0.5, 1, 1.5 and 2g of Ni-based catalyst [initial SCS mixture: 66.7% $Ni(NO_3)_2$, 33.3% glycine, 100ml distilled water] were tested in liquid-phase hydrogenation of maleic acid (0.26g – calculated for 50ml of hydrogen) at 80°C. The quantity of catalyst plays a significant role in the of catalytic reaction rate as the quantity directly affects the available surface for the catalytic reaction to happen. The measured results are presented on Figure 5.2 that follows.

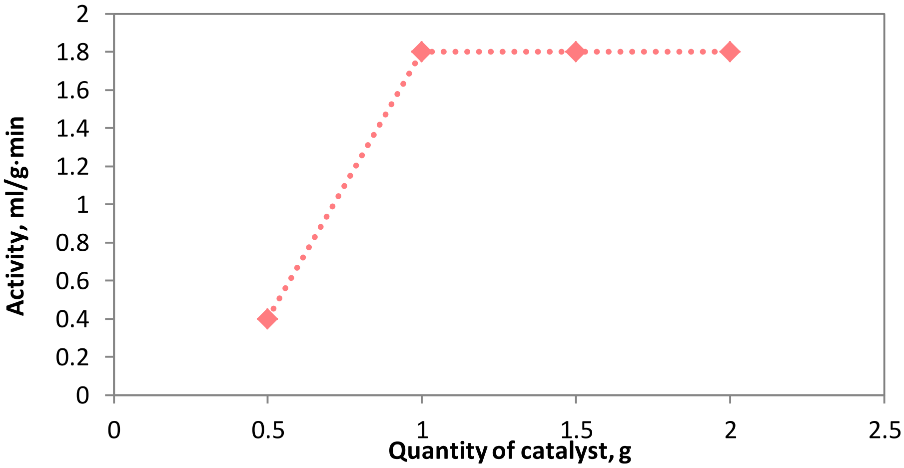

Figure 5.2. Correlation between the amount of catalyst and their activity in liquid-phase hydrogenation of maleic acid.

At such low temperature (80°C), it appears that for 0.5g of catalyst the provided surface area was very low for the adsorption of maleic acid and hydrogen. As a result, the reaction was limited by the adsorption stage. Activity reached its maximum at 1g of catalyst while, when the quantity of the employed catalyst exceeded the 1g (1.5 and 2g), the catalyst activity was not affected. That indicates that the catalyst activity is the controlling factor of the reaction rate and not its quantity. Further increase of the catalytic quantity above 1g did not affect the adsorption and the catalyst activity, because even at 1g, the reaction is only affected by the catalyst composition.

## 5.3. Diluter nature

### *5.3.1. Catalyst preparation*

The initial solution used for the employed catalyst consists of 66.7%wt. nickel nitrate hexahydrate [$Ni(NO_3)_2{\cdot}6H_2O$] as the oxidizer with 33.3%wt. glycine as the reducer for a total solid mass of 14g which gives 3g of Ni in the final catalyst. The solid mixture was then dissolved in 100ml of distilled water and the solution was pre-heated in a borosilicate glass beaker on a hot plate with mild magnetic stirring until the temperature reached 70°C and then placed in a pre-heated furnace at 500°C to enable SCS. Once SCS is completed, the beaker is removed from the furnace and allowed to cool at room temperature.

### *5.3.2. Results and discussion*

Water and isopropyl alcohol were tested as diluters for the maleic acid hydrogenation at 80°C on Ni-based SCS-derived catalysts. By changing the diluter in the liquid-phase hydrogenation reaction, the solubility of the reactive substances alters as well as the adsorption of hydrogen and reactants on the catalytic surface.

Water found to be a suitable diluent for the liquid-phase hydrogenation of maleic acid at 80°C. In the case of the alcohol, the reaction didn’t take place, because of its higher volatility. That can be justified by the boiling point of isopropyl alcohol, which is 82.5°C, and it was very close to our working temperature. Due to the evaporation of the diluent, adsorption became the limiting stage of the process and the catalyst was not active.

## 5.4. Parameters selected for liquid-phase hydrogenation

Thus, for all further tests involving the liquid-phase hydrogenation of maleic acid water was employed as diluent with 1g of catalyst at 80°C, as those appeared to be the optimum conditions for the selected reaction.

# 6. Nickel nitrate – glycine system

## 6.1. Influence of the nickel nitrate concentration

### *6.1.1. Materials preperation*

The precursor SCS mixture consisted of mixtures of nickel nitrate hexahydrate [$Ni(NO_3)_2{\cdot}6H_2O$] as oxidizer and glycine  as reducer. Four compositions were studied with different quantities (3, 6, 9, 12g) of the oxidizer in the SCS solution and 50%wt (of the oxidizer's quantity) glycine. The solid mixture was then dissolved in 75ml of distilled water and each solution was pre-heated in a borosilicate glass beaker on a hot plate with mild magnetic stirring until the temperature reached 70°C. At that point the beaker was placed in a pre-heated furnace at 500°C in air atmosphere for the SCS to take place. After the end of combustion the beaker was removed from the furnace and left to cool at room temperature.

### *6.1.2. Results and discussion*

The development of the phases in the materials produced by SCS is shown in the XRD patterns shown in Figure 6.1 below. The unidentified peaks that appear on the patterns below the 20 degrees are associated with the substrate employed for the XRD measurement, they were not taken into account during the analysis and they were not in conflict with any sample peaks.

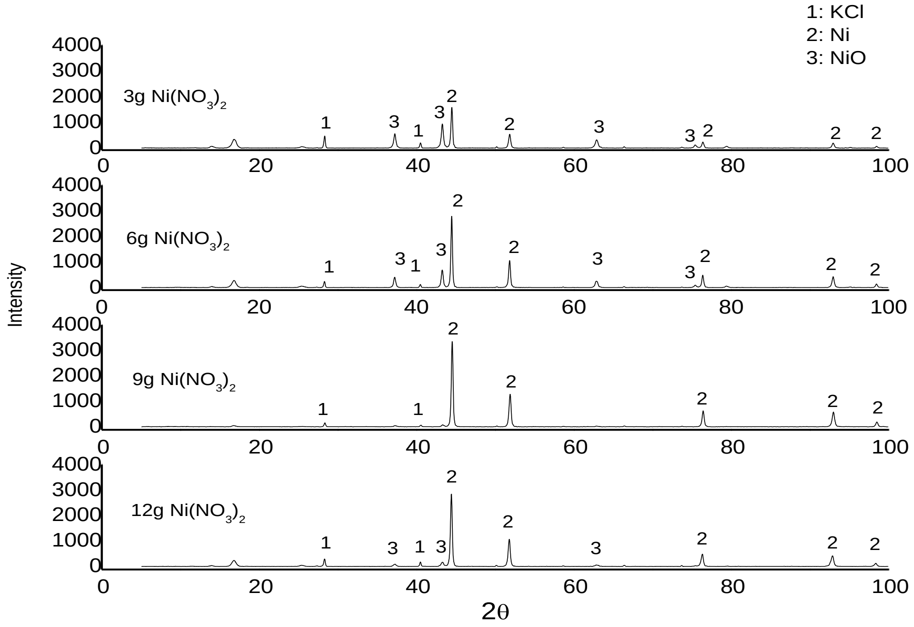

Figure 6.1. Development of crystal structure of SCS catalysts on the basis of initial composition of $Ni(NO_3)_2$, 50% glycine and 75ml distilled $H_2O$.

The two phases produced by SCS were metallic nickel and nickel oxide (NiO), as determined by XRD analysis. The relative phase concentration of Ni and NiO, determined by the comparative XRD analysis, as a function of nickel nitrate quantity in the precursor mixture are presented in Figure 6.2 where the variation between Ni/KCl and NiO/KCl are shown together for comparison.

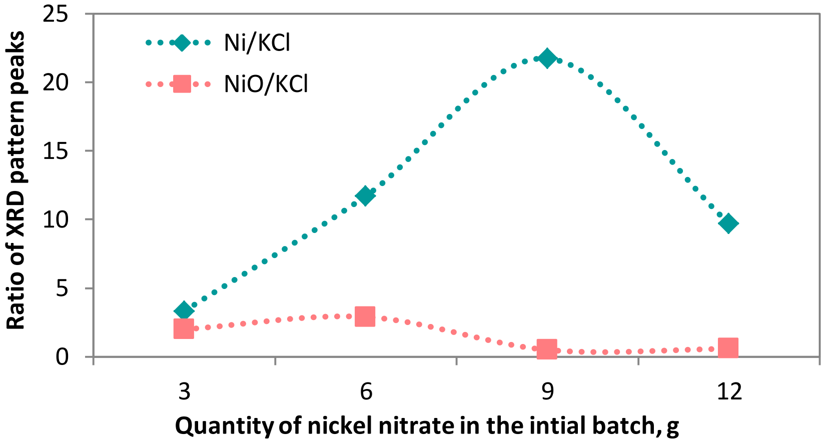

Figure 6.2. Semi-quantitative analysis of Ni and NiO phases in the resulting materials.

Figure 6.2 shows that the concentration of metallic nickel in the resulting product increases when the quantity of nickel nitrate increases up to 9g in the initial mixture. Interestingly, with further increase of nickel nitrate to 12g the concentration of nickel is reduced in the final material.

### *6.1.3. Conclusions*

The increase of the oxidizer quantity affects only the generated heat from the combustion, thus the cooling time is prolonged. On the other hand, there is a specific time for the formation of nickel as well as for its oxidation. Thus, the maximum in the concentration of nickel can be attributed to the initial increase of time for nickel formation, while after exceeding 9g, there is enough time for nickel oxidation as well. It is of high importance to have high nickel content in the final products, as they will be employed as catalysts toward liquid-phase hydrogenation and nickel is the active phase for this catalytic reaction.

## 6.2. The effect of the fuel quantity on the catalysts' properties

### *6.2.1. Catalysts preparation*

The initial aqueous solution contains nickel nitrate hexahydrate [$Ni(NO_3)_2\cdot 6H_2O$] as the oxidizer with glycine [$C_2H_5NO_2$] as the reducer. In the series of experiments carried out, four different samples were synthesized. The quantity of nickel nitrate and distilled water were kept constant at 9.3g and 100ml respectively. In each of the four samples, a different amount of glycine was added (4.7, 7.0, 9.3, 11.6g, which is calculated as 50, 75, 100 and 125wt% of nickel nitrate) for the production of Ni and NiO. The beaker was then placed in a pre-heated furnace at 500°C after the end of combustion the beaker was removed from the furnace and left to cool at room temperature.

### *6.2.2. Structural analysis*

The development of the various phases in the SCS-derived products is shown in the XRD patterns shown in Figure 6.3. The unidentified peaks that appear on the patterns below the 20 degrees are associated with the substrate employed for the XRD measurement, they were not taken into account during the analysis and they were not in conflict with any sample peaks.

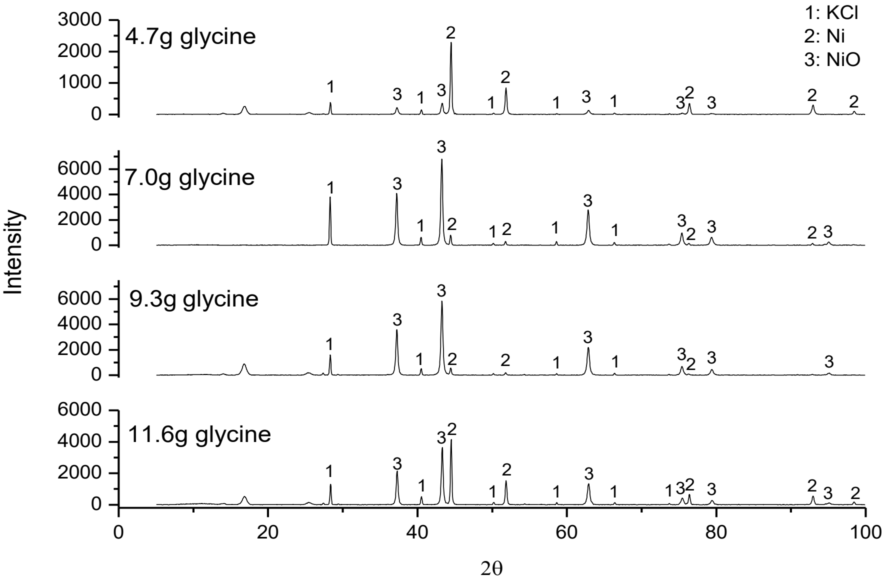

Figure 6.3. Development of the crystal structure of an SCS material on the basis of nickel nitrate hexahydrate with various glycine concentrations and 100ml water as diluent.

As it is illustrated on Figure 6.3, cubic nickel and nickel oxide are the products of the SCS in various concentrations. The products were examined using TEM analysis and the results are shown on Figure 6.4 below.

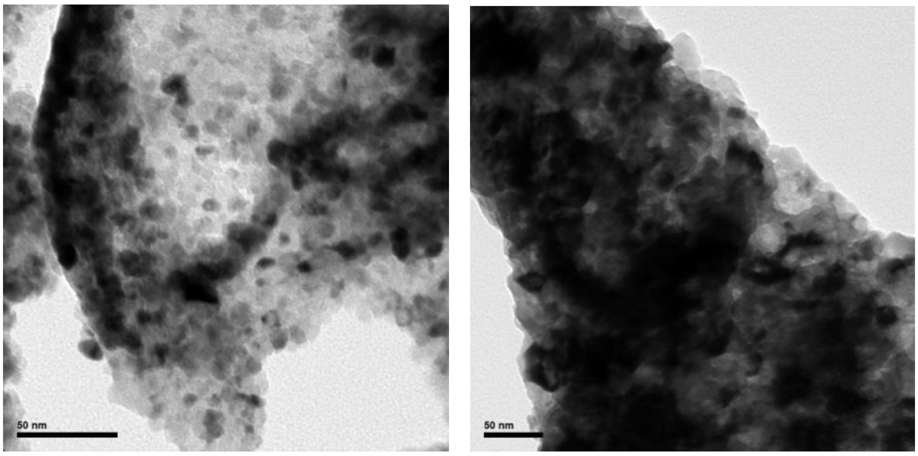

a b

Figure 6.4. TEM images of the sample prepared with 4.7g glycine in the initial solution [TEM analysis was performed by Dr. N. Boukos in "NCSR Demokritos"].

TEM bright field images of areas consist of 5-12nm crystallites (a) and of 15-50nm crystallites (b). They demonstrate that the as-synthesized crystallites and by extension, the SCS product is directly synthesized in nanoscale. The TEM images were taken from two different areas of the sample and are indicative of its crystallites size.

The relative phase composition of Ni and NiO, as determined by the comparative XRD analysis, as a function of the added quantity of glycine are presented in Figure 6.5 where the variation between Ni/KCl and NiO/KCl are shown together for comparison.

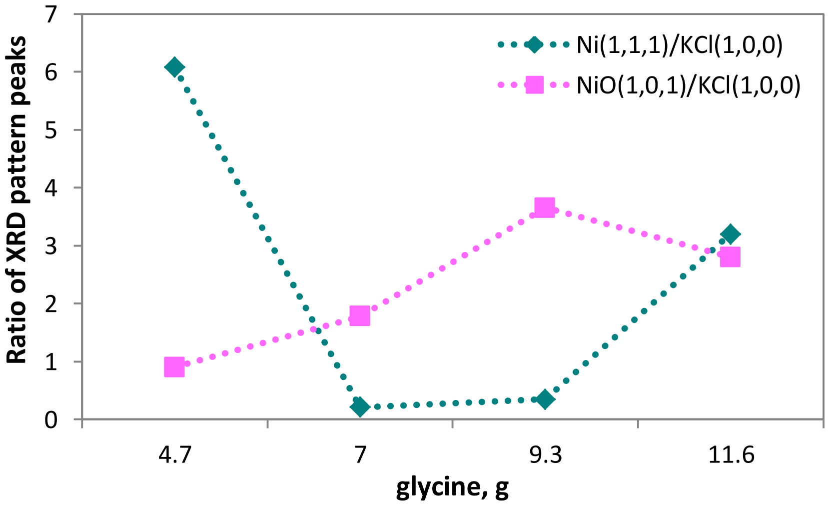

Figure 6.5. Semi-quantitative SCS final composition dependence from glycine concentration in SCS mixture [$Ni(NO_3)_2 \cdot 6H_2O$, glycine, 100ml $H_2O$].

According to Figure 6.5 above, the maximum nickel content in the SCS products occurs at the position of the minimum nickel oxide content when the amount of glycine employed in the initial solution is 4.7g. It appears that at this point, there is an optimum ratio between ammonia and nitric acid that react and produce hydrogen, creating a reduction atmosphere for the synthesis of nickel from nickel oxide. Conversely, as the glycine concentration increases up to 9.3g the nickel oxide content in the final product is maximized with a minimum of nickel. Initially, the increase of carbon concentration in the mixture leads to an increase of the reaction temperature, making the oxidation of the reduced nickel quicker. With further increase of glycine to 9.3g, the soot oxidation reaction is favoured on the expense of the nickel oxide reduction. Thus, the carbon originated from glycine is employed to the soot oxidation reaction yielding carbon monoxide and carbon dioxide. Additionally, the ammonia produced by glycine is in much excess for the reaction with nitric acid and as a result their non-stoichiometric reaction produces a relatively small amount of hydrogen. The combination of the small amount of produced hydrogen and the consumption of carbon in the oxidation reaction resulted in reduction of nickel content in the SCS product. On the other hand, when the glycine quantity reaches 11.6g, the combustion temperature rises and the carbon concentration is so high that both the nickel oxidation and the reduction of nickel oxide take place, resulting in the enhancement of the nickel concentration in the final product. Notably, in this case, carbon is the major element that reduces nickel oxide for the production of nickel, and not hydrogen as it was in the case of 4.7g glycine.

BET analysis was employed to perform measurements that provided information about the samples’ pore shape, pore volume and specific surface area. The results are presented in the figures that follow.

### *6.2.3. Pore shape and surface area measurements*

Adsorption-desorption curves obtained by the BET method are shown in Figure 6.6 for all four synthesized materials.

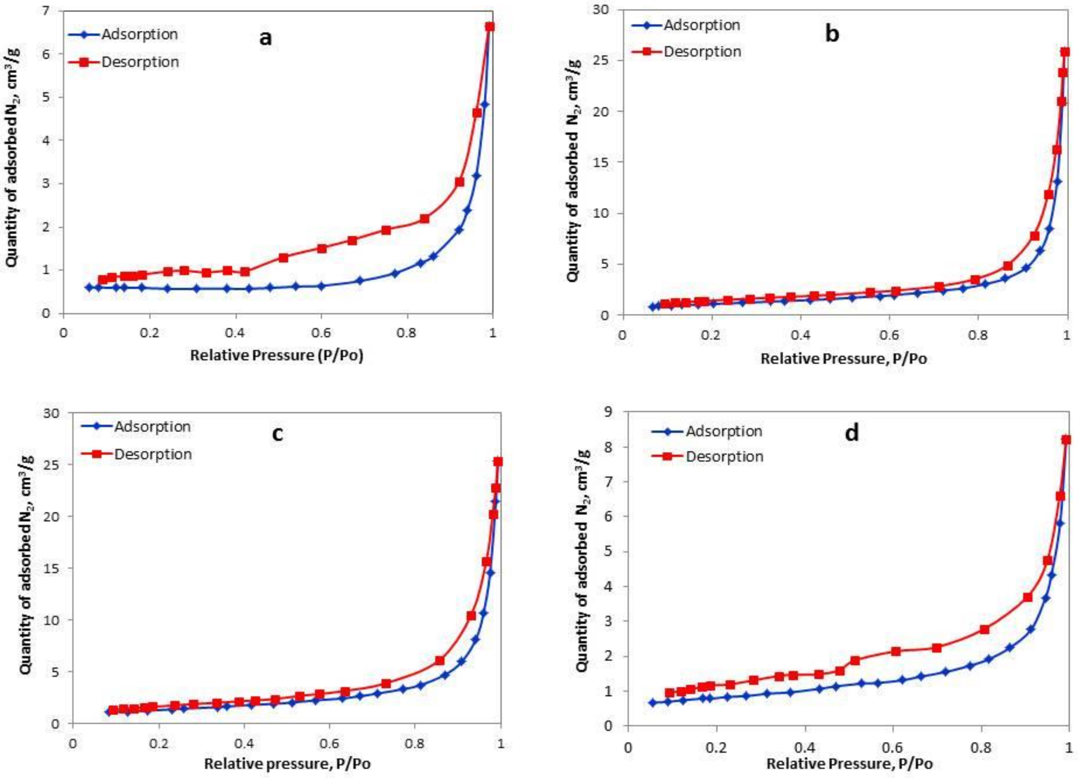

Figure 6.6. Hysteresis curve of SCS materials with a) 4.7g, b) 7g, c) 9.3g, d) 11.6g glycine.

The samples with 7g and 9.3g glycine that provided the (b) and (c) curves adsorbed the most nitrogen at the highest pressure, while the other two adsorbed the least nitrogen, indicating little microporosity. Moreover, all tested samples provided a hysteresis loop but the samples with 4.7g and 11.6g of glycine exhibited a distinct hysteresis loop, suggesting that the evaporation from the pores is a completely different process from the condensation in the pores, which indicates the occurrence of capillary condensation within mesopores.[18] Regarding the shape of the hysteresis loops, the adsorption/desorption isotherms of samples with 4.7g and 11.6g of glycine (a and d isotherms correspondingly) correspond to type B, suggesting the existence of large number of cylindrical and slit-shape pores with all open sides [302]. On the other hand, the type of loop in samples with 7g and 9.3g glycine (b and c isotherms accordingly) are type C indicating that the pores have a predominately wedge shape [302]. The pore shape affects the adsorption/desorption processes during catalysis influencing the catalysts' activity.

Specific surface area measurements as a function of the quantity of glycine in the initial solution of SCS are presented on Figure 6.7a. Specific surface area exhibits an increasing trend and reaches a maximum for 9.3g of glycine in the mixture. Furthermore, Scherrer formula for XRD was used to estimate the crystallite size of Ni and NiO which are shown in Figure 7b against the final products' specific surface area.

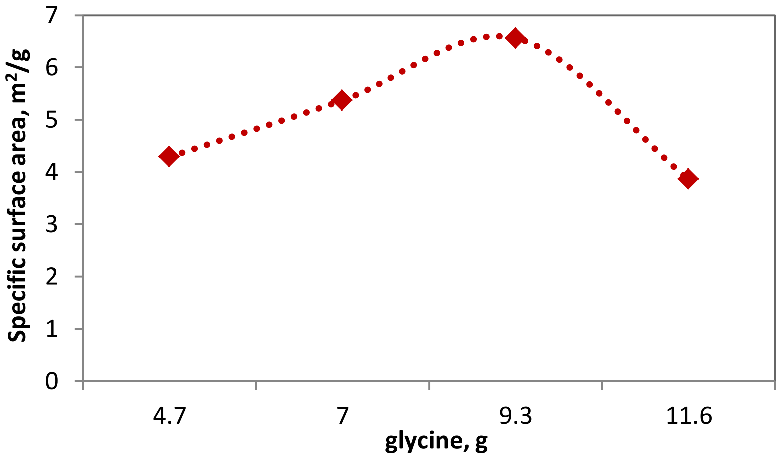

(a)

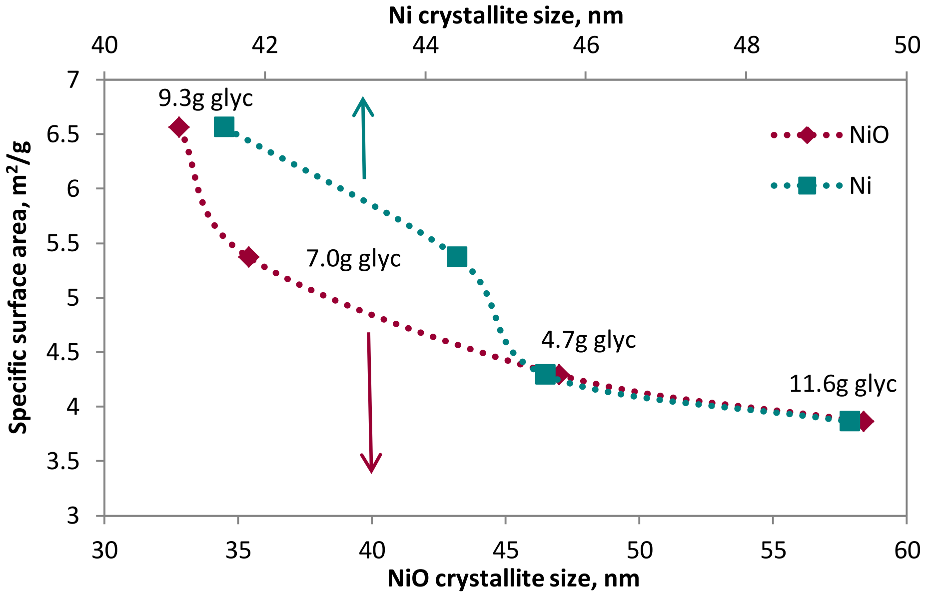

(b)

Figure 6.7. a) Influence of glycine quantity in SCS batch [$Ni(NO_3)_2{\cdot}6H_2O$, glycine, 100ml water] on the specific surface area of the final products and b) dependence of Ni and NiO crystallites size on SSA.

The crystallites size of both nickel and nickel oxide severely affects the materials' specific surface area. Figure 6.7b demonstrates that as the crystallites of nickel and nickel oxide grow, the nanomaterials' surface area reduces accordingly. Thus, when 11.6g of glycine was added in the initial mixture, the crystallites of nickel and nickel oxide were the largest of the measured samples, and that led to the material's smallest specific surface area. In addition it can be observed that by increasing the quantity of glycine the size of the crystallites is reduced. That can be justified by the increase of the generated gases (CO and $CO_2$) as the quantity of carbon increases, leading to quicker cooling rates that result in smaller crystallites. Furthermore, increasing of the crystallite size as the reducer increases can be attributed to the increase of the combustion temperature due to excessive quantity of glycine at high concentrations. That resulted in soot generation and additional heat input due to the reaction of soot combustion. Conversely, when the glycine concentration is maximized (11.6g) the crystallites size of nickel and nickel oxide reach their maximum as well, due to the excess of carbon concentration that causes sintering effect to take place.

Moreover, the average crystallite size for Ni was found to be approximately 45.5nm and 47 for NiO concerning the sample prepared with 4.7g glycine in the precursor solution. These calculations are in agreement with the crystallites detected by TEM analysis and were measured to be 5-15nm and 15-50nm in the two pictures presented on Figure 6.4.

Figure 6.8 shows the cumulative pore volume as a function of the pore diameter for the four samples prepared with different amounts of glycine in the SCS initial mixture.

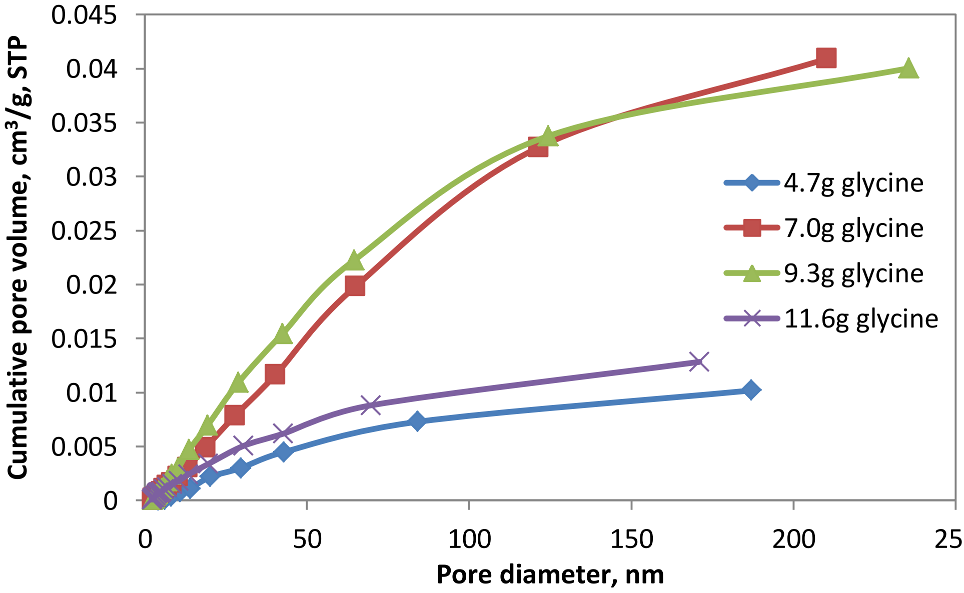

Figure 6.8. Cumulative pore volume of SCS Ni catalyst with various glycine concentrations.

The pore distribution measurements shed more light on the materials microstructure. The material prepared with 4.7g of glycine appears to possess the minimum volume of nanopores, but smaller crystallites than the one with 11.6g and that justifies its slightly better SSA. As the glycine increased up to 9.3g, the materials' total porosity as well as the volume of nanopores was increased and that resulted in their enhanced SSA, as the sample prepared with 9.3g glycine had the maximum SSA. On the other hand, the sample with 11.6g glycine had the lowest total porosity and large crystallites of nickel and nickel oxide, and these characteristics led to its lowest SSA. The nanomaterials with smaller crystallites (obtained with 7g and 9.3g glycine) have higher volume of nanopores as well as increased total porosity which leads to enhanced surface area.

### *6.2.4. Conclusions*

It was determined, that if crystallites of nickel and nickel oxide grow, the nanomaterials' surface area reduces accordingly. By increasing the percentage of glycine (from 4.7g to 9.3g) the size of the crystallites is reduced. That can be justified by the increase of the generated gases (CO and $CO_2$) as the quantity of carbon increases, leading to quicker cooling rates that result in smaller crystallites. Furthermore, increasing the crystallite size as the reducer increases can be attributed to the increase of the combustion temperature due to excessive quantity of glycine at high concentrations which lead to sintering process. Nanomaterials with smaller crystallites (7g and 9.3g glycine) have higher volume of nanopores and higher porosity which lead to enhanced specific surface area.

## 6.3. Influence of glycine concentration with slow heating mode

### *6.3.1. Catalysts preparation*

The initial solution of the resulted materials contained nickel nitrate hexahydrate [$Ni(NO_3)_2 \cdot 6H_2O$] as the oxidizer with glycine as the reducer. In the experiments carried out, four types of samples were synthesized keeping the quantity of nickel nitrate constant at 9.34g in the initial mixture with 75ml distilled water, adding specific amounts of glycine (80, 60, 50 and 40wt% of nickel nitrate) to achieve fuel to oxidizer molar ratio ($\phi$) of 2.78, 2.08, 1.74 and 1.4 for the production of Ni and NiO ($\phi$=1.0 corresponds to stoichiometry for the general SCS reaction). After preparation, the precursor solutions were placed in the furnace at room temperature and they were slowly heated up to 500°C with an average heating rate 3°C/min.

After the end of combustion the beaker was removed from the furnace and left to cool at room temperature.

### *6.3.2. Microstructural analysis*

The development of the various phases in the SCS-derived products is shown in the XRD patterns shown in Figure 6.9.

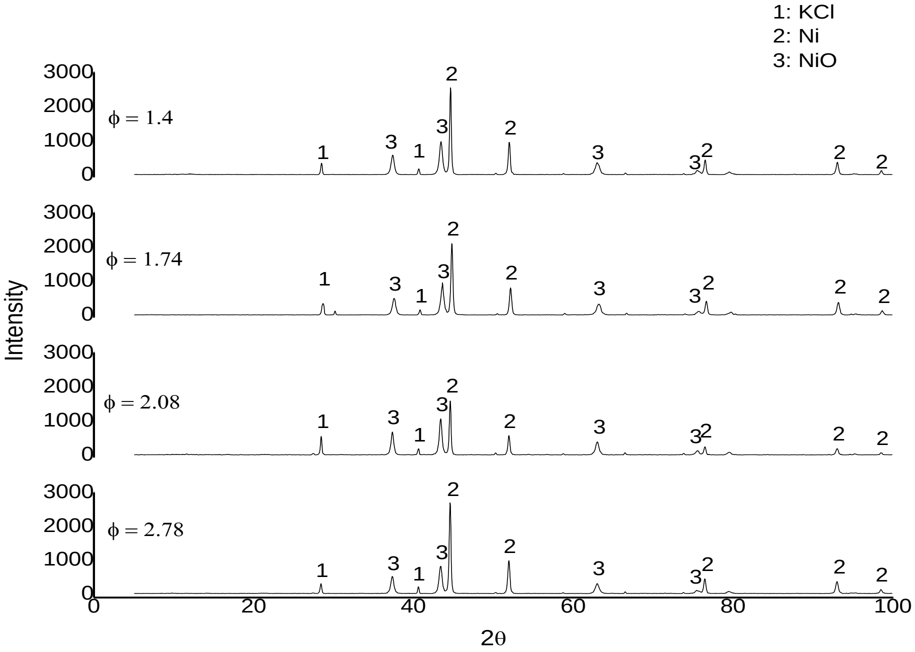

Figure 6.9. Development of crystal structure of an SCS catalyst on the basis of nickel nitrate hexahydrate with glycine in various ratios.

As it is illustrated on Figure 6.9, nickel oxide and metallic nickel are the products of the SCS in various concentrations. This cascade of the yielded reactions during SCS is described from the following equations.

$$Ni(NO_3)_2\cdot 6H_2O \xrightarrow{54℃} Ni(NO_3)_2\cdot 4H_2O \xrightarrow{85.4℃} Ni(NO_3)_2\cdot 2H_2O \quad \text{(i)}$$

$$2Ni(NO_3)_2\cdot 6H_2O + C_2H_5NO_2 \rightarrow Ni + NiO + NO_2 + 2NO + N_2 + 2CO_2 + \frac{29}{2}H_2O + \frac{5}{2}O_2 \text{ (ii)}$$

$$2Ni(NO_3)_2\cdot 6H_2O \rightarrow 2NiO + NO_2 + NO + N_2 + 12H_2O + \frac{7}{2}O_2 \quad \text{(iii)}$$

$$Ni(NO_3) + H_2O \rightarrow NiOHNO_3, NiOHNO_3 + H_2O \rightarrow Ni(OH)_2 + HNO_3 \quad \text{(iv)}$$[76]

$$CH_2NH_2COOH \rightarrow [CH_2COO]^- + NH_3 \quad \text{(v)}$$[76]

$HNO_3 + \frac{7}{3}NH_3 \rightarrow 3H_2O + \frac{5}{3}N_2 + H_2$ (vi) [76]

$2NH_3 \overset{Ni}{\rightarrow} 3H_2 + N_2$ (vii) [320]

$NiO + H_2 \rightarrow Ni + H_2O$ (viii)

$Ni + O_2 \rightarrow NiO + \frac{1}{2}O_2$ (ix)

$2CH_2NH_2COOH + 6O_2 \rightarrow 4CO_2 + 5H_2O + NO + NO_2$ (x)

$C + O_2 \rightarrow CO_2$ (xi)

$C + NiO \rightarrow Ni + CO$ (xii)

$CO + NiO \rightarrow Ni + CO_2$ (xiii)

The relative phase composition of Ni and NiO, as determined by the comparative XRD analysis, as a function of ϕ ratio are presented in Figure 6.10 where the variation between Ni/KCl and NiO/KCl are shown together for comparison.

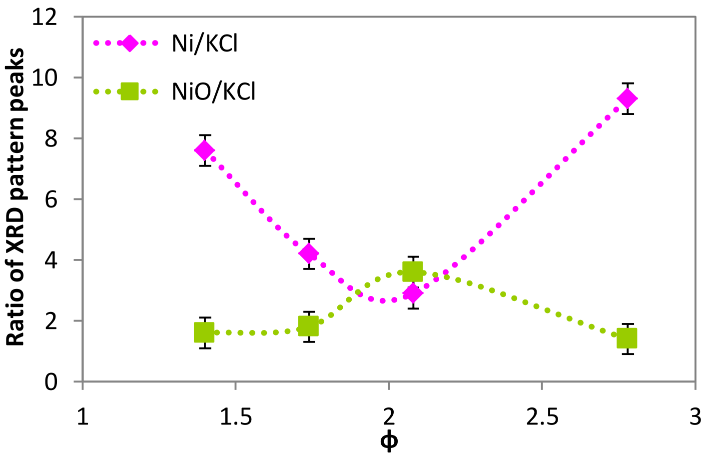

Figure 6.10. Dependence of XRD peak ratio on nickel nitrate/glycine ratio in the initial SCS solution.

Figure 6.10 illustrates that the variation of glycine content in the initial SCS mixture resulted in various concentrations of nickel and nickel oxide. According to the obtained data, the concentration of nickel is maximized when the concentration of the fuel is maximum as well (ϕ=2.78), while it is minimized at ϕ=2.08 ratio. The observed variation in the concentration of both nickel and nickel oxide is originated to the reactions' stoichiometry as well as the soot concentration in each case. The stoichiometry of reactions (vi & vii) influences the existence and the quantity of the hydrogen that it is employed for the nickel oxide reduction to produce nickel (reaction viii). Nevertheless, soot concentration, which increases by increasing the fuel content, plays a key role due to the fact that carbon is also used to reduce nickel for nickel production (reaction xii & xiii).

The extent of defect structure is a very important parameter for catalysts, as the defects act as active centres and influences the hydrogen adsorption on the catalytic surface in the specific case of hydrogenation reactions. On Figure 6.11 below, the degrees of the nickel peak (2, 0, 0) shifting in the XRD pattern as a function to ϕ ratio is presented.

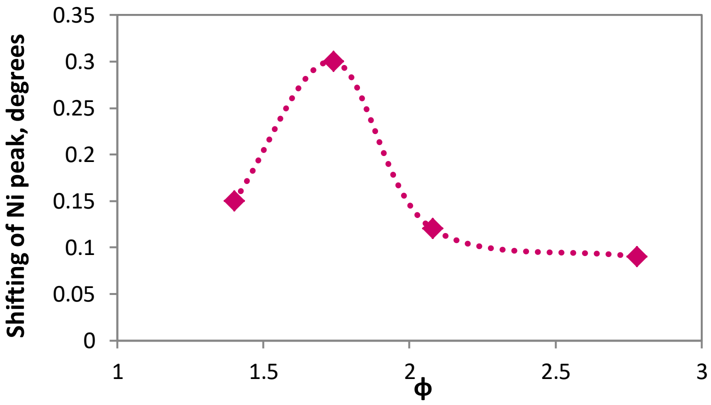

Figure 6.11. The degrees of a Ni peak (2, 0, 0) shifting in the XRD spectrum as a function to ϕ ratio.

According the data obtained by XRD measurements, the peak of nickel with (h,k,l)=(2,0,0) was shifted in all the examined samples to the right. The catalyst prepared with ϕ=1.74 ratio of nickel nitrate to glycine exhibited the highest shifting of the nickel peak, implying a high extent of defect structure in the crystal lattice. Generally, peak shifting is caused due to the stress, strain, dislocation and defects in the crystal induced by the synthesis parameters. In this case, there is no systematic shifting of all the peaks in the same way. It was also determined that the peak shifting is not due to the alignment of the instrument.

Bragg’s and Scherrer’s formulas for XRD were used to determine the crystal lattice spacing and crystallite size of Ni and NiO which are shown in Figures 6.12 and 6.13 against the ratio between nickel nitrate and glycine (ϕ).

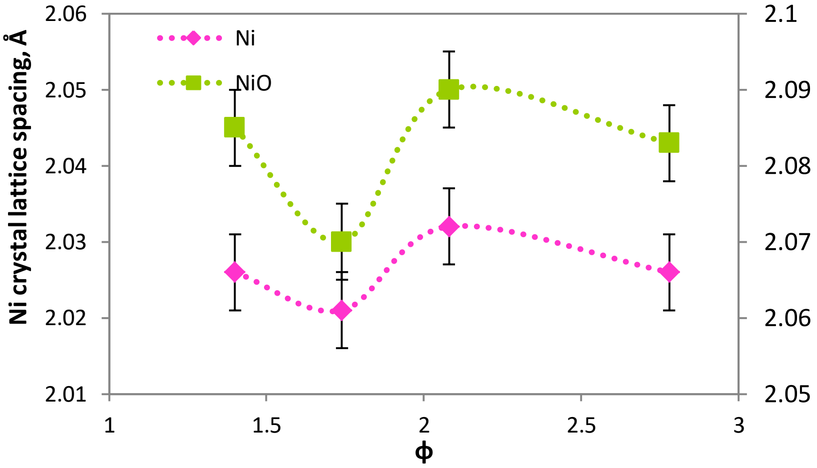

Figure 6.12. Influence of nickel nitrate/glycine ratio in initial solution on crystal lattice spacing of the products.

It can be observed on Figure 6.12 that increasing the fuel (increasing of ϕ ratio) in the SCS initial solution leads in minor changes in Ni and NiO crystal lattice spacing which reflect the crystallite nucleation conditions that are present in each case. The minimum value of lattice spacing in the case of ϕ=1.74 for both Ni and NiO, is in accordance with the highest measured shifting of the XRD peaks, indicating a greater extent of the defect structure in the lattice. Furthermore, the observed minimum in the distance between the crystal planes may result in a more strained crystal that is a possible cause for the shifting of the Ni peak in Figure 6.11.

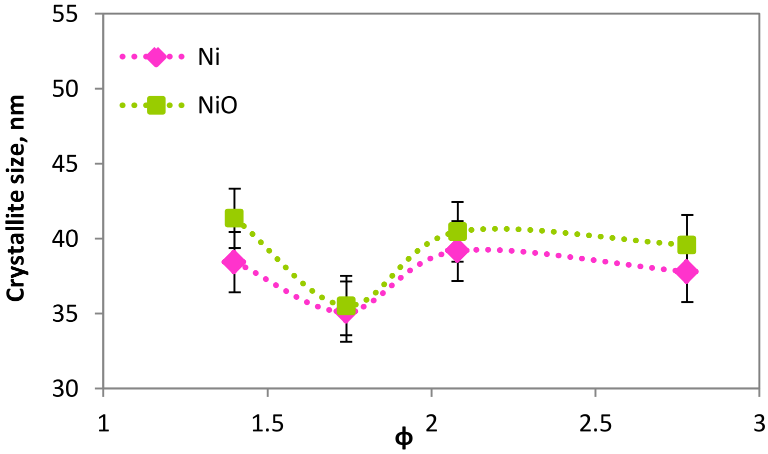

Figure 6.13. Influence of ϕ ratio on crystallite size of the final product.

Scherrer's formula revealed the crystallite size in the four catalysts for nickel and nickel oxide. There are only minor changes in the calculated crystallite size, as it is shown in Figure 6.13, while the nickel crystallite size of the catalyst produced with ϕ=1.74 is minimum, suggesting a better dispersion of the metallic phase on the nickel oxide.

Specific surface area measurements, determined by BET analysis, as a function of the ϕ ratio are presented on Figure 6.14 and the specific surface area shows an increasing trend, reaching its maximum when the fuel concentration is maximized.

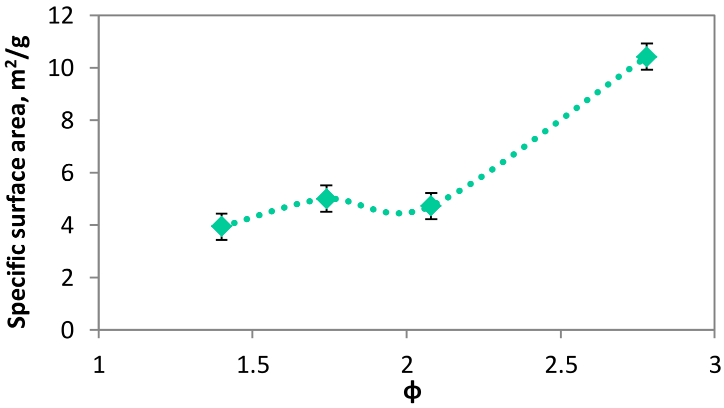

Figure 6.14. Influence of ϕ ratio on the final products specific surface area.

Generally, when the concentration of the reducer increases the carbon content increases as well, leading to an increase of the cooling due to the enhanced soot oxidation that yields during synthesis (refer to reaction xi). As a result, there is more time available for the pores to be formed, thus the highest porosity is expected in the highest fuel concentration. This justifies the maximum of the specific surface area in the catalyst prepared with the highest fuel content in its initial solution.

### *6.3.3. Catalytic studies*

The catalytic activity of the Ni-based SCS catalysts discussed above was examined in the liquid-phase hydrogenation of maleic acid. The kinetic and conversion curves that were obtained during hydrogenation are demonstrated in Figures 6.15 and 6.16.

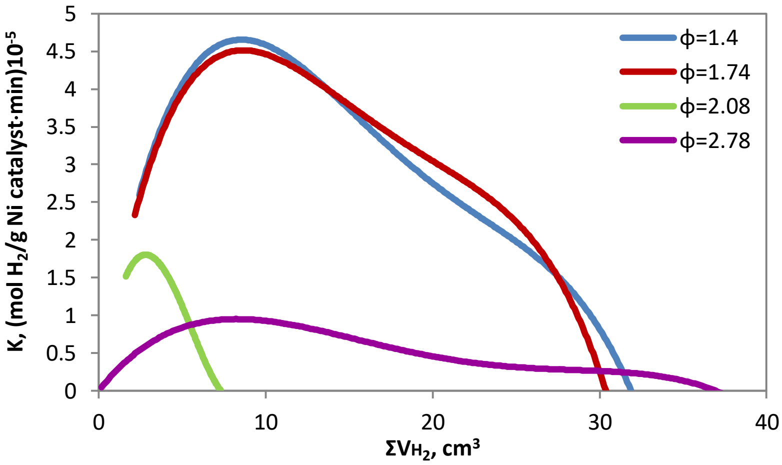

Figure 6.15: Dependence of observed maleic acid hydrogenation on the SCS Ni-based catalysts on the volume of absorbed hydrogen.

Figure 6.15 establishes the measured set of kinetics curves of the SCS catalysts with different ratio of reactants in their precursor solution. The catalysts prepared with relatively low ϕ ratio appear to be most active, while the catalysts made with higher ϕ exhibited very low activity (ϕ=2.78) or were almost inactive (ϕ=2.08). Conversion curves of the catalysts are displayed on Figure 6.16.

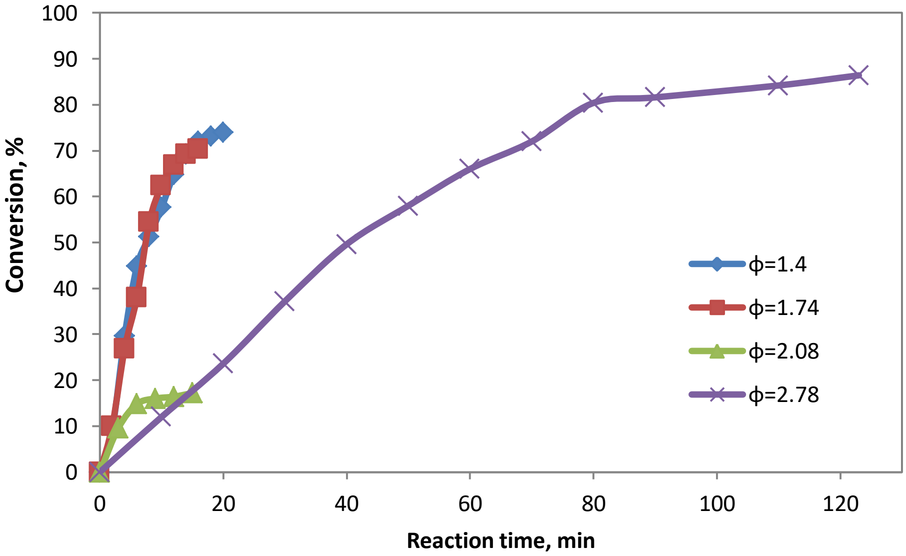

Figure 6.16: The dependence of maleic acid mass conversion on the SCS catalysts calculated from the quantity of absorbed hydrogen.

The degree of conversion of maleic acid into succinic acid is very low (17.2%) for the catalysts with ϕ=2.08, whereas the other three catalysts exhibit better catalytic activity, with the catalyst produced with ϕ=2.78 showing the highest conversion rates. These results correlate well with the catalysts' kinetic curves (Fig.6.15). Notably, the catalyst prepared with ϕ=2.78 exhibited higher percentage of conversion than those made with ϕ=1.4 and ϕ=1.74, even though the latter showed significantly higher velocity during hydrogenation. Catalysts with ϕ=1.40 and ϕ=1.74 exhibited high velocity towards the hydrogenation of maleic acid that can be attributed to the high concentration of Ni and in high defect concentration, accordingly. Furthermore, neither of the catalysts tested achieved 100% conversion, suggesting that the succinic acid produced was strongly adsorbed on the catalysts surface leaving no available space for new hydrogen molecule to adsorb and react with maleic acid.

The percentage of hydrogen surface coating is a crucial parameter for catalytic activity, as all catalytic reactions take place on the catalyst's surface. In the Figure 6.17 that is shown below, the percentage of hydrogen surface coating on catalysts in correlation with their activity in liquid-phase hydrogenation is illustrated as a function to the ϕ ratio.

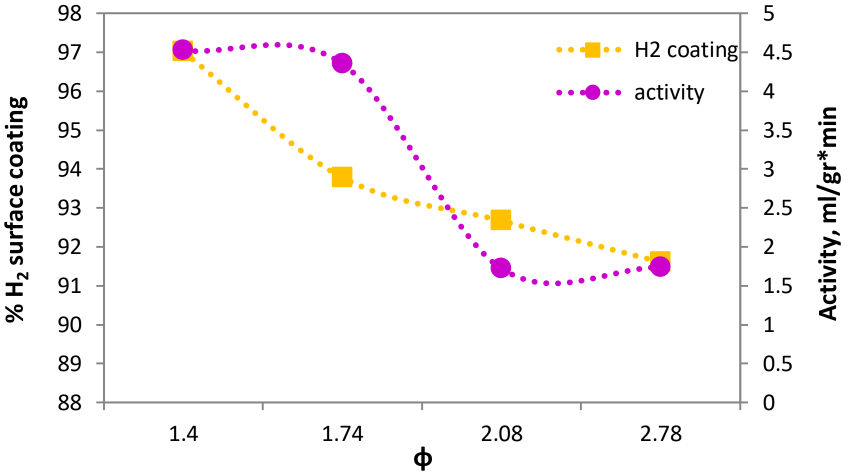

Figure 6.17. Extent of hydrogen surface coating and activity as a function of the reactants ratio (ϕ).

There is a correlation between the percentage of the hydrogen surface coating and the catalysts measured activity toward the maleic acid hydrogenation. The catalysts prepared with a relatively low ϕ ratio exhibited the maximum velocity over the reaction, while the catalyst made of ϕ=2.08 shown the lowest velocity. The percentage of the hydrogen surface coating is affected by various parameters. Some of the most important ones are the concentration of nickel and the extent of the defect structure in the catalyst volume. Specifically, the catalyst with ϕ=1.4 ratio of reactants has the maximum percentage of hydrogen coating on its surface due to its high nickel content (Fig.6.10) and as a result was the most active. By increasing ϕ to

1.74 the percentage of hydrogen decreases, due to its lower nickel content. Noticeably, the catalyst activity is not severely influenced because of its highest extent of defect structure, as presented on Figure 6.11 and its highest dispersion of nickel on nickel oxide (suggested by Fig.6.13). Moreover, when the fuel content in the initial mixture maximizes (ϕ=2.78), the additional heating provided by the soot oxidation leads to enhancement of the sintering process resulting in the elimination of defects in the metal crystallites, which are responsible for the catalytic activity [321]. This conclusion is consistent with the measured shifting of the nickel peak in the XRD spectrum (Fig.6.11) and explains the minimum percentage of hydrogen coating on the catalyst surface, despite its maximum nickel concentration. Finally, the catalyst prepared with ϕ=2.08 was almost inactive due to its lowest nickel content (Fig.6.10) with small dispersion on the nickel oxide (Fig.6.13) and its relatively low percentage of hydrogen surface coating.

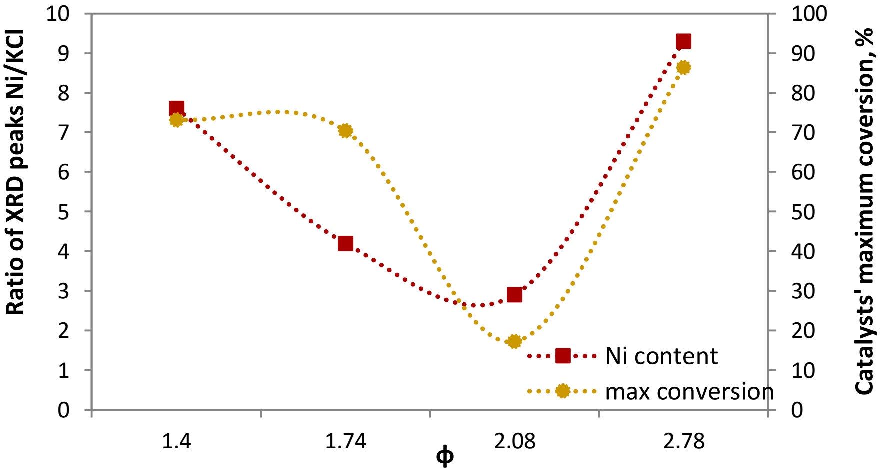

Figure 6.18. Dependence of nickel concentration and conversion of SCS catalysts on the reactants ratio (ϕ).

Nevertheless, there is a sufficing correlation between the catalytic' conversion of maleic acid to succinic acid during hydrogenation and the calculated nickel content in their mass (Fig.6.18). The decrease of nickel content from ϕ=1.4 to ϕ=1.74 is not accompanied with a decrease in the catalysts conversion as it has the highest dispersion of the metallic phase on nickel oxide and the highest shifting of nickel XRD peak that suggest highest extent of defect structure (Fig.6.11). Interestingly, in case of ϕ=2.78, the as-synthesized catalyst exhibited highest conversion, despite its low velocity during hydrogenation, originating to its maximum nickel content and specific surface area (Fig.6.14).

### *6.3.4. Conclusions*

The same series of experiments only with different heating mode were performed and published by Xanthopoulou *et al*.[322] In comparison with those experiments, it appears that when the slow heating mode is applied, the nickel content in the final catalytic nanomaterials is reduced. Moreover, the nickel crystallites is also reduced and ranges between 35-40nm, while in the other mode is ranges between 40-49nm. That can be explained as in the case of slow heating, a big part of the nickel nitrate is already decomposed in nickel oxide, before the time the mixture reaches its ignition point. As a result, there is less quantity of nitrate available to react and participate in the SCS, leading to lees nickel concentration in the final products. Moreover, the lessened quantity of nitrate that participates in the SCS reduces the heat that is emitted from the exothermic reaction. Consequently, there is less sintering process taking place that justifies the reduction in the size of nickel crystallites.

## 6.4. The impact of time in furnace after the completion of SCS

### *6.4.1. Materials preparation*

The precursor SCS mixture consisted of 66.7% nickel nitrate hexahydrate [$Ni(NO_3)_2{\cdot}6H_2O$] as oxidizer and 33.3% glycine as reducer. The total solid mass of the initial mixture was 14g. The solid mixture was then dissolved in 75ml of distilled water and each solution was pre-heated in a borosilicate glass beaker on a hot plate with mild magnetic stirring until the temperature reached 70$^o$C. At that point the beaker was placed in a pre-heated furnace at 500$^o$C in air atmosphere for the SCS to take place. After the completion of the SCS cascade of reactions the beaker was left in the furnace for various time periods (0, 2, 7, 10 min) and four materials were derived.

### *6.4.2. X-Ray and time resolved X-Ray diffraction analysis*

The as-produced materials were characterized by XRD analysis and the resulting patterns are exhibited on Figure 6.19. The unidentified peak that appeared on the patterns below the 20 degrees is associated with the substrate employed for the XRD measurement, it was not taken into account during the analysis and it was not in conflict with any sample peaks.

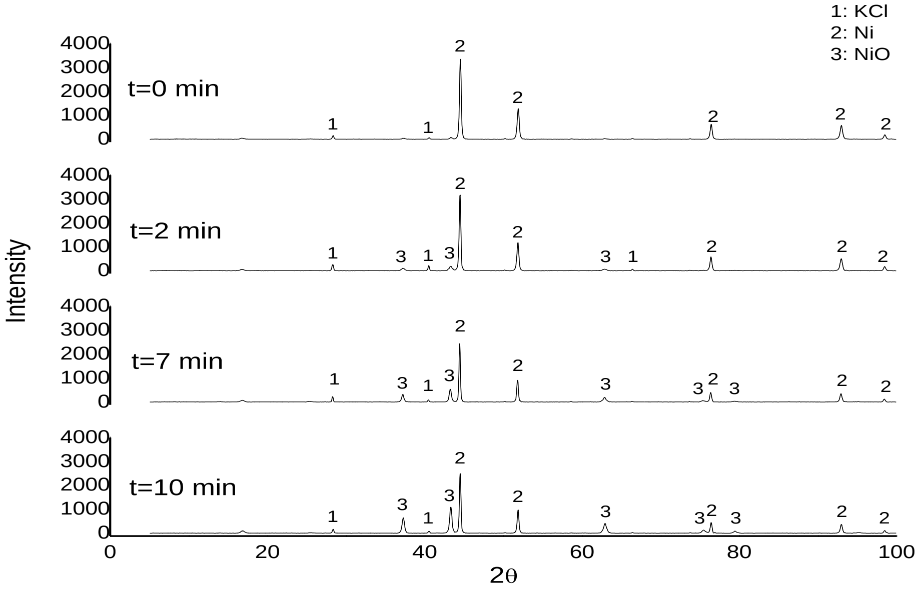

Figure 6.19. XRD patterns from the SCS-derived materials on the basis of initial mixture 66.7% $Ni(NO_3)_2{\cdot}6H_2O$ and 33.3% glycine with various periods of time remaining in the furnace after SCS was completed.

The XRD patterns show the structure of nickel and nickel oxide phases in the final materials. Their different concentrations in the as-burnt products are demonstrated on the semi-quantitative analysis, using KCl as an internal standard (Fig.6.20).

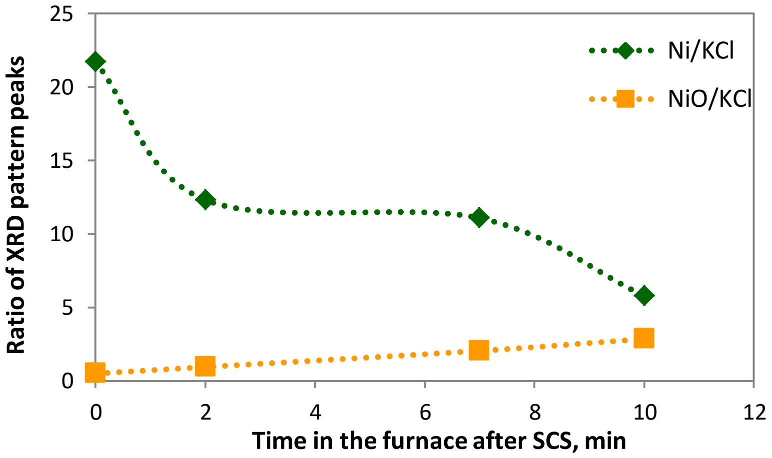

Figure 6.20. Semi-quantitative analysis of Ni and NiO phases in the resulting materials.

Figure 6.20 shows the concentration of nickel and nickel oxide in each sample that remained in the furnace after the SCS ended. Increasing the time that the sample remained in the furnace the concentration of nickel is reduced while the nickel oxide content increases. The fact that the samples remain in such a high temperature after the completion of SCS, provides more time for the oxidation of nickel to take place due to the oxidative atmosphere in the furnace. In conclusion, immediate cooling is suggested in order to achieve maximum nickel concentration in the final product. This can also be confirmed by the obtained time resolving XRD analysis pattern, which is presented on Figure 6.21.

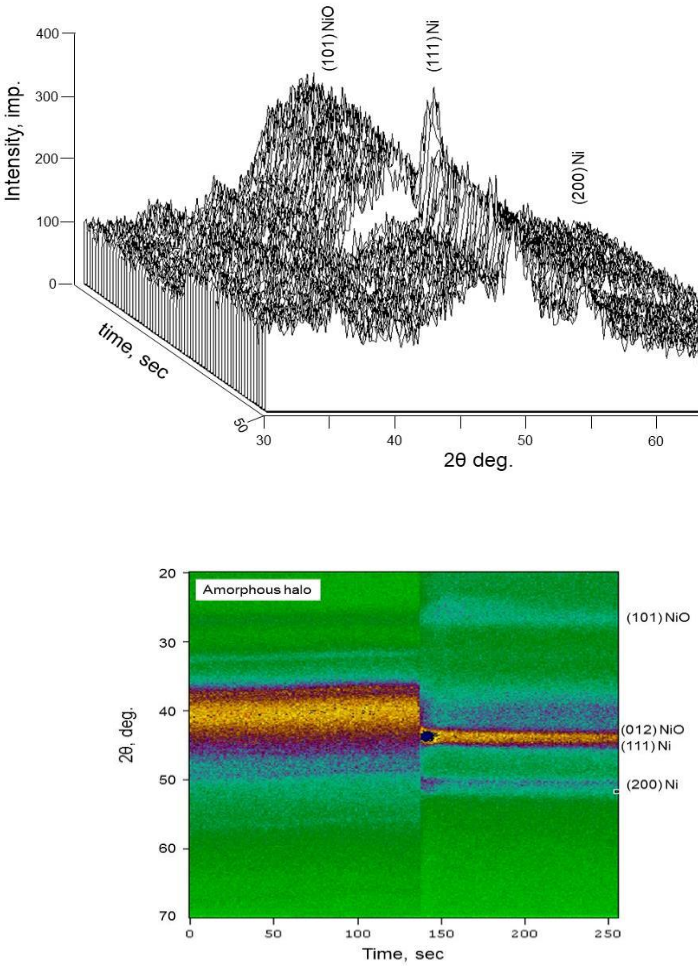

Figure 6.21. Results of time-resolved X-ray diffraction analysis in a SCS gel [Dr. D. Kovalev from the Institute of Structural Macrokinetics and Materials Science in Russia performed the TRXRD analysis].

In Figure 6.21 a sequence of 50 XRD traces obtained by time-resolved X-ray diffraction (*TRXRD*) studies (measured each second) depicts the process of phase formation during SCS. The spectra are presented in both 2D of 2θ versus time as well as in 3D of 2θ versus intensity versus time. The precursor nitrate-glycine mixture provides a diffraction spectrum with wide amorphous halo suggesting that the phases are not crystallized. During the ignition of combustion, nickel lines (111) and (200) appear first and within a few seconds their intensity increases. Thereafter, a reduction of their amplitude with simultaneous appearance of NiO lines (101) and (012) is exhibited. This indicates that after the formation of nickel, its concentration starts to decrease with time, while the concentration of NiO increases.

The influence of the time period that the samples remained in the furnace after SCS completion on the crystallites size of nickel and nickel oxide is presented on Figure 6.22.

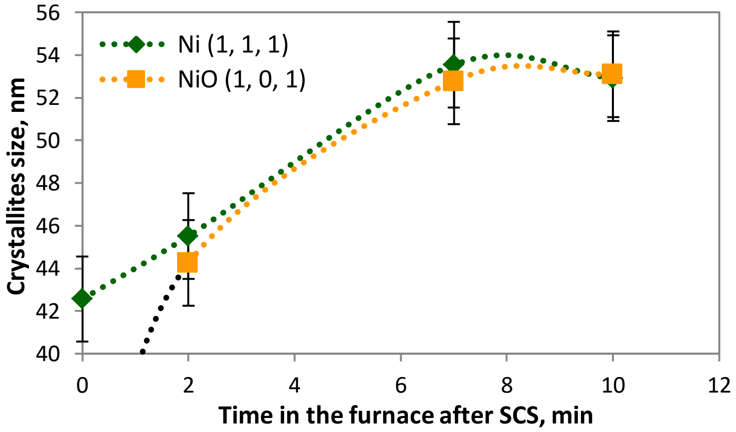

Figure 6.22. Influence of the timed remained in the furnace after the SCS completion on crystallites size of Ni and NiO.

According to the calculated results from Scherrer formula, by increasing the time in the furnace, the crystallites of both nickel and nickel oxide are increasing as well. The sintering process that takes place when the samples are not immediately removed from the furnace results in the observed growth of the crystallites for both phases. As a conclusion, smaller crystallites are obtained when the beaker is removed from the furnace by the time the SCS reactions are finished.

### *6.4.3. Conclusions*

As a conclusion, TRXRD measurements indicate that after the formation of nickel, its concentration starts to decrease with time, while the concentration of NiO increases. That explains the reason that the time in the furnace after SCS finalized leads to increasing of NiO/Ni phase ratio. By increasing the time in the furnace, the crystallites of both nickel and nickel oxide are increasing as well due to the sintering process that takes place.

## 6.5. Studies on the influence of preheating temperature on the nanopowders' properties

The results presented here have been published as: *O. Thoda, G. Xanthopoulou, V. Prokof'ev, S. Roslyakov, G. Vekinis, A. Chroneos, 2018, 27, 207-215.*

### *6.5.1. Materials preparation*

The initial solution used for SCS of our materials consists of 66.7% nickel nitrate hexahydrate as the oxidizer with 33.3% as the reducer for a total solid mass of 14g. The gel mixture was placed in a borosilicate glass beaker in a preheated furnace at 500, 600, 650 and 700°C to enable SCS yielding four different nano-structured foam-like materials. Neither additional water nor pretreatment was employed for the materials manufacturing. Once SCS is completed, the beaker is removed from the furnace and allowed to cool at room temperature.

### *6.5.2. Results and discussion*

The combustion temperature of solution combustion reaction plays a significant role in phase formation and physical characteristics of the products and depends on various process parameters.

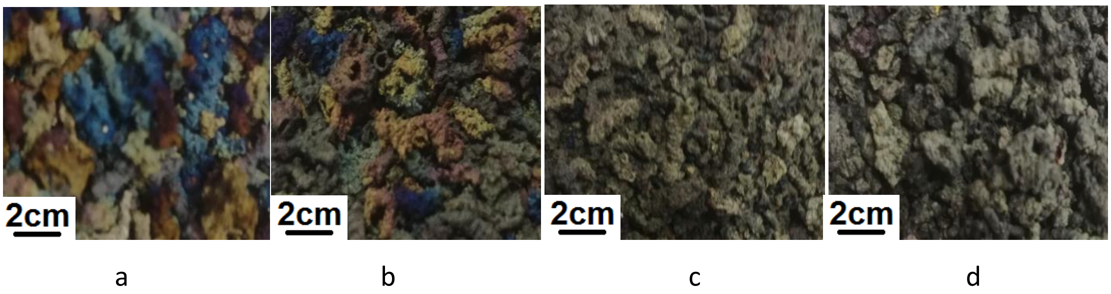

Figure 6.23. Influence of preheating temperature on the structure of SCS catalyst: a) 500°C b) 600°C c) 650°C d) 700°C. The photos were taken by camera.

The foam-like structure of products is illustrated on Figure 6.23 which shows how materials appear after gel-SCS (G-SCS). The different colours that appear indicate variations in crystal orientation. In case of SCS, the addition of water in the initial mixture provides enough volume and time for the hydrates to form. However, the lack of water in the precursor mixture of G-SCS inhibited the formation of hydrates during water vaporization and, as a result dendritic structure did not appear in this case.

### *6.5.3. X-Ray diffraction analysis*

XRD spectra of the resulting Ni/NiO nanocomposites are presented in Figure 6.24 synthesised at various preheating temperatures.

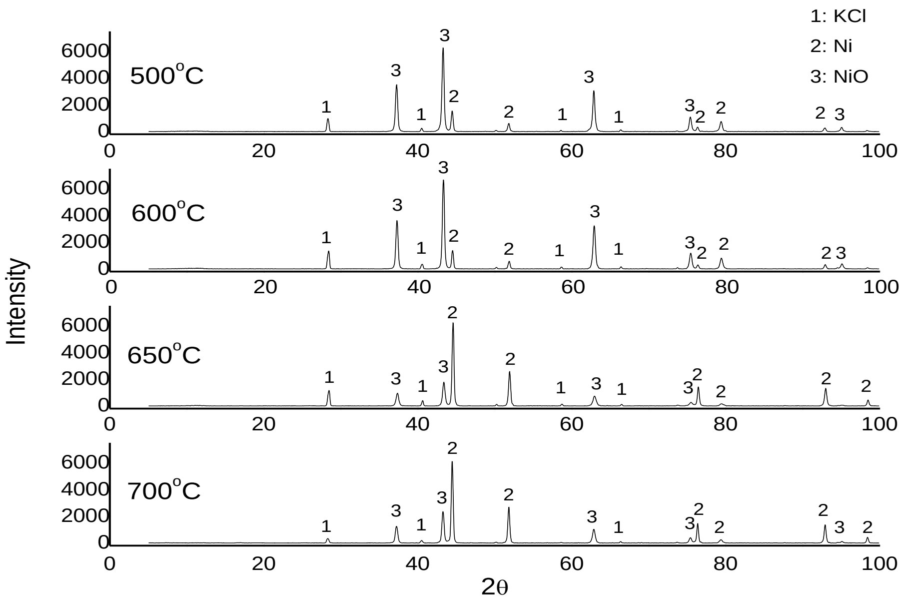

Figure 6.24. XRD diffraction patterns of Ni-NiO SCS catalysts produced at different preheating temperatures ($T_{fur}$).

All the manufactured materials have two products: metal Ni and NiO. A. Kumar *et al.* [65] found in their studies that an intermediate zone exists, where both Ni and NiO are equilibrium products, for fuel to oxidizer ratio varying between 1.5 and 2.5. In our case the fuel to oxidizer ratio is calculated to be 1.74 according to general equation (*) and two different products were detected. By changing the preheating temperatures the XRD analysis revealed that Ni and NiO are in different ratio in each case. Formation of Ni and NiO during G-SCS can be explained by a multi-branch reaction cascade:

$$M^v(NO_3)_v + (\tfrac{5}{9}v\varphi)CH_2NH_2COOH + v\tfrac{5}{4}(\varphi - 1)O_2 \rightarrow M^vO_{\frac{v}{2}}(s) + (\tfrac{10}{9}v\varphi)CO_2(g) + \tfrac{25}{18}\varphi H_2O(g) + v(\tfrac{5\varphi+9}{18})N_2(g) \quad (*)$$

$$2Ni(NO_3)_2 \cdot 6H_2O + C_2H_5NO_2 \rightarrow Ni + NiO + 2NO + NO_2 + N_2 + 2CO_2 + \tfrac{29}{2}H_2O + \tfrac{5}{2}O_2 \text{ (i)}$$

$$Ni(NO_3)_2 \cdot 6H_2O \xrightarrow{54°C} Ni(NO_3)_2 \cdot 4H_2O \xrightarrow{85.4°C} Ni(NO_3)_2 \cdot 2H_2O \text{ (ii)}$$

$Ni(NO_3)_2 \cdot 6H_2O \rightarrow 2NiO + NO_2 + NO + N_2 + 6H_2O + \frac{7}{2}O_2$ (iii)

$Ni(NO_3)(OH)_{2.5} \cdot H_2O \rightarrow 0.5Ni_2O_3 + HNO_3 + 1.25H_2O$ (iv) [76]

$CH_2NH_2COOH \rightarrow [CH_2COO]^- + NH_3$ (v) [76]

$HNO_3 + \frac{7}{3}NH_3 \rightarrow 3H_2O + \frac{3}{3}N_2 + H_2$ (vi) [76]

$2NH_3 \overset{Ni}{\rightarrow} 3H_2 + N_2$ (vii) [323]

$2CH_2NH_2COOH + 6O_2 \rightarrow 4CO_2 + 5H_2O + NO + NO_2$ (viii)

$2CH_2NH_2COOH + 4O_2 \rightarrow 2C + 2CO_2 + 5\mathrm{H_2O} + \mathrm{NO} + \mathrm{NO_2}$ (ix)

$C + O_2 \rightarrow CO_2$ (x)

$NiO + H_2 \rightarrow Ni + H_2O$ (xi)

$NiO + C \rightarrow Ni + CO$ (xii) [324]

$NiO + CO \rightarrow Ni + CO_2$ (xiii) [324]

$Ni + O_2 \rightarrow NiO + \frac{1}{2}O_2$ (xiv)

### *6.5.4. Thermogravimetric analysis*

Thermogravimetric analysis was employed to carry out the temperature-reactions investigation. As an example test, a precursor solution of 66.7% nickel nitrate and 33.3% glycine was heated up to 500°C and the TG/DTA curves as a function of heating temperature are presented on Figure 6.25.

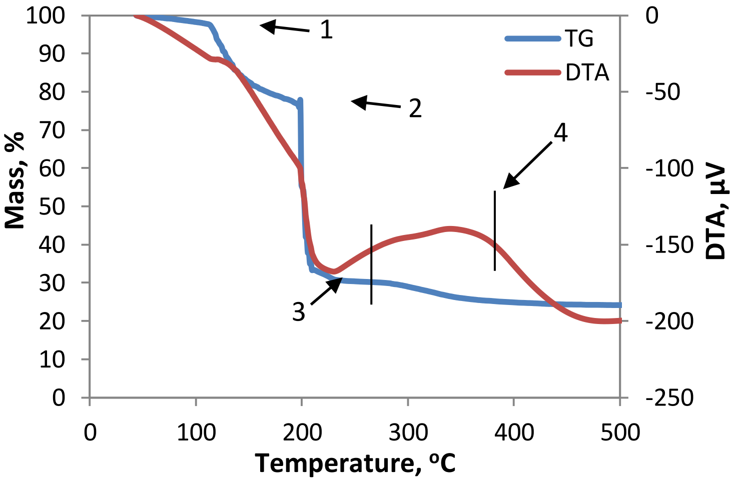

Figure 6.25. TGA-DTA analysis of sample with initial composition 66.7% $Ni(NO_3)_2$ and 33.3% glycine at 500°C. Arrows point the positions of decomposition of nitrates (1), combustion of glycine (2), maximum heat release (3) and an endothermic process (4) [Dr. A. Steinman conducted the TGA measurement in National University of Science and Technology "MISIS"].

Thermogravimetric analysis (TGA), presented in Figure 6.25, reveals the temperature regions in which the various SCS reactions and phenomena take place. At position 1 the mass loss is initiated with the loss of lattice water from nitrates. After the loss of all lattice water and completion of nitrates decomposition (reactions ii, iii & iv), point 2 signifies the initiation of the combustion of glycine (reactions viii & vix), which is the most exothermic process of the system. This exothermic reaction provides the system with extra energy for the reactions cascade of Solution Combustion Synthesis to take place. Between points 2 and 3 the oxidation of glycine is accompanied to multiple ongoing reactions that are initiated from the energy generated from the oxidation of glycine. Point 3 indicates the maximum heat release from the system while, after that point, the DTA curve increases implying the beginning of an endothermic process – possibly the reduction of nickel oxide for nickel production (reaction xi). After the completion of the endothermic process at point 4, the ongoing glycine reactions (reactions viii, ix) as well as the carbon oxidation reaction (reaction x) release heat to the system after SCS is over and that result in delay of the cooling process of the sample.

### *6.5.5. Comparison of theoretical and experimental results*

*[The theoretical modelling presented in this chapter was developed by Dr. V. Prokof'ev, in Tomsk State University, Russia. It is published in: O. Thoda, G. Xanthopoulou, V. Prokof'ev, S. Roslyakov, G. Vekinis, A. Chroneos, Influence of Preheating Temperature on Solution Combustion Synthesis of Ni–NiO Nanocomposites: Mathematical Model and Experiment, International Journal of Self-Propagating High-Temperature Synthesis, 2018, 27, 207-215.]*

Production of nano-sized materials by SCS method with ordered structure and properties is an extremely difficult problem. At the same time rapidly occurring physico-chemical processes such as evaporation, conductive, and radiative heat transfer, convective flow, reacting in the liquid and gas phases with the formation of condensed products of reactions and deposition of reaction products on the walls of the reaction vessel, does not allow the complete mathematical modeling of SCS. It is possible that these factors led to the lack of mathematical models of SCS works cited. Proposed in the present work a mathematical model SCS based on non-stationary theory of thermal explosion of N.N. Semenov [325].

Following these observations, an attempt has been made to analytically model (using the Semenov method)[325] and evaluate the influence of preheating temperature on the flame temperature as well as on the physico-chemical characteristics of the products. During modelling the following assumptions are made:

1. The SCS mixture (nickel nitrate + glycine) is homogeneous and its temperature depends only on time, which corresponds to zero-dimensional formulation of the problem.

2. Any relative movements of the different phases are neglected.

3. The formation and release of gaseous products are solely determined by the change in mass of the solution.

The simplest model to describe this behaviour is that developed by Semenov. In accordance with accepted assumptions, the model includes:

*Equation of heat balance*

$$c_{eff}(T)m(\eta)\frac{dT}{dt} = S\alpha(T_{fur} - T) + Qm(\eta)(1-\eta)k_0\exp(-E/RT)\,; \qquad (1)$$

*Effective heat capacity function*

$$c_{eff}(T) = c_0 + Q_{vap}\delta(T - T_{vap}), \quad (2)$$

where the $c_{eff}$ formulation allows the heat consumed to be utilised by the phase transition as described for melting in [326].

*Equation for evolution of condensed mass*

$$m = m_0 - (m_0 - m_s)\eta; \quad (3)$$

*Chemical kinetics equation*

$$\frac{d\eta}{dt} = (1-\eta)k_0 \exp(-E/RT) \quad (4)$$

with the initial conditions: $T(0)=T_0$, $\eta(0)=0$, $m(0)=m_0$ (5)

where: $\delta(T)$ is the Dirac delta function, $K^{-1}$; $Q_{vap}$ is the latent heat of phase transition, $kJkg^{-1}$; $T_{vap}$ is the temperature of phase transition, K; $c_0$ is condensed-phase heat capacity without phase transition, $kJkg^{-1}K^{-1}$; η is the depth of conversion; S is the area of the bottom of the container, $m^2$; α is the heat transfer coefficient, $Wm^{-2}K^{-1}$; $T_{fur}$ is the furnace pre-heating temperature, K; Q is the heat of reaction, $kJkg^{-1}$; E is the activation energy, $kJmol^{-1}$; R is the universal gas constant, $Jmol^{-1}K^{-1}$; $k_0$ is the pre-exponential factor, $s^{-1}$; $m_0$ is the initial mass of the mixture, kg and $m_s$ is the mass of the solid products (Ni & NiO), kg.

The formulated equations (1) - (5) can only be solved numerically. By numerical optimisation the parameters were found to be: $c_0=2.64$; $Q_{vap}=2260$; $T_{vap}=430$; $S=0.006$; $\alpha=200$; $T_{fur}=773÷973$; $Q=1050$; $E=150$; $k_0=10^{11}$; $m_0=0.014$; $m_s=0.0032$. The calculated results according to the system of equations (1) - (5) are presented in Figure 6.26a.

The numerical modelling showed that the system's combustion temperature is only slightly influenced by the tempereaure of the furnace. On the contrary, in the classical version of SHS the combustion temperature depends strongly upon the initial pre-heating temperature. Based on the demonstrated theoretical (a) and experimental results (b) on Figure 6.26, it is concluded that the preheating temperature does not have influence on the temperature of combustion.

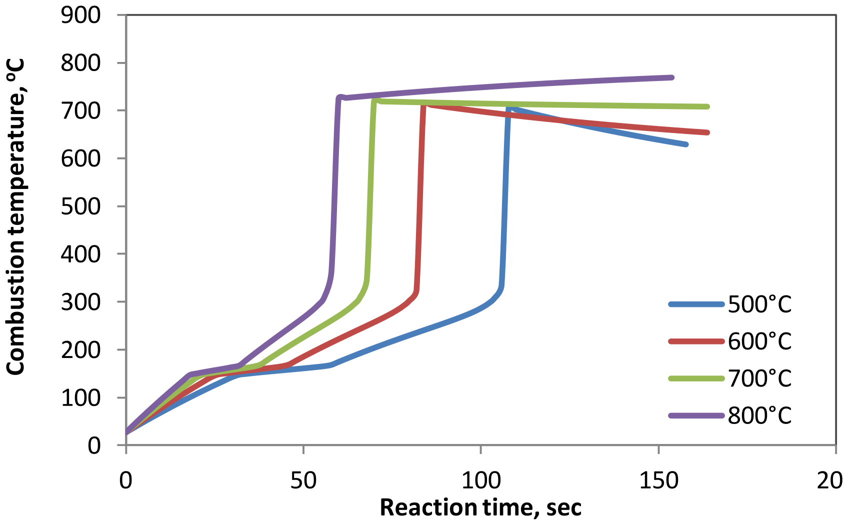

a

[Dr. V. Prokof’ev performed the mathematical modelling of the influence of preheating temperature on the combustion temperature in Tomsk State University, Russia]

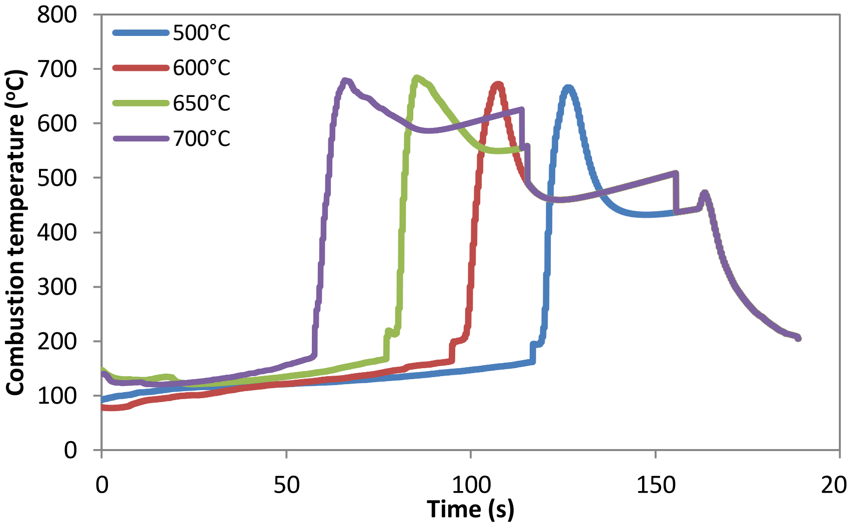

b

Figure 6.26. Influence of preheating temperature on the temperature during SCS with (a) theoretical and (b) experimental data.

A characteristic feature of the change in temperature with time is the isothermal region corresponding to the phase transition temperature ($T_{vap}$). The short duration of this region is a potential barrier for the main synthesis reaction. The temperature of the furnace ($T_{fur}$) determines the heating rate of the mixture and, due to the nonlinear behaviour of the system, the time for complete conversion to η=1 sharply decreases with increasing furnace temperature, as shown on Figure 6.26a in comparison with experimental results (Fig.6.26b).

This means that the combustion temperature of the system depends little on Tfur, in contrast to the classical version of SHS where the combustion temperature depends on the initial temperature.

At the same time, it was observed that preheating temperature ($T_{fur}$) influences the time of ignition. Hence, the ignition points of the theoretical model in comparison with the experimental data obtained by SCS are demonstrated on Figure 6.27.

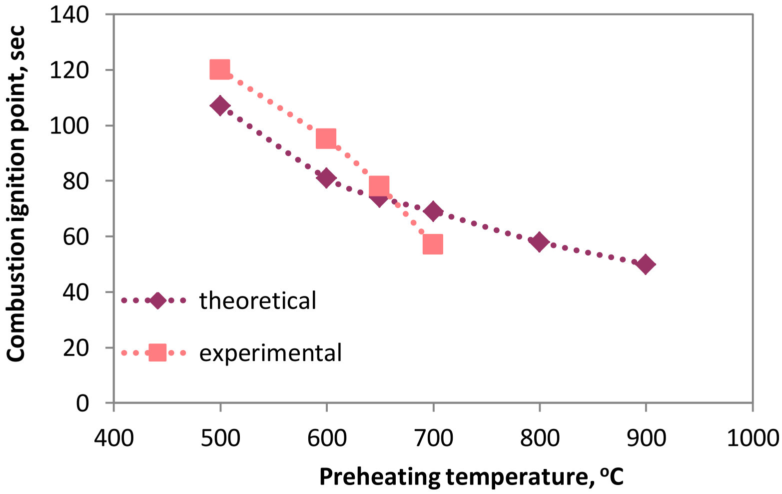

Figure 6.27. Influence of preheating temperature on the combustion ignition point.

As shown on Figure 6.27 above, the theoretical and experimental data are in adequate agreement. As expected, the time of ignition is reduced by the increase of preheating temperature. All reactions take place in the mixture start at a certain temperature, but when the preheating temperature increases the mixture reaches the ignition temperature on the surface of the gel more rapidly, thus the combustion ignition time decreases. The decrease of ignition point signifies that the precursor mixture remains for a shorter period of time in the gel phase before the initiation of SCS. This fact combined to the greater heat input, due to the increase of $T_{fur}$, leads to more violent reactions with increased velocity of the generated gases. As a result the localized cooling rates, where the reaction takes place at the moment, are quicker and there is less time available for nickel oxidation to synthesize nickel oxide. Hence, it is expected that maximum nickel content will appear in cases of higher preheating temperatures.

### *6.5.6. Microstructural analysis*

Despite the fact that the preheating temperature did not significantly influenced the combustion temperature, the final SCS products appear to comprise various compositions and the ratio between the two final products (Ni and NiO) also changed. Furthermore, the properties of the final SCS nanopowders such as crystal lattice parameters, specific surface area and porosity were severely affected. The influence of the furnace's preheating temperature on the catalysts' composition is shown in Figure 6.28, which indicates that increasing the preheating temperature results in increased nickel concentration in the final G-SCS product, taking standard error into account.

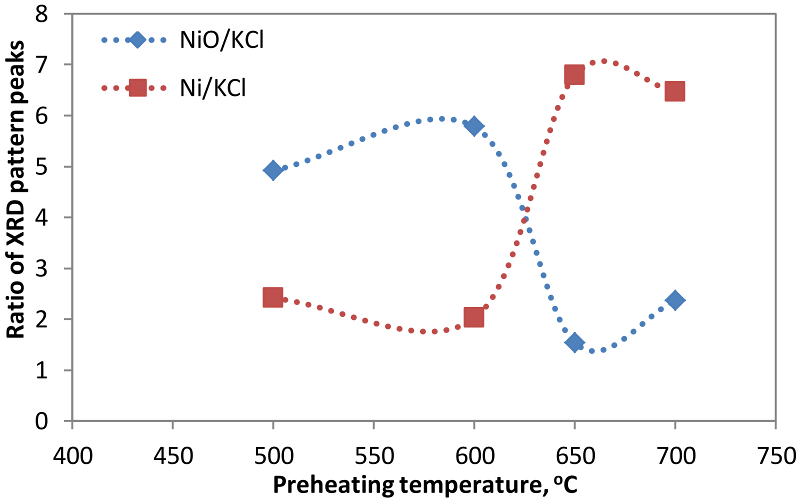

Figure 6.28. Influence of preheating temperature on the composition of G-SCS catalysts.

The calculated ratios of nickel and nickel oxide content in the final SCS product confirm the assumption made based on Figure 6.27. As appears on Figure 6.28, at 650 and 700°C there is maximum nickel content compared to samples prepared at 500 and 600°C, where there is low concentration of nickel and maximum concentration of nickel oxide. According to R. N. Ripan and I. Chetyanou [327], the reduction of nickel oxide to nickel formation starts at 350-400°C with a slow rate but they observed that the reduction acquires high rate between 600 and 700°C. In our studies, in the cases of 650 and 700°C, the precursor mixture remains longer at that optimum temperature region and reduction atmosphere permitting the nickel oxide reduction (mainly the reaction between NiO and C or CO) to take place in a high velocity for a longer period of time. Thus, the increase of nickel content in the final SCS product at these temperatures is possibly connected to the increased nickel oxide reduction.

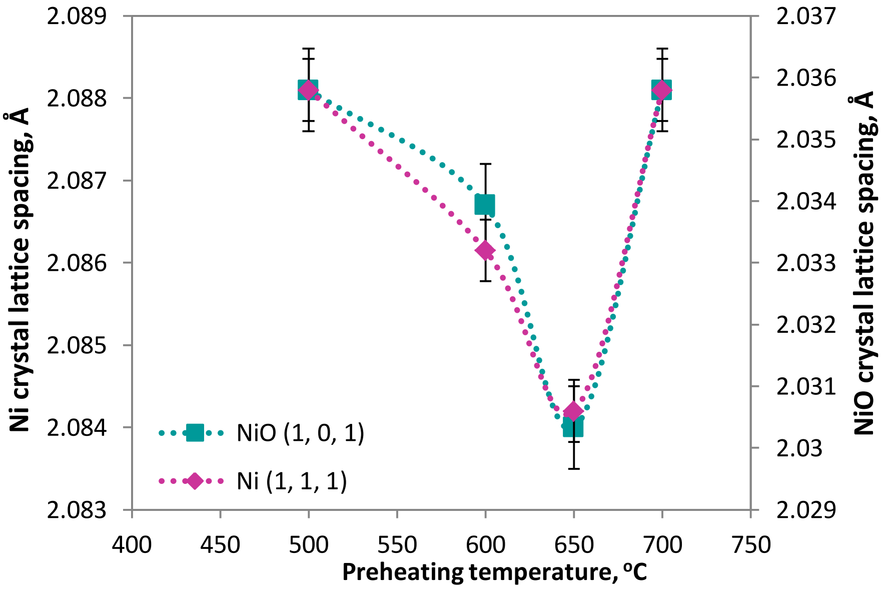

Figure 6.29. Ni & NiO crystal lattice spacing as a function to furnace's preheating temperature.

In general, higher furnace temperatures correspond to faster heating rates, which result in a more rapid volatilization of the precursor mixture. A faster heating rate may cause residual water to remain in the precursor mixture at the time of ignition. This water may cause a decrease in the adiabatic flame temperature, thus hindering the formation of completely organised structures [328]. This could justify the decrease of nickel and nickel oxide's crystal lattice spacing between 500 and 650°C, as demonstrated on Figure 6.29. However, as the temperature increases beyond 700°C, the atoms in the structure acquire enough energy to allow them to reach more energetically stable positions, to be better-organised and that is expressed as an increase of crystal lattice spacing of both nickel and nickel oxide.

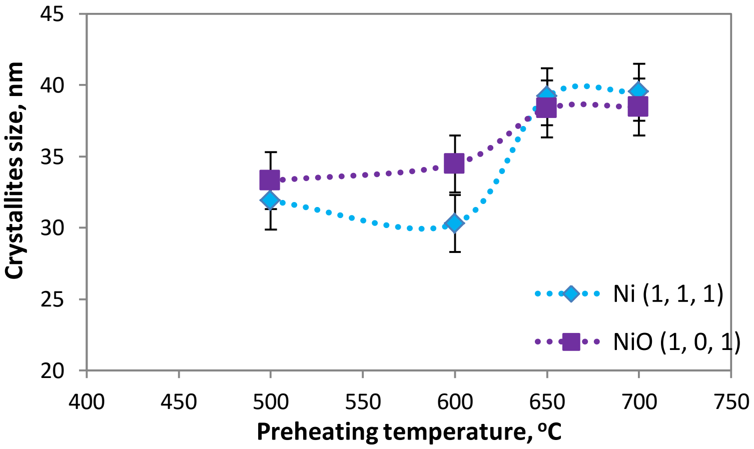

(a)

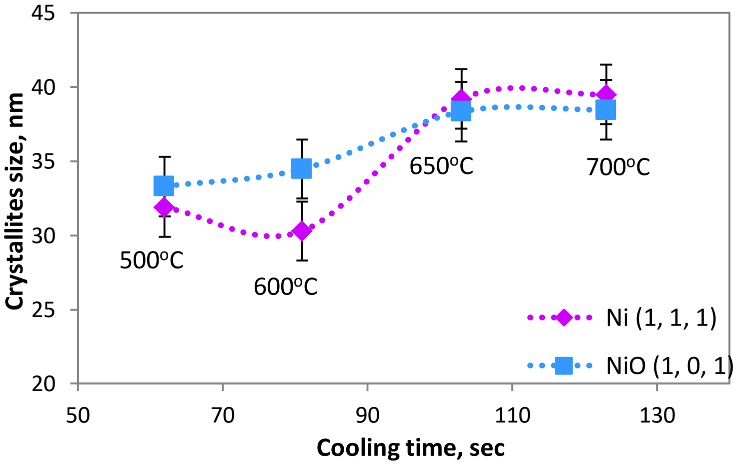

(b)

Figure 6.30. Influence of preheating temperature on Ni & NiO crystallites size in the final products and the correlation between crystallites particle size and cooling time after combustion.

The average crystallite size of the SCS derived nanopowder determined by Debye–Scherrer formula is found to be in the range of 31.9-39.5nm for Ni and 33.3-38.5 for NiO, as shown on Figure 6.30. As shown on Figure 6.26, as the preheating temperature increases, the samples are in a high temperature range for a longer period of time, the cooling time increases and consequently there is more time available for sintering process and the growth of crystallites. Larger crystallites have less surface energy and as a result they tend to agglomerate less. The extent of agglomeration of the crystallites is a significant parameter as it influences the materials' specific surface area, as it is presented on Figure 6.31.

### *6.5.7. Pore analysis and surface area measurements*

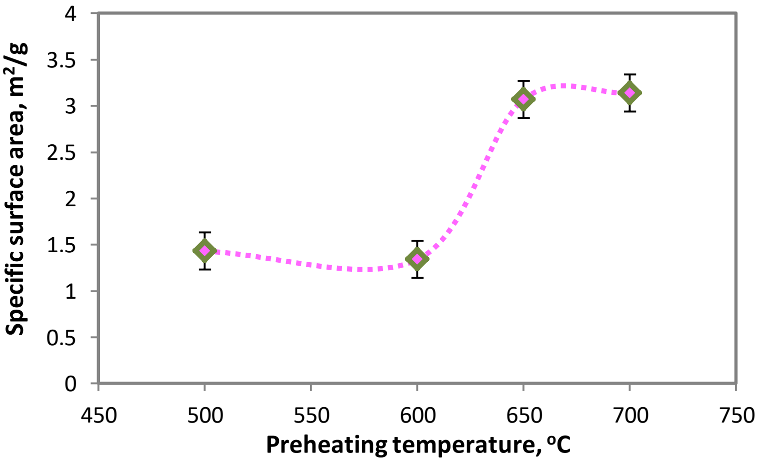

Figure 6.31. Influence of preheating temperature on final SCS products' specific surface area.

As it is demonstrated in Figure 6.31, the specific surface area of the SCS derived nanomaterials ranges from 1.3 to 3.1m$^2$/g. Furthermore, according to the obtained data of crystallites size (Fig.6.30), when the crystallites size increases (from 600 to 650$^o$C), the total surface energy of the particles is reduced and thus, they tend to agglomerate less. That results in increase of the SSA (in the same temperature range) and possibly, the volume of nanopores that were formed in the final SCS products.

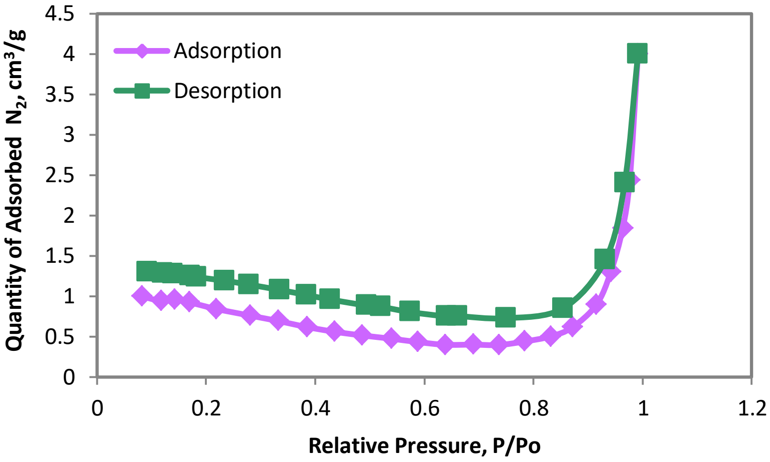

Figure 6.32. Hysteresis curve of a SCS Ni-NiO final product.

Adsorption-desorption curves obtained by the BET method are shown in Figure 6.32, where a representative example of the hysteresis curve of a SCS-derived nanomaterial can be seen. It appears to be a type V isotherm with type H3 hysteresis loop according to IUPAC classification [302]. Typically, type V isotherms are characterized by the uncontrolled formation of the multilayer. It appears that the final nano-structrured product consists of aggregates of plate-like particles forming slit-like pores. The form of the pores affects heat release during SCS as well as the cooling rate after the completion of combustion reactions. Figure 6.33 shows the BJH adsorption pore volume for the four samples prepared from the same precursor solution, but different preheating temperature.

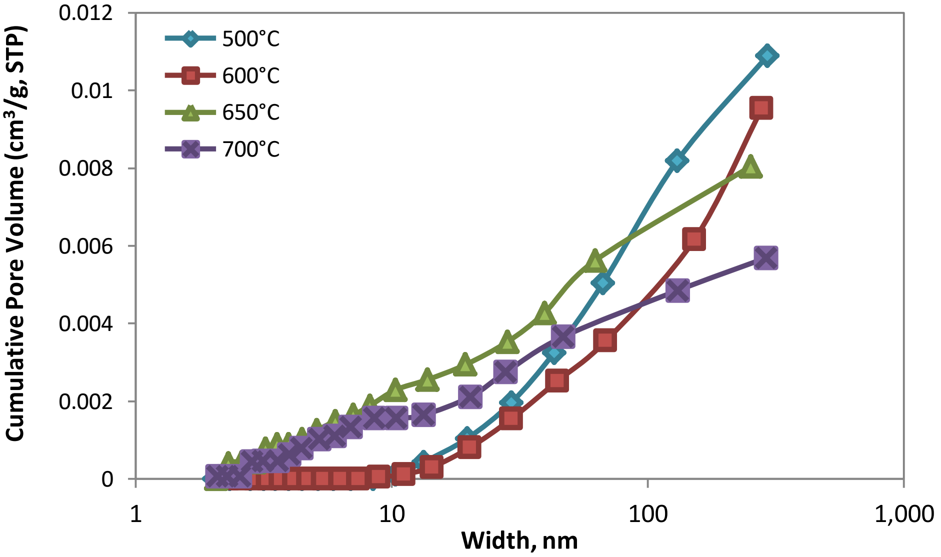

Figure 6.33. BJH adsorption pore volume on the basis of initial mixture 66.7% $Ni(NO_3)_2$ and 33.3% glycine.

As it is indicated from Figure 6.33, by increasing the preheating temperature the measured volume of nanopores increases as well. Thus, there is maximum nanopore volume for 650 and 700$^{o}$C preheating temperature due to the less agglomeration and the intensive gas formation, which led to increased pore volume, higher specific surface area and the maximum Ni and NiO crystallites size at this temperature range. These outcomes support the results obtained from Figures 6.30 and 6.31, concerning the increased volume of nanopores at higher temperatures (650 and 700$^{o}$C). However, at lower temperatures (500, 600$^{o}$C) the mixture reacts slower than in higher temperatures, resulting in higher total porosity, as there was more time available for the pores to form. [317]

SEM images of the microstructure of the SCS derived nanomaterials with the corresponding EDX (energy dispersive X-ray spectroscopy) spectra are presented in Figure 6.34. The existence of all phases detected in XRD patterns was confirmed. The Au element that is shown in the EDX analyses came from the gold-spatter deposition.

### *6.5.8. SEM/EDX analysis*

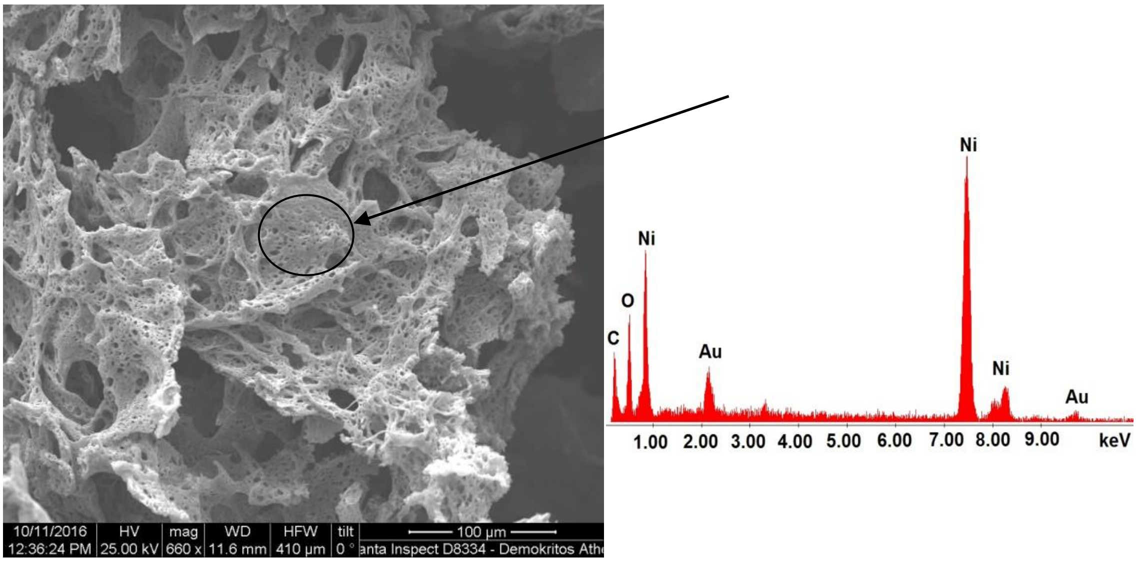

(a)

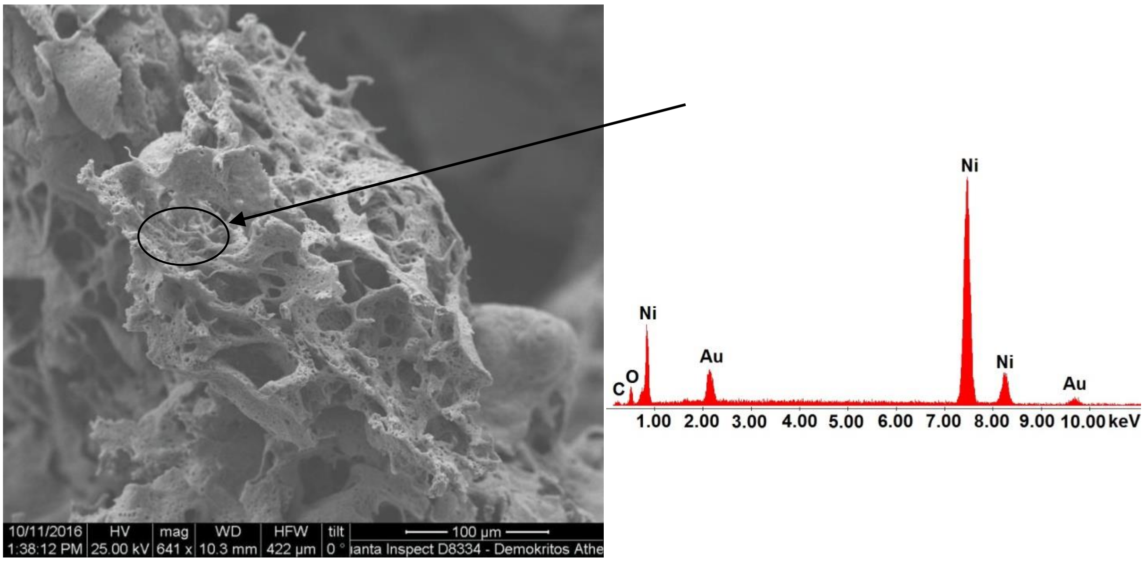

(b)

Figure 6.34. SEM/EDX results of SCS final products for preheating temperature ($T_{fur}$): a) 500°C and b) 700°C.

Figure 6.34 depicts the SEM images and the EDX spectra of the produced Ni-NiO nanoparticles at two different preheating temperatures: 500 and 700°C. Comparing Figures 6.34 a & b, the nanomaterial with 500°C as preheating temperature is depicted to have higher porosity confirming the BET analysis findings (Fig.6.33). Moreover, an important factor that influences the nanomaterials porosity is the gas generation during combustion. The more violent reactions that take place in higher preheating temperatures (700°C) generate gases with high velocity. In addition, the EDX spectrum, which demonstrates that oxygen and by extension the nickel oxide content is much lower in the 700°C case, confirmed that the concentration of nickel is enhanced, compared to 500°C, as it was established on Figure 6.28. Last but not least, the soot concentration appears to be significantly higher for the nanomaterial prepared at 500°C and that can be justified as at higher temperatures the possibility of soot oxidation is enhanced.

In SEM analysis, the largest detected pores were approximately 10μm, while the largest measured pores by BJH is ~0.4 μm. The porosimetry analyzer is only able to measure up to 0.4 μm pores, which in any case are known to provide more than 99% of the total specific surface area.

### *6.5.9. Temperature profiles and IR-camera photos of nanomaterials*

Figures 6.35a-d show the temperature profiles of nanomaterials during synthesis. There were three different thermocouples placed in various heights registering the temperature changes during SCS.

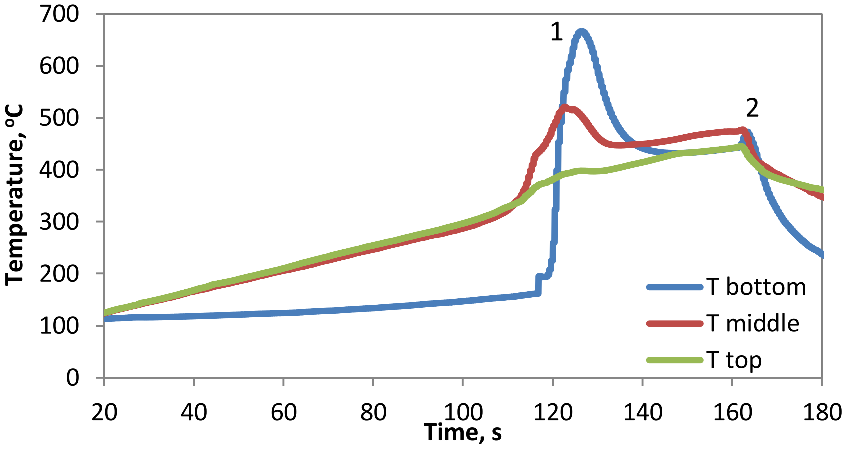

(a)

Figure 6.35. Measured temperature during combustion at 3 different heights of the beaker for a) 500°C preheating temperature.

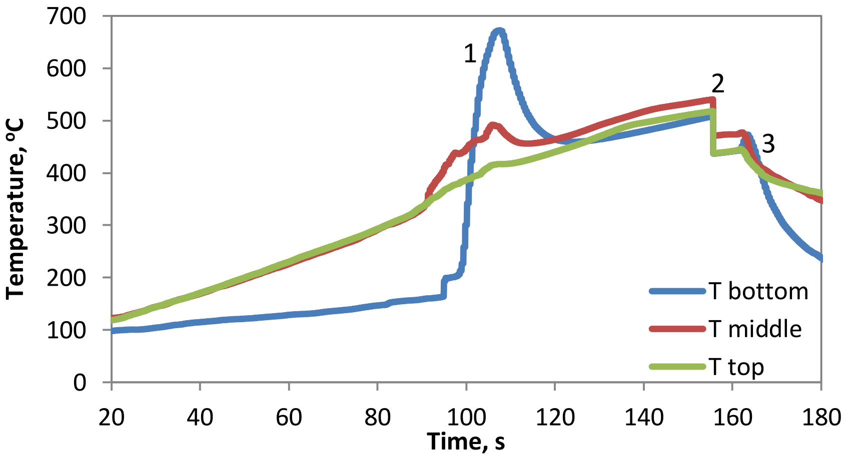

(b)

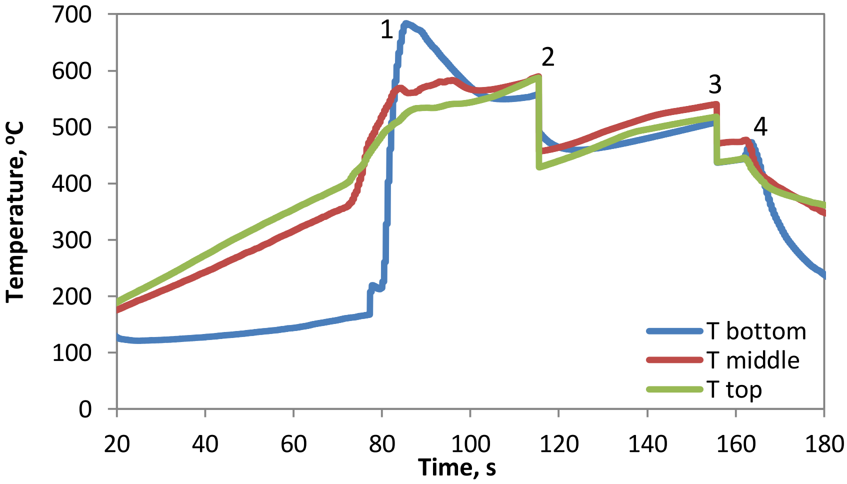

(c)

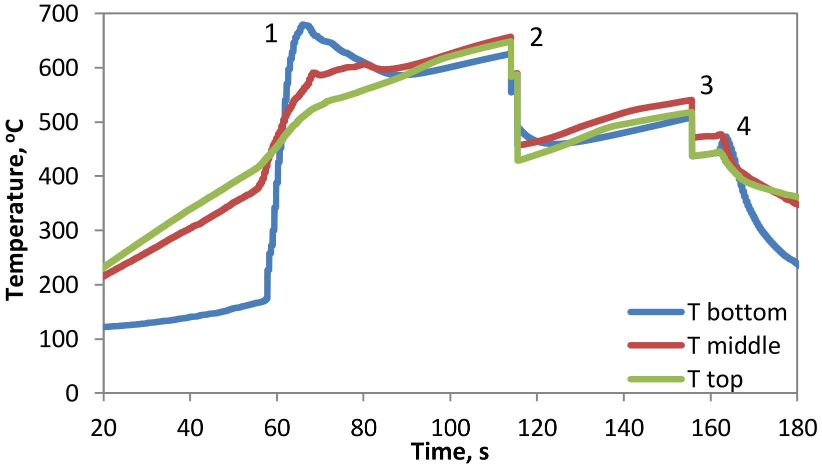

(d)

Figure 6.35. Measured temperature during combustion at 3 different heights of the beaker for b) 600 c) 650 and d) 700°C preheating temperature.

Figures 6.35 a-d demonstrate the measured temperature during synthesis at three different points of the mixture (0.5cm, 1.5cm and 2.5cm from the bottom of the beaker). The multiple peaks on these figures signify that there are many consequent reactions taking place during SCS. It appears that the number of these peaks increases by the increase of the preheating temperature.

In all studied preheating temperatures, the first peak (*point 1*) represents the reaction between glycine and nickel nitrate (reaction i) which is an exothermic reaction that mainly provides the energy to the system. The first peak includes many peaks corresponding to various parallel reactions (iii, v, vi, vii, ix) that take place simultaneously. On Figure 6.35a, where the sample is preheated at 500$^{o}$C, *point 2* signalizes the oxidation of nickel to yield nickel oxide, which is also an exothermic reaction ($\Delta$H=-1324.6 kJ/mol). In the 600$^{o}$C case, there are three distinct peaks registered from the thermocouples. The second peak (*point 2*) represents the exothermic oxidation of nickel for nickel oxide production, while the third peak (*point 3*) is the endothermic process reaction ($\Delta$H=68.2 kJ/mol) of nickel oxide reduction by residual soot (xii). The presence of this reaction's product, which is carbon monoxide (CO) was detected by gas analyzer. At higher temperatures it is more possible for the carbon oxidation, thus there is no soot in the products at high temperatures.

The samples prepared at 650 and 700$^{o}$C appeared to possess four distinct points during combustion. The forth peak could be connected with the exothermic reaction of nickel oxide reduction from carbon monoxide (reaction xiii, $\Delta$H=-379.5 kJ/mol) as consequent reaction of the previous one (xii), where CO is a product. At this point, there is also another exothermic peak due to the soot oxidation (reaction x). According to Figure 6.35, the temperature studies by the three thermocouples clarified that the reactions during SCS take place mainly in gel (bottom), but also in gas-gel interface (middle and top thermocouple measurements).

Comparing the Figure 6.35a-d with Figure 6.26, it is evident that in case of high temperatures (650 and 700$^{o}$C), more peaks are apparent, some of which represent exothermic processes. The heat produced by them keeps the system's temperature high for a longer period of time than in case of lower preheating temperatures. This could be related to the change of reactions' mechanism, when the preheating temperature varies, as different reactions take place or are favored and the cooling time is influenced accordingly. The nanomaterials prepared at higher preheating temperature appear to have more consistent crystal lattice structural formation, as they remain in higher temperature for a longer period of time.

The evolution of combustion temperature with time for two different preheating temperatures (500 and 700°C) is demonstrated on Figure 6.36. Despite the fact that the combustion temperature is only slightly influenced, the combustion regime is doubtlessly affected.

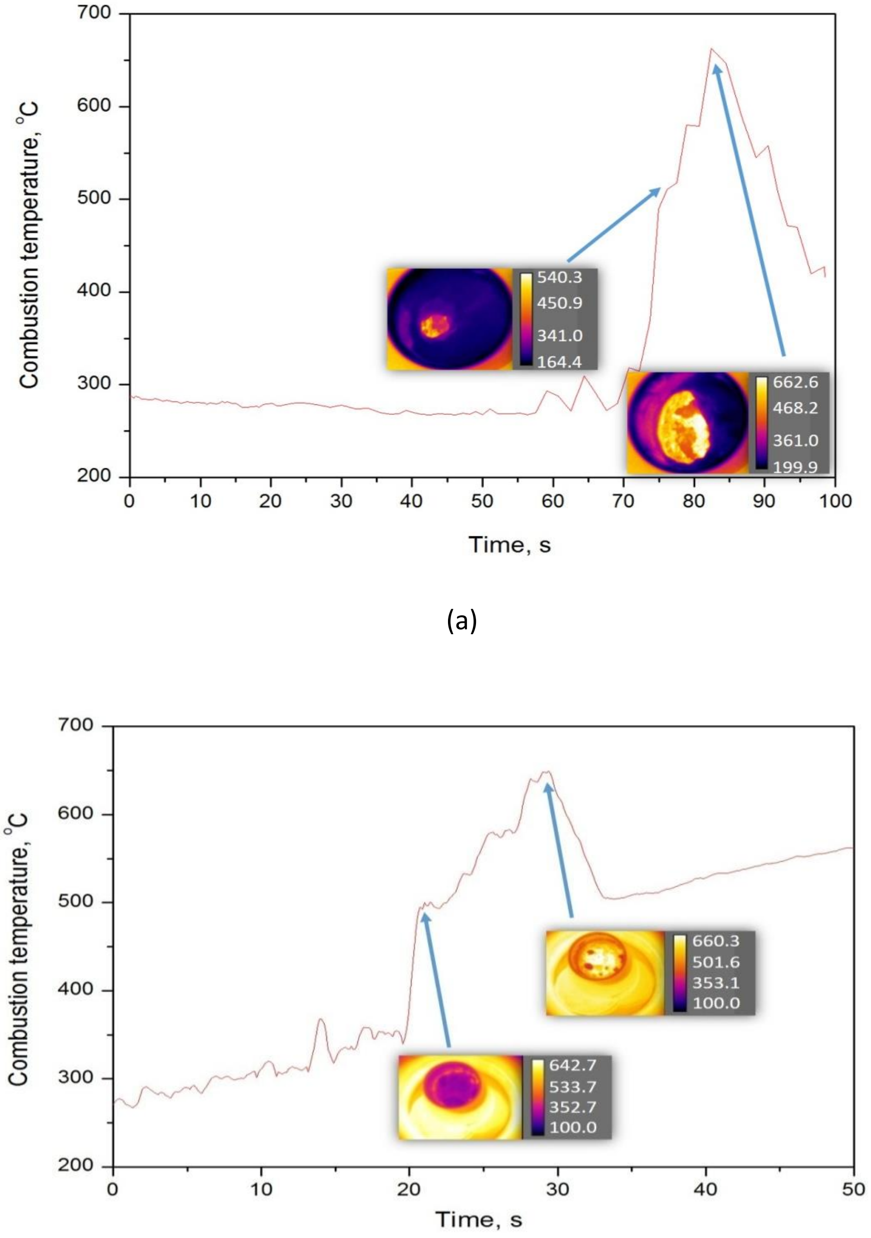

(a)

(b)

Figure 6.36. Temperature profile for SCS in the $Ni(NO_3)_2$-glycine system at: a)500°C and b) 700°C [The IR-camera measurements were performed by S. Roslyakov in National University of Science and Technology “MISIS”].

Figure 6.36 demonstrates the appeared differences in the temperature profile for preheating temperatures of 500°C and 700°C, studied with infra-red camera. When the preheating temperature is higher (700°C) the time period of reaction initiation is shorter, there are more exothermic-endothermic peaks appeared (showing that the mechanism of reactions is more complicated than at lower temperature) and the reaction is more violent, as the velocity of combustion increases. These results support the data that were obtained by the thermocouples measurements and the numerical modelling of flame temperature during G-SCS. It has been concluded that the reactions yield during SCS in the gel phase have a profoundly complicated mechanism. The reactions are initiated at the liquid - gas interface and the immediately originated solid product becomes the third phase. The heat provided by the solid phase is propagated to the adjacent not-yet-reacted gel, where SCS starts. During the cooling period, the phase and structure formation is continued in solid product. As a result of the increased cooling period at higher temperatures (700°C), more reactions take place and the derived product has different composition, in comparison with its analogous at lower temperatures (500°C). Furthermore, the ongoing structure formation during cooling period resulted in various crystal lattice parameters and crystallite size, while cooling period alters. The reason of the observed changes in cooling period is that, at higher temperatures, the additional exothermic reactions (mainly the soot oxidation) that take place elongate this period of time.

### *6.5.10. Conclusions*

- The results demonstrated that the preheating temperature only slightly influences the combustion temperature during SCS.
- The SCS preheating temperature influences the structural formation and the final composition of the nanocomposite metal-oxide product.
- Increasing the SCS preheating temperature leads to a decrease of combustion initiation period due to the enhanced heating velocity and an increase of cooling time as a result of the additional exothermic reactions taking place at higher temperatures.
- The variations in cooling period provoked changes in the final product composition and microstructure, because of the ongoing phase and structural formation during cooling period.

## 6.6. Influence of the reactants concentration in the precursor solution on catalysts' characteristics

The results presented here have been published as: G.Xanthopoulou, O.Thoda, E.D.Metaxa, G.Vekinis, A.Chroneos, *Journal of Catalysis, 2017, 348, 9-21*.

### *6.6.1. Catalysts preparation*

The initial solution used for SCS of our materials consists of 66.7% nickel nitrate hexahydrate [$Ni(NO_3)_2{\cdot}6H_2O$] as the oxidizer with 33.3% glycine as the reducer for a total solid mass of 14g which gives 3g of Ni in the final catalyst. The solid mixture was then dissolved in 25, 50, 75 or 100ml of distilled water and each solution was pre-heated in a borosilicate glass beaker on a hot plate with mild magnetic stirring until the temperature reached 70$^o$C and then placed in a pre-heated furnace at 500$^o$C to enable SCS, thereby yielding four different nano-structured powdered catalysts differing only in the amount of water used in the solution. Once SCS is completed, the beaker is removed from the furnace and allowed to cool at room temperature.

### *6.6.2. Structural analysis*

SCS products have a pronounced 3-dimensional dendritic structure as shown in the photo in Figure 6.37a, which shows the material as it emerges from the beaker during SCS, and in Figure 6.37b, at higher magnification. This structure is probably due to hydrates formation on the stage of nitrates heating in water and extensive gas generation during SCS. Different colours are indicative of the different orientation of the crystals that resulted in various diffraction angles.

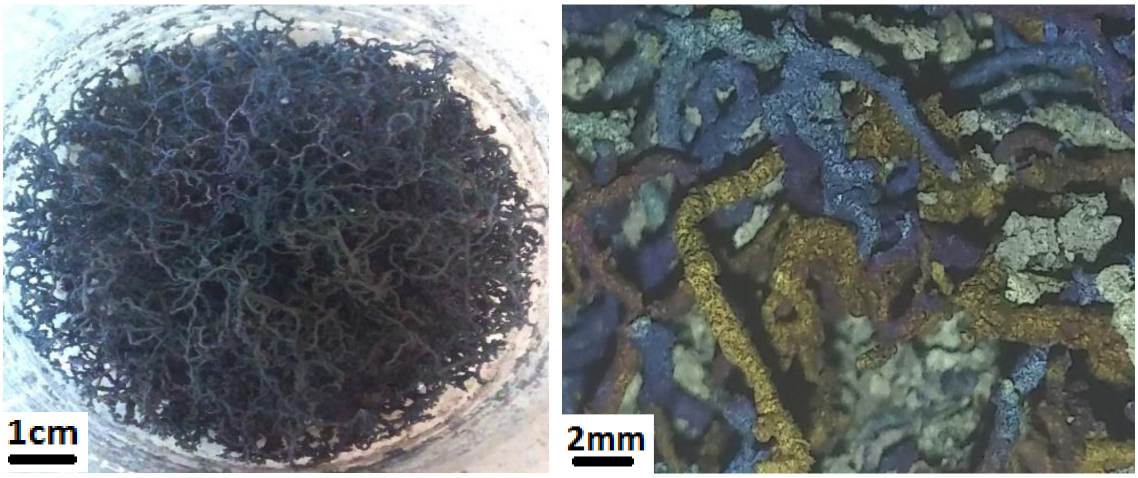

Figure 6.37: Structure of the catalyst as it emerges during SCS: near actual size (left) and x30 (right).

The development of the various phases in one of the SCS materials produced is shown in the series of XRD patterns in Figure 6.38 of a catalyst made with a solution of nickel nitrate and glycine at a ratio of 2:1 in various dilutions in water. The unidentified peak that appeared on the patterns below the 20 degrees is due to the substrate employed for the XRD measurement, it was not taken into account during the analysis and it was not in conflict with any sample peaks.

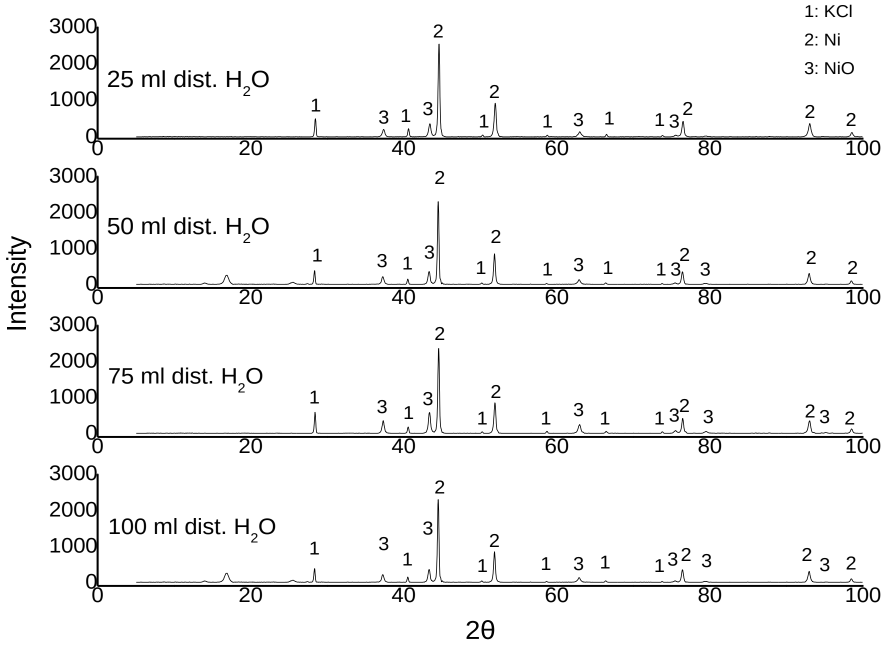

Figure 6.38: Development of crystal structure of an SCS catalyst on the basis of nickel nitrate hexahydrate with glycine (ration 2:1) with various amounts of water as diluent.

All catalysts tested (Fig.6.38) had two main products: metal Ni and NiO. These products are the result of the following multi-branch reaction cascade:

$$Ni(NO_3)_2 \cdot 6H_2O \xrightarrow{54℃} Ni(NO_3)_2 \cdot 4H_2O \xrightarrow{85.4℃} Ni(NO_3)_2 \cdot 2H_2O \quad \text{(i)}$$

$$2Ni(NO_3)_2 \cdot 6H_2O + C_2H_5NO_2 \rightarrow Ni + NiO + NO_2 + 2NO + N_2 + 2CO_2 + \frac{29}{2}H_2O + \frac{5}{2}O_2 \ \text{(ii)}$$

$$2Ni(NO_3)_2 \cdot 6H_2O \rightarrow 2NiO + \ NO_2 + NO + N_2 + 12H_2O + \frac{7}{2}O_2 \quad \text{(iii)}$$

$$Ni(NO_3)(OH)_{2.5} \cdot H_2O \rightarrow 0.5Ni_2O_3 + \mathrm{HN}O_3 + 1.25H_2\mathrm{O} \ \text{(iv)}$$ [76]

$$CH_2NH_2COOH \rightarrow [CH_2COO]^- + NH_3 \ \text{(v)}$$ [76]

$HNO_3 + \frac{7}{3}NH_3 \rightarrow 3H_2O + \frac{5}{3}N_2 + H_2$ (vi)[76]

$2NH_3 \overset{Ni}{\rightarrow} 3H_2 + N_2$ (vii)[323]

$NiO + H_2 \rightarrow Ni + H_2O$ (viii)

$Ni + O_2 \rightarrow NiO + \frac{1}{2}O_2$ (ix)

$2CH_2NH_2COOH + 6O_2 \rightarrow 4CO_2 + 5H_2O + NO + NO_2$ (x)

The phase composition of the products, as determined by the comparative XRD analysis, as a function of water content in the SCS solution are presented in Figure 6.39 where the variation between Ni/KCl and NiO/KCl are shown together for comparison.

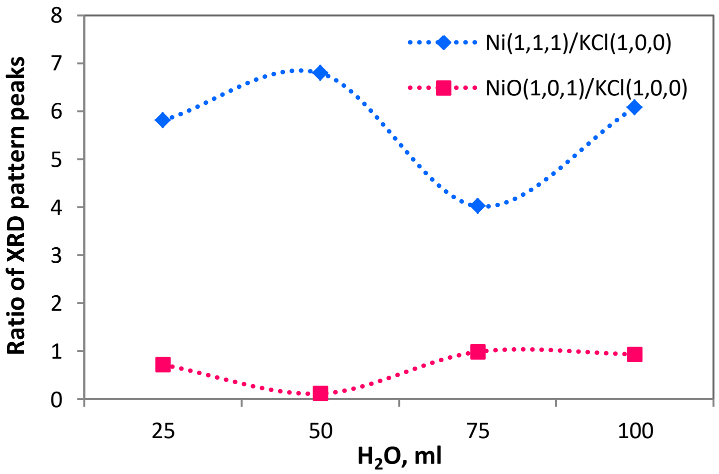

Figure 6.39: Dependence of XRD peak ratio on water solvent quantity in initial SCS solution.

It can be seen that the maximum nickel content in the SCS products occurs at the position of the minimum nickel oxide content when the amount of water diluent is 50ml. Conversely, when the water in the solution is increased to 75 ml, a maximum of nickel oxide and a minimum of Ni were detected in the product. This is because, during SCS, nickel oxide is reduced by hydrogen (reaction viii), but during cooling nickel is oxidised again (reaction ix). In fact, during SCS, both oxidation and reduction processes take place and their relative rates of reaction depend on the rate of cooling and heating. This explains the complicated form of the curves in Figure 4 since the amount of water in the solution changes the heating rate during the pre-heating period until SCS initiates and cooling rate after SCS. If cooling is slow, the probability of oxidation of Ni is high, leading to more NiO. Once the product is formed, its cooling rate depends on its pore structure and so the SCS products have different structure and different composition as they are subjected to different cooling conditions. As the pore size decreases, the temperature inside the pores decreases at a slower rate and there is more time for oxidation to occur and the microstructure is also different.

Bragg's and Scherrer's formulas for XRD were used to determine the crystal lattice spacing and crystallite size of Ni and NiO which are shown in Figures 6.40 and 6.41 against amount of water in initial SCS solution.

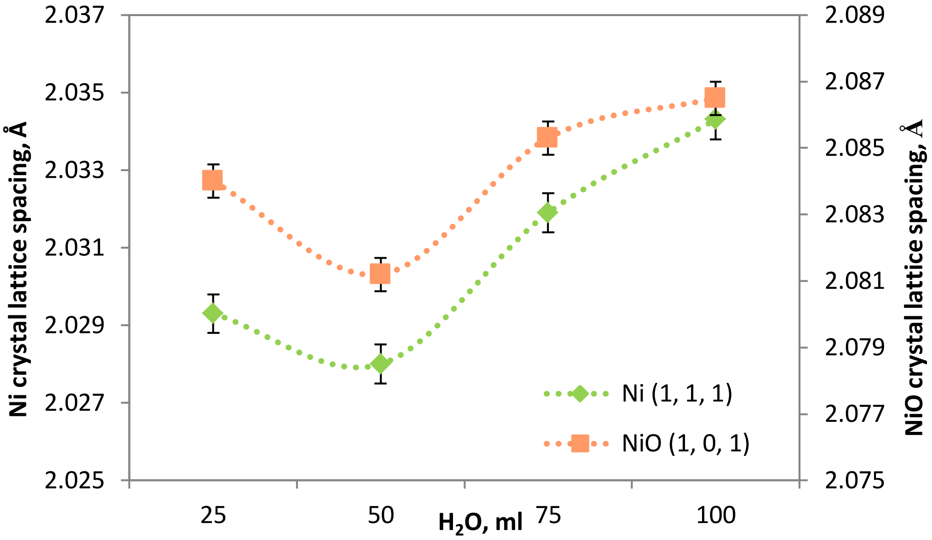

Figure 6.40: Influence of water content in initial solution on crystal lattice spacing.

As can be observed in Figure 6.40, increasing the water in the SCS initial solution results in small changes in Ni and NiO crystal lattice spacing which reflect the crystallite nucleation conditions that are present in each case. In Figure 6.40 there is a minimum of lattice spacing for 50 ml of water in the initial solution for both Ni and NiO. As water content increases, the nitrate and glycine transient structures that are created in the liquid phase before SCS initiates change, which results in different structures of Ni and NiO in the final product. When SCS initiates, the combustion mechanisms change as well. From 25 to 50 ml of water the combustion mechanism changes from combustion in emulsion to combustion in solution. This leads to less organised structures as indicated in Figure 6.40 by the measured reduction in crystal lattice spacing.

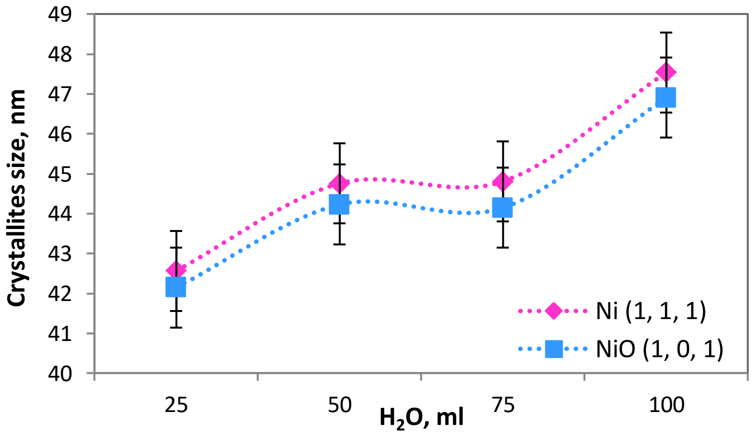

Figure 6.41: Influence of water quantity in initial SCS solution on crystallite size (as determined by XRD) in the final product

The influence of the water content on the crystallite size of Ni and NiO is shown in Figure 6.41. In general, the smaller the nickel crystallites form during combustion, the better the dispersion of the metallic phase on the NiO. Conversely, larger crystallites have less surface energy and as a result they tend to agglomerate less. The extent of agglomeration of the crystallites is very important as it influences the catalysts' specific surface area which is critical for catalytic activity.

### *6.6.3. Pore analysis and surface area measurements*

Specific surface area measurements (determined by BET analysis) as a function of the quantity of water in the initial solution of SCS are presented on Figure 6.42. Specific surface area shows an increasing trend and reaches a maximum for 75 ml of water in the solution.

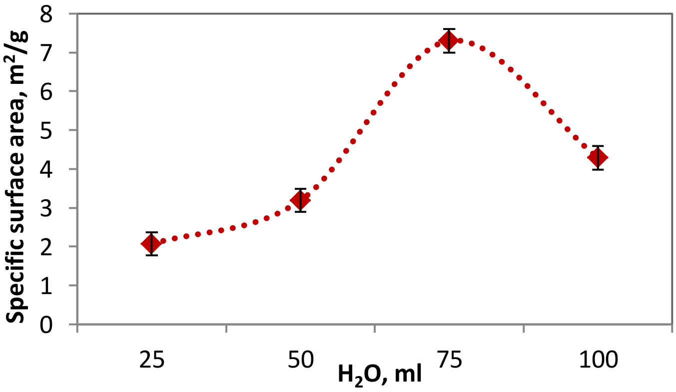

Figure 6.42: Influence of water quantity in SCS solution on specific surface area (BET).

Total porosity of the material affects specific surface area. Further BET measurements indicate strong dependence of surface area on the nano-pores size and quantity.

Adsorption-desorption curves obtained by the BET method are shown in Figure 6.43 where a representative example of the hysteresis curve of a SCS Ni catalyst can be seen. Based on the shape of this curve, it appears that the pores of the catalysts tested have a predominantly wedge shape [320]. The form of the pores affects heat release during SCS, the cooling rate after SCS and hydrogen adsorption-desorption i.e. pore shape influences catalysts' structure formation and their activity.

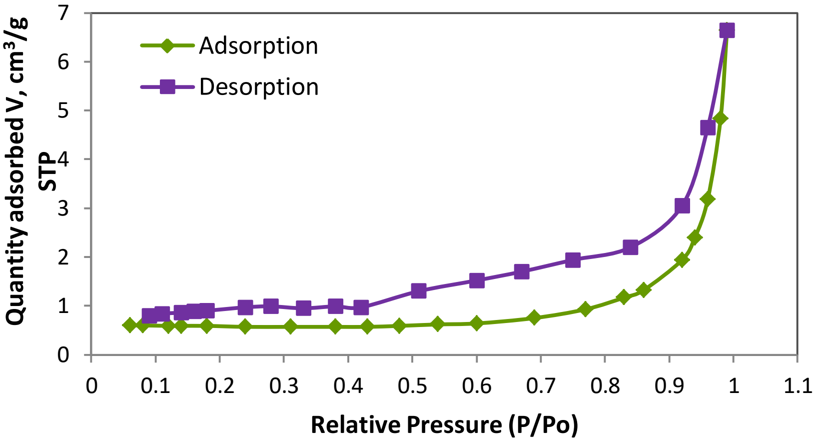

Figure 6.43: Hysteresis curve of a SCS Ni catalyst.

Figures 6.44a-d show the pore size distribution for the four samples prepared with different amounts of distilled water in the SCS initial mixture. It is clear that the transient structures formed in solution during SCS pre-treatment affect directly the properties of the SCS products, such as pore size and distribution.

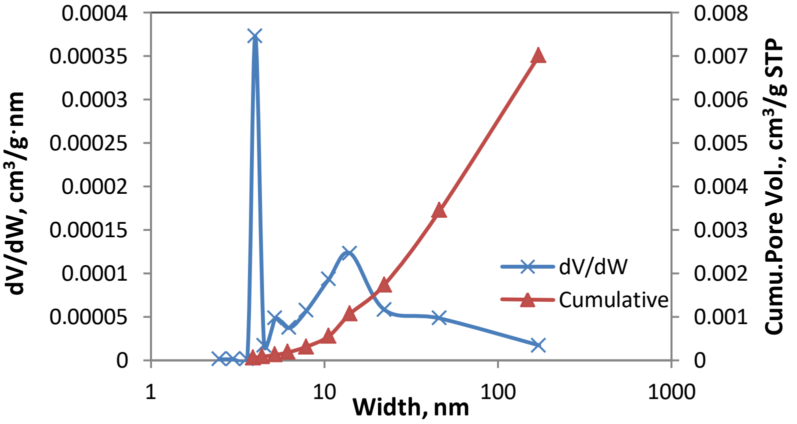

(a)

Figure 6.44. BJH adsorption pore distribution results for a) 25ml of water in initial SCS solution.

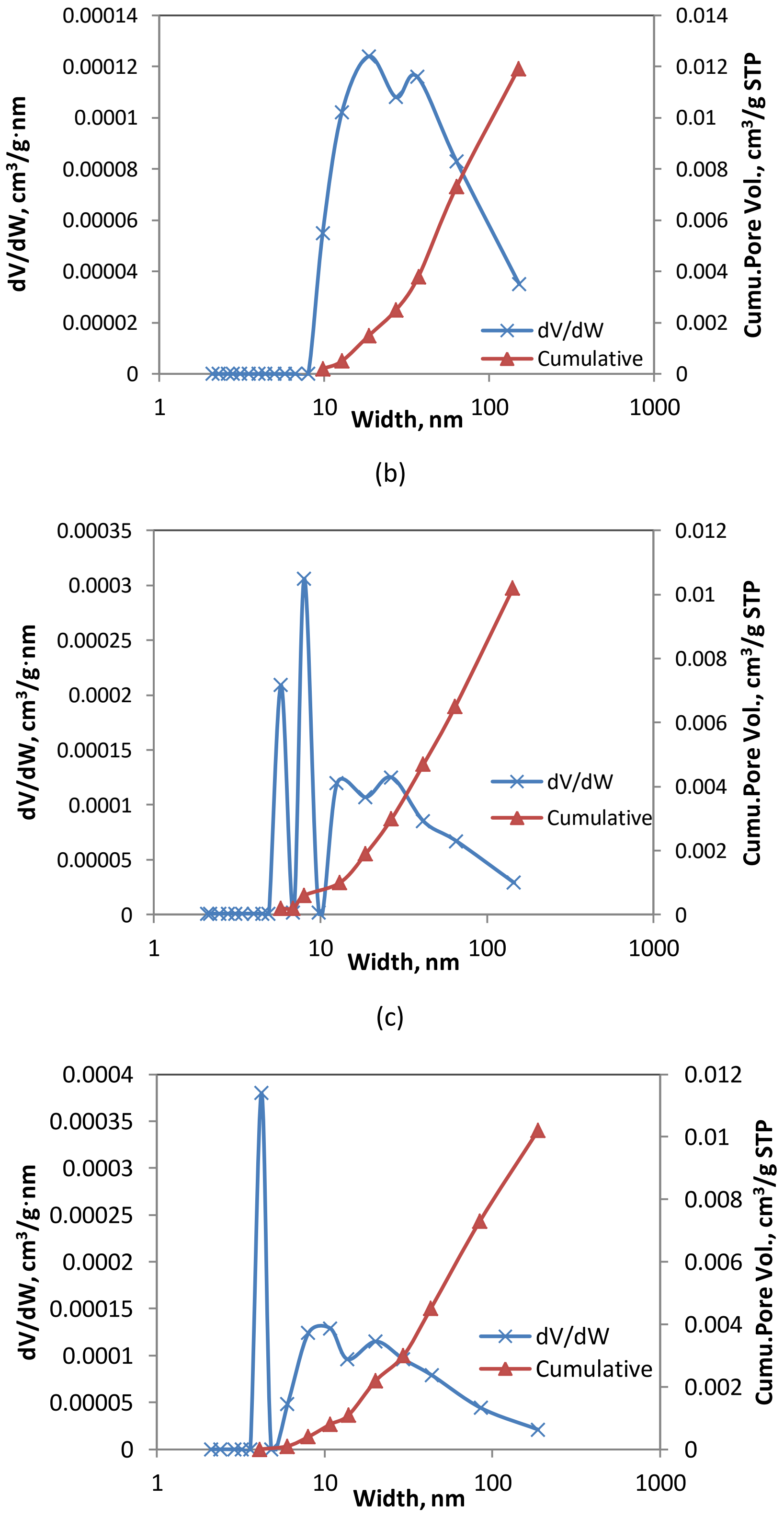

(b)

(c)

(d)

Figure 6.44. BJH adsorption pore distribution results for a) 25, b) 50, c) 75 and d) 100ml of water in initial SCS solution.

The results of the pore distribution analysis appear to support our conclusions that for the samples with 25 ml of water in the initial solution, which have a sol-gel consistency, the relatively large amounts of energy that are released during the SCS reaction result in localised melting and sintering and therefore give lower porosity in the material. This explains the lower overall surface area shown in Figure 6.42. It appears therefore that, in this case, it is the decomposition of nitrates that plays the most important role in pore formation than the amount of water used. Gas formation during decomposition of nitrates would be expected to lead to the formation of nano-pores under these conditions, as shown in Figure 6.43. Conversely, in the samples produced with 50 ml of water, the amount of water is now a more important factor than decomposition of the nitrates. The more intensive gas formation tends to form many more and larger pores, even micro-pores, increasing only slightly the overall specific surface area. The larger size of these micro-pores reduces oxidation during cooling, since the temperature inside these larger pores would be expected to decrease more rapidly. This helps to explain the finding of predominantly Ni as a product with just traces of NiO in the catalyst, as shown in Figure 6.39.

With the use of even more water (75 ml) in the initial solution, the temperature of combustion decreases substantially and as a result the rate of formation of pores is lower. Moreover, the SCS reaction rate is lower, and as a consequence the formation of the gases $NO_x$, $N_2$ and $CO_2$ (reactions ii, iii, vi, vii, x), as well as the evaporation of water are slower, giving more time for nano-pores to form. At even higher water content (100 ml), a smaller total volume of nano-pores and a larger volume of micro-pores are obtained because of the larger amount of water that evaporates and passes through the pores. For the SCS catalyst with 100 ml of water in the initial solution, total porosity of the material is the highest (the pore distribution curve is the widest), but the volume of nano-pores shaped in it is minimised, as compared to the catalysts with 75 ml of water in their initial solution and this results in the observed decrease in its specific surface area (Figure 6.42).

Gas adsorption curves are shown in Figure 6.45 where the quantity of the gas adsorbed is plotted against relative gas (hydrogen) pressure.

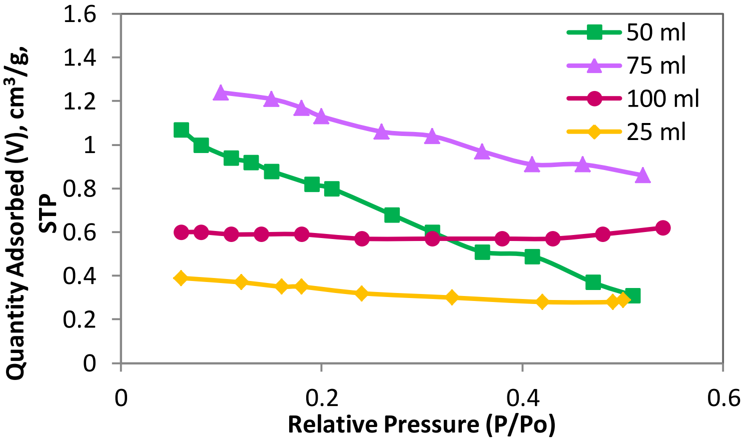

Figure 6.45: Hydrogen adsorption curves for the SCS Ni-based catalysts with different amount of water in the initial solution.

The results show that for 50 and 75 ml of water content, the gradient of adsorbed quantity of hydrogen with increasing relative pressure is negative. This may be understood in terms of the concentration of nano-pores since lower concentration of nano-pores implies lower adsorbed quantity at higher pressures. Indeed, the gradients of the curves for 75 and 100 ml are higher showing higher adsorbed quantity at higher pressures due to the higher concentration of nano-pores.

### *6.6.4. Catalytic studies*

The catalytic activity of the Ni-based SCS catalysts discussed above was examined in liquid-phase hydrogenation of maleic acid. In all cases, the kinetic and conversion curves were obtained for the first twenty minutes of the hydrogenation of maleic acid.

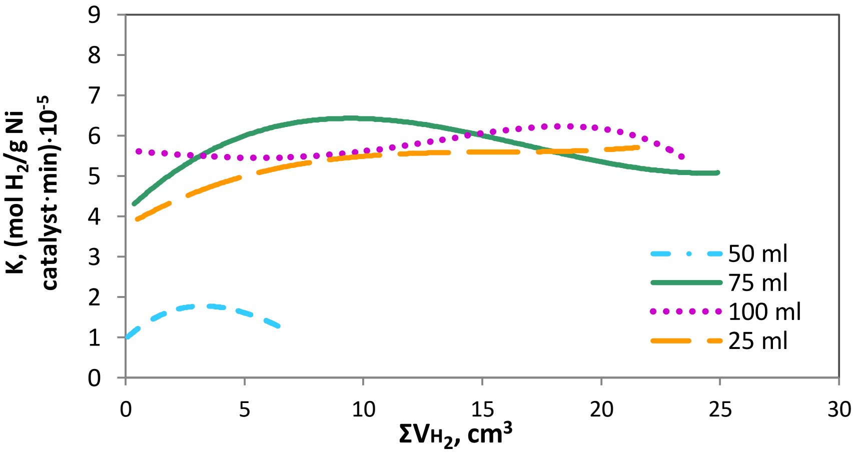

Figure 6.46: Dependence of observed maleic acid hydrogenation on the SCS Ni-based catalysts on the volume of absorbed hydrogen.

Figure 6.46 shows the resulting set of kinetics curves of the SCS catalysts with different amount of water in their initial solution. The catalysts made with 75 ml and 100ml of water appear to be most active, while the catalyst made with 50 ml in the initial solution was almost inactive. Conversion curves of the catalysts are shown in Figure 6.47.

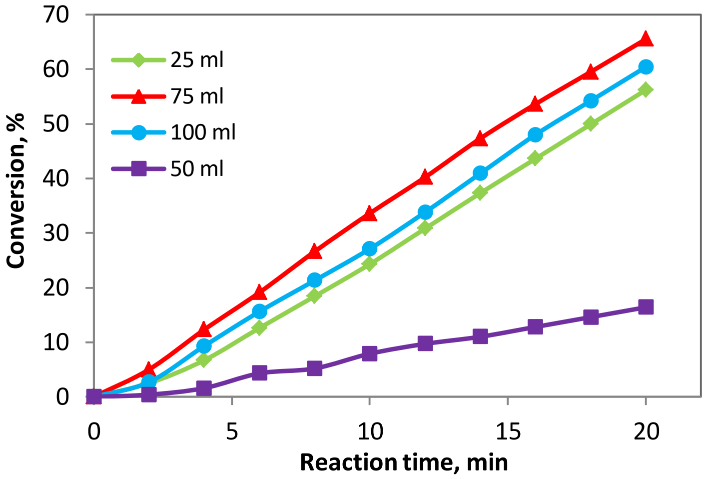

Figure 6.47: The dependence of maleic acid conversion on the SCS catalysts calculated from the quantity of absorbed hydrogen.

The degree of conversion of maleic acid into succinic acid is very low (16,4%) for the catalysts with 50 ml of water whereas the other three catalysts exhibit better catalytic activity, with the catalyst prepared with 75 ml of water showing the highest conversion rates. These results correlate well with the catalysts' kinetic curves (Figure 6.46). Interestingly, the catalyst made with 75 ml of water shows higher conversion rate than the one made with 100 ml water, even though the latter catalyst gave higher rate of hydrogenation per minute. The dependence of the catalytic activity – maximum rate of hydrogenation measured per minute – during hydrogenation on the quantity of water in the initial SCS solution is presented in Figure 6.48.

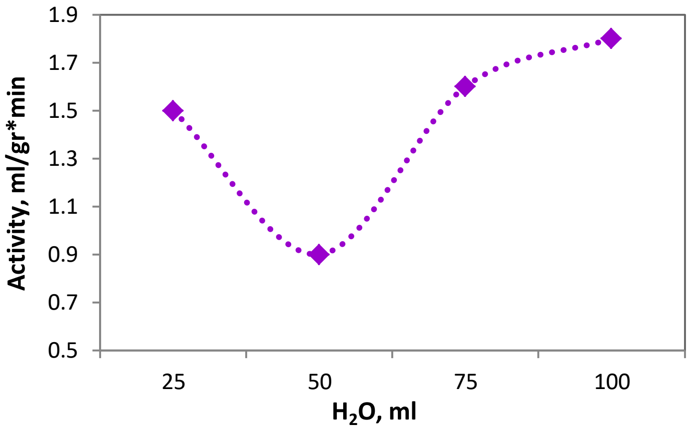

Figure 6.48: Correlation between the amount water in the initial solution and the catalysts' activity in liquid-phase hydrogenation of maleic acid.

Activity depends on many physical properties of the catalysts such as surface area, crystal lattice spacing, crystallite size, particle size, pore size and pore shape and this is confirmed in the present study. The catalyst with 25 ml of water in the initial solution shows a relatively moderate activity since, although it contains many nano-pores its overall surface area is moderate (Figure 6.43). On the other hand, the catalyst made with 50 ml of water has almost no nano-pores and just traces of NiO (Figure 6.40) and displays lower activity. This is because NiO acts as a carrier for the metallic Ni catalyst whose quantity and structure determine the overall activity of catalysts. In its absence the catalytic activity decreases significantly. With further increase in the amount of water in the initial SCS solution to 75 ml, the total amount of nano-pores increases together with the amount of NiO and so does the measured activity. Lastly, the catalyst made with 100 ml of water has a lower measured surface area, but the ratio between the metallic and non-metallic phase is higher (Figure 6.40) which leads to a slight increase of activity.

The catalyst activity results are correlated with the hydrogen adsorption results in Figure 6.45. For example, for the catalyst with 50 ml of water the activity is very low, because there is almost no adsorbed hydrogen on the surface. Surface area is crucial in this regard and since the catalyst produced with 75 ml of water has higher surface area, its' adsorption gradient is higher. The higher hydrogen adsorption of the catalyst with 25 ml of water also helps to explain its satisfactory catalytic behaviour, despite of its lower specific surface area.

Further clarification of the above conclusions may be obtained by considering the correlations between the various measured parameters of the four types of catalysts. Figure 6.49 plots the measured catalytic activity in liquid-phase hydrogenation of maleic acid against the catalysts' specific surface area.

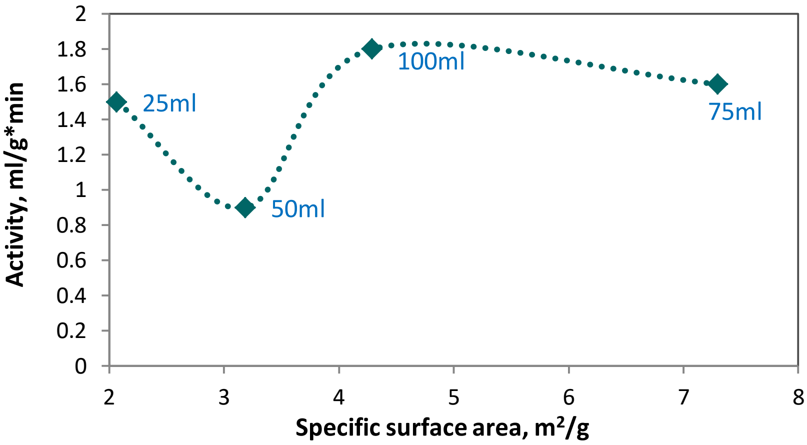

Figure 6.49: Dependence of SCS catalysts' activity upon their specific surface area.

In the case of the catalysts made with 25 ml of water in the initial SCS solution, although their specific surface area is the lowest, its activity is not due to the existence of nano-pores (Figure 6.44a). Furthermore, despite the fact that the specific surface area of the catalyst with 50 ml of water increases, its hydrogenation rate decreases significantly which may be explained by the fact that it contains only traces of nickel oxide as a carrier (Figure 6.39). Catalysts made with higher amounts of water (75 and 100 ml) results in increased catalysts' specific surface area and concomitant increase of their catalytic activity in hydrogenation of maleic acid. Catalytic activity is also dependent on the nickel oxide's content in the final product, as presented in Figure 6.50.

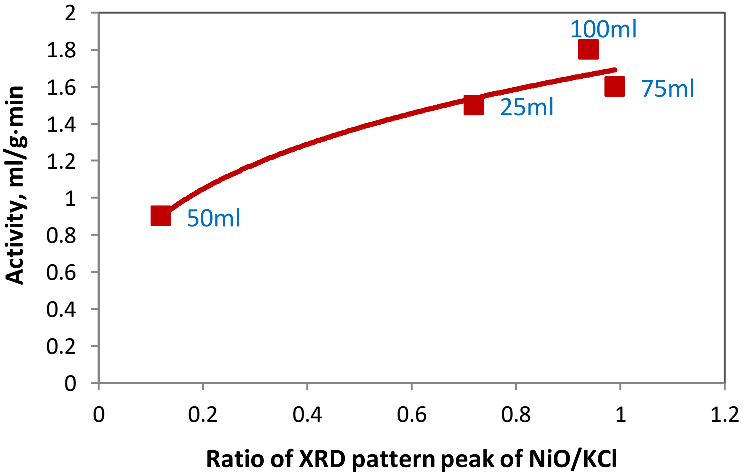

Figure 6.50: The catalytic activity of the four SCS catalysts against XRD peak ratio of NiO/KCl.

As shown in Figure 6.50 increasing the amount of nickel oxide in the catalyst increases their catalytic activity in hydrogenation. This agrees with the earlier premise that nickel oxide acts as a carrier for nickel metal in liquid-phase hydrogenation of maleic acid and that its presence is essential for the hydrogenation reaction.

Catalytic performance is also correlated with some of the catalysts' physical properties. Figures 6.51a-b and 6.52a-b show the dependence of the activity of the SCS catalysts upon Ni and NiO crystal lattice spacing and crystallite size.

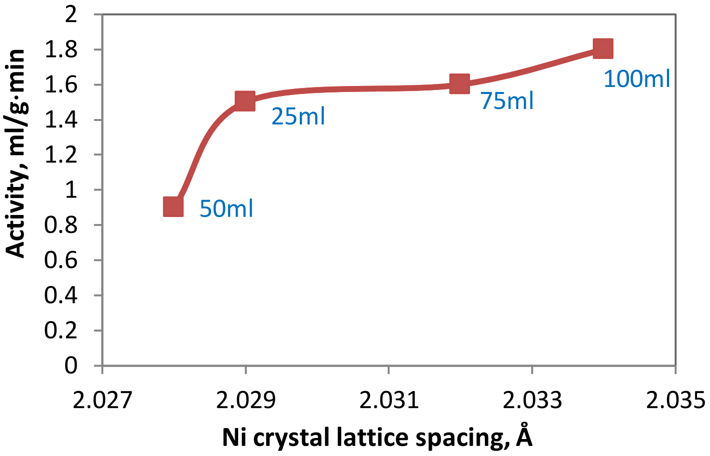

(a)

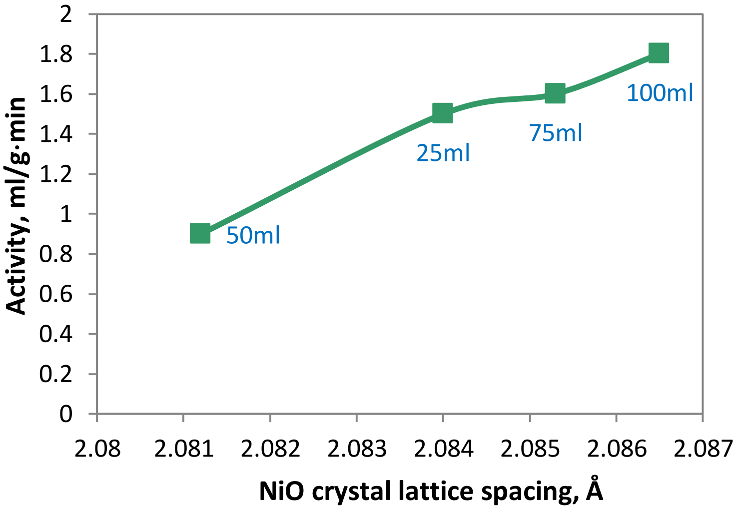

(b)

Figure 6.51: Dependence of catalytic activity on (a) Ni and (b) NiO crystal lattice spacing.

Figure 6.51 indicates a correlation between activity and Ni and NiO crystal lattice spacing for the four types of catalysts studied. With increasing crystal lattice spacing the atomic structure of the materials is more stable and this enhances hydrogenation rate since, for each hydrogenation reaction there is optimum crystal lattice spacing for optimum adsorption of hydrocarbons including hydrogen. The results indicate that, for maleic acid hydrogenation, the optimum crystal lattice parameter for nickel is at least 2.034 Å whereas for nickel oxide it is at least 2.0865 Å.

Finally, the size of the crystallites in the four types of catalysts studies correlates with their catalytic activity in liquid-phase hydrogenation, as presented on Figure 6.52.

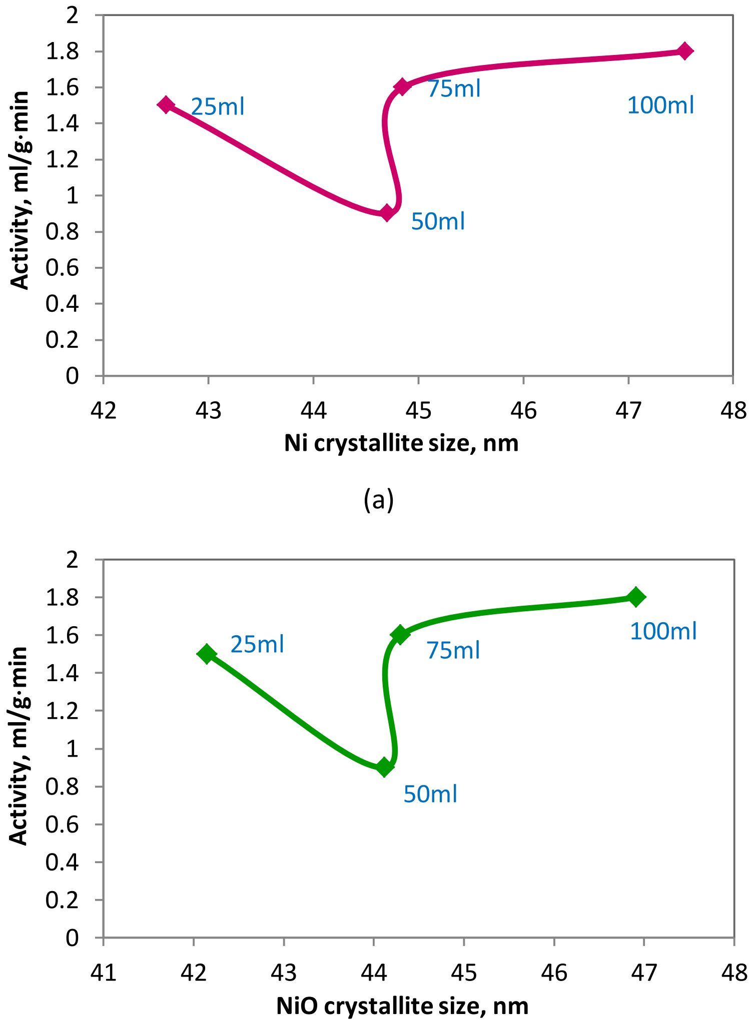

(a)

(b)

Figure 6.52: Dependence of catalytic activity upon Ni (a) & NiO (b) crystallite size.

Generally, as crystallite size increases, the tendency for agglomeration of crystals decreases and this, in most cases, results in higher specific surface area and activity. The dependence however is complicated, because the actual pore size also plays a significant role which is indicated by the higher than expected activity of the catalyst made with 25ml water.

### *6.6.5. Gas chromatography measurements*

The results of the study of the adsorption of hydrogen gas on the surface of the SCS catalysts carried out by RF-IGC are shown in Figures 6.53a-d.

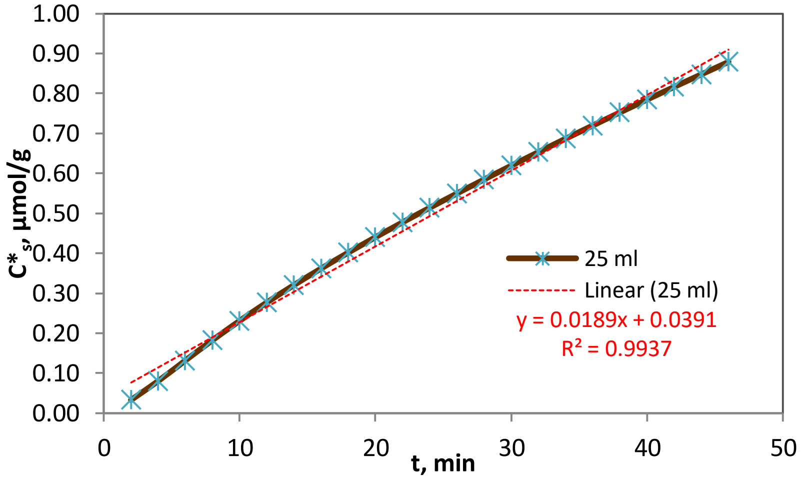

(a)

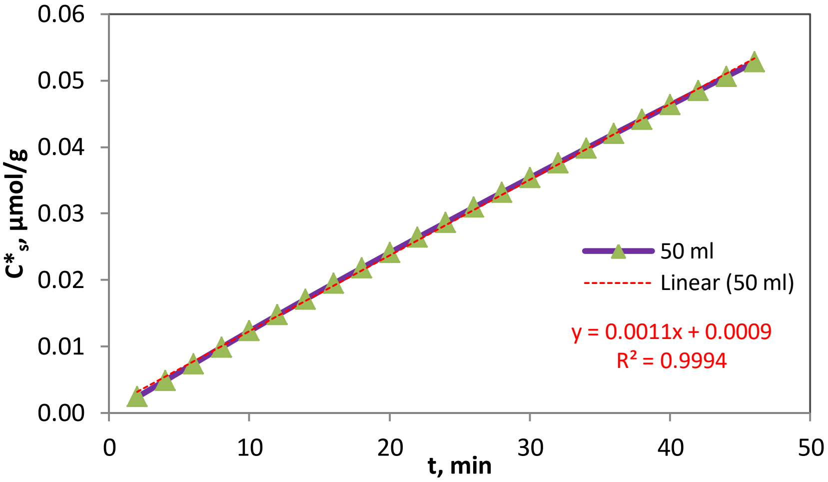

(b)

Figure 6.53: Time-variation of the equilibrium adsorbed concentration of the gas adsorbate ($H_2$) on the surface of the powdered catalysts with (a) 25 and (b) 50 ml of water in the initial SCS mixture, at 80°C.

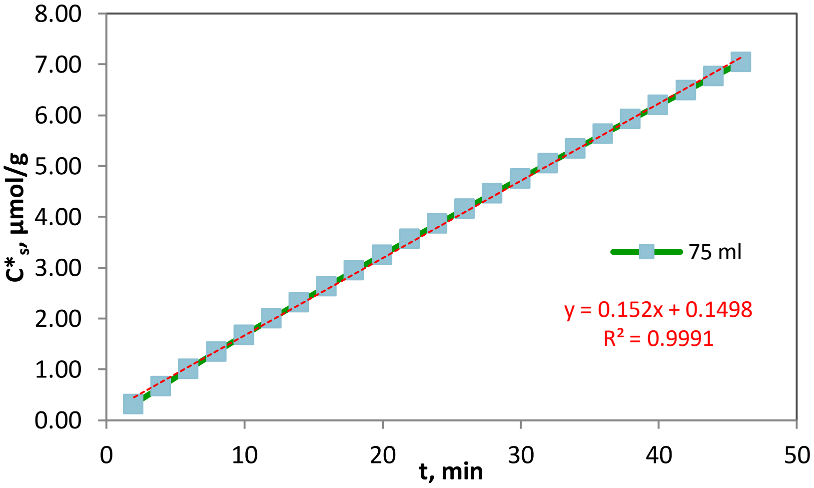

(c)

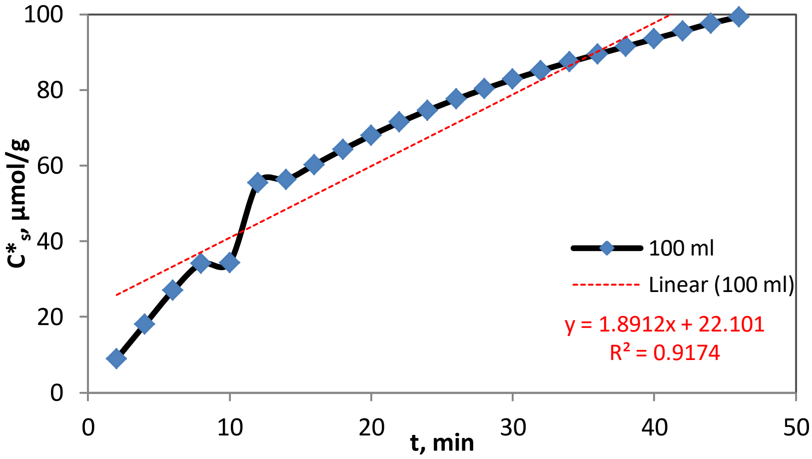

(d)

Figure 6.53: Time-variation of the equilibrium adsorbed concentration of the gas adsorbate ($H_2$) on the surface of the powdered catalysts with (c) 75 and (d) 100 ml of water in the initial SCS mixture, at 80°C [The RF-IGC measurements and data analysis conducted in collaboration with Dr. E. Metaxa in School of Chemical Engineering, NTUA].

The time-variation curves of the equilibrium adsorbed concentration, $c^*_s$ are shown in Figure 18a-d, where a linear regression fit is attempted in each case, show that the highest gradient is found for the catalyst with 100 ml of water in the initial SCS solution and the smallest for 50 ml water with the other two types in-between. This fact, as well as the fact that the highest values for the equilibrium adsorbed concentration were measured for the catalysts with 100 ml and 75 ml water, allows determining the apparent activity ranking of the four types of catalysts as follows: 100ml > 75 ml > 25 ml > 50ml.

The variations observed in hydrogen's adsorbed concentration shown in Figures 6.53a-d are probably connected with the catalysts' active centers topography. This is depicted in the results in Figure 6.54.

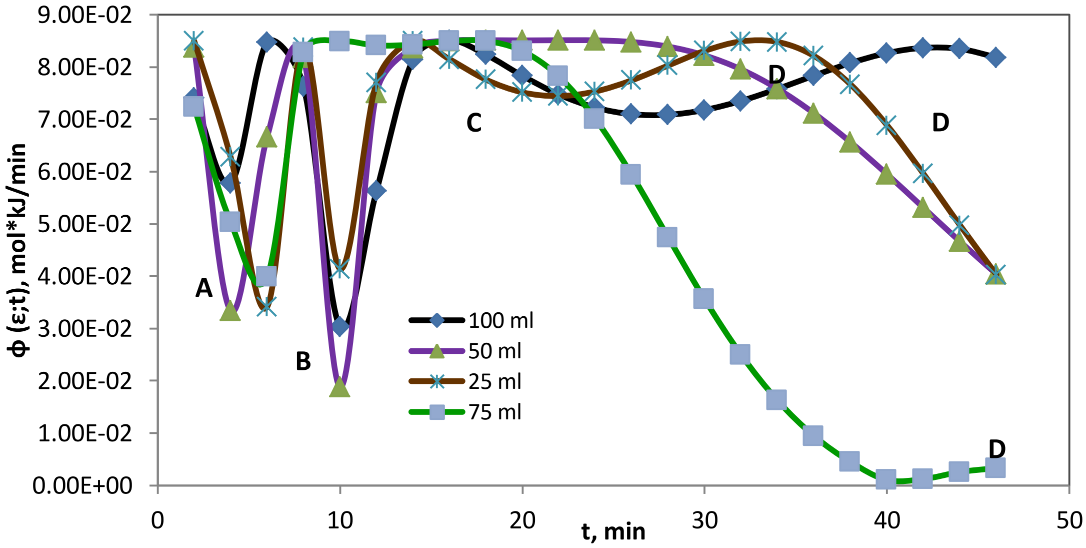

Figure 6.54: Surface topography of catalytic active sites through the distribution function of the local adsorption energies for the four different SCS catalysts, at 80°C [The RF-IGC measurements and data analysis conducted in collaboration with Dr. E. Metaxa in School of Chemical Engineering, NTUA].

Figure 6.54 depicts the time-variation of the probability density function, *φ(ε;t)*, of the local adsorption energy, *ε*, and the points where a local minimum in each graph *φ(ε;t)=φ(t)* is found which are the points distinguishing the different types of each catalyst's active sites. Analysis of these results show that up to four different kinds of active sites (A,B,C,D) are fully activated and clearly distinguishable for each of the catalysts made with 100 ml, 25ml and 75 ml water. In the case of the catalyst made with 50 ml water (which displays the lowest activity in hydrogenation of maleic acid), no type D active sites were detected indicating that the type D active sites plays a significant role in determining the overall activity of these catalysts. It is interesting to note that, for the catalyst made with 75 ml water, the distinction between site groups B and C is not particularly clear indicating that they are possibly of similar structure. In addition, the type A and type B active sites in the three active catalysts show lower measured energy in comparison with the same sites in the low activity catalyst made with 50 ml of water. This may be related to high desorption energy of low activity catalyst and low energy desorption of active catalysts.

### *6.6.6. Conclusions*

The relative amount of water in the initial solution for Solution Combustion Synthesis has generally been assumed to be of minor significance to the final product. However, in this work it was found that the initial concentration of nitrates in the aqueous solution affects the characteristics and properties of Ni-based catalysts including their final composition, crystallite size and parameters of crystal lattice, pores size distribution and surface area. In addition, the relative amount of water in the initial aqueous solution appears to have a substantial effect on their catalytic activity in maleic acid liquid phase hydrogenation. The underlying mechanism for this effect appears to be the prolonged persistence and delayed decomposition of hydrates that form during the early preheating stages of SCS. This is especially significant for structure-sensitive catalytic reactions, such as catalysis in the liquid-phase. Last but not least, the results show that NiO acts as an enabling carrier for the metallic nickel in such catalysts; when NiO was not present in the materials, the nickel-containing catalysts were mostly inactive.

Furthermore, there are strong indications that the effect of the strength of the initial aqueous solution that is reported here may be relevant for other catalytic synthesis processes which use aqueous solutions of salts, such as impregnation, precipitation, sol-gel and other methods and which employ further thermal treatments during synthesis. This work shows for the first time, that compounds, such as hydrates, which form in solution appear to persist even after all the water has evaporated and influence the physico-chemical properties of the products formed during later stages. This apparent "memory effect" exists even during the later sintering stages and may explain many of the difficulties reported in repeating synthesis results since the strength of the initial aqueous solution is generally not taken into consideration during analysis of catalytic synthesis.

## 6.7. The effect of precursor solution pretreatment on the final products' properties

The results presented here have been pubished as: O. Thoda, G. Xanthopoulou, G. Vekinis, A. Chroneos, *Applied Sciences journal, 2019, 9(6), 1200.*

### *6.7.1. Catalysts preparation*

Nickel nitrate hexahydrate (66.7%wt) and glycine (33.3%wt) - for a total solid mass of 14g - were mixed with various quantities of water (25, 50, 75, 100ml) and 8 solutions were prepared

– 2 with each quantity of water. One solution from each water quantity was pre-heated in a borosilicate glass beaker on a hot plate with mild magnetic stirring until the temperature reached 70°C. At that point the beaker was placed in a pre-heated furnace at 500°C in air atmosphere for the SCS to take place. The other four solutions (with 25, 50, 75 and 100ml of water) were placed directly in the furnace without any pretreatment. In all experiments, after the completion of the SCS cascade of reactions, the beaker was removed from the furnace and left to cool down in room temperature.

### *6.7.2. Infra-red camera analysis*

An infra-red camera was employed to take captions of the samples with 75 ml of water in the precursor solution during combustion and they are presented below on Figure 6.55. The photos were taken approximately at the same time for the not-pretreated (a) and pretreated (b) samples at 70°C.

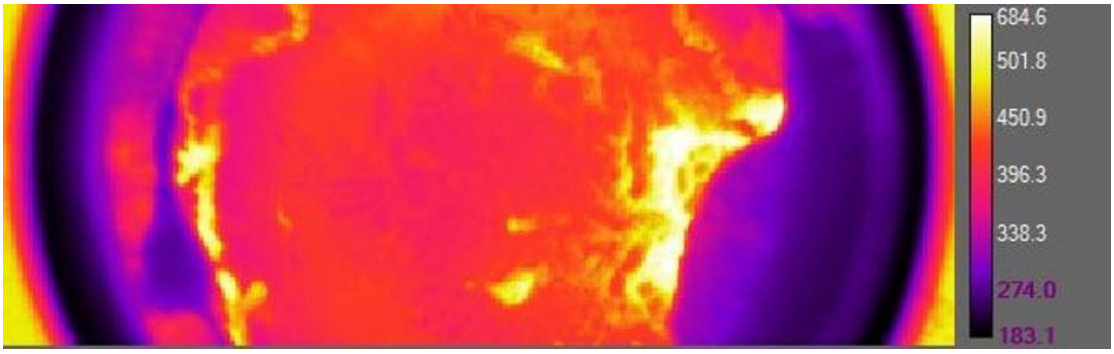

a

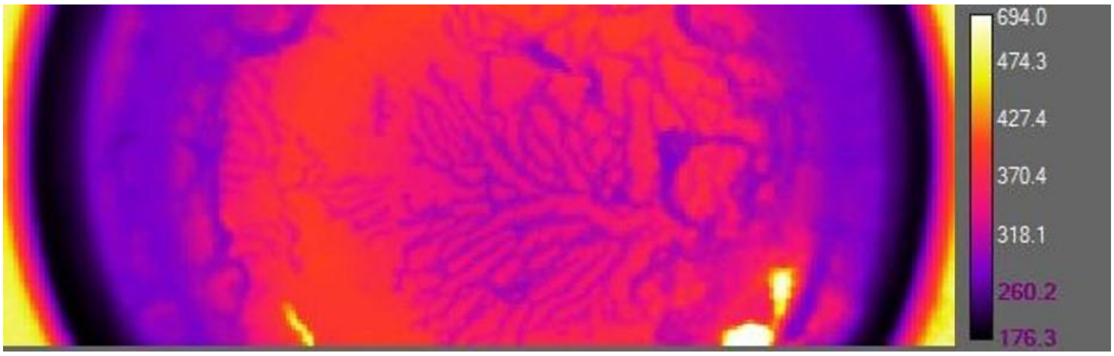

b

Figure 6.55. Captions of the a) not-pretreated and b) pretreated samples during combustion using IR-camera at 70°C [The IR-camera photos were taken by Dr. S. Roslyakov in National University of Science and Technology “MISIS]

As can be seen from the images above, there are well-developed and clearly distinguished dendrites, when the pretreatment is applied on the precursor solution. On the other hand, in the not-pretreated sample there are no developed structures, indicating different mechanism during SCS that results in different composition and microstructure of the obtained nanopowders. The combustion process for the other three water quantities was also investigated with the IR - camera and the results obtained were similar to those presented in Figure 6.55.

The formation of the dendritic structure is originated to the hydrates formation in the solution phase, combined to the extensive gas emission during SCS. These results are attributed to several controlling factors: the nickel nitrate crystal structure, the nature of diffusion through the water as solvent, the formation of nickel and nickel oxide, the formation of strong bonds of glycine-nickel nitrate tetrahydrate [$C_2H_{13}N_3NiO_{12}$] during reaction of glycine with nickel nitrate. The pretreatment of the initial SCS solution facilitates the formation of hydrates due to the slow heating and mild stirring that are applied during this stage. The formed hydrates still exist in the gel phase after the evaporation of water (during heating in the furnace) and they participate in the exothermic reaction. It appears that when these dendrites exist (with pretreatment) the reaction takes place in lower velocity as it takes place through their complicated structure and thus, there is less time available for the oxidation of nickel.

### *6.7.3. Structural analysis*

Figure 6.56 illustrates the patterns obtained from XRD analysis for the nanopowders examined. The unidentified peak that appeared on some of the patterns below the 20 degrees is associated with the substrate employed for the XRD measurement, it was not taken into account during the analysis and it was not in conflict with any sample peaks.

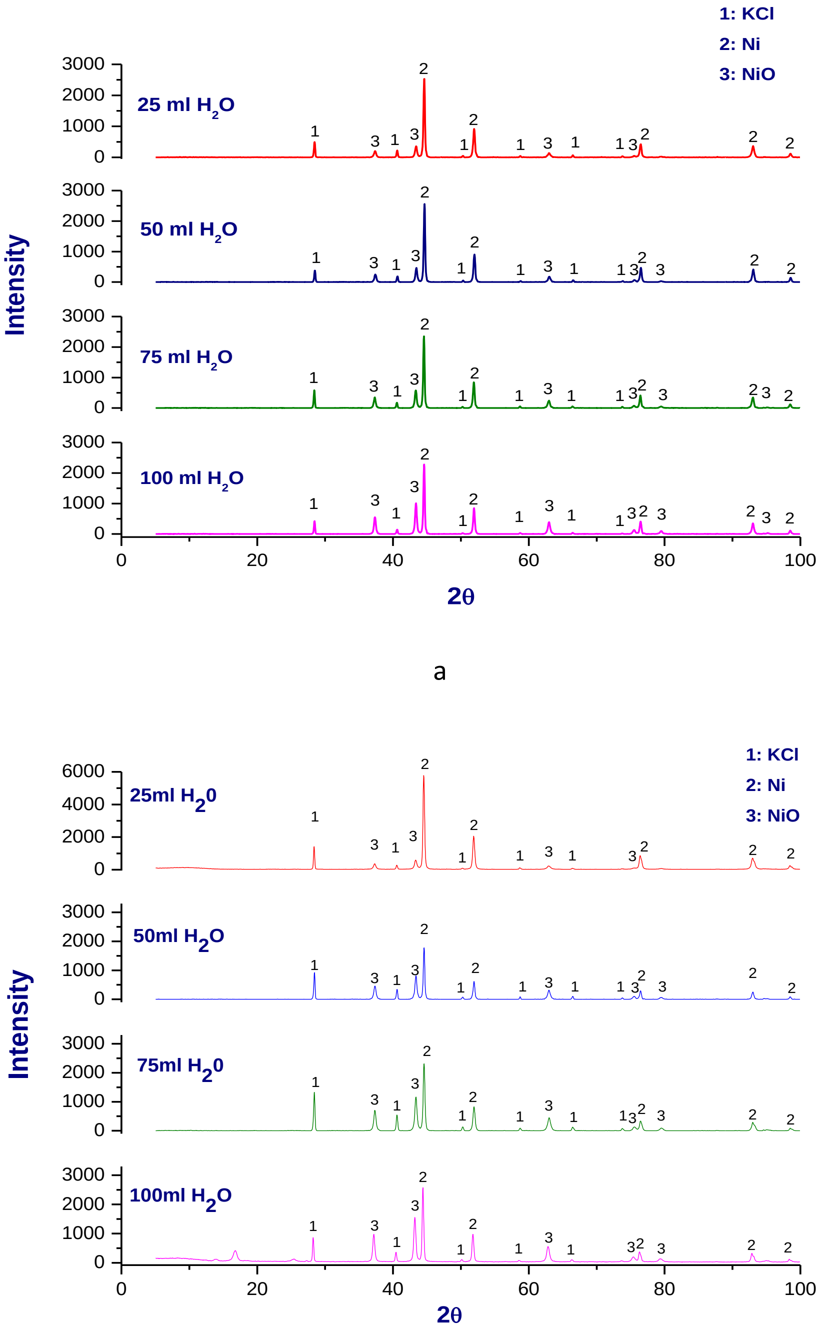

a

b

Figure 6.56. XRD patterns from the SCS-derived materials on the basis of initial mixture 66.7% $Ni(NO_3)_2 \cdot 6H_2O$ and 33.3% glycine with different amount of water added in the initial solution a) with and b) without heated stirring.

XRD analysis revealed the major impact of the precursor solution's pretreatment. The two resulting phases – Ni and NiO – appear to exist in various ratios in the final product. On Figure

6.57 below, the semi-quantitative analysis of these two phases is presented as a function of the preparation conditions.

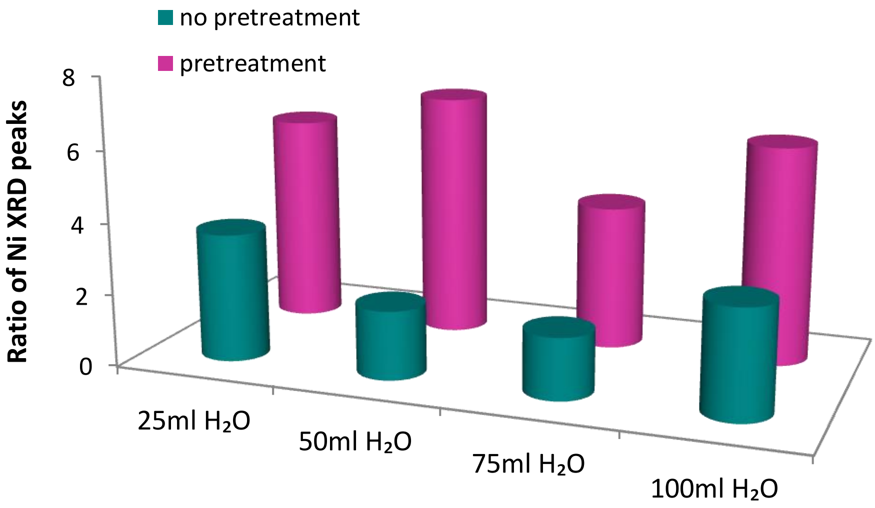

a

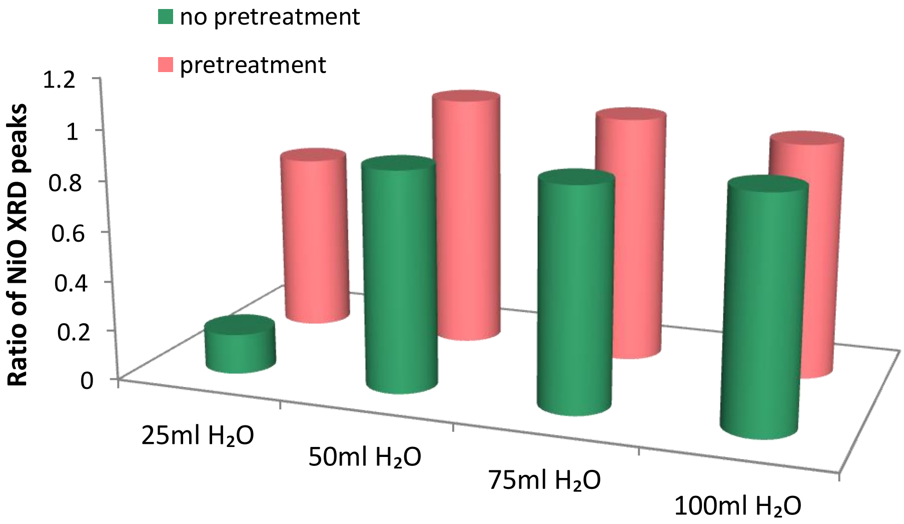

b

Figure 6.57. Semi-quantitative analysis of a) Ni and b) NiO phases in the resulting materials.

Based on the data obtained by XRD patterns, the heated stirring appears to have a major influence on the final products' composition. When heated stirring is applied in the precursor SCS solution up to 70°C, the concentration of nickel in the final product is greatly enhanced, thus improves their catalytic activity toward the liquid-phase hydrogenation. The pretreatment influences the nickel nitrate-glycine complexes that are formed in the precursor solution in the form of dendrites, which play a key role in the SCS reaction mechanism and the formation of nickel. It appears that when these dendrites exist (with pretreatment) the reaction takes place more slowly as it yield through their complicated structure and thus, there is less time available for the oxidation of nickel. Furthermore, the heated stirring before SCS has a considerable effect on the nanopowders microstructure, as shown on Figures 6.58 and 6.59 that exhibit the calculated crystal lattice spacing and crystallite size for nickel and nickel oxide. The standard deviation for crystal lattice spacing values is estimated to be ± 0.0005Å and that for crystallite size ±2nm.

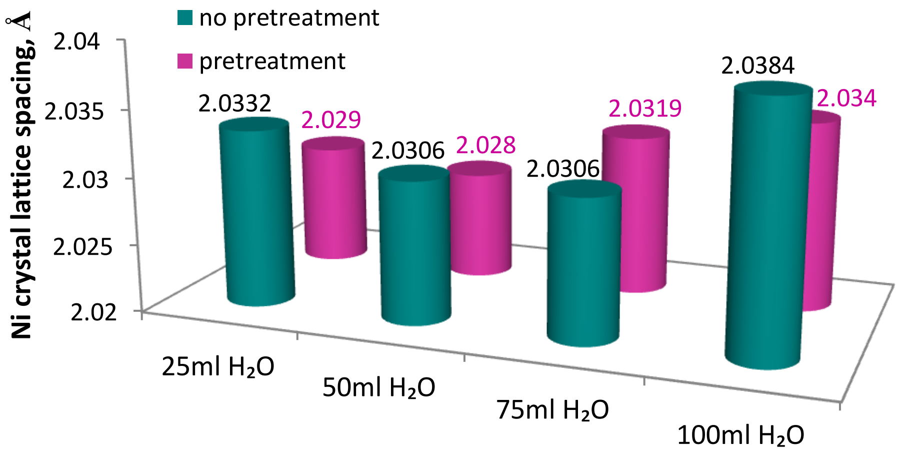

a

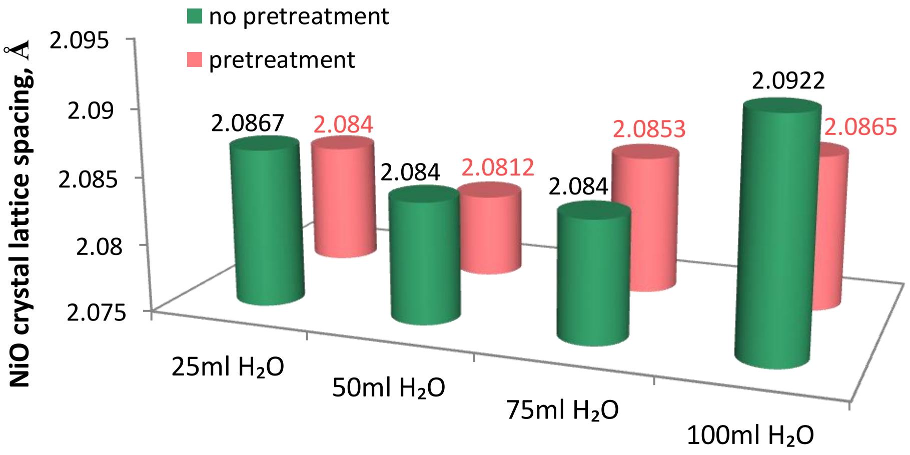

b

Figure 6.58. Influence of heated stirring on the crystal lattice spacing of a) Ni and b) NiO.

The pretreatment on the precursor solution appear to have a more complicated influence on the crystal lattice spacing of nickel and nickel oxide. In the case of 50ml and 100ml of water, pretreatment resulted in a reduction of crystal lattice spacing for both phases. On the other hand, when 75ml of water were added in the initial mixture, the applied heated stirring did not significantly influence the crystal lattice spacing. The observed changes in the lattice spacing suggest alteration of the materials' defect structure, which is a major characteristic concerning their catalytic performance.

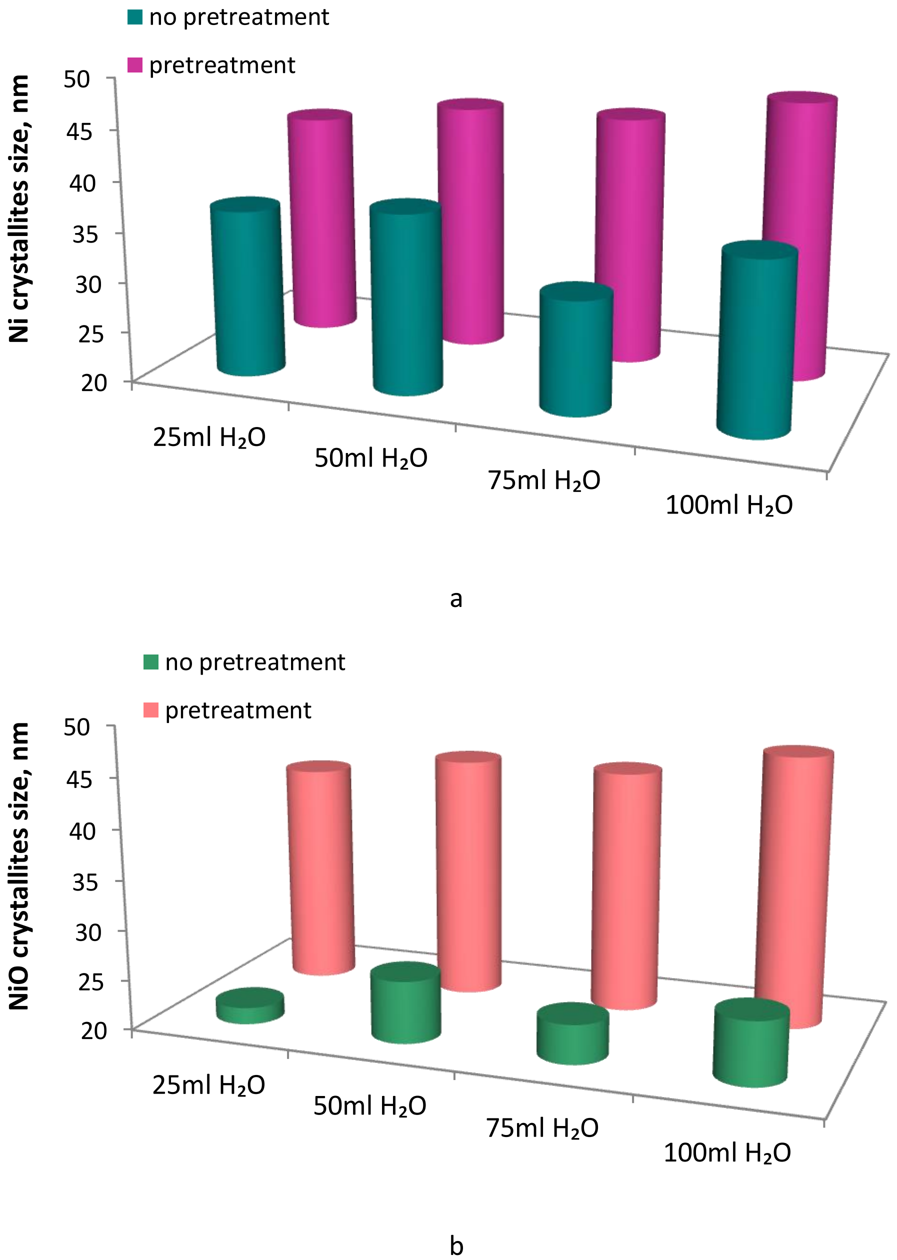

Figure 6.59. Influence of water quantity and heated stirring on the a) Ni and b) NiO crystallites size.

The influence of pretreatment is clearly observed on crystallite size of nickel and nickel oxide as well. The calculated crystallite size of both phases appears to increase when the pretreatment is applied on the initial SCS solution. The existence of dendrites led to the inhibition of the oxygen diffusion on the foam-like structure, due to the resulting more dense structure (lower height of dendrites in the final product). In accordance, the oxidation of glycine is not complete, yielding carbon and carbon monoxide which reduce nickel oxide to nickel. This double thermal treatment led to the occurrence of sintering process and the increase of crystallite size. Larger crystallites have less surface energy and as a result they tend to agglomerate less. The extent of the crystallites agglomeration severely influences the material's specific surface area that is shown on Figure 6.60. The standard deviation of the surface analyzer's values is estimated to be ±0.2 $m^2/g$.

### *6.7.4. Pore analysis and surface area measurements*

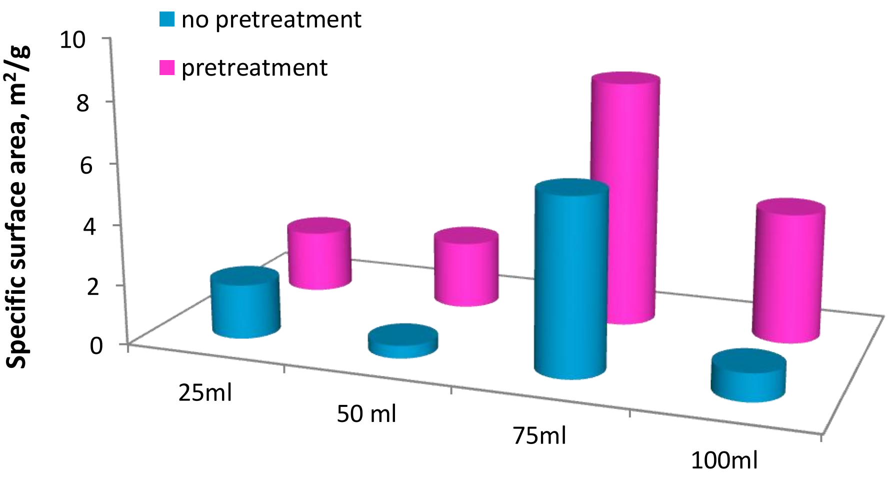

Figure 6.60. Influence of water quantity and heated stirring on the specific surface area of the produced materials.

The specific surface area (SSA) of the as-burnt materials was also altered by the pretreatment of the precursor solution, as it is demonstrated on Figure 6.60. The effect of pretreatment on the materials specific surface area was beneficial as for all water quantities examined the SSA increased, suggesting its advantageous nature. These results are in accordance with the previous calculated crystallites size for the pretreated and not pretreated materials. The heated stirring resulted in larger crystallites for both of the phases, inhibiting sintering process and leading into larger specific surface area.

Adsorption-desorption curves obtained by the BET method are shown in Figure 6.61 where the hysteresis curves of SCS products from a not-pretreated and a pretreated solution can be seen with 75ml added in the initial mixture.

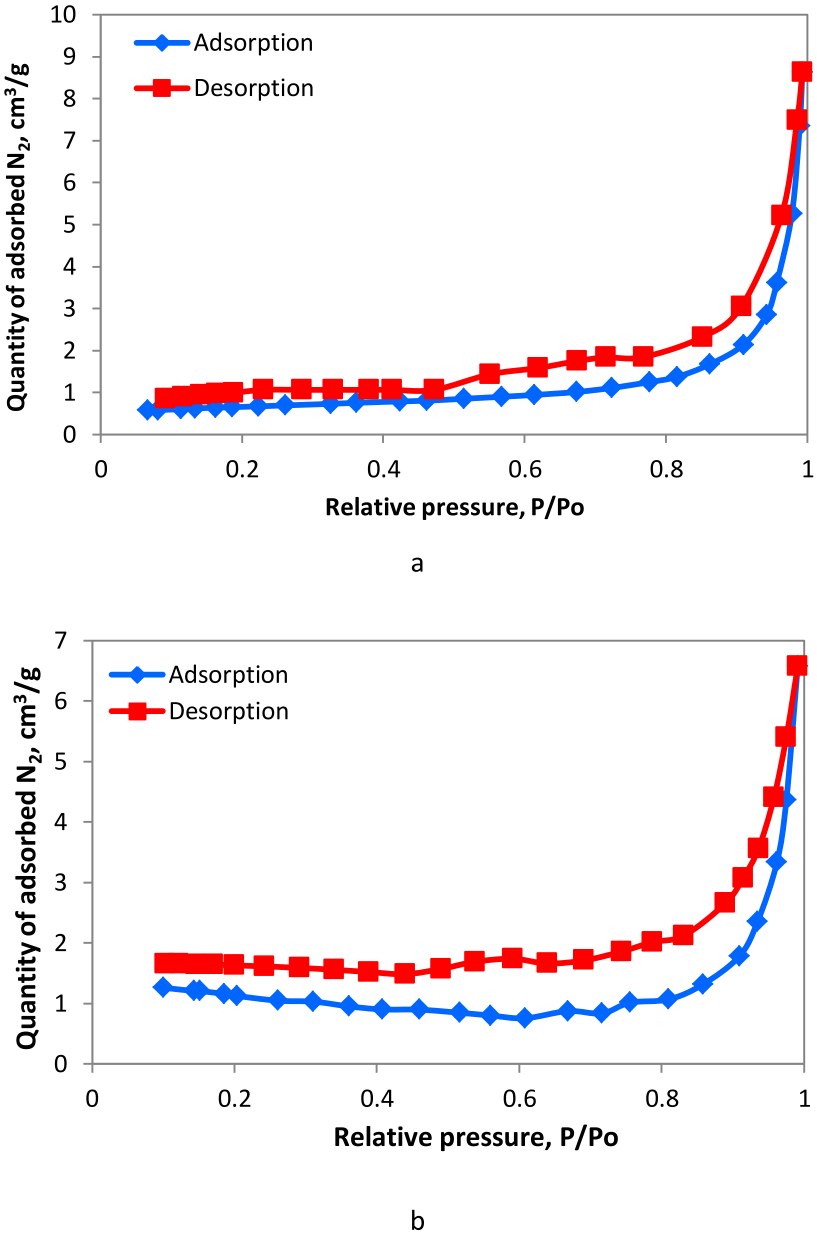

Figure 6.61. Hysteresis curves of SCS materials prepared from a) not-pretreated and b) pretreated precursor solution with *75ml* $H_2O$.

The adsorption/desorption curves of the sample prepared without pretreatment of the initial SCS solution with 75 ml of added water are demonstrated on Figure 6.61a and the pretreated one on Figure 6.61b. Both materials exhibited a distinct hysteresis loop, indicating that evaporation from pores and condensation in the pores are two completely different processes, which implies that capillary condensation occurs within mesopores. The shape of the hysteresis loop of the pretreated sample is type A, according to De Boer categorization, suggesting the existence of mainly cylindrical pores. Moreover, the bigger loop indicates the better pore connection, thus there are many open pores. On the other hand, the type of loop in the not-pretreated sample corresponds to type C and its distinctly smaller hysteresis loop reflects the presence of many closed or semi-closed pores, such as wedge-shaped, cylindrical and slit-shaped pores with one closed side or a dead end.[304]

In addition, BET measurements provided the pore size distribution of the pretreated and not samples in the case of 75ml of water.

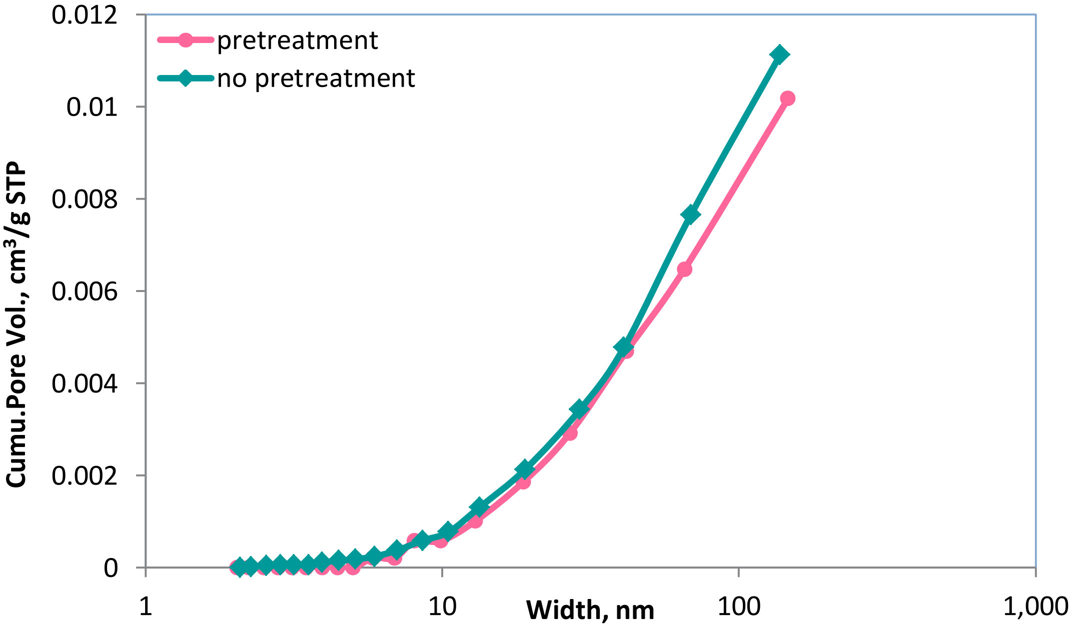

Figure 6.62. BJH adsorption cumulative pore volume concerning the influence of pretreatment on the basis of initial mixture 66.7% $Ni(NO_3)_2$, 33.3% glycine, *75ml* $H_2O$*.*

Pore analysis measurements are exhibited on Figure 6.62. The results showed that there is no significant effect of the pretreatment on the final product’s volume of nanopores and total porosity. The porosity as well as the volume of the nanopores is mainly influenced by the volume and the velocity of the generated gases, considering that the composition of the precursor solution is identical. Thus, the similar resulting porosity can be originated to the same initial composition and the identical behaviour of the generated gases, as the reaction taking place is the same. In conclusion, the different values of specific surface area can be attributed to the various crystallite sizes of the resulting phases, and not the materials' porosity characteristics.

### *6.7.5. Temperature profiles*

Thermal measurements concerning the reaction temperature as a function of the reaction time were occurred and they are presented on Figure 6.63.

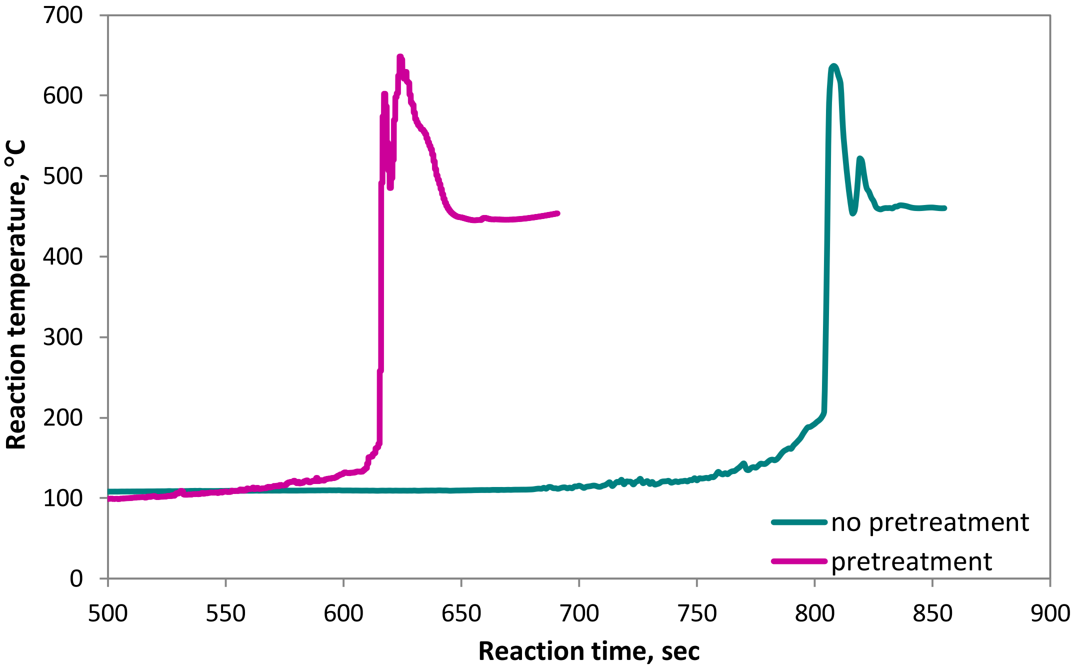

a

Figure 6.63. Reaction temperature as a function of reaction time during SCS for the samples with and no pretreatment on the basis of initial mixture: 66.7% $Ni(NO_3)_2$, 33.3% glycine a) *75ml $H_2O$.*

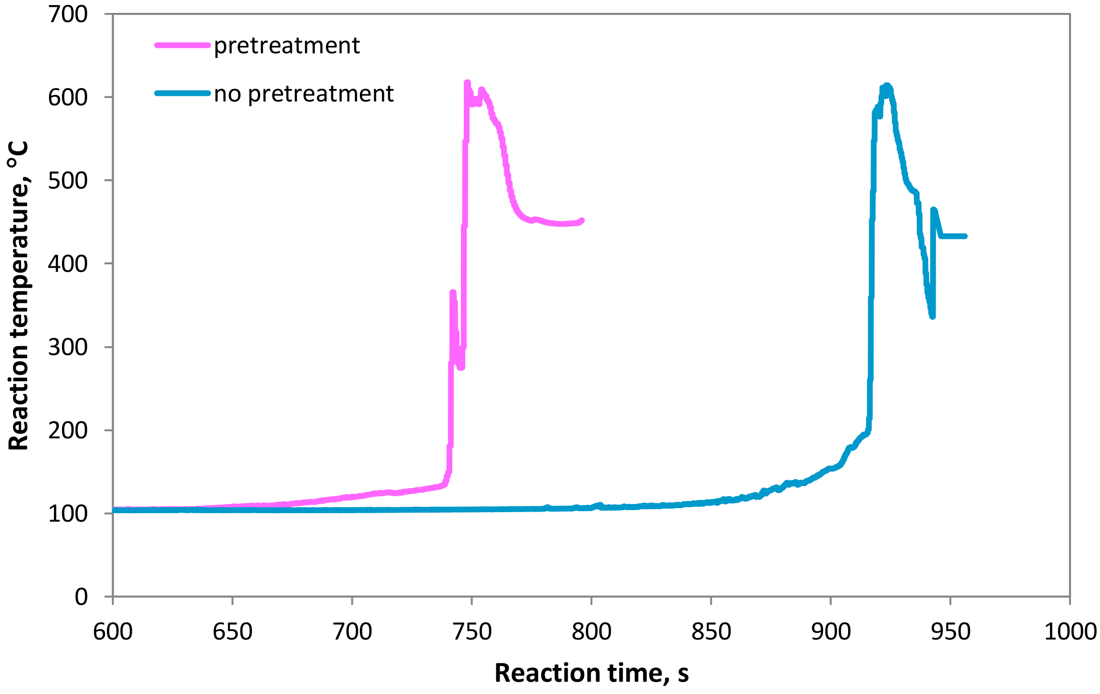

b

Figure 6.63. Reaction temperature as a function of reaction time during SCS for the samples with and no pretreatment on the basis of initial mixture: 66.7% $Ni(NO_3)_2$, 33.3% glycine b) *100ml* $H_2O$*.*

According to the obtained data, the pretreatment did not influence the combustion temperature. The belated time of the combustion initiation for the not-pretreated sample is attributed to the quantity of the water that evaporated during the heated stirring. Nevertheless, the two observed peaks during SCS have different intensity and duration, implying a mechanism modification triggered only by the pretreatment application on the precursor solution. The first peak is attributed to the exothermic reaction of glycine with nickel nitrate, while the second to the reduction of nickel oxide with hydrogen and carbon. The resulting material of the pretreated solution has a more intensive and wider peak accorded to the nickel production, suggesting the higher concentration of nickel in the final product, compared to the not-pretreated product. This is confirmed by the semi-quantitative analysis (Fig.6.57), where the nickel concentration is indeed enhanced when pretreatment is applied.

The well-developed dendrites in the pretreated sample resulted in the alteration of combustion mechanism, in comparison with the not-pretreated one. When the pretreatment was applied the reaction between glycine and nickel nitrate was slower, while in the second case was more violent. The existence of dendrites led to the inhibition of the oxygen diffusion on the foam-like structure, due to the resulting more dense structure (lower height of dendrites in the final product). Correspondingly, the oxidation of glycine is not complete, yielding carbon and carbon monoxide which reduce nickel oxide to nickel. That explains the higher second peak of the pretreated sample, compared to the not-pretreated one as well as its higher concentration of nickel in the final product composition. The formation of carbon monoxide was confirmed using a KANE-450 gas sensor.

### *6.7.6. Catalytic studies*

The Ni-based synthesized materials were employed as catalysts. Their catalytic activity was tested in liquid-phase hydrogenation of maleic acid and conversion curves were obtained. The catalysts which were prepared from pretreated precursor solutions appear to more active, and the obtained conversion curves of the catalysts are shown in Figure 6.64.

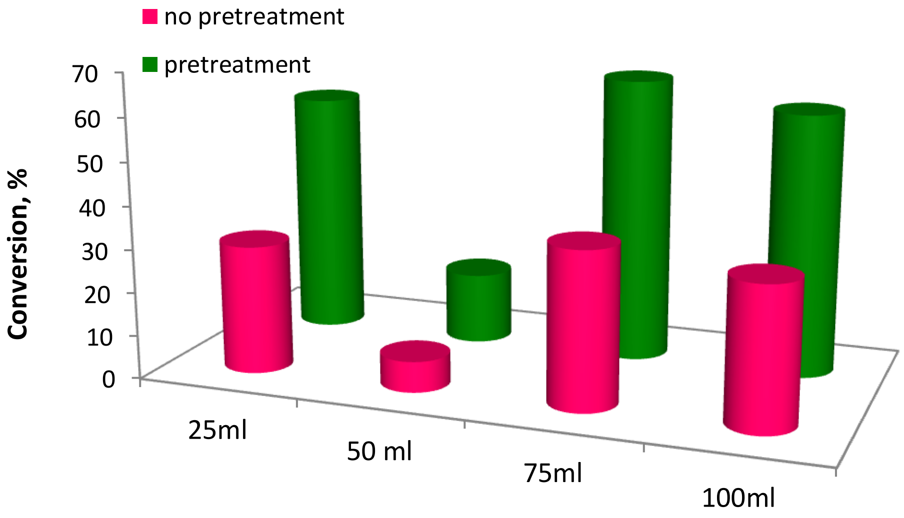

Figure 6.64. The dependence of maleic acid conversion on the SCS catalysts calculated from the quantity of absorbed hydrogen after 20 min of hydrogenation.

The degree of conversion of maleic acid into succinic acid is very low for the catalysts produced from not-pretreated solution whereas the catalysts made from pretreated solutions exhibit better catalytic activity, with the catalyst prepared with 75 ml of water showing the highest conversion rates. The enhanced catalytic performances of the catalysts prepared from the pretreated initial SCS solutions can be originated to their increased concentration of metallic nickel in the final products' concentration, their improved specific surface area as well as the open porosity for the catalyst with 75ml of water as the obtained adsorption/desorption curves suggested.

### *6.7.7. Conclusions*

This research revealed that:

- The pretreatment influences the nickel nitrate-glycine complexes that are formed in the precursor solution and are responsible for the dendritic formation of the final products. This dendritic formation influences the microstructure of the final products and their composition. The form of dendrites affects the SCS reaction mechanism and the cooling time. These parameters have a major effet on the catalyst composition, porosity, specific surface area ans as a result their catalytic performance varies.
- When the dendritic structure appears (with pretreatment) the reaction rate is lower as it takes place through their complicated structure and thus, there is less time available for the oxidation of nickel. Furthermore, the existence of dendrites led to the inhibition of the oxygen diffusion on the foam-like structure resulting in inhibition of nickel oxidation during cooling. The combination of those two conditions led to the increase of nickel concentration in the synthesized catalysts.
- In accordance, the oxidation of glycine is not complete, yielding carbon and carbon monoxide which reduce nickel oxide to nickel. This “double thermal treatment” led to the occurrence of sintering process and the increase of crystallite size.
- Larger crystallites have less surface energy and as a result they tend to agglomerate less, leading to enhanced specific surface area.

These results help to explain phenomena which have been observed during SCS, such as dendrites formation. The influence of pretreatment may explain many of the difficulties reported in repeating synthesis, since this parameter generally was not taken into consideration during the investigation of nanomaterials synthesis.

Thus, taking into consideration pretreatment influence has significant potential applications in the preparation other nanocomposite catalysts for engineering highly efficient catalysts and also for researchers that are occupied with nananomaterials.

## 6.8. Solution Combustion Synthesis of nano-catalysts with a hierarchical structure

The results presented here have been published as: G.Xanthopoulou, O.Thoda, S.Roslyakov, A.Steinman, D.KovalevdE.Levashov, G.Vekinis, A.Sytschev, A.Chroneos, *Journal of Catalysis, 2018, 364, 112-124*.

Of particular current interest worldwide is the development of technological methods for obtaining hierarchical three-dimensional network structures permeated with nano-sized pores. Such three-dimensional percolation structures of nano-composites on the basis of metal oxides and metals obtained by combustion in solution provide the capability for increasing the selectivity and activity in catalysis.

### *6.8.1. Catalyst preparation*

The initial solution contains nickel nitrate hexahydrate [$Ni(NO_3)_2 \cdot 6H_2O$] as the oxidizer with glycine as the reducer. In the series of experiments carried out, four types of samples were synthesized keeping the quantity of nickel nitrate constant at 9.34g in the initial mixture with 75ml distilled water, adding specific amounts of glycine (80, 60, 50 and 40wt% of nickel nitrate) to achieve fuel to oxidizer molar ratio (ϕ) of 2.78, 2.08, 1.74 and 1.4 for the production of Ni and NiO where ϕ=1.0 corresponds to the stoichiometric composition for the equation below.

$$2Ni(NO_3)_2 \cdot 6H_2O + C_2H_5NO_2 \rightarrow Ni + NiO + NO_2 + 2NO + N_2 + 2CO_2 + \frac{29}{2}H_2O + \frac{5}{2}O_2$$

### *6.8.2. In-situ monitoring and characteriation of the SCS process*

During the SCS combustion experiment with ϕ=1.4, two different cameras were used in order to observe combustion synthesis processes as well as to capture the combustion wave during its development. As shown in Figure 6.65, the width of the combustion wave is approximately 1mm and the temperature during combustion in the wave is in the range of 650-730$^{o}$C.

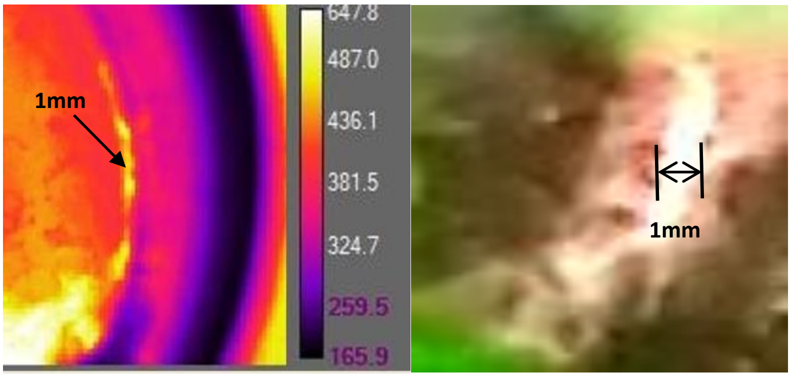

Figure 6.65. Thermal photos of the combustion wave during SCS in the system with ϕ = 1.4 using IR camera (left) and high speed camera (right) [The IR and high speed camera measurements were performed by S. Roslyakov in National University of Science and Technology “MISIS”].

The evolution of combustion temperature with time for the three different ϕ values used is presented in Figures 6.66a-c. In each case, combustion regime and maximum combustion temperature change.

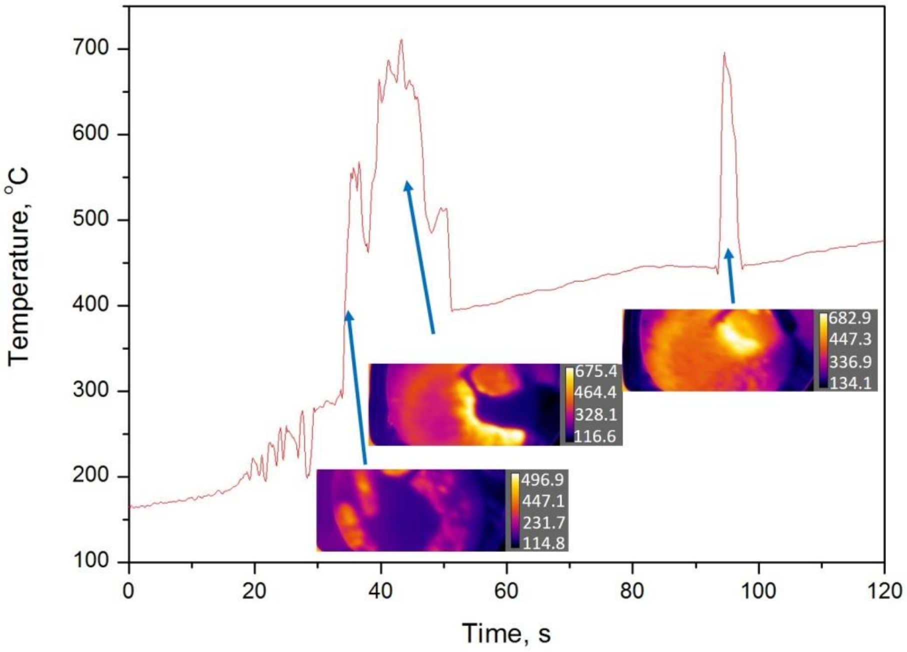

a

Figure 6.66. Temperature evolution during SCS for ϕ values a) ϕ=1.4

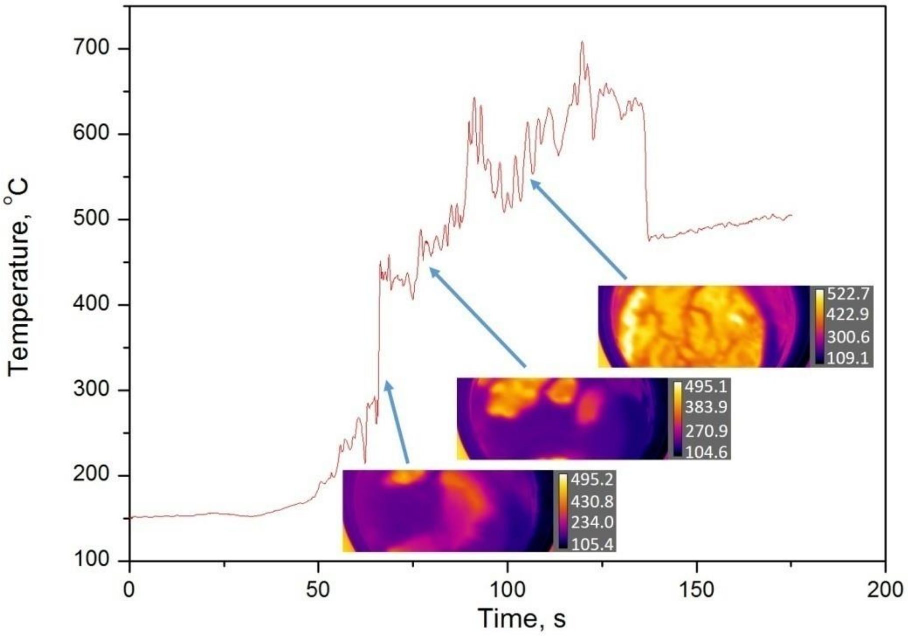

b

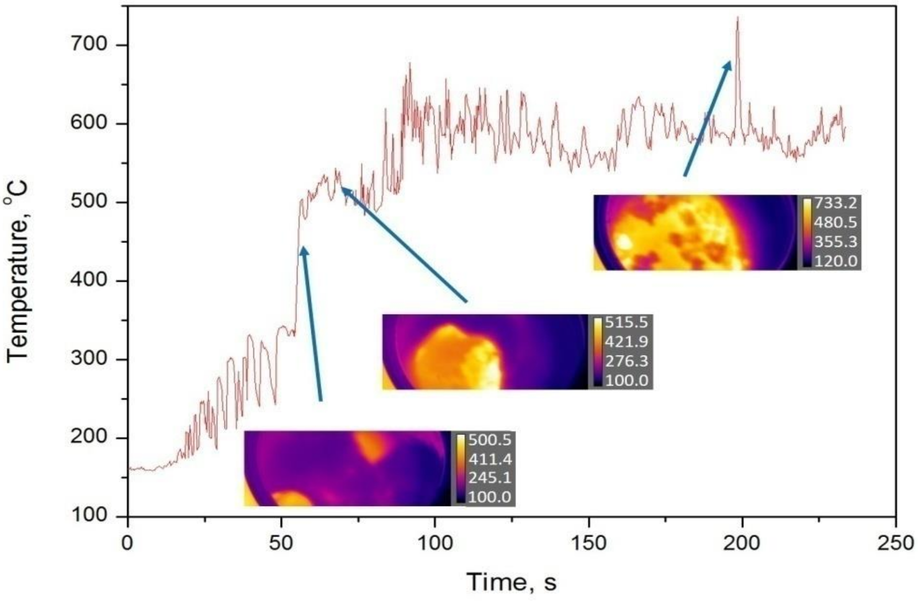

c

Figure 6.66. Temperature evolution during SCS for ϕ values b) ϕ=2.08 c) ϕ=2.78 (SCS preheating temperature 300°C). [The IR - camera measurements were performed by S. Roslyakov in National University of Science and Technology "MISIS"].

As indicated in Figure 6.66a-c and taking into account additional temperature measurements with thermocouples in and above the solution, increasing glycine concentration in the initial mixture from ϕ=1.4 to ϕ=2.78 leads to a decrease in the maximum combustion temperature from ~750 °C for ϕ=1.4 to ~ 680°C for ϕ=2.78. Interestingly, in the case of the fuel-rich specimen (ϕ=2.78), after the end of the reaction, carbon particles were observed, coating the inside of the container which continued to burn in a flash mode, indicated by the small sharp peak at approximately 200 sec (Fig. 6.66c).

These results are in line with expectations since the maximum combustion temperature would be expected to decrease as we move away from the stoichiometric composition ϕ=1.0. In addition, these combustion observations also allowed a clarification of the changes in the combustion regime itself. While for ϕ=1.4 combustion occurred "in the volume", where combustion initiates from many points in the whole volume of the gel, in the cases where ϕ is higher combustion initiates and proceeds in the self-propagating wave regime (starts from one small area and then it is self-propagated to the remaining gel). For example, in the sample with ϕ=2.08 (Figure 6.66b), two combustion waves were observed: one wave ran from top to bottom with a low speed (about 0.06 cm/s) and as soon it reached the centre a second wave started at the bottom of the specimen which propagated towards the first with a higher speed of about 0.3 cm/s. Therefore, in this sample the two-wave combustion resulted in a double heat treatment of the products, one from each wave. These differences in regime of combustion are reflected in the products' composition and structure (Figure 6.67).

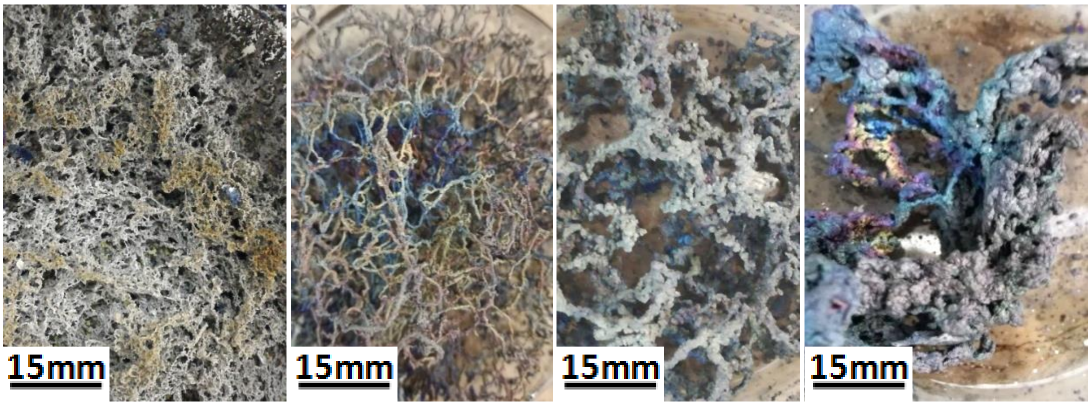

a b c d

Figure 6.67. Influence of ϕ (glycine/nitrate molar ratio) on the structure of SCS catalyst: a) ϕ=1.4 b) ϕ=1.74 c) ϕ=2.08 d) ϕ=2.78.

SCS products in general display a pronounced 3-dimensional dendritic foam-like structure as illustrated on Figure 6.67 which shows how materials appear after SCS. The different colours that appear in Figure 6.67 indicate variations in microstructure. The hydrates that are formed in the precursor solution are preserved in the gel phase after the evaporation of the water. As the combustion takes place through their complicated structure, the 3-dimensional dendritic structure occurs.

Significantly, the SCS products' final structure exhibited noticeable differences when the glycine concentration was varied. A possible explanation of this phenomenon would be that increasing the fuel concentration leads to higher combustion temperatures, thereby enhancing sintering. On the other hand, the observed aggregation process at high ϕ could be connected with extended combustion due to fuel excess, soot origination and soot burning-out process after combustion. Under these conditions, sintering of nanoparticles is possible even as low as 500°C. Results obtained from the thermogravimetric (TG) and differential thermal analysis (DTA) analysis results seem to support such a conclusion. These tests were carried out for compositions with φ = 1.4 and φ= 2.8 and are shown in Figure 6.68. It can be seen that the auto-ignition temperature for both cases is very low at about 200°C.

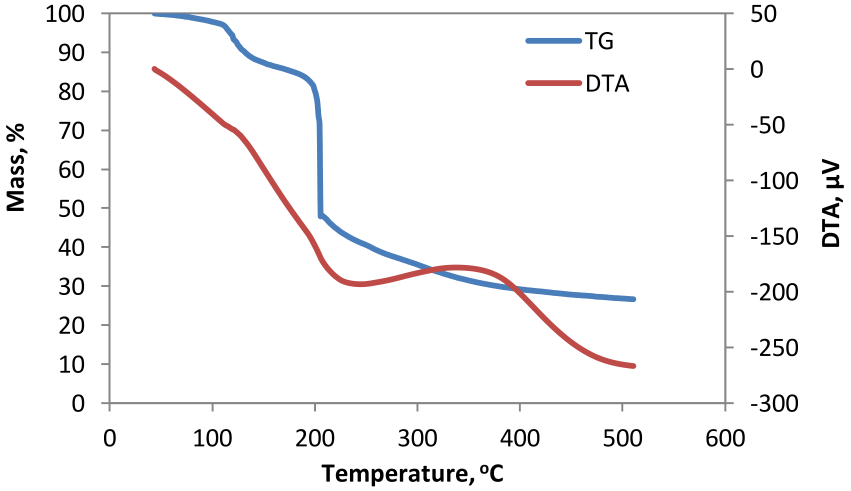

(a)

Figure 6.68. TGA-DTA analysis of samples with (a) φ = 2.78.

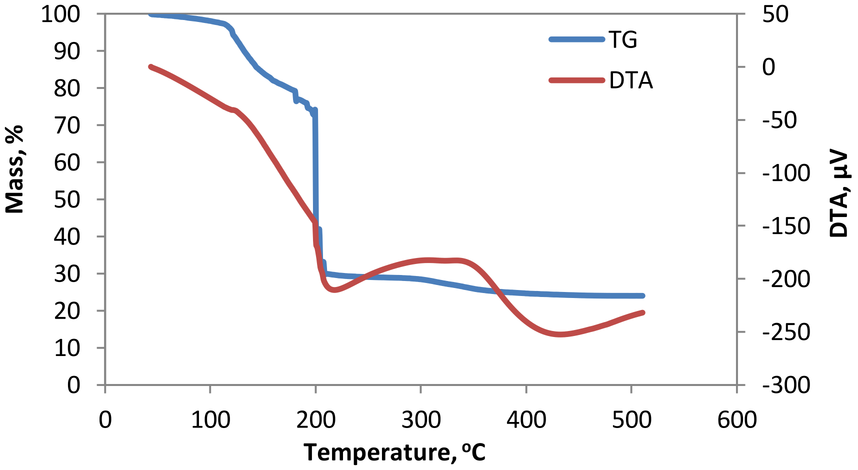

(b)

Figure 6.68. TGA-DTA analysis of samples with (b) φ= 1.4 [Dr. A. Steinman conducted the TGA measurement in National University of Science and Technology “MISIS”].

Decreasing nickel nitrate concentration in the initial SCS mixture results in decreasing formation of nitrogen oxides gases. As shown in Figure 6.68, TG curve drops 50% (ϕ = 2.78) and 70% (ϕ = 1.4) in the range of temperatures 25-200°C due to the decreased amount of released NO and $NO_2$. Moreover, according to the literature [65], the step-like weight loss is connected to the loss of three lattice water molecules from nickel nitrate hexahydrate at 95°C and all lattice water molecules at 110°C. At approximately 150°C glycine starts to burn and at 200° C there is a local minimum of the DTA curve, which signifies maximum heat release from solution combustion synthesis. Even after SCS has completed, a further weight loss is recorded as glycine’s decomposition products have only reacted partially during combustion and soot burning-out takes place at this point. In the case of ϕ=2.78 (Figure 6.68a) this process is more noticeable on the TG curve. This is also shown in the DTA curves where in both cases two exothermic peaks are evident corresponding to the SCS exothermic effect and the burning out soot process.

### *6.8.3. Structural analysis*

The development of the various phases as a function of amount of water in the SCS mixture is shown in the series of XRD spectra in Figure 6.69.

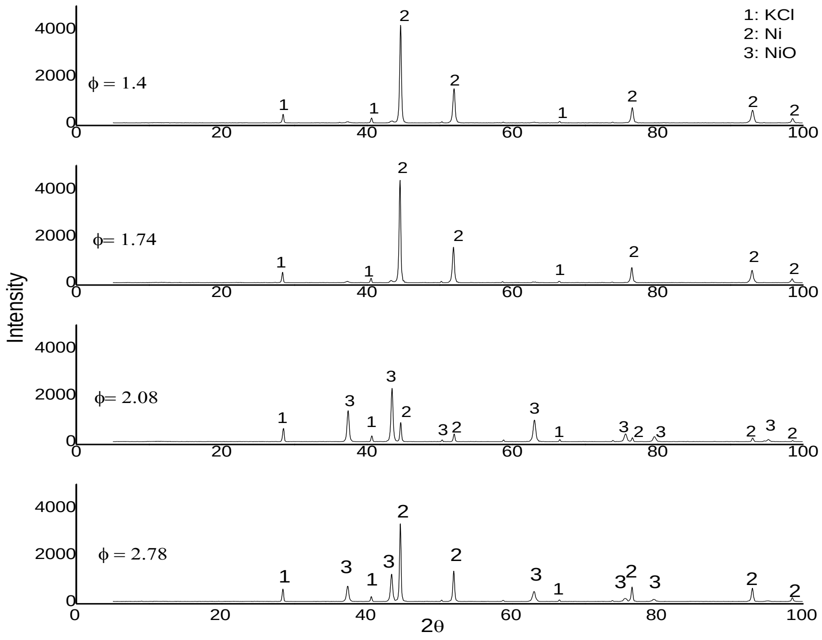

Figure 6.69: XRD patterns of the SCS catalysts on the basis of various ratios (ϕ) between nickel nitrate hexahydrate and glycine.

All catalysts tested (Figure 6.69) had two main products: metal Ni and NiO. These products are the result of the following multi-branch reaction cascade:

$Ni(NO_3)_2 \cdot 6H_2O \xrightarrow{54℃} Ni(NO_3)_2 \cdot 4H_2O \xrightarrow{85.4℃} Ni(NO_3)_2 \cdot 2H_2O$ (i)

$2Ni(NO_3)_2 \cdot 6H_2O + C_2H_5NO_2 \rightarrow Ni + NiO + NO_2 + 2NO + N_2 + 2CO_2 + \frac{29}{2}H_2O + \frac{5}{2}O_2$ (ii)

$2Ni(NO_3)_2 \cdot 6H_2O \rightarrow 2NiO + NO_2 + NO + N_2 + 12H_2O + \frac{7}{2}O_2$ (iii)

$Ni(NO_3) + H_2O \rightarrow NiOHNO_3, NiOHNO_3 + H_2O \rightarrow Ni(OH)2 + HNO_3$ (iv)

$CH_2NH_2COOH \rightarrow [CH_2COO]^- + NH_3$ (v)

$HNO_3 + \frac{7}{3}NH_3 \rightarrow 3H_2O + \frac{5}{3}N_2 + H_2$ (vi)

$2NH_3 \overset{Ni}{\rightarrow} 3H_2 + N_2$ (vii)

$NiO + H_2 \rightarrow Ni + H_2O$ (viii)

$Ni + O_2 \rightarrow NiO + \frac{1}{2}O_2$ (ix)

$2CH_2NH_2COOH + 6O_2 \rightarrow 4CO_2 + 5H_2O + NO + NO_2$ (x)

$2CH_2NH_2COOH + 4O_2 \rightarrow 2C + 2CO_2 + 5\mathrm{H_2O} + \mathrm{NO} + \mathrm{NO_2}$ (xi)

$C + O_2 \rightarrow CO_2$ (xii)

The phase composition of the products, as determined by the comparative XRD analysis and crystal lattice spacing relative ratio, as a function of fuel to oxidizer ratio (ϕ) in the SCS solution are presented in Figure 6.70, where the variation between Ni/KCl and NiO/KCl are shown together for comparison in Figure 6.70a where the catalytic activity is also shown.

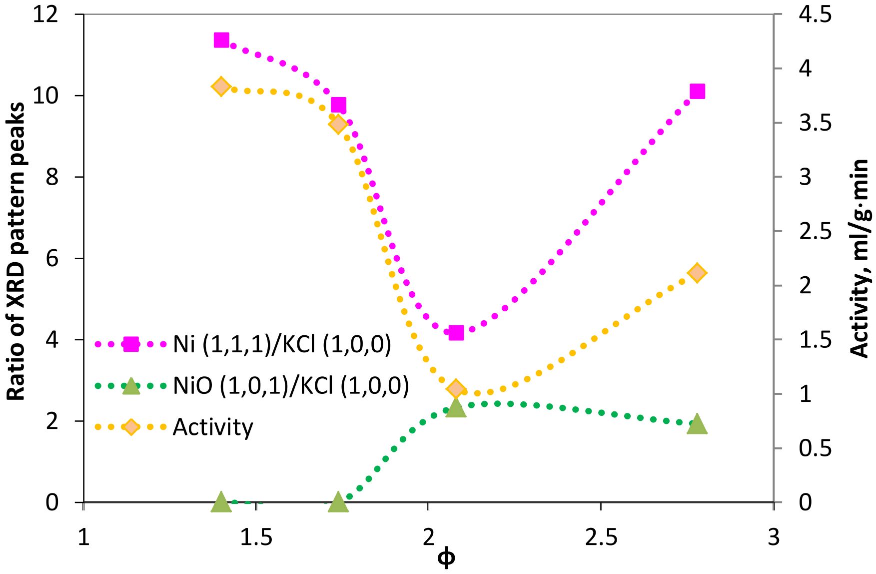

(a)

Figure 6.70. a) Dependence of ratio of XRD peaks and catalytic activity on fuel to oxidizer ratio in initial SCS mixture.

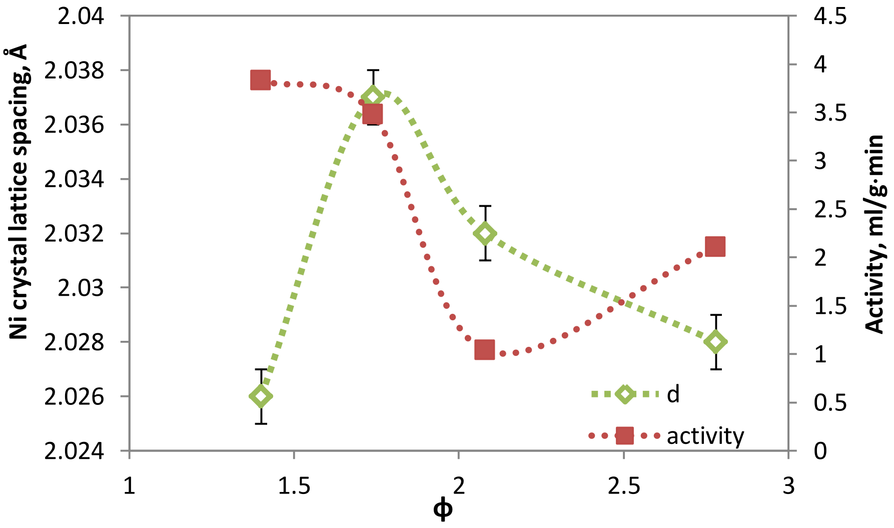

(b)

Figure 6.70. b) Dependence of relative crystal lattice spacing and catalytic activity on fuel to oxidizer ratio in initial SCS mixture.

As shown in Figure 6.70a, the maximum nickel content in the SCS products is found for ϕ=1.4, where the nickel oxide's concentration is minimum. In addition, the catalytic activity shows a direct dependence on nickel concentration in the final product which is correlated with the finding that the curve of activity has the same gradient as the nickel concentration curve. Comparing results in figures 6.70a and 6.66b, it is seen that during the SCS reaction for ϕ=2.08 two well-defined combustion waves (expanding from top to bottom) appeared during SCS. It is probable that during the first wave, there was hydrogen formation in the gas phase (reaction (vi)) followed by further reduction of NiO (reaction (viii) in liquid phase and immediate partial oxidation of nickel (reaction (ix)) during the second wave as a result of the high temperatures achieved during the previous exothermic reactions. In the other cases, the oxidation process is less intense which explains the minimum observed in the Ni concentration curve and the maximum of NiO concentration for this particular sample. The concentration of nickel is similar in the nanocatalysts produced with ϕ=1.4, 1.74 and 2.78 though the sample with ϕ=1.4 (minimum ϕ value) was measured to have the highest concentration. That can be justified by the increased oxidation process that occurs during the prolonged cooling as ϕ increases and so does the soot concentration in the mixture.

The reason why only for ϕ=2.08 were two combustion waves observed is that this is the stoichiometric ratio for hydrogen production (reaction (vi)), which is a highly exothermic reaction and under these conditions reduction of nickel oxide is favoured. The results shown in

Figure 6.70b also reveal that the nickel crystal lattice spacing of 2,037Å for hkl = 111 is (close to) optimum for maleic acid hydrogenation. Furthermore, it appears that there is slight correlation between the crystal lattice spacing of nickel and the activity of catalysts.

In Figure 6.71 a sequence of 50 XRD traces obtained by Time-resolved X-ray diffraction (*TRXRD*) studies (measured each second) describes the process of phase formation during SCS for composition with $\phi$ =2.08. The spectra are presented in both 2D of 2θ vs time as well as in 3D of 2θ vs intensity vs time. The initial solution nitrate-glycine gives a diffraction spectrum with wide amorphous halo that indicates an absence of phases in the crystalline state. On SCS ignition nickel lines (111) and (200) appear first and within 6 seconds their intensity increases. A little later, a reduction of their amplitude with simultaneous appearance of lines (101), (012) and (110) of NiO is observed. This implies that after the formation of nickel from the reduction of nickel oxide, nickel concentration decreases with time while the concentration of NiO increases. It is therefore feasible to conclude that the second wave observed during SCS with $\phi$=2.08, is connected with oxidation of Ni which was formed in the initial stage.

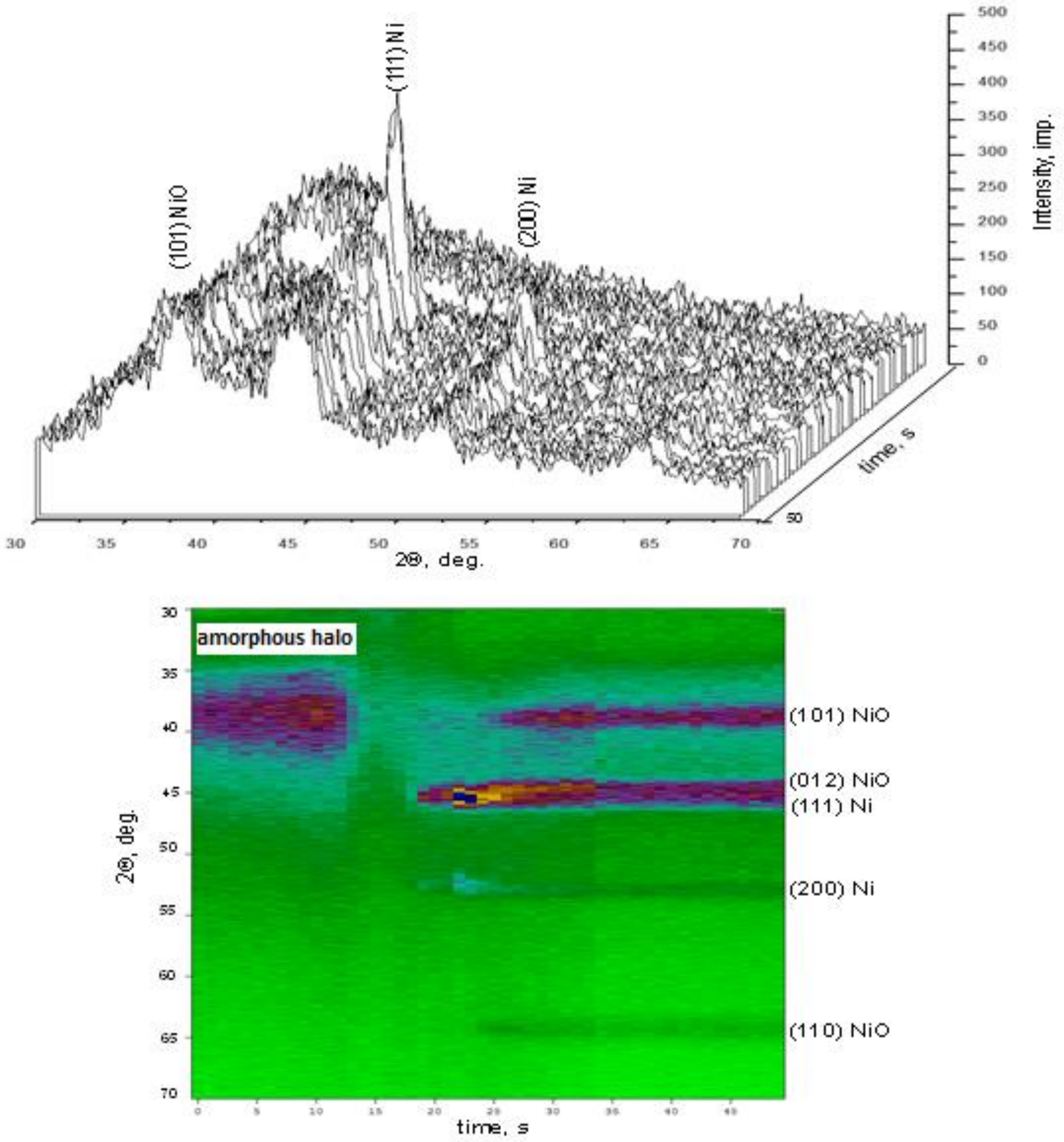

Figure 6.71. Results of time-resolved X-ray diffraction analysis in an SCS gel with ϕ=2.08 [Dr. D. Kovalev from the Institute of Structural Macrokinetics and Materials Science in Russia performed the TRXRD analysis].

The temperature profile measured during actual SCS combustion is presented on Figure 6.72. The exothermic peaks visible correspond to the formation of hydrogen (reaction vi), nickel (reaction viii) and soot combustion (reaction xii). Note that the speed of heating during the DTA tests and temperature profile analysis was different which explains the different number of detected exothermic peaks in each analysis. In Figure 6.72, the measurements were taken within the gel ("bottom thermocouple") and within the gas phases ("top thermocouple").

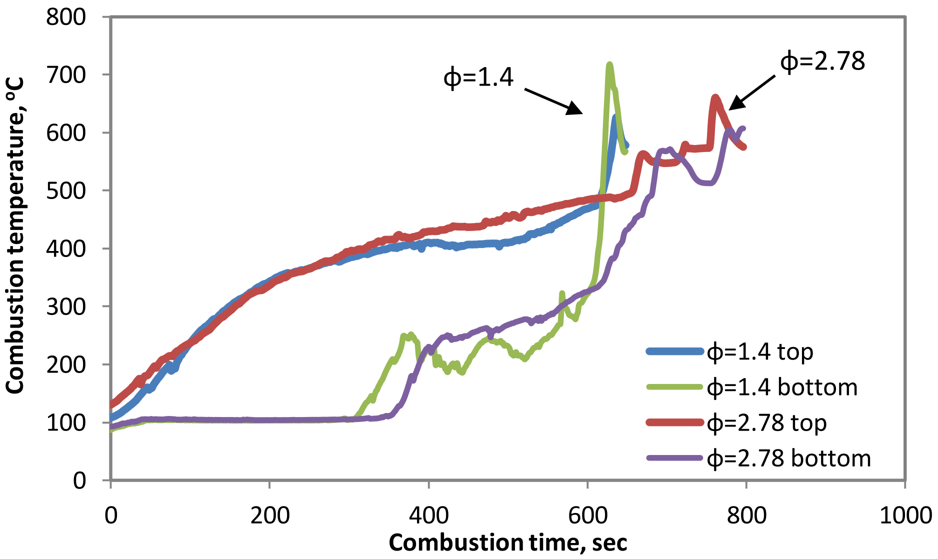

Figure 6.72. Temperature curves for samples with ϕ=0.4 and ϕ=0.8 in the initial mixture (preheating temperature 500°C). These measurements were carried out during actual SCS and resulted in more detailed data concerning all the reactions yielded.

Figure 6.72 (bottom thermocouple) indicates that the SCS reactions were mainly active within the gel where the concentration of components is higher. In the gas phase (top thermocouple) the exothermic effects detected were mainly due to reactions (vi) and (vii), which concern hydrogen formation. It is also possible that reaction (viii), where nickel is formed, influences the formation of dendrites (when volume of product is significantly increased) which results in the exothermic effect detected by the bottom thermocouple. Comparison of Figures 6.66 and 6.72 indicates that, at 500 °C, there are bigger differences in combustion temperature than at 300°C, which may be attributed to the different conditions of the experiments (temperature and volume of initial mixture) and the different methods of measurement.

### *6.8.4. Catalytic studies*

The kinetic and conversion curves obtained from catalytic maleic acid hydrogenation to succinic acid on nickel SCS catalyst are presented on Figure 6.73.

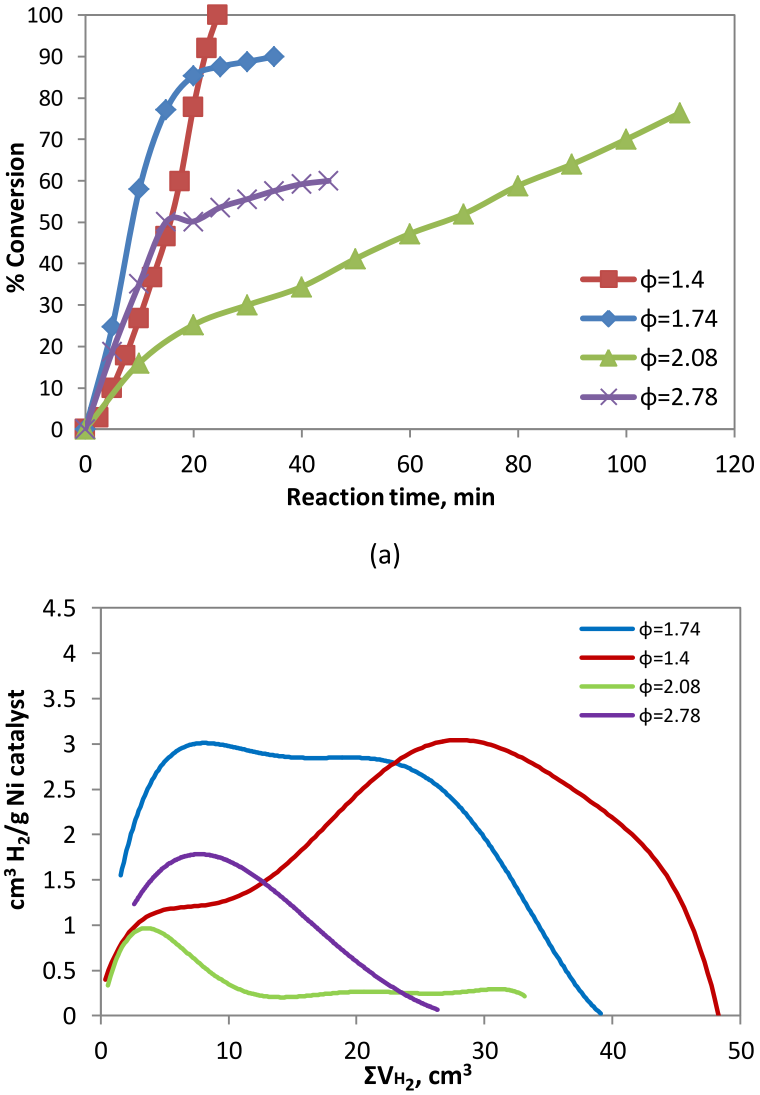

(a)

(b)

Figure 6.73. Dependence of maleic acid hydrogenation (a) conversion and (b) velocity on fuel to oxidizer ratio ϕ.

As shown on Figure 6.73a, maximum conversion of maleic acid was measured for the catalysts produced with ϕ=1.4 and ϕ=1.74. The most active catalyst (Figure 6.73b) and the one with the highest conversion is the one with fuel/oxidizer ratio of 1.4.

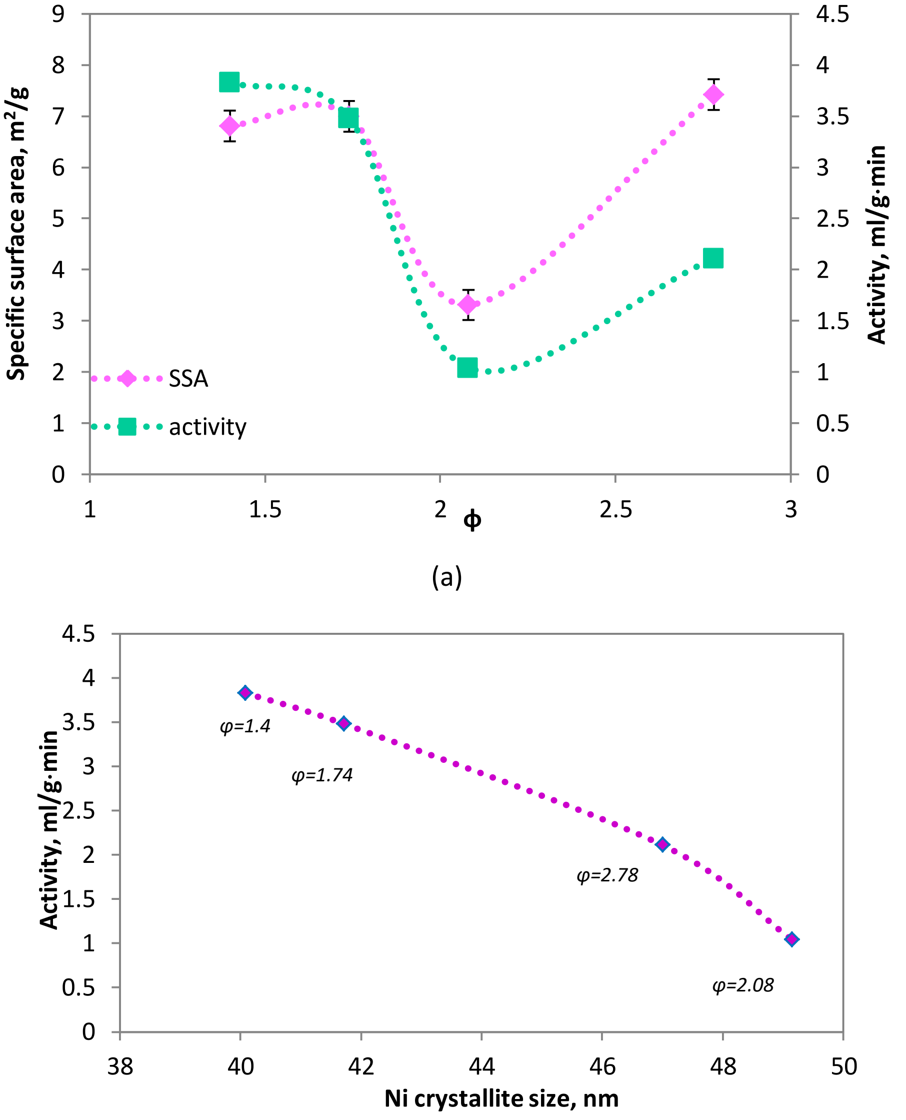

(a)

(b)

Figure 6.74. a) Influence of glycine concentration on the surface area and activity of the SCS catalysts and b) influence of Ni crystallite size on the activity for various ϕ values.

### *6.8.5. Pore analysis*

BET specific surface area measurements indicate strong dependence of surface area on the ϕ ratio in the initial SCS mixture (Figure 6.74a). The most active catalysts (with ϕ=1.4 and ϕ=1.74) display higher specific surface area (≈7m$^2$/g) than the catalyst with ϕ=2.08, which would explain the enhanced activity. On the other hand, the catalyst with ϕ=2.78 also displays high specific surface area, but is less active in hydrogenation process which illustrates the fact that there are many parameters that influence specific surface area - in complex and often opposing ways - and subsequently catalytic activity. The measured decrease in the specificsurface area of the catalysts (and associated decrease of their catalytic activity) with increasing fuel content is probably related to the increase in Ni crystallite size which results from increasing sintering of crystallites (Fig.6.74b). The measured increase of specific surface area and activity at ϕ=2.78 (Fig.6.74a) is probably connected with changing of the SCS mechanism at high concentration of fuel as hydrogen production is favoured which also leads to reduction of NiO to Ni (Fig.6.70a) which is a catalyst in this reaction. The catalyst's crystallite size is an important factor for catalytic activity and, as can be seen in Figure 6.74b, reduction of crystallite size leads to increased specific surface area. This is mainly attributed to the better dispersion of nickel on nickel oxide when the nickel crystallites are smaller. According to the obtained data, for ϕ=1.4, the minimum of nickel crystallite size corresponds to maximum activity in maleic acid's hydrogenation.

The hydrogen adsorption-desorption curves obtained by the BET method are shown in Figure 6.75a-b, where the hysteresis curves obtained for SCS Ni catalysts produced here are shown. Based on the IUPAC classification of isotherms [314], the curves obtained are probably Type IV. Their main characteristic is their hysteresis loop, which is associated with capillary condensation taking place in mesopores and limited uptake over a range of high $P/P^o$. The type of hysteresis loop (at ϕ=1.4) shown in Figure 6.75 is Type H3, which is generally observed with aggregates of plate-like particles giving rise to slit-shaped pores. In the case of SCS composition with ϕ=2.78 (Fig.6.75b) the hysteresis loop is much wider than in case of ϕ=1.4 (Fig.6.75a) probably because of difficulty in desorption due to different pore structure, since in this case, pores are cylindrical with narrow necks.

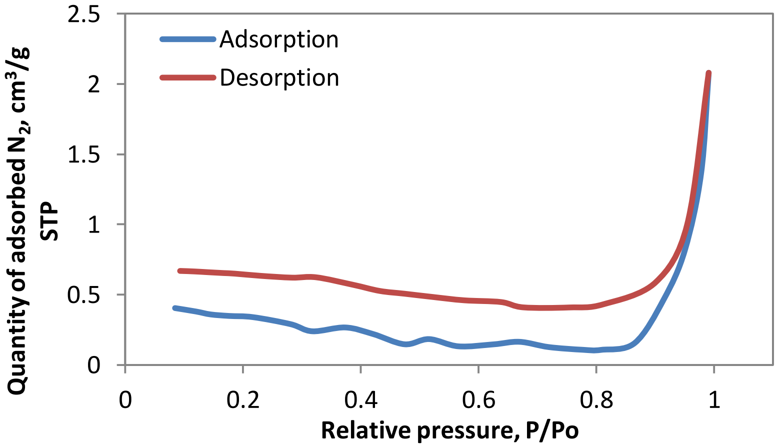

(a)

Figure 6.75: a) Hysteresis curve of a SCS Ni catalyst with ϕ=1.4.

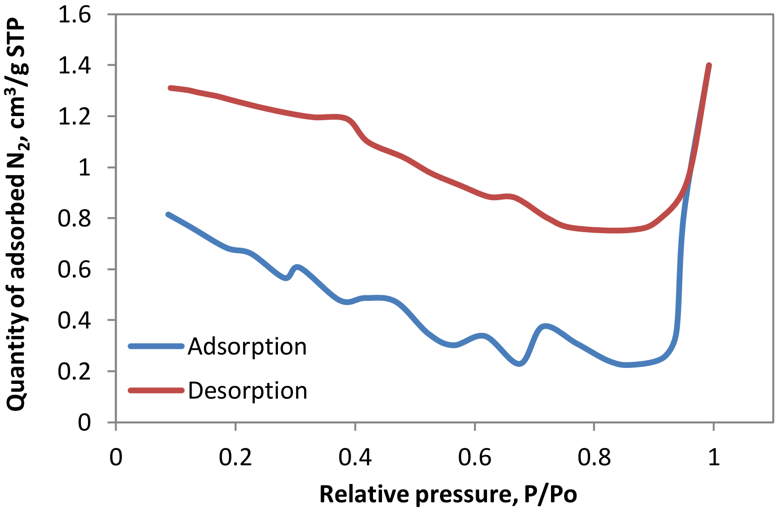

(b)

Figure 6.75: b) Hysteresis curve of a SCS Ni catalyst ϕ=2.78.

Such narrow "bottle neck" pores may be the result of soot oxidation on the surface of the catalyst, since the pores on the surface become narrower due to sintering. In such narrow neck pores, nitrogen desorption is slow, and so is for maleic acid as well. With such a pore shape, adsorption and desorption phenomena are quite difficult to take place, and consequently reactions cannot proceed which leads to low catalytic activity for the catalyst (ϕ=2.78) which has relatively high specific surface area (Figure 6.75a).

The shape of the pores affects heat release during SCS, the cooling rate after SCS and hydrogen adsorption-desorption, all of which influence the structure of the catalysts and their activity. The pore shape of the catalysts made with ϕ=2.78 means that heat release is slow and cooling rate is low in comparison with the other compositions. The above contribute to more intense sintering conditions which results in larger crystallites (Fig.6.74b). It also explains why in the catalyst with ϕ=2.78 there are more mesopores than in case of catalyst with ϕ=1.4 as shown in Figure 6.76a. As a result, the structure of all four synthesized catalysts is highly complicated: they display nanopores, mesopores and macropores, but proportion between them is different, as illustrated in the example of two of the catalysts in Figure 6.76.

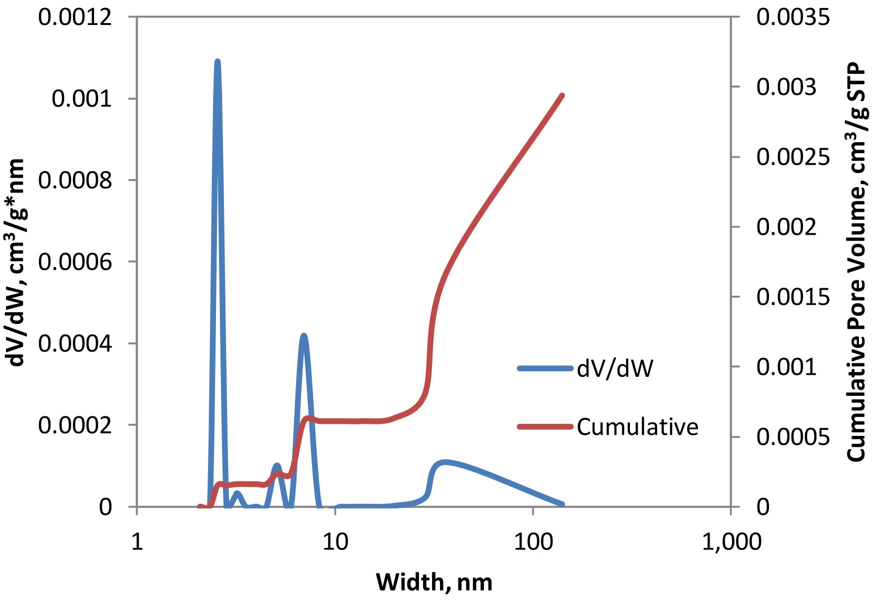

(a)

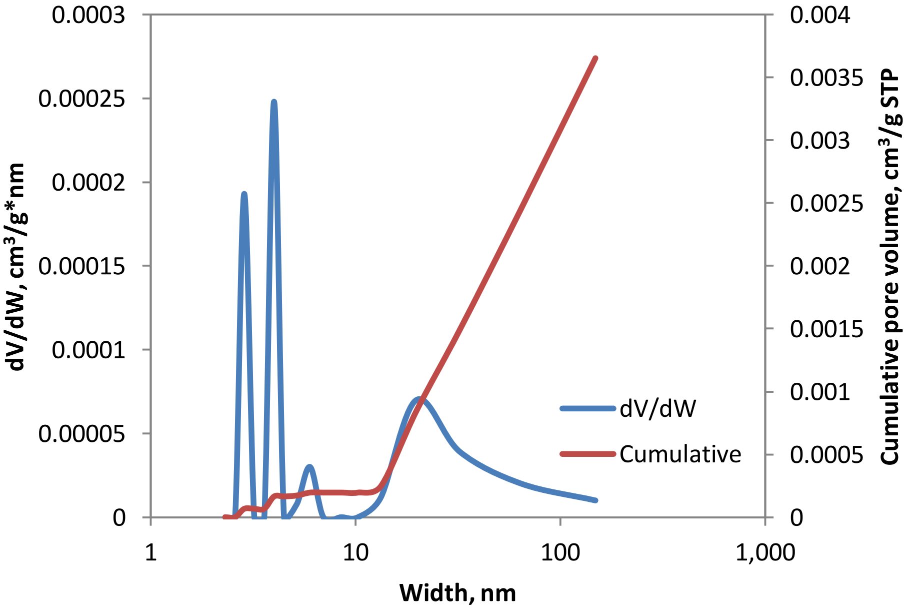

(b)

Figure 6.76: Pore size distribution curves and cumulative pore volume of SCS Ni catalyst a) ϕ=1.4, b) ϕ=2.78.

Diffusion of the initial hydrogenation components (maleic acid and hydrogen) into the catalysts' pores plays a significant role due to the fact that the hydrogenation reaction of maleic acid is in the liquid phase and at relatively low temperature (80$^oC$). For the same reason, adsorption of maleic acid and hydrogen is the limiting stage in the liquid phase hydrogenation. Figure 6.77 shows the dependence of the catalysts' activity for hydrogen adsorption in the solvent (water) on their specific surface area.

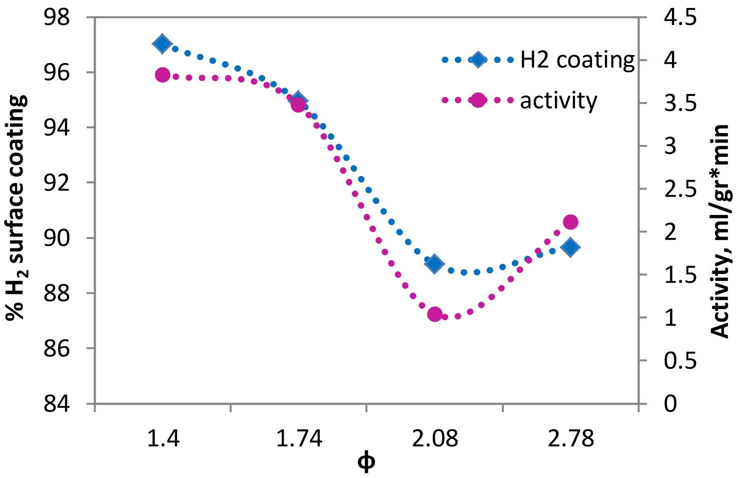

Figure 6.77: Influence of glycine concentration (ϕ ratio) on the hydrogen adsorption on SCS nickel catalysts and their catalytic activity.

The above results show that the concentration of glycine with respect to the amount of nickel nitrate in the SCS mixture (i.e. ratio ϕ) influences the catalyst's composition, structure, surface and activity.

### *6.8.6. Microstructural analysis*

The results of TEM and SEM examinations of the Ni nanopowder produced by SCS are shown in Figures 6.78 and 6.79, together with EDX analyses of selected structures.

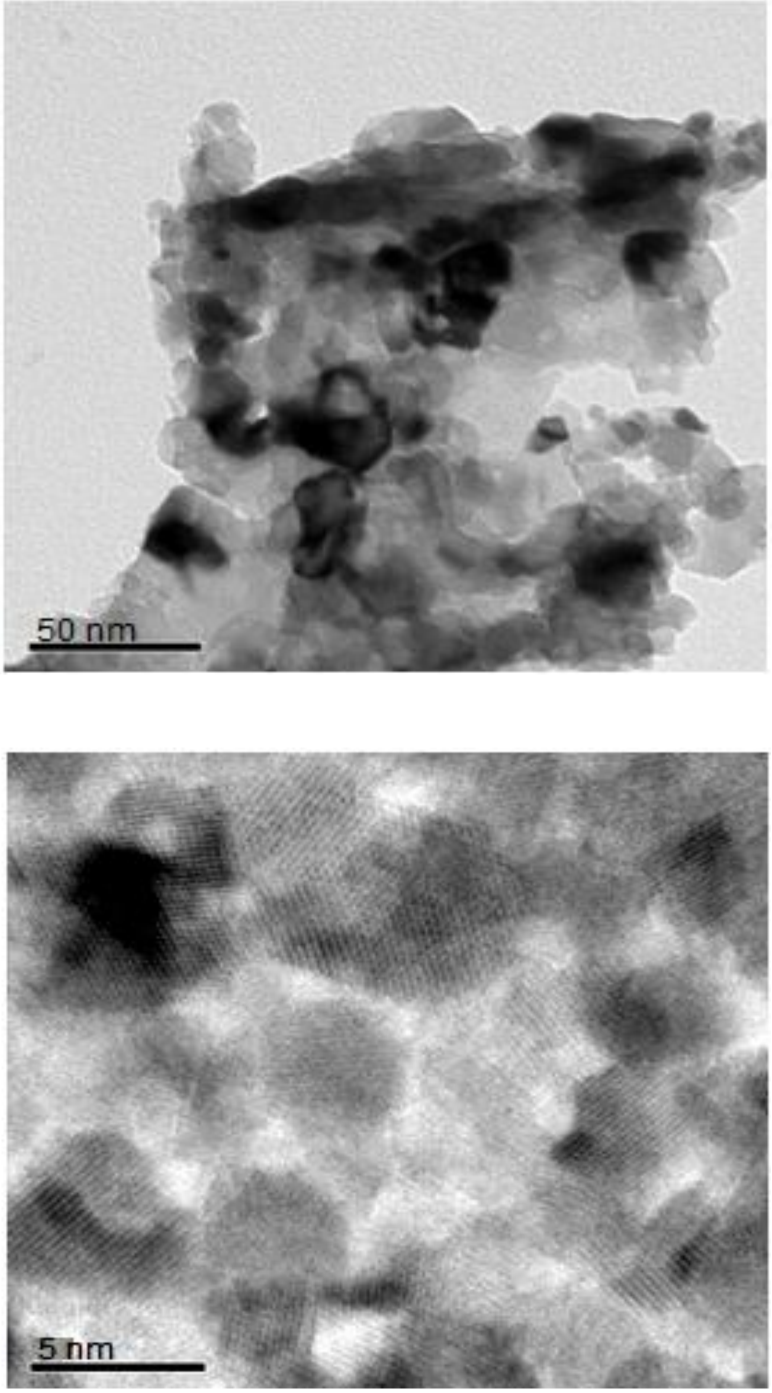

Figure 6.78. TEM images of SCS Ni-based nano-powders (ϕ=1.74) with 75ml distilled water. The particle size on the left is several hundred nanometers; while the particle size of the powder on the right is only 20-30 nm [TEM analysis performed by Dr. N. Boukos in NCSR "Demokritos"].

The images in Figures 6.78 and 6.79 indicate that the nano-structured SCS catalyst has hierarchical percolation structure. Moreover, the lines that appear on Figure 6.78 depict the atomic planes.

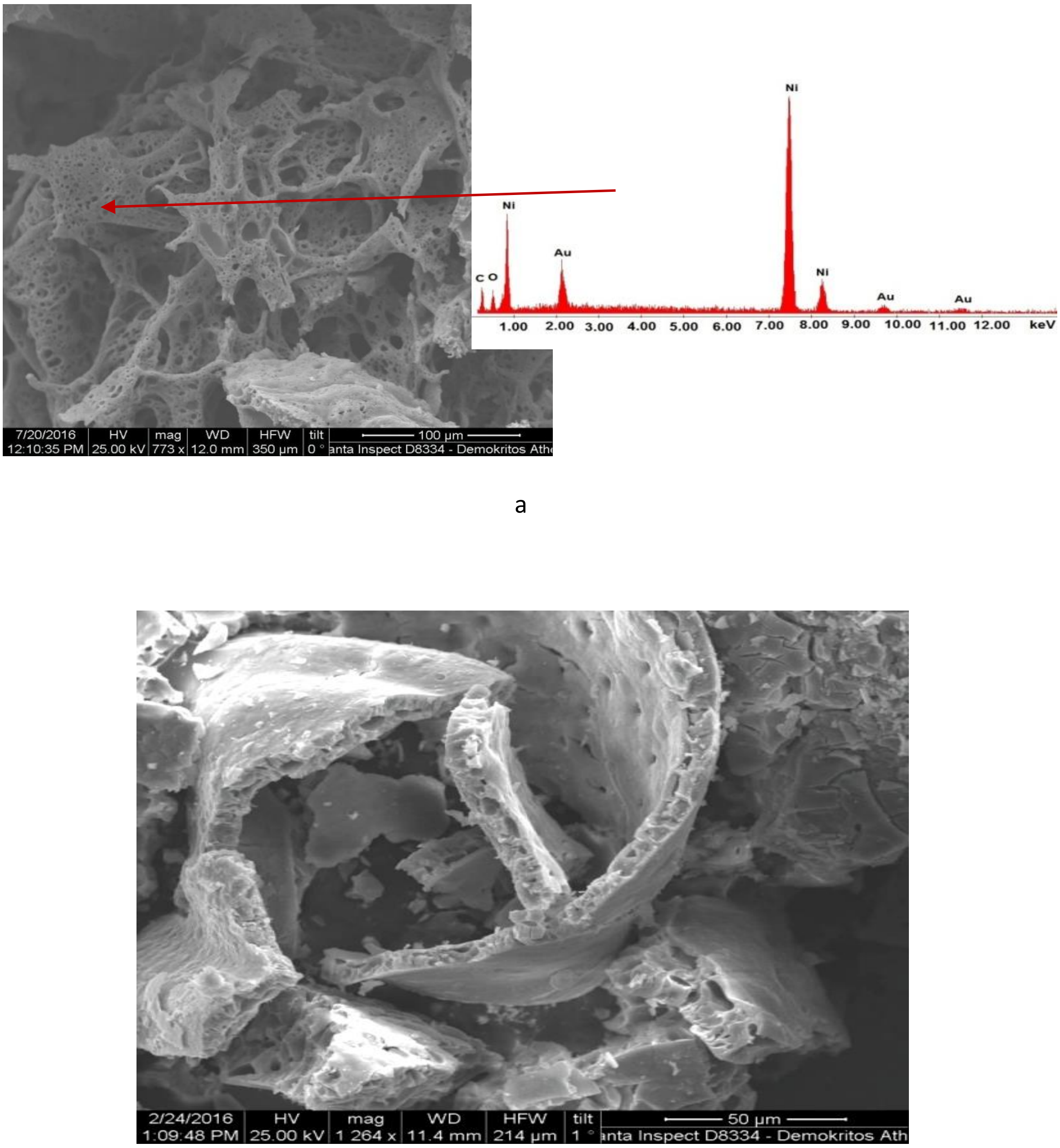

a

b

Figure 6.79. SEM examination and EDX analysis of SCS catalyst (φ=2.08) of “wall” of pores (a) and of inner surface of pores (b).

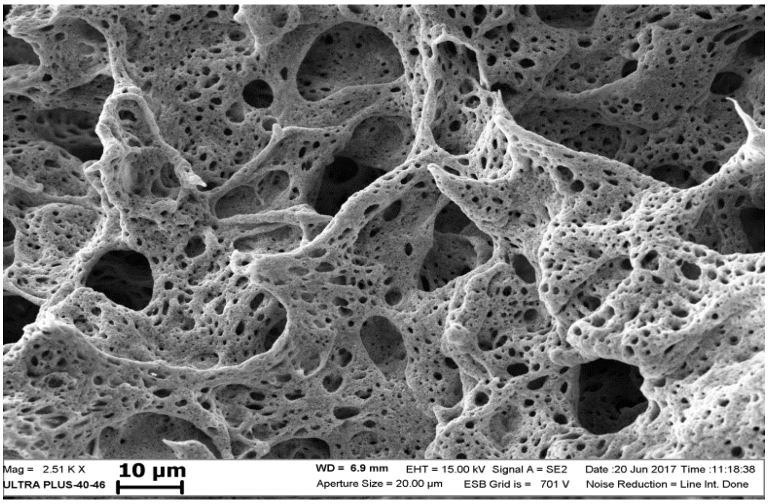

c

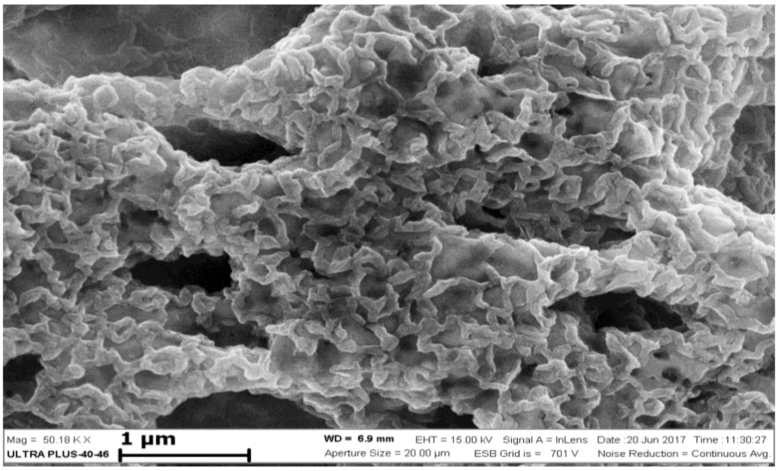

d

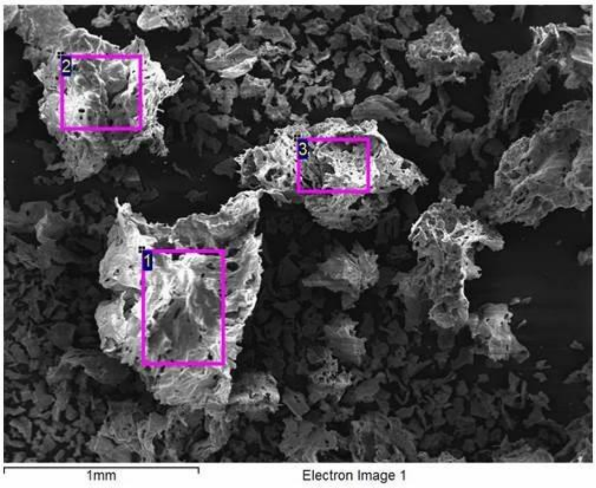

| Spectrum | O | Ni |
|---|---|---|
| 1 | 44.5 | 55.5 |
| 2 | 44.6 | 55.4 |
| 3 | 31.9 | 68.1 |
| Mean | 40.3 | 59.7 |
| Std. deviation | 7.3 | 7.3 |
| Max. | 44.6 | 68.1 |
| Min. | 31.9 | 55.4 |

e

Figure 6.79. SEM examination of SCS catalyst (φ=2.08). The morphology of the synthesized Ni-NiO high porosity agglomerates is shown in c, d and e.

The TEM images (Figure 6.78) showed that the NiO nanoparticles were highly aggregated. The particles were found to be very close to spherical with a homogeneous distribution. Figure 6.79a depicts typical aggregates derived by SCS, displaying tight three-dimensional flakes tens of micrometers in size. The flakes possess a relatively smooth surface. Inside the three-dimensional flake structure fluffy and porous networks consisting of fine nanoparticles were observed (Figure 6.79b).

The aggregates shown in Figure 6.78 were very similar throughout, indicating uniform particle shape and size. Their microstructure exhibits uniformly distributed foam-like (membrane) structure with a “wall” of about 5-7 µm in thickness (Figure 6.79b). Figure 6.79a shows large pores in the sub-mm range, while Figure 6.79b displays the higher magnification with sub-µm pores; the constituting NiO particles are not yet visible. We suggest that such high amount of porosity is the result of extensive gas release during combustion. According to the EDS data in Figure 6.79, the porous “wall” consists mainly of fine porous nanoparticles based on Ni and O (Figure 6.79e).

Figures 6.79e illustrate that the catalyst surface composition is different from the bulk composition (Fig.6.69 and 6.79a). The bulk composition for this catalyst is mainly Ni (Fig.6.69) with traces of NiO which is also confirmed in the SEM/EDX examination in Figure 6.79a. Surface analysis of pores by high resolution SEM (Fig.6.79b and d) show that the surface of the pores is covered by NiO (estimated at 55.4-68.1% NiO). This means that during SCS the dendrites formed consist mainly of Ni but the surface of the pores is oxidized because of lower heat loss, lower rate of cooling after reaction which means there is enough time for oxidation inside the pores. The hierarchical order of a structure or a material may be defined as the number of levels of scale with recognized structure. Uniform three-dimensional (3D) flowerlike Ni-NiO hierarchical architectures assembled from nanosheet building blocks have been successfully fabricated via a simple and direct SCS method (Fig.6.79b and d). Hierarchically nanoporous catalysts have versatile structural properties such as increased surface area and large pore volume that can alleviate diffusional limitations of conventional nanocatalysts with solely microporous framework (which is important for liquid phase heterogeneous catalysis). Hierarchical structure formation was also confirmed by TEM analysis (Fig.6.78)

This kind of structure and composition of the catalysts as shown in Figures 6.79a and 6.79c strongly indicate some kind of percolation type of hierarchical structure, where the sponge like structures are nickel with NiO on the inner surfaces of pores.

It is possible that such a distinctive difference in composition between the body of the pores and their surface may result in higher selectivity of these catalysts since the difference in microstructure of Ni and NiO plays different roles in the adsorption- desorption process of hydrogenation reaction. It therefore appears that SCS offers an efficient route for the production of high selectivity three-dimensional percolation network hierarchical structures of catalytic nano-composites of metals with metallic oxide coatings.

### *6.8.7. Conclusions*

- The catalytic activity of SCS-derived nano-structured Ni-based hydrogenation catalysts depend on composition (nickel and nickel oxide), specific surface area, crystal lattice spacing and pore size and shape.
- Thermogravimetric analysis showed that for glycine concentration greater than the stoichiometric ratio ($\phi$=2.08) between nickel nitrate and glycine, the decomposition product (soot) reacts partially during combustion but most of soot oxidation takes place after SCS is completed. This leads to increased sintering and aggregation processes, changing the open shape of the pores to “bottle neck”, changing the ratio between nano-micro and macro pores and consequently changing adsorption – desorption process and catalytic activity.
- Data obtained from IR high speed camera show that the combustion mechanism depends on the glycine concentration – at high glycine concentration there is a mechanism change from combustion in volume to combustion in self-propagating regime.
- It was found by temperature profile measurements during SCS that the reactions take place mainly within the gel where the concentration of components is higher. In the gas phase, above the SCS solution, the exothermic effects detected mainly concern hydrogen formation.
- Uniquely, in sample with $\phi$=2.08 (stoichiometric ratio) two waves occurred during combustion: hydrogen formation takes place in first wave followed by reduction of nickel oxide in the second wave together with Ni oxidation. This is illustrated by the observed minimum of Ni and maximum of NiO in this case. When hydrogen is formed in the gas phase, a combustion wave propagates from the top to the bottom of the reactor while the second combustion wave is initiated at the bottom (within the gel) –

first by reduction of Ni and then by partial Ni oxidation, because of the higher temperature developed.

- The three-dimensional percolation-like network and hierarchical structure of nano-composites on the basis of metal oxides and metals obtained by combustion in solutions provides a distinct possibility of increasing the selectivity and activity of such catalysts.

# 7. Nickel nitrate – Aluminium nitrate – reducer system

After the investigation of nickel nitrate-glycine system, an attempt was made to shed some light on a more complicated system. Nickel nitrate and aluminium nitrate were selected, as nickel nitrate provides nickel to the final product, while aluminium nitrate produces alumina ($Al_2O_3$) which is a well-known catalytic support. Furthermore, the synthesis of Ni-Al alloy was aimed as well as the study of its potential influence toward the hydrogenation reaction, as alloys can act as catalysts. Finally, as the system in study changed, the synthesis of nickel had to be tested with different fuels, as the reducer plays a key role to the nickel synthesis, due to the fact that it provides the carbon in the sytem during combustion.

## 7.1. Effect of reducer's nature on the properties of the resulting powders

### *7.1.1. Materials preparation*

Three different fuels (glycine, urea and carbohydrazide) were added in the initial mixture with initial concentration: 40%wt nickel nitrate hexahydrate, 60%wt aluminium nitrate nonahydrate, 40%wt (of nickel nitrate and aluminium nitrate) fuel and 75ml of water. Each solution was pre-heated in a borosilicate glass beaker on a hot plate with mild magnetic stirring until the temperature reached 70$^{o}$C and then placed in a pre-heated furnace at 500$^{o}$C to enable SCS. Once SCS is completed, the beaker is removed from the furnace and allowed to cool at room temperature.

### *7.1.2. Results and discussion*

The morphology of the final SCS nanopowders is demonstrated on Figure 7.1.

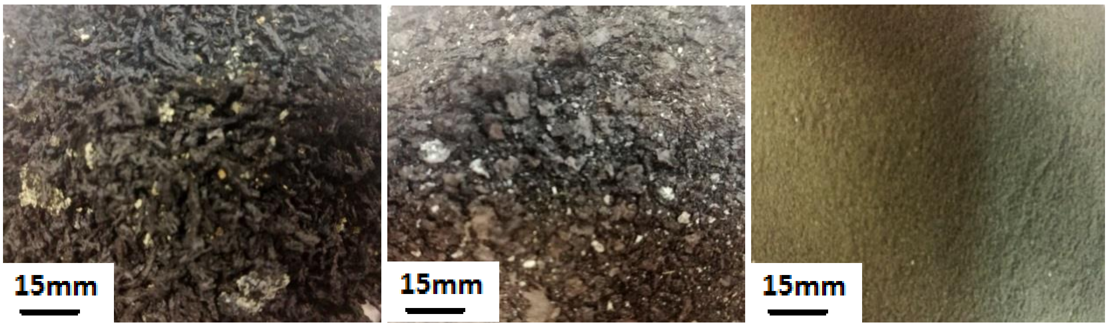

a b c

Figure 7.1. Influence of reducer type on the structure of the SCS nanopowders: a) glycine b) carbohydrazide c) urea.

As it appears on the Figure 7.1 above, the samples with glycine and carbohydrazide are crystallized, while the produced nanopowder with urea as fuel is amorphous. The samples were analyzed by XRD which provided the diffraction patterns that appear on Figure 7.2 below. The two unidentified peaks (2θ~14.1, 17) that appear on the first pattern below the 20 degrees are associated with the substrate employed for the XRD measurement, they were not taken into account during the analysis and they were not in conflict with any sample peaks.

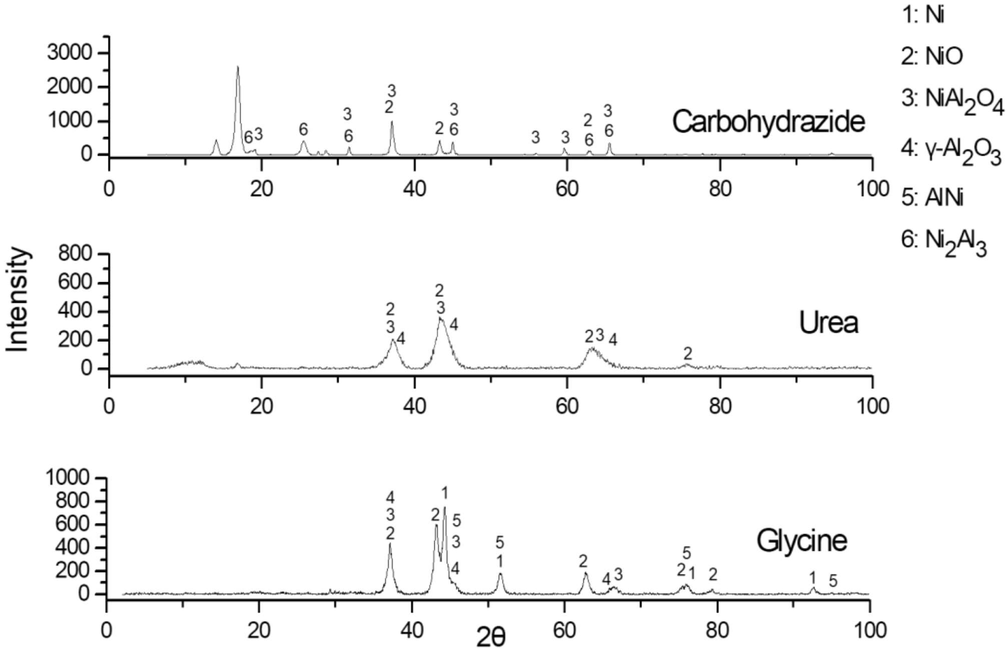

Figure 7.2. XRD diffraction patterns of Ni-based nanopowders with different fuels (glycine, urea and carbohydrazide).

As it can be observed the as-burnt nanopowders had various phases in their final composition. Metallic nickel was produced only with the employment of glycine as fuel. The presence of nickel in the final product is fundamental, in order for the nanopowders to operate as catalysts. Moreover, in the case of urea, the diffraction pattern indicates that the final product is very fine powder with very small crystallites, while carbohydrazide provided the most crystallized nanopowder. The equations above describe the total SCS reaction according to the detected phases.

$4Ni(NO_3)_2 \cdot 6H_2O + 5Al(NO_3)_3 \cdot 6H_2O + CH_6N_4O \rightarrow NiO + NiAl_2O_4 + Ni_2Al_3 + 27NO_2 + CO_2 + 72H_2O + 3O_2$ : *Carbohydrazide*

$2Ni(NO_3)_2 \cdot 6H_2O + 4Al(NO_3)_3 \cdot 6H_2O + CH_4N_2O \rightarrow NiO + NiAl_2O_4 + Al_2O_3 + 18NO_2 + CO_2 + 50H_2O + \frac{1}{2}O_2$ : *Urea*

$6Ni(NO_3)_2 \cdot 6H_2O + 8Al(NO_3)_3 \cdot 6H_2O + C_2H_5NO_2 \rightarrow Ni + NiO + NiAl_2O_4 + Al_2O_3 + Ni_2Al_3 + NiAl + 36NO_2 + NO + 2CO_2 + \frac{221}{2}H_2O + \frac{45}{4}O_2$ : *Glycine*

The temperature profiles of nanomaterials during synthesis were monitored and the results are presented on Figure 7.3.

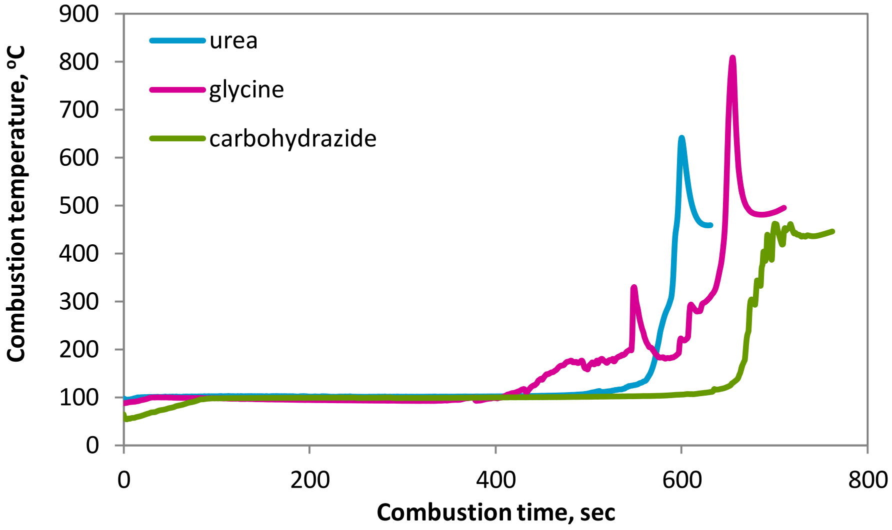

Figure 7.3. Time of combustion as a function of recorded temperature during combustion using three different fuels.

Figure 7.3 illustrates the measured temperature during synthesis for the three organic substances. Carbohydrazide is burned slowly and the reached combustion temperature is low compared to the other two fuels. Thus, there is a lot of residual carbon that has not been burnt during the SCS. This quantity of residual carbon reacts with aluminium oxide and as a result the final product is enriched with Ni-Al intermetallics. Urea has an average combustion temperature, but it possesses only one carbon atom in its molecule. Due to the high combustion temperature it is completely burned out quickly, and thus, there is not enough available time for the reduction of alumina and nickel oxide.

### *7.1.3. Conclusions*

Glycine appears to be ideal amongst the examined substances, as it has two carbon atoms in its molecule and resulted in the highest combustion temperature providing high enough temperature for the soot reduction to take place. The two carbon atoms provide enough carbon for the reaction of Ni-Al intermetallics formation through the reduction of alumina and nickel oxide from carbon, while the highest combustion temperature provided high enough temperature for the reduction to take place. Furthermore, it is possible that in the chosen conditions with glycine as fuel, there is an optimum ratio between ammonia and nitric acid that react and produce hydrogen that is used for the further reduction of nickel oxide for the final synthesis of metallic nickel.

## 7.2. Solution Combustion Synthesis catalysts based on the Ni-Al system

The results presented here have been published as: O. Thoda, G. Xanthopoulou, G. Vekinis, A. Chroneos, *Catalysis Letters, 2018, 148,* 764–778.

### *7.2.1. Catalysts preparation*

The initial solution used for the SC Synthesis of the materials studied in this work consisted of mixtures of nickel nitrate hexahydrate [$Ni(NO_3)_2{\cdot}6H_2O$] and aluminium nitrate nonahydrate [$Al(NO_3)_3{\cdot}9H_2O$] as oxidizers and glycine  as the reducer. Four compositions were studied with different concentration of oxidizers in the SCS solution. The concentrations studied were based on 20%, 40%, 60% and 80% nickel nitrate monohydrate as a percentage of both oxidizers' total amount. The total solid mass of both oxidizers was 10g and the solid mass of the reducing agent was 4g (40wt%). The solid mixture was then dissolved in 75ml of distilled water and each solution was pre-heated in a borosilicate glass beaker on a hot plate with mild magnetic stirring until the temperature reached 70$^o$C. At that point the beaker is placed in a pre-heated furnace at 500$^o$C in air atmosphere and once SCS is completed, the beaker is removed from the furnace and allowed to cool at room temperature.

### *7.2.2. Structural analysis*

The development of the various phases in the materials produced by SCS is shown in the XRD patterns shown in Figure 7.4. The catalysts shown were made with a solution of various concentrations of nickel nitrate and aluminium nitrate, 40% glycine and 75ml of distilled water.

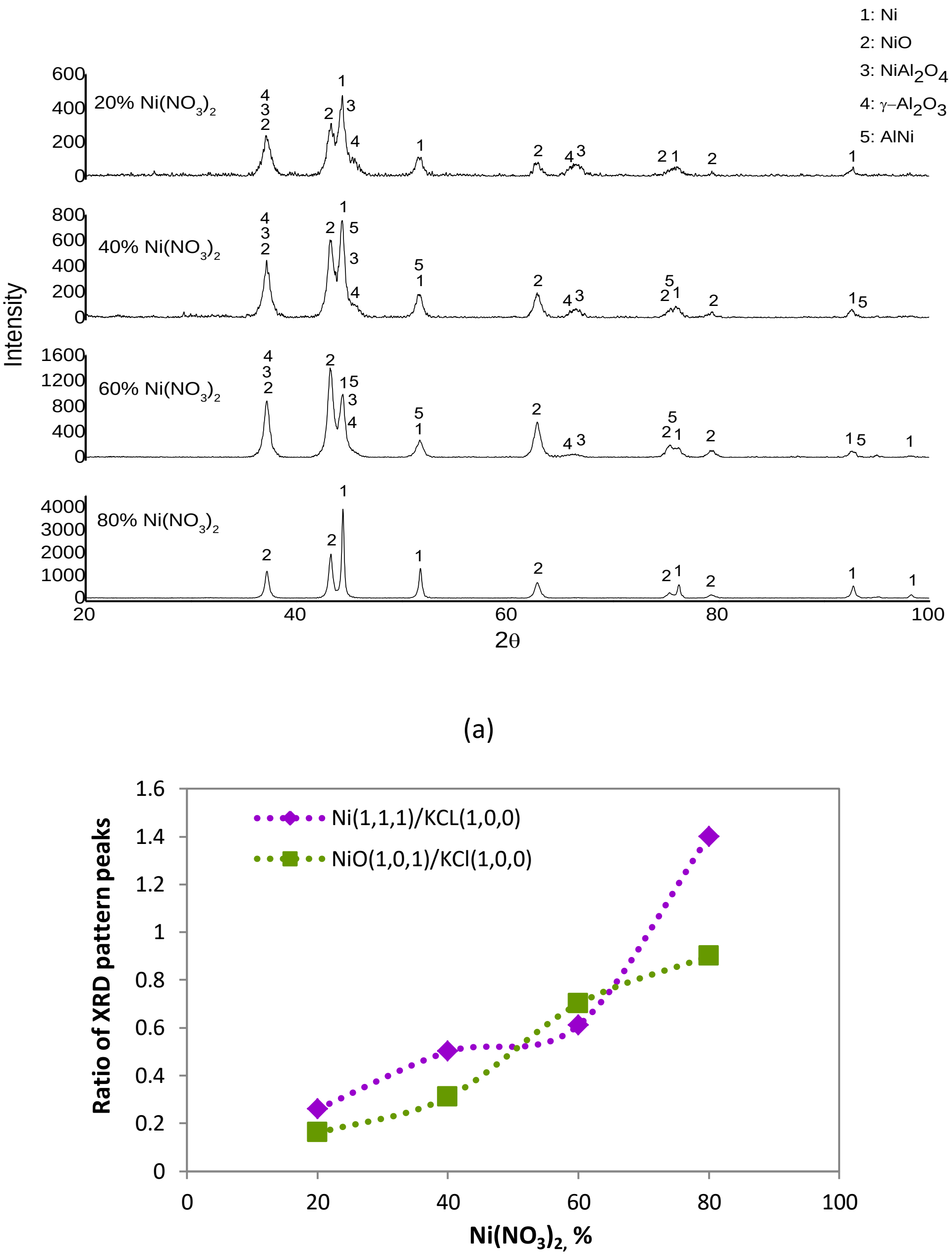

(a)

(b)

Figure 7.4. Development of crystal structure of SCS catalysts (a) and semi-quantitative analysis (b) of Ni and NiO on the basis of initial composition of $Ni(NO_3)_2$, $Al(NO_3)_3$, 40% glycine and 75ml distilled $H_2O$.

The relative phase composition of Ni and NiO, as determined by the comparative XRD analysis, as a function of nickel nitrate concentration in the initial SCS solution are presented in Figure 7.4b where the variation between Ni/KCl and NiO/KCl are shown together for comparison. The products that did not have clear peak in the XRD spectra were not analyzed and are not presented.

Figure 7.4b shows that the maximum nickel content in the SCS products occurs at the position of the maximum nickel oxide content when the amount of nickel nitrate concentration is also maximum in the initial SCS mixture. As expected, the quantity of both Ni and NiO increases by increasing the $Ni(NO_3)_2$ initial concentration.

Each catalyst tested has different phase composition depending upon the ratio between $Ni(NO_3)_2$ and $Al(NO_3)_3$ in the initial SCS mixture. However, cubic Ni and NiO were detected in all catalysts studied. These products are the result of the following multi-branch reaction cascade:

$Ni(NO_3)_2 \cdot 6H_2O \xrightarrow{54℃} Ni(NO_3)_2 \cdot 4H_2O \xrightarrow{85.4℃} Ni(NO_3)_2 \cdot 2H_2O$ (i)

$Al(NO_3)_3 \cdot 9H_2O \xrightarrow{130℃} Al(NO_3)_3 \xrightarrow{200℃} \frac{1}{2}Al_2O_3 + \frac{3}{2}NO_2 + \frac{3}{2}NO + \frac{3}{2}O_2$ (ii) [329]

$Ni(NO_3)_2 \cdot 6H_2O + C_2H_5NO_2 \rightarrow Ni + NiO + NO_2 + 2NO + N_2 + 2CO_2 + \frac{29}{2}H_2O + \frac{5}{2}O_2$ (iii)

$6Al(NO_3)_3 \cdot 9H_2O + 10C_2H_5NO_2 \rightarrow 3Al_2O_3 + 14N_2 + 20CO_2 + 79H_2O$ (iv) [330]

$Ni(NO_3)_2 \cdot 6H_2O \rightarrow NiO + NO_2 + NO + 3O_2 + 6H_2O$ (v)

$Ni(NO_3)(OH)_{2.5} \cdot H_2O \rightarrow 0.5Ni_2O_3 + HNO_3 + 1.25H_2O$ (vi) [76]

$CH_2NH_2COOH \rightarrow [CH_2COO]^- + NH_3$ (vii) [76]

$HNO_3 + \frac{7}{3}NH_3 \rightarrow 3H_2O + \frac{5}{3}N_2 + H_2$ (viii) [76]

$2NH_3 \xrightarrow{Ni} 3H_2 + N_2$ (ix) [323]

$NiO + H_2 \rightarrow Ni + H_2O$ (x)

$Ni + O_2 \rightarrow NiO + \frac{1}{2}O_2$ (xi)

$2CH_2NH_2COOH + 6O_2 \rightarrow 4CO_2 + 5H_2O + NO + NO_2$ (xii)

$$CH_2NH_2COOH + \frac{5}{2}O_2 \rightarrow C + CO + NO + 5H_2O \qquad \text{(xiii)}$$

$$Al_2O_3 + 3C + 2Ni \rightarrow 2NiAl + 3CO \qquad \text{(xiv)}^{[331]}$$

At the $Al_2O_3$ interface:

$$3Al_2O_3 + 2Ni^{+} \rightarrow 2NiAl_2O_4 + 2Al^{3+} + \frac{1}{2}O_2 \qquad \text{(xv)}^{[332]}$$

At the NiO interface:

$$3Al^{3+} + 3NiO + \frac{1}{2}O_2 \rightarrow NiAl_2O_4 + 2Ni^{2+} \qquad \text{(xvi)}^{[332]}$$

Generally, a compound's formation tendency increases with decreasing of Gibb's free energy. Gibb's free energies of γ-$Al_2O_3$ (-211.7 kJ/mol) and NiO (-155 kJ/mol) are lower than those of NiAl (-133.0 kJ/mol) and $NiAl_2O_4$ (-57.9 kJ/mol). Therefore, the complexity of the multiple reactions taking place simultaneously during the combustion, in both gas and aqueous phase, complicates the absolute determination of which reaction is favoured and the electrochemical studies helped to clarify this. The existence of alumina in the final products composition, which is a well-known carrier, suggests that it could act as a carrier for nickel and other active phases. Moreover, the role of NiO as a possible carrier for catalysts active phases has been investigated in previous chapter.

SEM images of the microstructure of the SCS catalysts with the corresponding EDX (energy dispersive X-ray spectroscopy) spectra are presented in Figures 7.5-7.8. The existence of all phases detected in XRD patterns was confirmed and elemental analysis on various areas of the examined samples shed light on the catalysts' co-existing phases. The Au element that is shown in all EDX analyses came from the gold-spatter deposition.

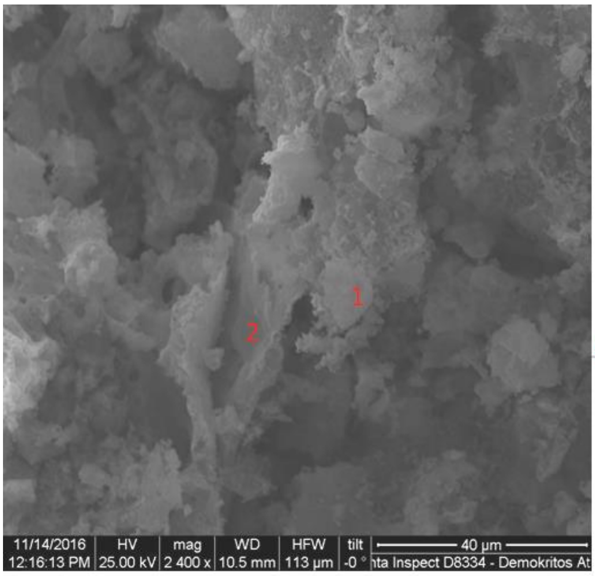

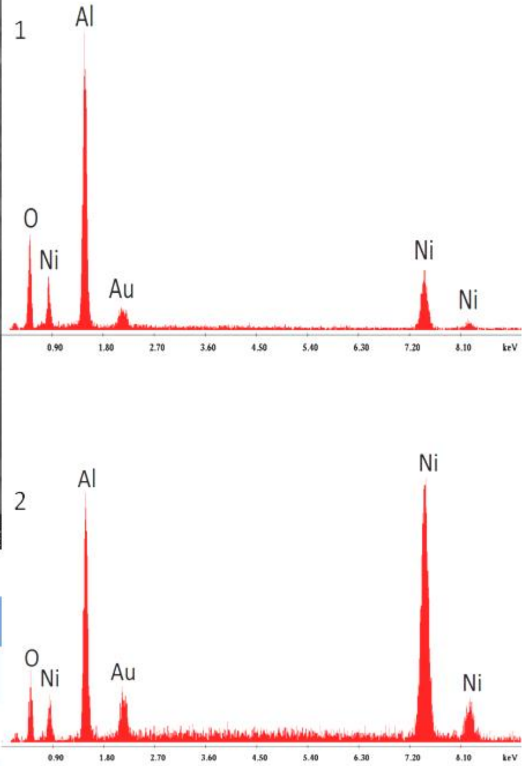

| 1 | | | 2 | | |
|---|---|---|---|---|---|
| **Element** | **Wt%** | **At %** | **Element** | **Wt%** | **At%** |
| Ni | 27.24 | 12.14 | Ni | 63.23 | 40.60 |
| Al | 46.80 | 45.40 | Al | 28.41 | 39.70 |
| O | 25.96 | 42.46 | O | 8.36 | 19.70 |

Figure 7.5. SEM image, EDX and elemental analysis of Ni-Al-O spinels on the basis of initial SCS mixture of 20% $Ni(NO_3)_2$, 80% $Al(NO_3)_3$, 40% glycine and 75ml distilled $H_2O$.

Figure 7.5 depicts the EDX spectrum of the nanoparticles and gives quantitative information of their chemical composition, which confirms the existence of Ni-Al-O spinel in two different stages of formation. The $Al(NO_3)_3/Ni(NO_3)_2$ ratio in this sample is close to the calculated stoichiometric ratio for the production of $NiAl_2O_4$ spinel. This is probably why $NiAl_2O_4$ spinel was found to be in the highest concentration in this sample, compared to the other samples examined.

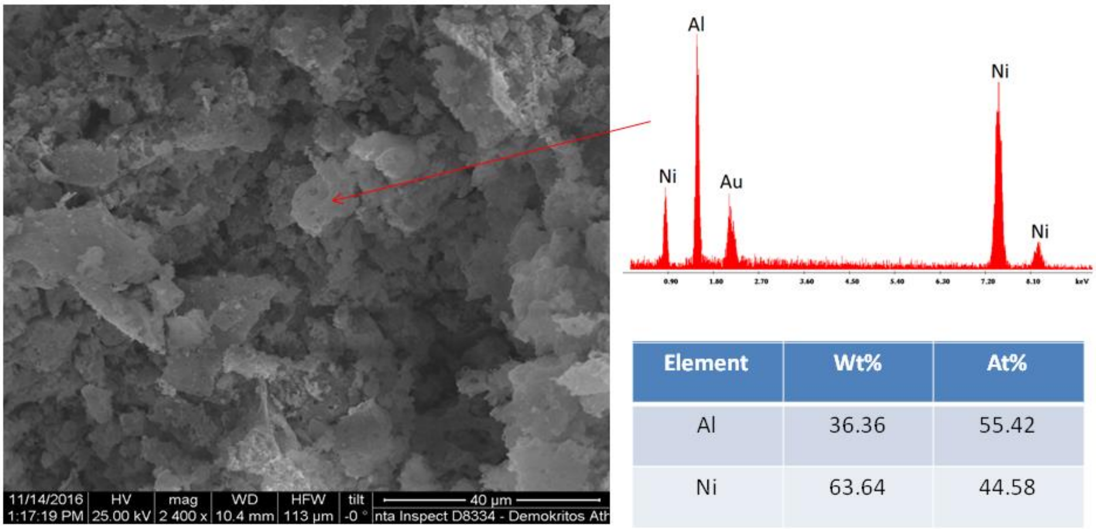

| Element | Wt% | At% |
|---|---|---|
| Al | 36.36 | 55.42 |
| Ni | 63.64 | 44.58 |

Figure 7.6. SEM image, EDX and elemental analysis of Ni-Al alloy in SCS catalyst on the basis of initial SCS mixture 40% $Ni(NO_3)_2$, 60% $Al(NO_3)_3$, 40% glycine and 75ml distilled $H_2O$.

The SEM image with the corresponding EDX and quantitative analysis in Figure 7.6 confirms the existence of Ni and Al elements with a Ni/Al ratio closer to 1:1 in the sample. This finding is consistent to the XRD analysis data and further confirms the formation of NiAl. Complementary, the calculated stoichiometry for NiAl synthesis is cited between 1.5 and 0.9 $Al(NO_3)_3/Ni(NO_3)_2$ ratio and this results in maximum concentration of NiAl in this sample.

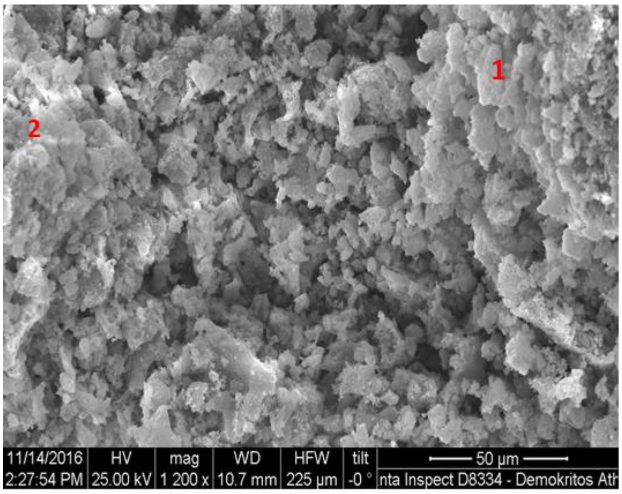

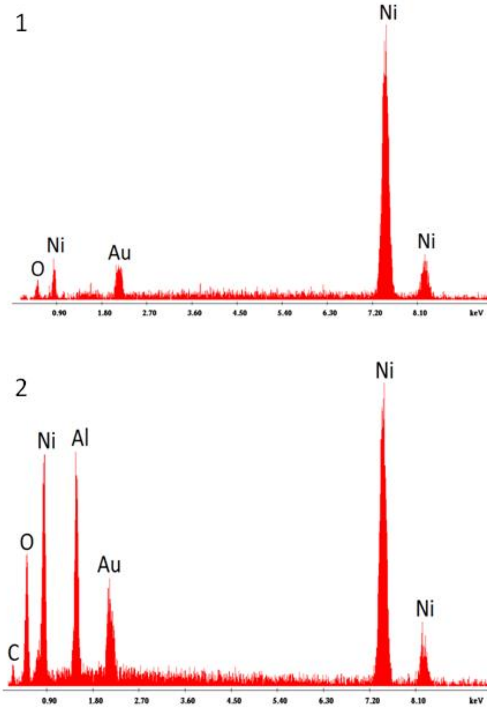

2

| Element | Wt% | At% |
|---|---|---|
| Ni | 62.18 | 36.97 |
| Al | 21.96 | 28.41 |
| O | 15.87 | 34.62 |

Figure 7.7. SEM image, EDX and elemental analysis of Ni and Ni-Al-O phases in SCS catalyst on the basis of initial SCS mixture 60% $Ni(NO_3)_2$, 40% $Al(NO_3)_3$, 40% glycine and 75ml distilled $H_2O$.

In Figure 7.7, two different areas were analysed. The first one was found to be mostly cubic nickel with traces of NiO. The second analyzed area is more complicated as it contains Ni, Al, O and traces of carbon. In accordance with the quantitative analysis included in Figure 7.7 and the sample's XRD pattern, the second area is possibly a mixture of Ni-Al-O spinel with NiO and NiAl.

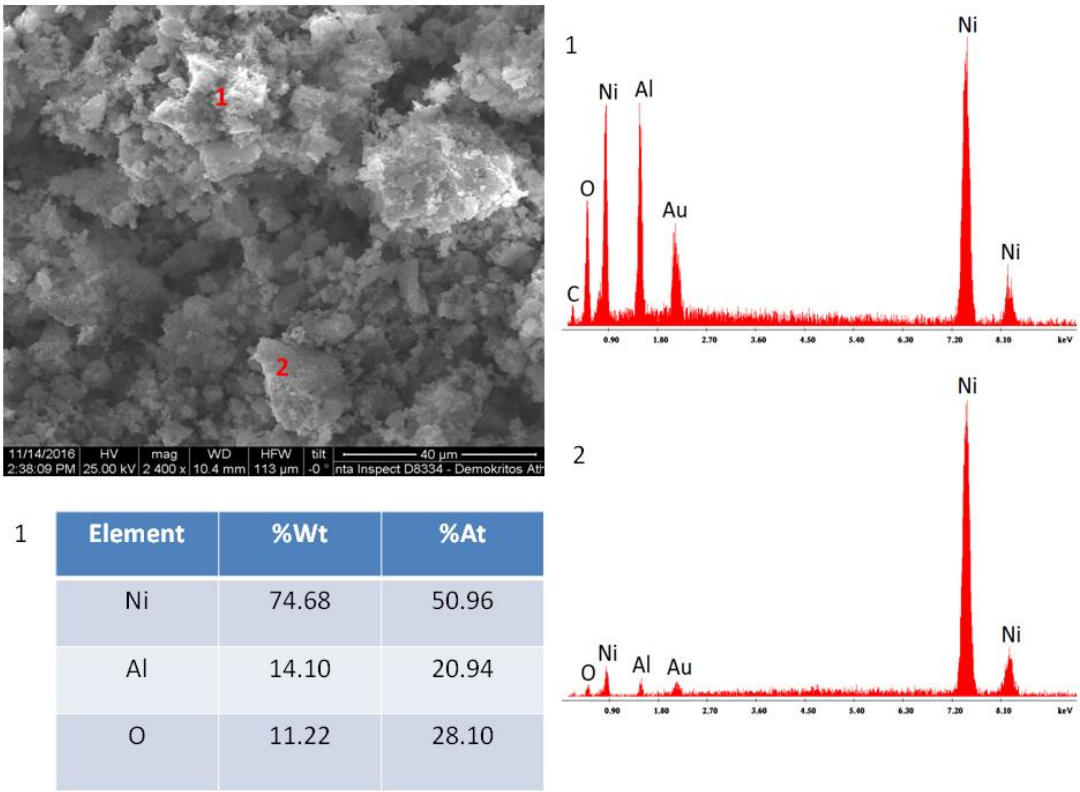

1

| Element | %Wt | %At |
|---|---|---|
| Ni | 74.68 | 50.96 |
| Al | 14.10 | 20.94 |
| O | 11.22 | 28.10 |

Figure 7.8. SEM image, EDX and elemental analysis of metallic Ni and Ni-Al-O phases in SCS catalyst on the basis of initial SCS mixture of 80% $Ni(NO_3)_2$, 20% $Al(NO_3)_3$, 40% glycine and 75ml distilled $H_2O$.

Finally, Figure 7.8 shows the results of analyses also of two different areas of the analyzed sample. The first area examined by EDX showed that there is a mixture of oxides (NiO & γ-$Al_2O_3$) co-existing with non-stoichiometric Ni-Al-O spinel. The rapid cooling after synthesis doesn’t provide enough time for the spinel to form. This is caused by the large amounts of gases ($N_2$, NO, $NO_2$, CO, $CO_2$, $H_2$) that are generated during SCS from the reactions ii, iii, iv, v, viii, ix, xii, xiii and xiv especially in this case.

The concentration of carbon monoxide in gaseous products during glycine’s combustion and during Solution Combustion Synthesis in the Ni-Al system is presented in Figure 7.9 below.

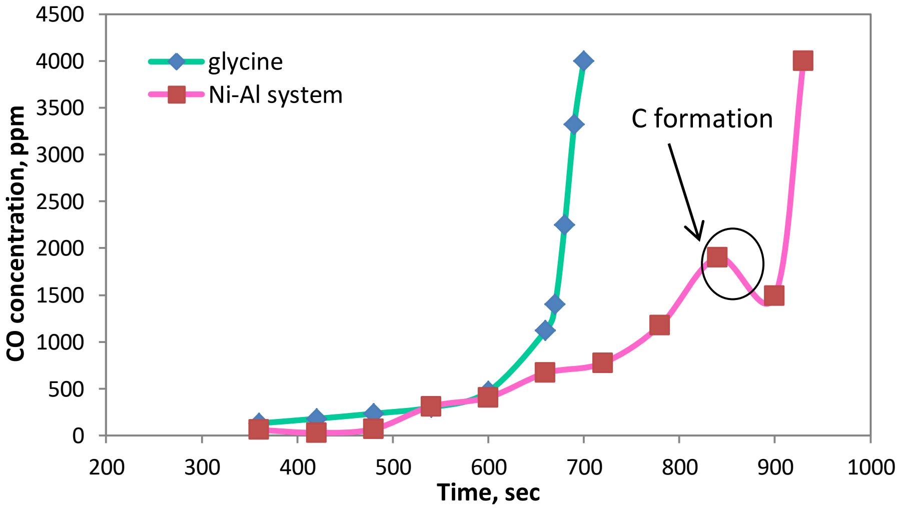

Figure 7.9. CO concentration in gas products measured during glycine combustion & SCS of Ni-Al system [initial composition: 60% $Ni(NO_3)_2$, 40% $Al(NO_3)_3$, 40% glycine, 75ml $H_2O$].

As shown in Figure 7.9 there is a delay in Ni-Al system's start up point, due to the many reactions that take place simultaneously compared to glycine's combustion. In the Ni-Al system, glycine participates in both its oxidation and in the reactions with the nitrates. Glycine is only partially oxidized until the local maximum on Ni-Al system's curve. During the decomposition of nitrates there is no oxygen diffusion in the reaction zone due to intensive gas formation and that results in carbon formation, which is yielded from the point that the curve exhibits the local maximum until the local minimum. Once the nitrates' decomposition is finished, the oxygen diffusion increases significantly. Thus, the formed carbon is able to oxidize and that results in curve increasing after its drop. Moreover, after the local minimum, the reaction (xiv) contributes to the Ni-Al curve's increase, as it synthesizes carbon monoxide as a gas product.

Bragg's and Scherrer's formulas for XRD were used to determine the crystal lattice spacing and crystallite size of Ni and NiO which are shown in Figure 7.10 against SCS initial composition.

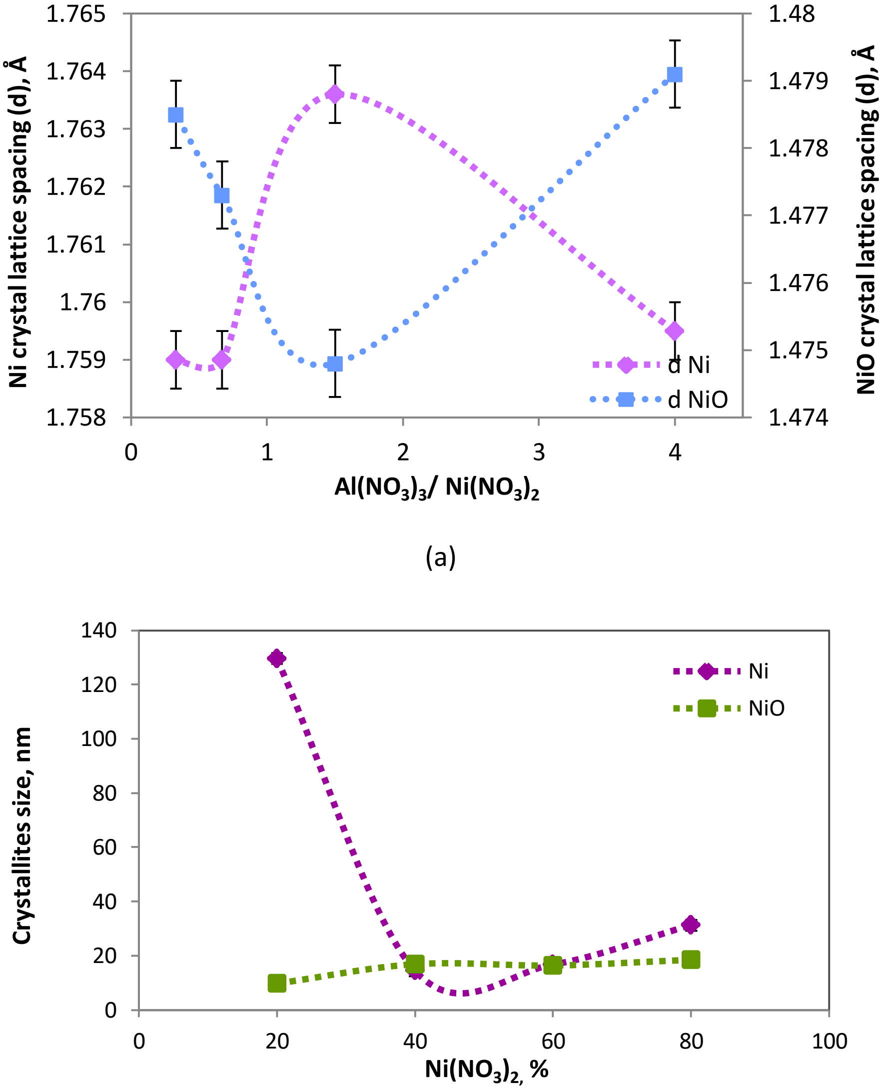

(a)

(b)

Figure 7.10. Influence of the concentration of reactants in initial SCS solution on Ni & NiO (a) crystal lattice spacing and (b) crystallites size.

As can it be observed in Figure 7.10a, increasing the concentration of nickel nitrate in the initial SCS solution results in small changes in Ni and NiO crystal lattice spacing, which reflect the crystallite nucleation conditions that are present in each case. During heating, the nitrate and glycine transient structures that are formed in the liquid phase before SCS initiates, change which results in different structures of Ni and NiO in the final product. There is a maximum for Ni crystal lattice spacing where aluminium nitrate to nickel nitrate ratio equals to 1.5 (that corresponds to 40% of nickel nitrate in the initial SCS mixture), which indicates more organised structures and it is the preferable concentration ratio for Ni synthesis.

The influence of initial composition on the crystallite size of Ni and NiO is shown in Figure 7.10b. In general, the smaller the nickel crystallites form during combustion, the better the dispersion of the metallic phase on the NiO. At 40% nickel nitrate, where nickel crystallite size is minimum, the reaction is violent due to fact that is close to stoichiometry. That increases the foaming of the material and thus, the crystallites cannot bond and grow. More than that, the increased gas formation prevents the agglomeration and augments the heat release from the reaction zone. By the increase of nickel nitrate concentration at 80%, the reaction is slower and that provides more time to the nickel particles to agglomerate and their crystallite size to grow. In addition, nickel's melting point is at 1455°C while for nickel oxide is at 1990°C. That signifies easier agglomeration of nickel particles and is illustrated by nickel's higher crystallite size value, compared to nickel oxide, at 20% nickel nitrate. The extent of agglomeration of the crystallites is very important as it influences the catalysts' specific surface area which is critical for catalytic activity.

### *7.2.3. Temperature profiles of catalysts*

Thermal measurements concerning the combustion temperature were occurred and they are presented on Figure 7.11.

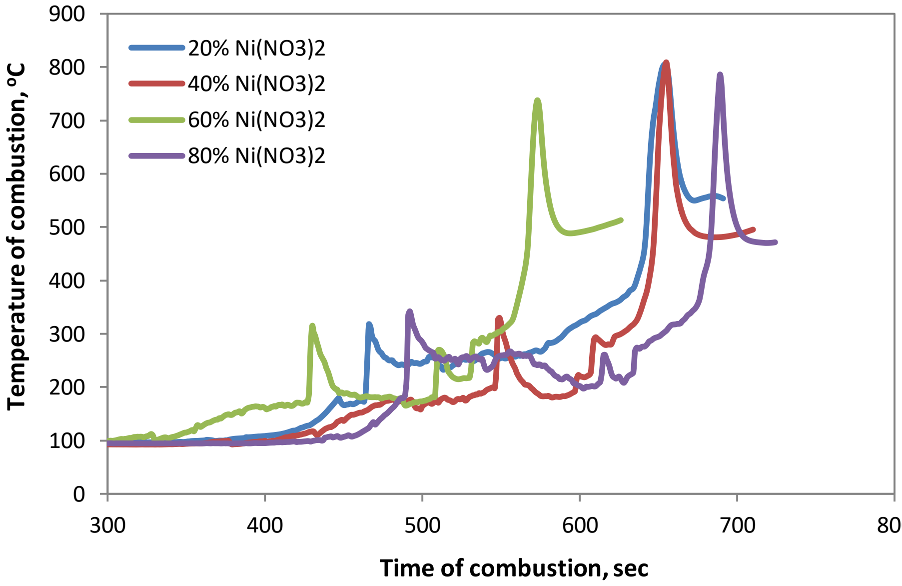

Figure 7.11. Dependence of SCS Ni-Al catalysts' combustion temperature as a function of reaction time.

Despite the fact that the initial preheating temperature of the furnace was 500°C, the combustion temperature of the examined samples is significantly higher. The exothermic reactions that take place during Solution Combustion Synthesis as well as the glycine's (which also participates to SCS reactions) combustion raise the combustion temperature. In all curves presented on Figure 6.90, three peaks are standing out. The first concerns the glycine's oxidation (reactions xii & xiii), the second peak represents the reduction of nickel oxide to produce nickel (reaction x) and the last peak is attributed to the reaction between aluminium oxide and Ni for the NiAl formation (reaction xiv).

### *7.2.4. Pore analysis and surface area measurements*

Brunauer–Emmett–Teller (BET) analysis was used to perform measurements concerning the samples' pore shape, pore volume and specific surface area. The results are presented in Figures 7.12 and 7.13 including the most important - for catalysis - calculated parameters of the samples' nano-particles.

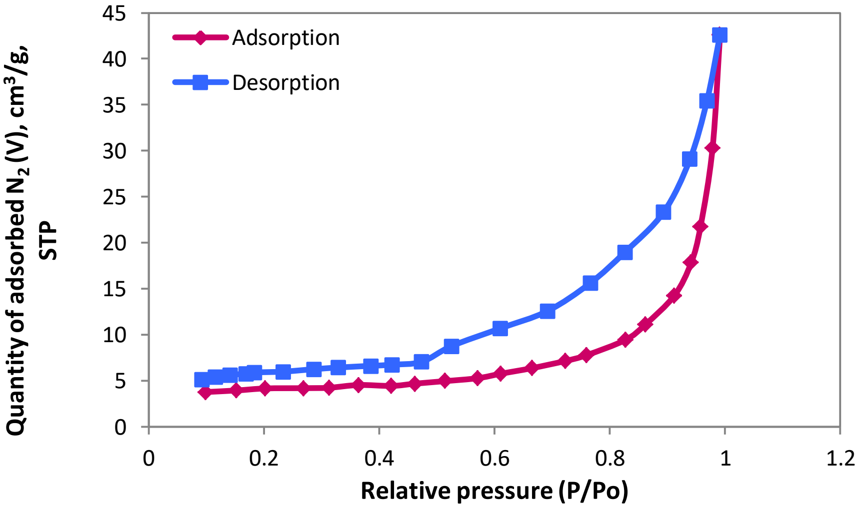

(a)

Figure 7.12. a) Hysteresis curve on the basis of initial mixture $Ni(NO_3)_2$, $Al(NO_3)_3$, 40% glycine, 75ml $H_2O$.

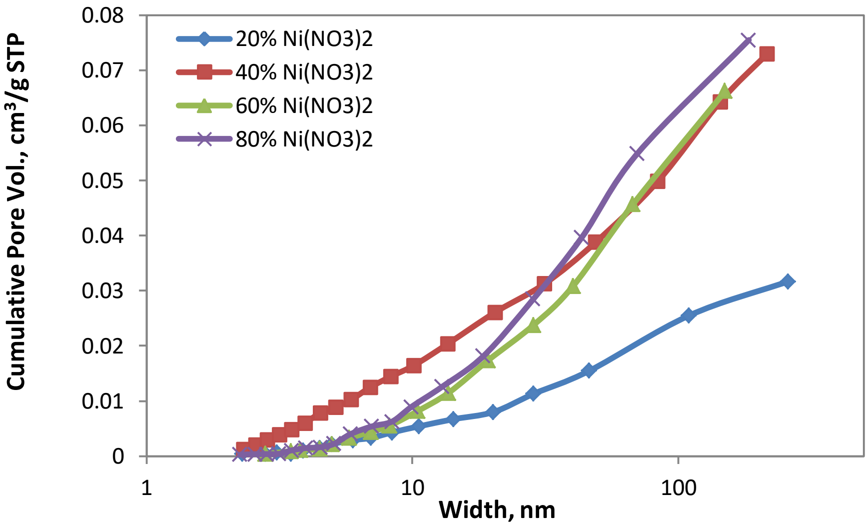

(b)

Figure 7.12. b) BJH adsorption pore volume on the basis of initial mixture $Ni(NO_3)_2$, $Al(NO_3)_3$, 40% glycine, 75ml $H_2O$.

Adsorption-desorption curves obtained by the BET method are shown in Figure 7.12a, where a representative example of the hysteresis curve of a SCS catalyst can be seen. It appears to be a type V isotherm with type H3 hysteresis loop according to IUPAC classification [302]. Typically, type V isotherms are characterized by the uncontrolled formation of the multilayer. It appears that the final nano-structrured product consists of aggregates of plate-like particles forming slit-like pores. The form of the pores affects heat release during SCS, the cooling rate after SCS, hydrogen adsorption-desorption and subsequently the catalysts' catalytic behaviour. Figure 7.12b shows the BJH adsorption pore volume for the four samples prepared with different ratio between nickel nitrate and aluminium nitrate in the SCS initial mixture.

According to pore size measurements that are demonstrated on Figure 7.12b, at 40% nickel nitrate in the initial SCS solution, the concentration of nanopores is utmost, as for this concentration the nickel's crystallite size is minimum and thus the agglomeration is decreased. On the other hand, at the concentration (20% nickel nitrate) close to stoichiometry for the spinel $NiAl_2O_4$ formation, which is an endothermic reaction, the system's energy is lower and results in low rate formation of the pores. In addition to that, the maximum concentration of aluminium nitrate increases the gas formation during combustion synthesis, as it has more crystal lattice water than nickel nitrate. For 80% nickel nitrate concentration, the reaction rate is lower and so do the gas formation and the water evaporation. In this way, there is more time for the pore formation, resulting in maximized total porosity.

Figure 7.13 presents specific surface area measurements as a function of the nickel nitrate concentration in the initial solution of SCS. Specific surface area shows an increasing trend until 60% nickel nitrate concentration where it reaches its maximum value.

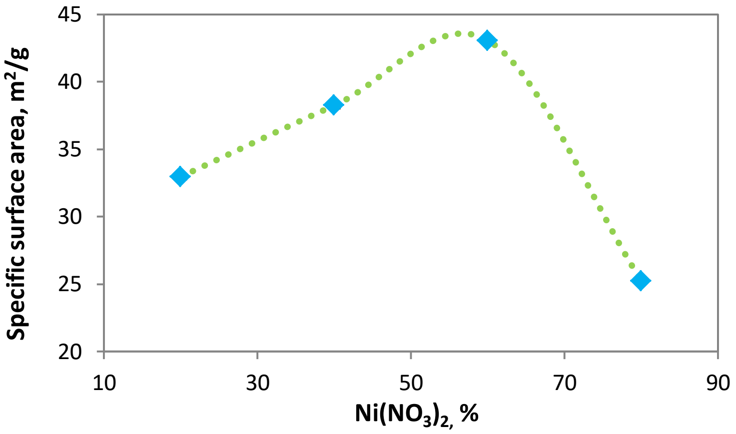

| Catalyst | Cumulative Surface Area of Pores, $S_{BJH}$ | Cumulative Pore Volume of Pores, $V_{BJH}$ | Average Pore Diameter, $d_{BJH}$ |
|---|---|---|---|
| 20% $Ni(NO_3)_2$ | 32.97 $m^2/g$ | 0.03 $cm^3/g$ | 18.3 nm |
| 40% $Ni(NO_3)_2$ | 38.24 $m^2/g$ | 0.07 $cm^3/g$ | 12.5 nm |
| 60% $Ni(NO_3)_2$ | 43.06 $m^2/g$ | 0.07 $cm^3/g$ | 19.35 nm |
| 80% $Ni(NO_3)_2$ | 25.25 $m^2/g$ | 0.08 $cm^3/g$ | 19.25 nm |

Figure 7.13. Influence of initial nickel nitrate in SCS solution on the specific surface area (SSA) of Ni – Al catalysts and pore structure parameters of Ni-Al-O nanoparticles.

The volume of nanopores, total porosity and the system's temperature are the most important factors that affect severely the specific surface area. From 20% to 40% nickel nitrate, the SSA increases as at 40% the volume of nanopores is maximum, while at 20% the total porosity as well as the volume of nanopores is minimum. Further increase is reached at 60% nickel nitrate, as the combustion temperature is the lowest (Fig.7.11). Conversely, at 80% nickel nitrate the nickel concentration is the highest, which leads to the conclusion that the reduction of nickel oxide to form nickel (reaction x) is favoured. As it is an exothermic reaction, the system's temperature is temporarily increasing leading to the decrease of SSA.

### *7.2.5. Thermogravimetric analysis*

To carry out the temperature-reactions investigation thermogravimetric analysis was used. The TG and DTA curves as a function of heating temperature are presented on Figure 7.14.

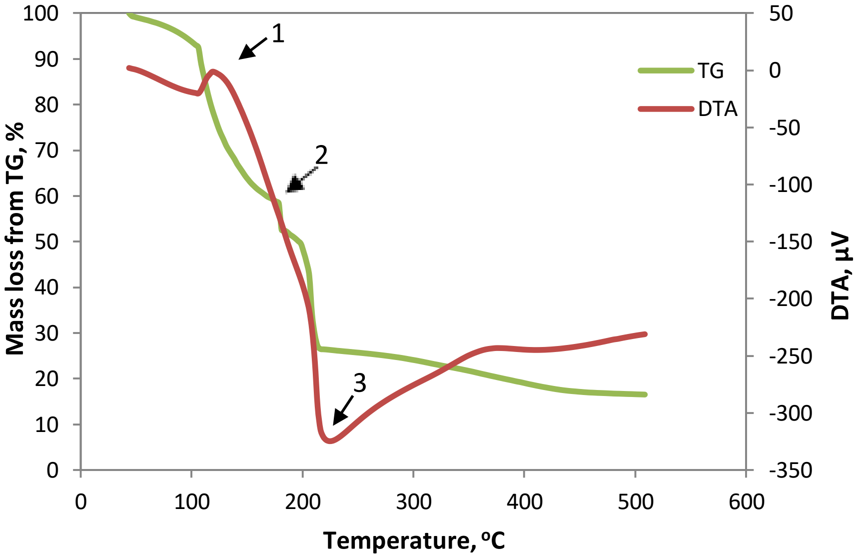

Figure 7.14. TGA of Ni-Al catalyst on the basis of initial mixture 20% $Ni(NO_3)_2$, 80% $Al(NO_3)_3$, 40% glycine, 75ml $H_2O$. Arrows point the positions of decomposition of nitrates (1), combustion of glycine (2) and maximum heat release (3) [Dr. A. Steinman conducted the TGA measurement in National University of Science and Technology "MISIS"].

Thermogravimetric analysis (TGA), presented in Figure 7.14, reveals the temperature regions in which the various SCS reactions and phenomena take place. An endothermic effect is evident at position 1 which is due to the decomposition of the nitrates. After the completion of nitrates decomposition and the loss of all lattice water from nitrates, point 2 signifies the initiation of glycine's combustion. This exothermic reaction provides the system with extra energy for the Solution Combustion reactions' cascade to yield. Point 3 signalizes the maximum heat release from the system while, after that point the DTA curve is becoming smoother. The ongoing glycine reactions as well as the carbon's oxidation reaction release heat to the system after SCS is over and that result in delay of the sample's cooling process.

### *7.2.6. Catalytic studies*

The catalytic activity of the Ni-based SCS catalysts was tested in liquid-phase hydrogenation of maleic acid. The kinetic and conversion curves were obtained until the whole quantity of hydrogen (50ml) was consumed.

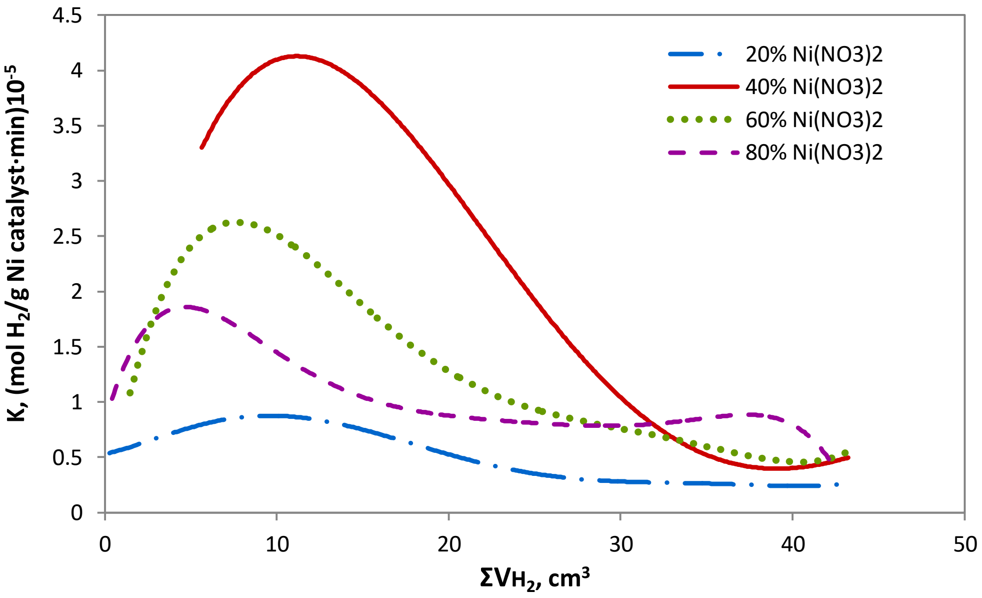

(a)

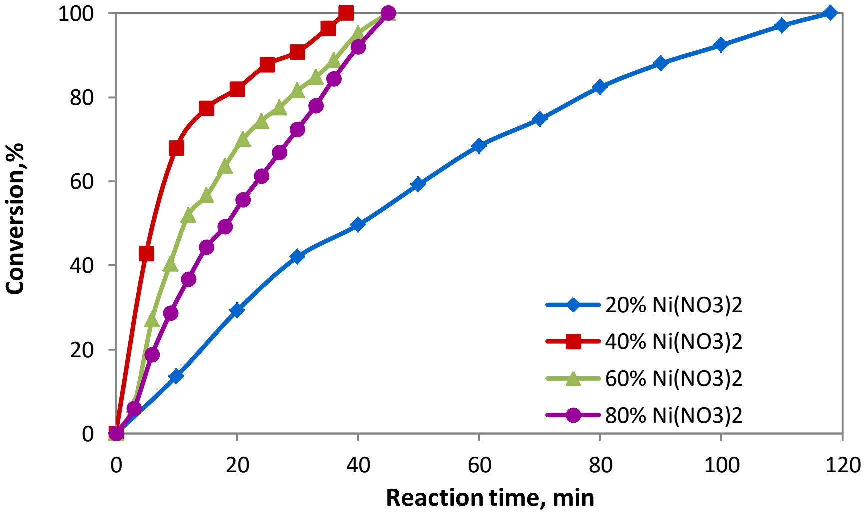

(b)

Figure 7.15. Dependence (a) velocity and (b) conversion of maleic acid hydrogenation on initial SCS concentration.

Kinetics curves of the SCS catalysts with different composition in the initial SCS solution are presented on Figure 7.15. Catalyst with 40% nickel nitrate in the initial mixture appears to be the most active catalyst, while the catalyst with 20% nickel nitrate showed the lowest catalytic activity. Conversion curves of the catalysts are shown as well.

The catalyst with 40% nickel nitrate in the initial solution has the highest rate of maleic acid's conversion to succinic acid. This fact can be easily justified, as the catalyst had the highest concentration of NiAl intermetallic compounds (as determined from SEM/EDX analysis), the maximum volume of nanopores (Fig.7.12b) as well as the lowest crystallite size (Fig.7.10). Second best catalyst (60% nickel nitrate) had also high concentration of NiAl intermetallic compounds and the highest specific surface area (Fig.7.13). The next, in the catalytic activity row, catalyst with 80% nickel nitrate in its initial composition has the highest metallic nickel concentration (as calculated by the XRD spectrum – Fig.7.4) and the highest total porosity (Fig.7.12), but the lowest surface area (Fig.7.13). Finally, the catalyst with the lowest catalytic activity and conversion rate (20% nickel nitrate) had the minimum quantity of nickel and nickel oxide as calculated and shown on Figure 7.4 and the lowest volume of pores (Fig.7.12b). There seems to be a cumulative effect of nickel and NiAl intermetallic compound active phases on the activity of SCS catalysts in liquid-phase hydrogenation of maleic acid. NiAl intermetallic compounds have shown catalytic activity in hydrogenation processes, thus their presence in the SCS final product possibly acts complementary to metallic nickel in the calculated catalytic activity.

The catalysts' composition and surface area were checked after hydrogenation and no changes were observed, due to the very mild conditions of reaction that are employed in our work: 80°C with water solvent. Under such conditions sintering or reduction processes cannot take place.

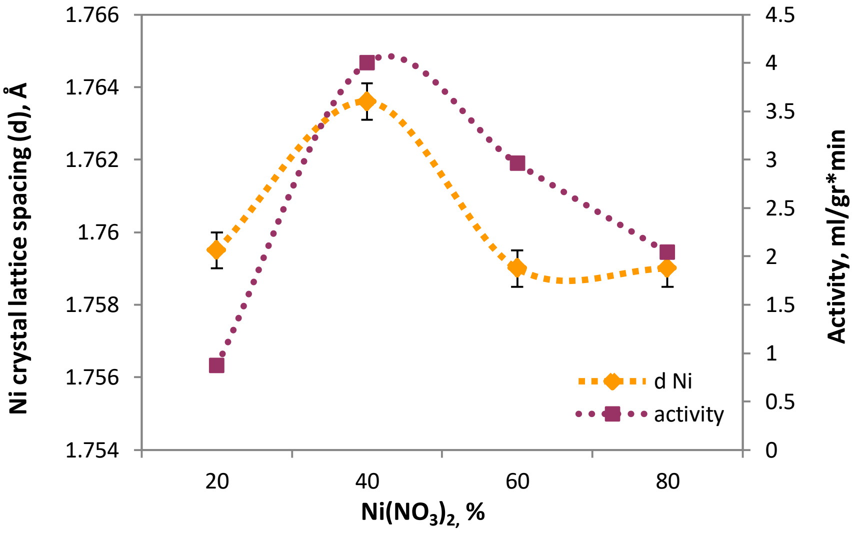

Figure 7.16. Influence of $Ni(NO_3)_2$ concentration on Ni crystal lattice spacing and on the catalysts' activity towards the hydrogenation of maleic acid.

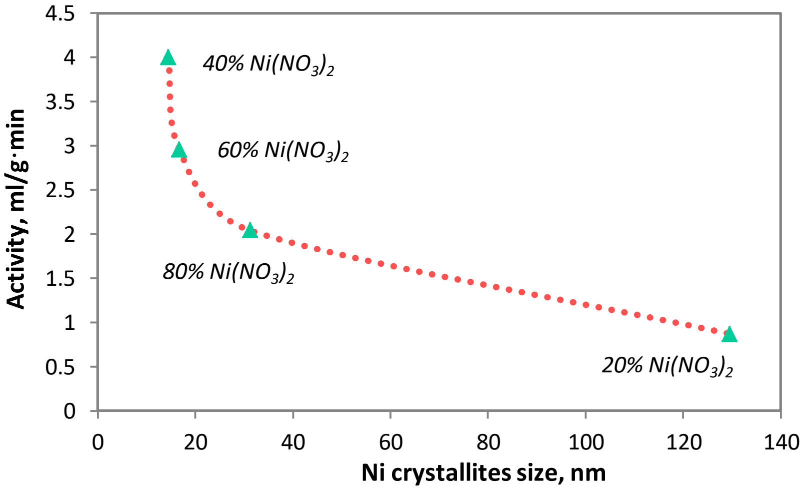

Figure 7.17. Correlation between Ni crystalllites size and catalysts' activity.

Generally, increase of crystal lattice spacing results in high degree of crystallization. The more organized the crystal is the higher the activity is and the obtained results that are presented on Figure 7.16 appear to support this conclusion. 40% nickel nitrate in the initial mixture seems to be the optimum concentration for organized nickel structures. For that concentration the produced catalyst showed the highest activity in maleic acid's hydrogenation. From 60% to 80% concentration of nickel nitrate, nickel's crystal lattice spacing does not change, though the activity drops due to the specific surface area decrease.

The dependence of catalysts' activity in aqueous-phase hydrogenation of maleic acid from nickel's crystallite size is represented as well on Figure 7.17. According to the obtained data, as nickel's crystallite size increases the catalyst's activity lowers. This can be explained as the smaller nickel crystal is, the better the dispersion of the metallic phase gets. In this way, there is higher possibility for defect structures to be created, which act as active centres in catalysis. Consequently, the best dispersion of nickel happens for the catalyst with 40% nickel nitrate in the initial SCS solution and this same catalyst appeared the best catalytic behaviour among the tested ones.

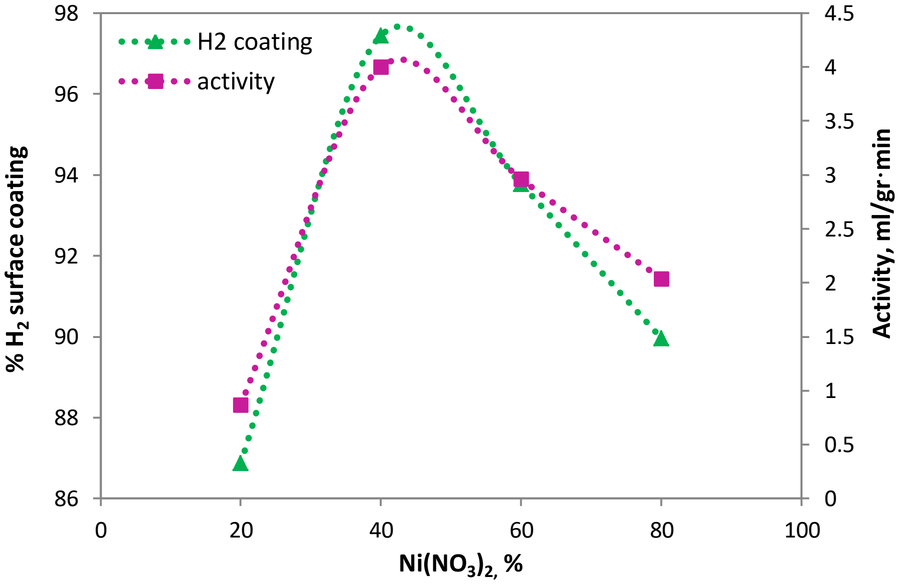

Figure 7.18. SCS catalysts' hydrogen surface coating and activity dependence from nickel nitrate concentration in the initial mixture [$Ni(NO_3)_2$, $Al(NO_3)_3$, 40% glycine, 75ml $H_2O$].

The percentage of hydrogen surface coating is a crucial parameter for catalytic activity, considering the fact that all reactions take place on the catalyst's surface. As demonstrated on Figure 7.18, there is absolute accordance of hydrogen surface coating with the catalytic behaviour of the four catalysts tested in liquid-phase hydrogenation of maleic acid. In accordance to the above graph, the optimal concentration for the catalyst's preparation is 40% nickel nitrate in the initial SCS mixture. In other words, that nickel's crystallite size (14.48nm) is the optimum value for hydrogen adsorption. Undoubtedly, concentration of NiAl intermetallic in the catalyst is of the same importance as nickel's concentration.

### *7.2.7. Conclusions*

Catalyst with 40% nickel nitrate in the initial composition has proved to be the best among those tested. This can be attributed to that fact that nickel in this concentration had the higher crystal lattice spacing and the minimum crystallite size. Furthermore, BET analysis showed the maximum volume of nanopores, the smallest average pore diameter as well as very high total porosity and specific surface area for this catalyst.

In conclusion, catalytically active nano-structured catalysts containing nickel, nickel oxide and nickel aluminium alloys were prepared by a novel and rapid one-pot Solution Combustion Synthesis method. The crystallites of Ni and NiO produced are nanosized - Ni less than 130nm and NiO about 20 nm - and their size can be controlled by controlling the SCS combustion temperature. Crystallite size affects the effective specific surface area of the material and thereby the catalytic activity. The method developed also enables the "tuning" of the catalytic performance by adjustment of the Ni crystal lattice plane spacing from 1.757 Å to 1.764 Å by variation of the composition of the initial SCS mixture and the SCS combustion temperature. Catalytic studies of liquid phase hydrogenation of maleic acid using these catalysts showed that the degree of catalysts' surface hydrogen coating, which plays a significant role in the hydrogenation reaction, can also be regulated by adjusting the synthesis parameters. A multistage, cascade-like mechanism of the formation of the Ni-NiAl catalysts was identified which indicates that the one-pot SCS method is general and can be utilized for the preparation of many different types of metal-alloys nanostructures. Particularly, the synthetic strategy has significant potential applications in the preparation other nanocomposite catalysts for engineering highly efficient catalysts.

# 8. Study of catalytic coatings on carriers for future industrial application

## 8.1. Introduction

Solution Combustion Synthesis (SCS) is one of the most efficient techniques used to synthesize high selectivity catalysts directly at the nanoscale [57], including Ni-based catalysts which are widely used in various catalytic processes. Most of the industrial hydrogenation processes use supported catalysts, because, on an industrial scale, fixed-bed reactors are generally used for these types of reactions in the gas phase. Carriers are employed in situations where high demands are placed on the mechanical strength of the catalyst, the active catalytic substance must be present in a thin layer or there is a need to conserve valuable catalyst substances.

One of the prospective methods to prepare nanocatalysts on carrier/substrate is CAFSY method. Combustion-assisted flame spraying ("CAFSY") was recently developed to produce catalytically active nickel aluminide coatings on ceramic substrates [298]. The CAFSY process showed that combustion synthesis occurs both in-flight as well as on the substrate.

## 8.2. In-flight SCS specifications

In this work, Ni-based catalysts were produced by in-flight SCS during flame spraying, a novel method which combines conventional flame spraying and solution combustion synthesis into a single step. A fine spray of the aqueous SCS solution is inserted into the flame wherein the water is evaporated and the SCS catalyst is synthesized rapidly in the flame. The fine particles of nanostructured catalysts are then applied as coating on the $MgAl_2O_4$ carrier and penetrate very efficiently into all the surface pores.

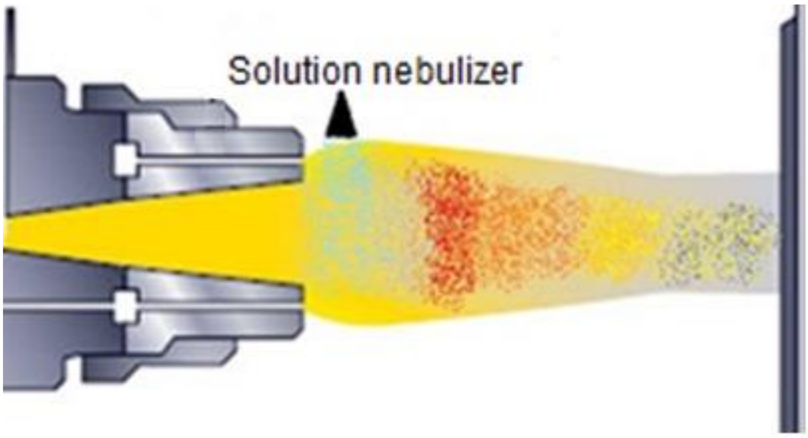

Figure 8.1. Schematic diagram of flame zones during flame spraying.

Four zones are distinguished in the flame (Fig.8.1):

- ☐ Initial SCS solution evaporation
- ☐ Initiation of reactions
- ☐ Completion of reactions
- ☐ Acceleration and impact on the substrate

The solution nebulizer inserts fine droplets directly into the hot zone of the flame. The water is evaporated and the SCS catalyst is synthesized rapidly (few ms) in the flame. The fine particles of nanostructured catalysts are accelerated until they impact and penetrate into the spinel carrier (substrate). The oxyacetylene flame raises the temperature of the solution significantly almost instantaneously which triggers the exothermic SC process within the time available. This is significantly different from previously reported in-flight synthesis of catalysts using added methane gas to induce reaction [333].

The spraying parameters that were applied are:

- $O_2/C_2H_2$=1.18 (oxidizing flame)
- Additional air in the flame=1bar
- Distance (between the gun and the substrate)=10cm
- Spraying duration=2min
- Carrier gas ( the air that flows through the nebulizer)=4bar

The additional air circulates around the flame and keeps it in a specific diameter and acetylene ($C_2H_2$) was chosen due to its ability to reach the highest temperature of the flame.

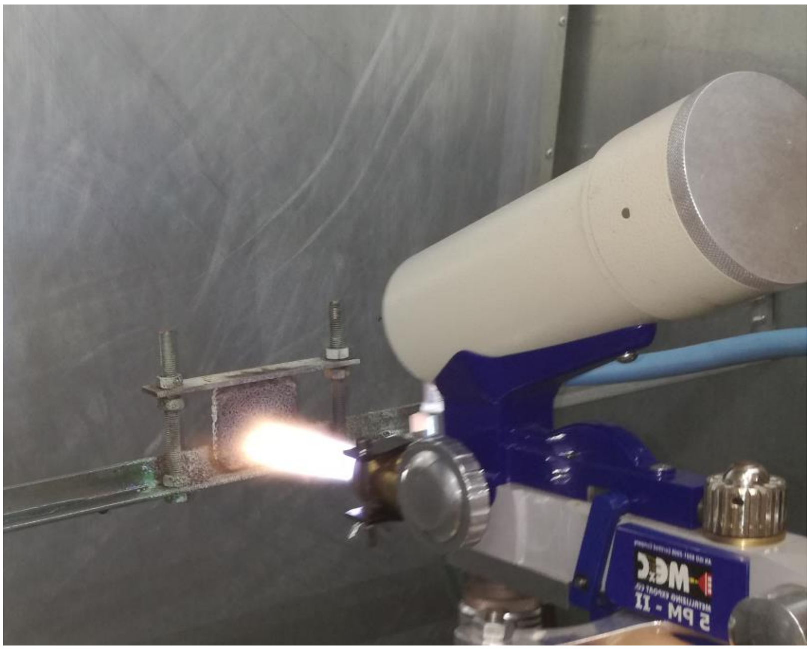

Figure 8.2. In-flight SCS on a ceramic substrate.

## 8.3. Results and discussion

In this attempt, nickel-based nanocatalyst was synthesized by in flight Solution Combustion Synthesis (SCS) from starting solutions of nickel nitrate $Ni(NO_3)_2{\cdot}6H_2O$ with glycine as fuel in the ratio of 2:1. In order to facilitate the homogenization 100ml distilled water was added to the initial SCS mixture. Flame spraying was carried out by a Sulzer's Metco Thermospray Gun (5P-II) and the solution was inserted into the flame using an adjustable nebuliser. The synthesized SCS nano-catalysts were deposited as thin coatings on a ceramic Mg-Al-O carrier previously made by SHS from an initial mixture of 7.41% Al + 8.33% Mg + 39.63% $Mg(NO_3)_2$ + 32.41% $Al_2O_3$+ 4.81% MgO + 7.41% $H_2BO_3$. [334]

The nano-structured catalysts were characterised by SEM, EDAX and XRD analysis in order to characterise their phase composition and morphology.

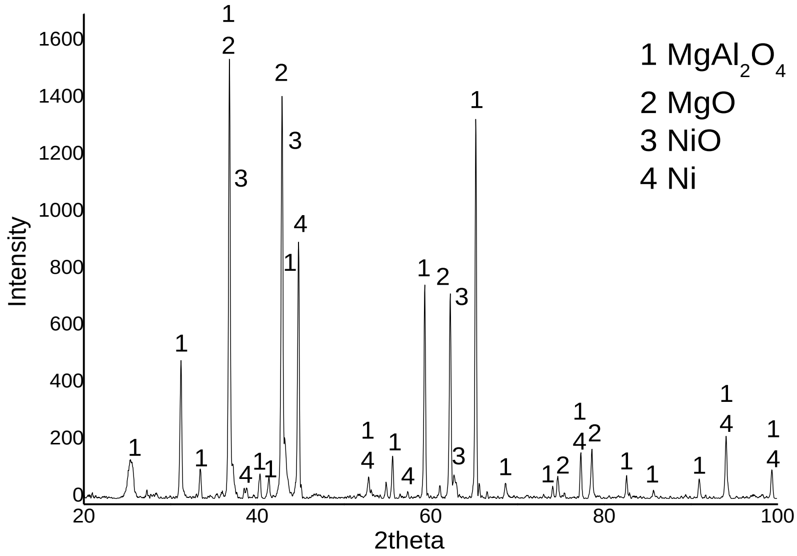

Figure 8.3. XRD pattern of the substrate (Mg-Al-O) with the deposited SCS-derived nanopowder.

XRD analysis (Fig.8.3) shows that the coatings consist of Ni and NiO phases (the other phases shown are from the substrate) which indicates that SCS was completed in-flight. The following reactions take place by in-flight SCS in the flame over times of milliseconds:

$Ni(NO_3)_2 \cdot 6H_2O + C_2H_5NO_2 \rightarrow Ni + NiO + NO_2 + 2NO + N_2 + 2CO_2 + \frac{29}{2}H_2O + \frac{5}{2}O_2$(i)

$Ni(NO_3)_2 \cdot 6H_2O \xrightarrow{54℃} Ni(NO_3)_2 \cdot 4H_2O \xrightarrow{85.4℃} Ni(NO_3)_2 \cdot 2H_2O$ (ii)

$Ni(NO_3)_2 \cdot 6H_2O \rightarrow 2NiO + NO_2 + NO + N_2 + 6H_2O + \frac{7}{2}O_2$ (iii)

$2CH_2NH_2COOH + 6O_2 \rightarrow 4CO_2 + 5H_2O + NO + NO_2$ (iv)

$C_2H_2 + \frac{3}{2}O_2 \rightarrow 2CO + H_2O$ (v)

$C_2H_2 + \frac{5}{2}O_2 \rightarrow 2CO_2 + H_2O$ (vi)

$NiO + C \rightarrow Ni + CO$ (vii) [335]

$NiO + CO \rightarrow Ni + CO_2$ (viii) [336]

$Ni + O_2 \rightarrow NiO + \frac{1}{2}O_2$ (ix)

$Ni(NO_3)(OH)_{2.5} \cdot H_2O \rightarrow 0.5Ni_2O_3 + HNO_3 + 1.25H_2O$ (x)

$CH_2NH_2COOH \rightarrow [CH_2COO]^- + NH_3$ (xi)

$HNO_3 + \frac{7}{3}NH_3 \rightarrow \frac{5}{3}N_2 + H_2 + 3H_2O$ (xii)

$NiO + H_2 \rightarrow Ni + H_2O$ (xiii)

As it can be observed from the chemical equations above, metallic nickel is synthesized from the reduction of nickel oxide reacting with hydrogen, carbon monoxide and carbon. The hydrogen is originated from the reaction between the nitric acid (from nitrates decomposition) and ammonia (from glycine decomposition). In addition, carbon monoxide and carbon dioxide are originated from the combustion of both organic substances (glycine and acetylene). There are various reactions that take place in the flame, thus atmospheric microcells are created. Consequently, the nature of the flame changes locally, depending upon the nature of the reactions that take place. As a result, the localized nature of the flame can change from oxidizing to carburizing or even neutral flame.

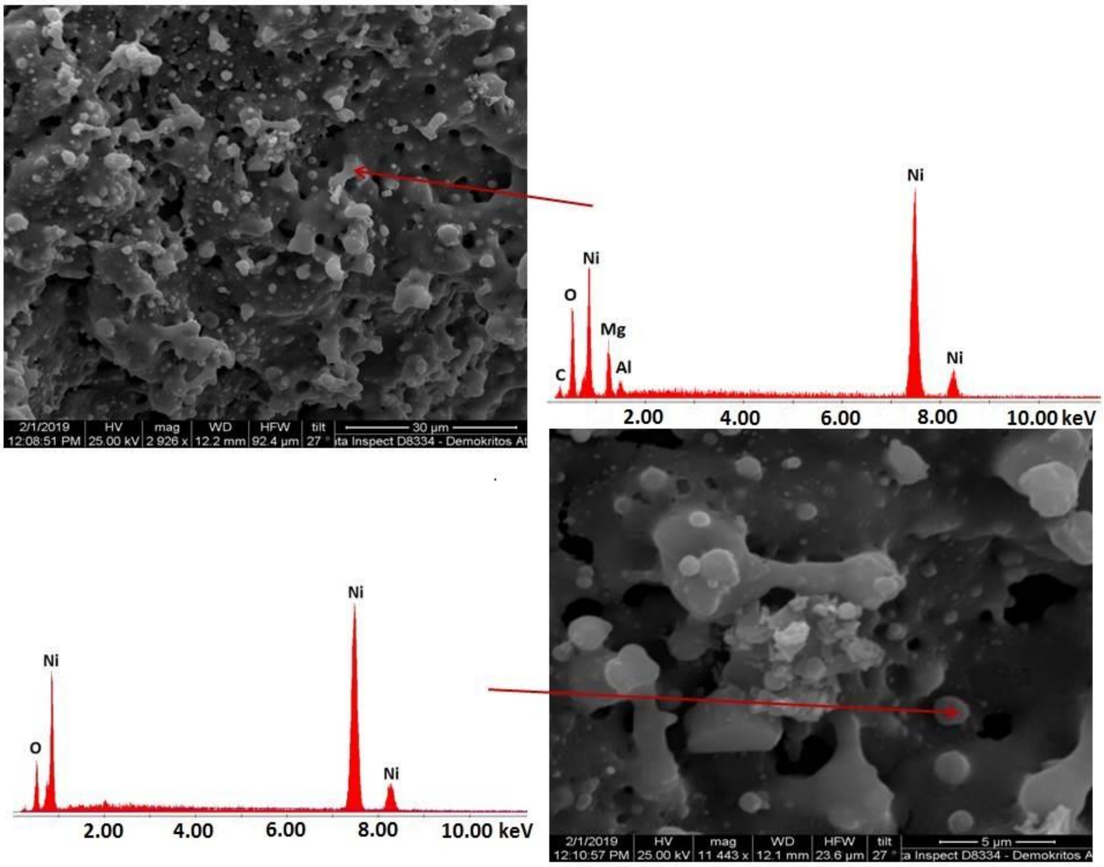

Figure 8.4. a) SEM photos of the surface of the catalyst and EDX analysis.

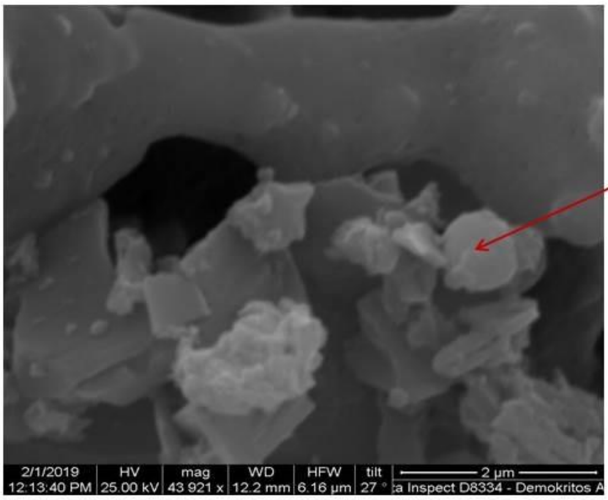

| Element | Wt % | At % |
|---|---|---|
| O | 0.18 | 0.67 |
| Ni | 99.82 | 99.33 |
| Total | 100.00 | 100.00 |

Figure 8.4. b) SEM photo of the surface of the catalyst and quantitative analysis.

SEM microstructural examinations of the surface of the coating (Fig.8.4) confirmed the presence of NiO and Ni phases. The spherical phases are identified by EDX as phases of metallic nickel. Moreover, the as-burnt powder has penetrated into the pores of the employed substrate. The pores of the deposited layer are ranging between the micro and the nanoscale, some of the observed pores are less than micron (~100-1000nm), while the pores of the substrate appear to be open, indicating that the deposited powder did not close its pores. Thus, even after the flame spraying, the as-synthesized coating consists of nanosized material and this method can be considered as new method of production supported catalysts.

BET analysis was employed to reveal the pore size, morphology and distribution as well as its specific surface area. The results of BET analysis using nitrogen as adsorbent are shown in Figures 8.5 and 8.6.

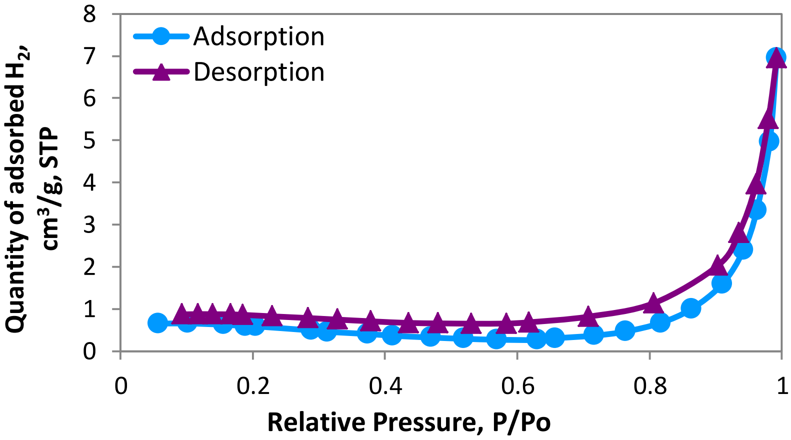

Figure 8.5. Hysteresis curve of the in-flight SCS synthesized material.

The type V isotherm, presented on Figure 8.5 above, indicates uncontrolled formation of the multi-layer followed by capillary condensation [313]. Such structures results because lateral interactions between adsorbed molecules are stronger than those between the measured product and the adsorbate (nitrogen). A characteristic feature of type V isotherm is its hysteresis loop which is associated with capillary condensation taking place in mesopores. Based on the hysteresis loops classification, the obtained adsorption-desorption curves are ranked as type H3. This indicates that the final nano-structured product consists of aggregates of plate-like particles forming slit-like pores. BJH pore analysis was also carried out in the BET surface area analyzer and is presented in Figure 5.

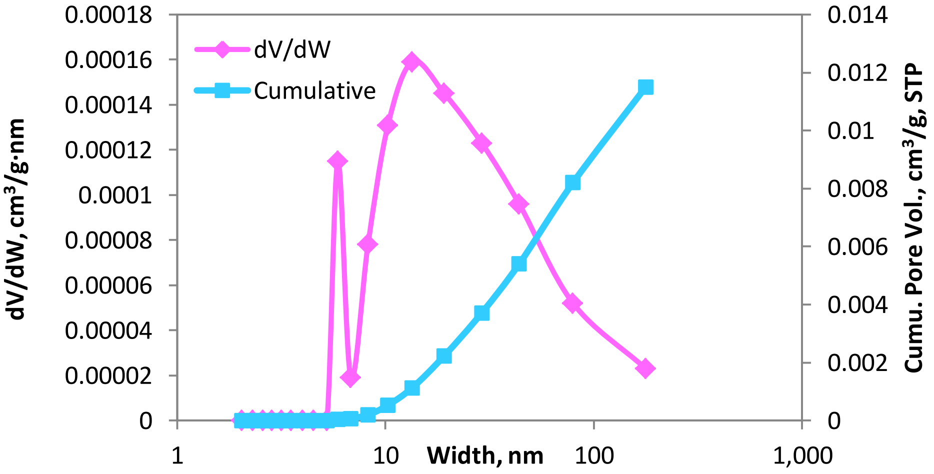

Figure 8.6. BJH pore analysis of in-flight SCS Ni-based nano-catalysts.

The BJH pore size analysis confirms the existence of nano-pores in the SCS Ni-based powder which resulted in a measured specific surface area (SSA) of 2.5m$^2$/g. The substrate's specific surface area was measured to be 2m$^2$/g. The produced powder adopted the substrate's pore morphology while there was a 25% increment in the SSA of the resulting supported catalyst due to the enhanced SSA of the deposited powder. When the same powder was synthesized with the SCS approach, the measured specific surface area was 7.3m$^2$/g and it appears that the catalytic powder synthesized by in-flight SCS had also higher SSA, compared to the SSA of the substrate. Moreover, it is suggested that, in order to increase the resulting SSA, a substrate with a larger SSA should be employed.

The catalytic activity of the Ni-based SCS catalysts discussed above was tested toward the liquid-phase hydrogenation of maleic acid (0.26g of maleic acid for 50ml $H_2$ on 1g of catalyst). Conversion curves of the Ni-based catalysts with and without substrate are shown in Figure

8.7. In both experiments, the conversion curves were obtained for the first twenty minutes of the hydrogenation of maleic acid.

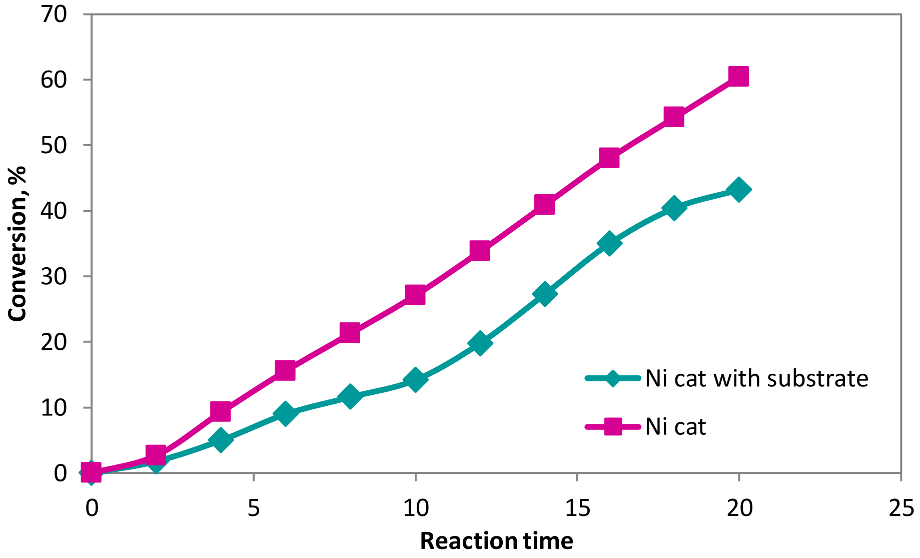

Figure 8.7. The dependence of maleic acid conversion on the SCS catalysts calculated from the quantity of absorbed hydrogen.

The degree of conversion of maleic acid into succinic acid is lower for the catalyst with the substrate. This can be originated to the lower quantity of the active phase in the 1g employed for the experiment. Furthermore, the concentration of nickel on the catalytic surface is lower due to the residuals of the Mg-Al-O and Mg-O phases from the substrate.

## 8.4. Summary

Thus, combustion-assisted flame spraying ("CAFSY") was used for in-flight solution combustion synthesis and developed to produce catalytically active Ni/NiO nanocoatings on ceramic substrate. This can be considered as new method of preparation nanocatalysts on carrier for industrial application.

# 9. Concluding remarks and future work

Solution combustion synthesis meets the demands of material science and engineering in tailoring and producing a plethora of novel materials with desired composition, structure and properties which is a very important issue for synthesis of selective catalysts. It is possible to produce high-surface area nanocatalysts and supported catalysts by SCS. This clearly explains and justifies the increasing interest in this method of catalyst synthesis worldwide.

SCS is a very popular experimental process as it is studied in more than 50 countries all over the world. On the other hand, there is little information on the literature concerning the systematic investigation of the parameters that influence the mechanism of the product formation during SCS. As liquid-phase hydrogenation was selected to evaluate the catalysts performance, a thorough investigation of those parameters was crucial.

Liquid-phase hydrogenation was selected as it an extremely sensitive technique for the detection of differences in activity that are originated to structural changes of the catalysts. Furthermore, there are hydrogenation processes in industry that take place in liquid phase, frequently using nickel catalysts. It is also used as a model reaction for the gas-phase hydrogenation, as the activity ranking of the catalysts is the same. Last but not least, the hydrogenation in the liquid phase is simpler to be performed in the lab scale because it requires less time to take place, lower reaction temperatures, no pressure is required and it involves lower risk.

The main aim of the project was to understand the mechanism of reactions during SCS in order to produce active catalysts with tailored properties. The SCS parameters that were investigated are:

- The quantity of the oxidizer
- The quantity of fuel
- The heating mode
- The time in furnace after the completion of SCS
- The preheating temperature
- The concentration of reactants in the water
- The pretreatment of the SCS precursor solution
- The fuel-to-oxidizer ratio

- The type of reducer
- The quantity ratio of two oxidizers: $Ni(NO_3)_2 – Al(NO_3)_3$

Some of the above mentioned parameters were previously considered to have no influence on the composition and the microstructure of the final products. It was found for the first time that some of those parameters have a significant influence on the final products properties, such as the reactants concentration in the aqueous precursor solution and the pretreatment of the initial SCS solution. The initial systems that were employed were nickel nitrate hexahydrate and glycine system as well as nickel nitrate hexahydrate, aluminium nitrate nonahydrate and glycine system.

## 9.1. Nickel nitrate hexahydrate and glycine system

The relative amount of water in the initial solution for Solution Combustion Synthesis has generally been assumed to be of minor significance to the final product. However, in this work for the first time it was found that the initial concentration of nitrates in the aqueous solution affects the characteristics and properties of Ni-based catalysts. In addition, the relative amount of water in the initial aqueous solution appears to have a substantial effect on their catalytic activity in maleic acid liquid phase hydrogenation. The underlying mechanism for this effect appears to be the prolonged persistence and delayed decomposition of hydrates that form during the early preheating stages of SCS. This work shows for the first time, that compounds, such as hydrates, which form in solution appear to persist even after all the water has evaporated and influence the physico-chemical properties of the products formed during later stages. This apparent "memory effect" exists even during the later sintering stages and may explain many of the difficulties reported in repeating synthesis results since the strength of the initial aqueous solution is generally not taken into consideration during analysis of catalytic synthesis.

The volume of water (that determines the reactants concentration in the initial aqueous solution) affects the volume and the structure of the dendrites, as they grow in this space due to the fact that the complexes are originated in the water. When water is added in the initial SCS mixture 3-dimensional dendrites are formed. On the other hand, without the addition of water the resulting dendrites are 2-D with significantly less volume.

Moreover, the pretreatment of the precursor solution facilitates the formation of hydrates (which still exist in the gel phase after the evaporation the water) due to the slow heating and the mild magnetic stirring that is applied in the pretreatment stage. The hydrates participate in the exothermic reaction yielding solid product with dendritic structure, as the reaction takes place through their complicated structure. Those results are very important not only for those who work with SCS, but also for all those who use aqueous solutions of salts to synthesize catalysts, such as the impregnation, the precipitation and the sol-gel approaches.

The dendritic formation influences the microstructure of the final products as well as their composition. The form of dendrites affects the way of combustion and as a result the cooling time. These factors have a major effect on the composition of catalysts (as the oxidation and the reduction processes are affected), porosity (as the time for the formation of the pores alters), pore shape (due to changes in the velocity of the generated gases), specific surface area (which is affected by the porosity, the pore shape and the crystal lattice parameters) and as a result their catalytic performance varies.

In addition, the experimental results demonstrated that the preheating temperature only slightly influences the combustion temperature during SCS. The SCS preheating temperature influences the structural formation and the final composition of the nanocomposite metal-oxide product. Moreover, increasing the SCS preheating temperature leads to a decrease of combustion initiation period due to the enhanced heating velocity and an increase of cooling time as a result of the additional exothermic reactions taking place at higher temperatures. The variations in cooling period provoked changes in the final product composition and microstructure, because of the ongoing phase and structural formation during cooling period.

Furthermore, all the used methods for the product characterization provided valuable information. TEM analysis proved that the products are in the nanoscale, while SEM analysis showed that the products are in some cases organized in flakes and there are well developed structures inside the flakes as well. The three-dimensional percolation-like network and hierarchical structure of nano-composites on the basis of metal oxides and metals obtained by combustion in solutions provides a distinct possibility of increasing the selectivity and activity of such catalysts. EDX revealed different ratio between Ni and O at different points of the product. This could be connected to the multi-waved combustion mechanism in the gel.

Data obtained from IR high speed camera showed that the combustion mechanism depends on the glycine concentration – at high glycine concentration there is a mechanism change from “in volume combustion” to combustion in “self-propagating” regime. Uniquely, in the sample with stoichiometric ratio between glycine and nickel nitrate, two waves occurred during combustion: hydrogen formation takes place in first wave followed by reduction of nickel oxide in the second wave together with Ni oxidation. When hydrogen is formed in the gas phase, a combustion wave propagates from the top to the bottom of the reactor while the second combustion wave is initiated at the bottom (within the gel) – first by reduction of Ni and then by partial Ni oxidation, because of the higher temperature developed.

Dynamic XRD shed light on the small time interval between the formation of nickel and its further oxidation to nickel oxide, depending upon the oxygen concentration in the reaction environment. The combination of measuring the combustion temperature with thermocouples and EDX analysis indicated that the reduction of nickel oxide can also happen with carbon or carbon monoxide for the production of nickel. The measurements with RF-IGC demonstrated the surface topography of the catalytic active sites and the fact that there are various types of active sites that are possibly connected to different processes.

## 9.2. Nickel nitrate hexahydrate, aluminium nitrate nonahydrate and glycine system

Catalytic studies of liquid phase hydrogenation of maleic acid using Ni/Al - based catalysts showed that the degree of catalysts' surface hydrogen coating, which plays a significant role in the hydrogenation reaction, can also be regulated by adjusting the synthesis parameters. A multistage, cascade-like mechanism of the formation of the Ni-NiAl catalysts was identified and it is suggested that one-pot SCS method can be utilized for the preparation of many different types of metal-alloys nanostructures. Particularly, the synthetic strategy has significant potential applications in the preparation other nanocomposite catalysts for engineering highly efficient catalysts.

On the table that follows, all the parameters of SCS that were investigated are presented as well as their catalytic performance toward the liquid-phase hydrogenation of maleic acid to produce succinic acid. In the cases that the as-synthesized materials were not catalytically tested the nickel concentration is mentioned as it is the most major parameter to characterize the catalyst. The highlighted conditions are those that were found to be more suitable for maximum nickel concentration and those which demonstrated the highest activity and conversion towards the liquid-phase hydrogenation of maleic acid.

Table 6.1: Table of the synthesis parameters that were investigated and their catalytic properties.

| | Changing parameter | Experiments | | | |
|---|---|---|---|---|---|
| $Ni(NO_3)_2$ – glycine system | Concentration of $Ni(NO_3)_2$ | 3g | 6g | 9g<br>Max Ni concentration | 12g |
| | Quantity of glycine | 50%<br>Max Ni concentration | 75% | 100% | 125% |
| | Heating mode | Slow heating (25⟶500°C) | | Preheated furnace (500°C)<br>Max Ni concentration | |
| | Time in furnace after SCS | 0min<br>Max Ni concentration | 2min | 7min | 10min |
| | Preheating temperature | 500°C | 600°C | 650°C<br>Max Ni concentration | 700°C<br>Max Ni concentration |
| | Reactants concentration in the aqueous solution | 25ml $H_2O$ | 50ml $H_2O$ | 75ml $H_2O$<br>Highest conversion rate | 100ml $H_2O$<br>Highest activity |
| | Pretreatment of the precursor solution | Pretreated samples<br>Highest conversion degree | | No-pretreated samples | |
| | Fuel-to-oxidizer ratio (ϕ) | ϕ=1.4<br>-Highest conversion degree<br>-Highest activity | ϕ=1.74<br>Highest conversion rate | ϕ=2.08 | ϕ=2.78 |
| $Ni(NO_3)_2$ – $Al(NO_3)_3$ – glycine system | Nature of fuel | Carbohydrazide | Urea | Glycine<br>Production of Ni in the final product | |
| | Ratio of oxidizers $Ni(NO_3)_2$ – $Al(NO_3)_3$ | 20% $Ni(NO_3)_2$ | 40% $Ni(NO_3)_2$<br>-Highest conversion rate<br>-Highest activity | 60% $Ni(NO_3)_2$ | 80% $Ni(NO_3)_2$ |

### 9.3. In-flight SCS

In industry, catalysts on carriers are always employed for cost-efficiency, as only the surface participates in the catalytic reaction. Moreover, in the gas-phase hydrogenation supported catalysts are necessary in order to be placed inside the catalytic column. For all these reasons, an effort was made to place the as-synthesized catalytsts on carriers with a new approach.

Combustion-assisted flame spraying ("CAFSY") was used for in-flight solution combustion synthesis and developed to produce catalytically active Ni/NiO nanocoatings on ceramic substrate (Mg-Al-O). This can be considered as new method of preparation nanocatalysts on carrier for industrial application.

It is pointed out that the improvements in the performance of SCS catalysts will depend critically on the success of understanding the reaction mechanisms. The challenge of obtaining tailored SCS catalysts was also highlighted, while suggestions for the suitability of various chemical elements that could be employed to reach this goal. There is still a long way to go before the many studies of regularities of this process can clarify the underlying issues. It is clear that fundamental understanding of mechanisms during self-sustained reactions is of high importance. This knowledge will lead in controlling the textural and microstructural properties as well as the shape of the SCS-derived products. The broad variety of the applications that SC synthesized materials will also be expanded, including the major field of catalysis.

## 9.4. Suggestions for further research

A few suggestions for further research are:

- *To investigate the liquid phase hydrogenation of triple bond compounds in order to study the way that the variation of active centers influences the activity of the catalysts.*

  Our investigation revealed that SCS-derived catalysts have various types of active cites, some of which play a significant role in determining the overall activity of the catalysts. The hydrogenation of triple bond is a widely used catalytic reaction in industry (such as petrochemical, pharmacological and agrochemical) but its mechanism is more complicated than the double bond hydrogenation, as the reaction includes more stages and more side reactions that influence the final product of the catalytic reaction as well as the byproducts. Classical heterogeneous catalysts were used to hydrogenate multiple carbon-carbon bonds which contained noble metals such as Pd, Pt, Ru and Rh, which are highly active and selective.[337] It would be very interesting to study the way these active sites of SCS Ni-based catalysts influence the mechanism of triple bond hydrogenation and the possibility to enhance both activity and selectivity when the active sites alter in terms of existence or structure.
- *To study liquid phase oxidation to find out how the studied parameters influence catalytic activity in other processes.*

Liquid phase oxidation finds widespread application in the chemical industry for the manufacture of a variety of chemicals ranging from the commodities to fine chemical specialties. About half of the overall capacity of oxidation processes take place in the liquid phase.[338] Thus, it is important to investigate the activity of the SCS-produced catalysts toward the liquid-phase oxidation by varying the synthesis parameters of the employed catalysts. Despite the fact that SCS derived catalysts are widely used to catalyze oxidation reactions, there are little information in the literature concerning the catalytic behavior of Ni-based catalysts synthesized by SCS. This is worth of investigation, as SCS is a quick, cost effective and environmentally friendly approach and nickel catalysts are cheaper that the noble metals group of catalysts.

- *To study the formation of dendrites in the systems on the basis of metal nitrates other than nickel and aluminum nitrate, such as cobalt nitrate, copper nitrate, calcium nitrate, magnesium nitrate, etc.*

  Dendritic formation was found to play a key role in the composition and the microstructure of the final products. It was revealed for the first time that the hydrates that form in the early stages of the solution heating, participate in the exothermic reaction resulting in solid product with dendritic structure. It would be of great significance to expand this novel investigation to other initial systems besides nickel nitrate and glycine and test different oxidizers (such as such as cobalt nitrate, copper nitrate, calcium nitrate, magnesium nitrate, etc.) researching their reaction mechanism with glycine.

- *To further explore In-flight SCS as a new method of preparing supported catalysts and study the influence of various processing parameters ($C_2H_4$:$O_2$ ratio, spraying distance, type of support, etc.).*

  In-flight SCS is a new approach to deposit the SCS-derived nanopowders on carriers. In industry, catalysts on carriers are usually employed for cost efficiency, thus it is crucial to study the influence of various processing parameters ($C_2H_4$:$O_2$ ratio, spraying distance, type of support, solution composition, etc.) on the resulting supported Ni-based catalysts. The aim of this research is to explore the catalytic activity of the as-synthesized supported catalysts, how the various processing parameters will influence their catalytic behavior towards the liquid-phase hydrogenation and the optimization of this new method to maximize their activity and selectivity.

## References

1. Catalytic Kinetics, Chemistry and Engineering, 2nd Edition, D. Yu. Murzin and T. Salmi, Elsevier, ISBN: 978-0-444-63753-6.
2. The Catalyst Group Resources, Intelligence report: Business shifts in the global catalytic process industries 2017-2023, Study presentation, May 2018, Pennsylvania, USA.
3. S. Bhaduri, D. Mukesh, HOMOGENEOUS CATALYSIS Mechanisms and Industrial Applications, 2000, John Wiley & Sons, Inc., ISBN: 0-471-37221-8.
4. E. Roduner, Understanding Catalysis, Chemical Society Reviews, 2014, 1-33.
5. Ertl G., Knozinger H., Weitkamp J. (ed.) - Handbook of Heterogeneous Catalysis. v.3, 1997.
6. Principles and Practice of Heterogeneous Catalysis, J. M. Thomas and W. J. Thomas, 2nd ed., Wiley-VCH, 2015, Print ISBN: 978-3-527-31458-4.
7. Modern Heterogeneous Catalysis: An Introduction, Editor(s): Rutger A. van Santen, First published:24 February 2017, Print ISBN:978352733961.
8. Concepts of Modern Catalysis and Kinetics, Second Edition. I. Chorkendorff, J. W. Niemantsverdriet, 2007 WILEY-VCH Verlag GmbH & Co. KGaA, Weinheim ISBN: 978-3-527-31672-4.
9. C. H. Bartholomew, Mechanisms of catalyst deactivation, Applied Catalysis A: General, 2001, 212, 1–2, 17-60.
10. Edward Richmond, Joseph Moran, Recent Advances in Nickel Catalysis Enabled by Stoichiometric Metallic Reducing Agents, SYNTHESIS, Georg Thieme Verlag, 2017, 50, 3, 499-513.
11. S. Z. Tasker, E. A. Standley, T. F. Jamison, Recent advances in homogeneous nickel catalysis, 2014, Nature, 509, 299-309.
12. Handbook of heterogeneous catalytic hydrogenation for organic synthesis, S. Nishimura, J. Wiley & sons, 2001, Canada, ISBN 0-471-39698-2.
13. D. Goupil, P. Fouilloux, R. Maurel, Activity and selectivity of Pt− Fe/C alloys for the liquid phase hydrogenation of cinnamaldehyde to cinnamyl alcohol, Reaction Kinetics and Catalysis Letters, 1987, 35, 185-193.
14. X. Chen, H. Li, H. Luo, M. Qiao, Liquid phase hydrogenation of furfural to furfuryl alcohol over Mo-doped Co-B amorphous alloy catalysts, Applied Catalysis A: General, 233, 1-2, 13-20.
15. P. N. Rylander, Hydrogenation methods, Academic Press, New Jersey, USA, 1985.

16. G. Xanthopoulou, Catalytic properties of the SHS products-Review, Advances in Science and Technology, 2010, 63, 287-296

17. J. W. E. Coenen, Hydrogenation of edible oils, Journal of the American Oil Chemists' Society, 1976, 53, 382–389.

18. R.R. Allen, Principles and catalysts for hydrogenation of fats and oils, Journal of the American Oil Chemists' Society, 1978, 55, 792-795.

19. R. E. Harmon, S. K. Gupta, D. J. Brown, Hydrogenation of organic compounds using homogeneous catalysts, Chemical Reviews, 1973, 73, 21-52.

20. X. L. Yang, H. F. Liu, Influence of metal ions on hydrogenation of *o*-chloronitrobenzene over platinum colloidal clusters, Applied Catalysis A: General, 1997, 164, 197-203.

21. X. X. Han, R. X. Zhou, X. M. Zheng, H. Jiang, Effect of rare earths on the hydrogenation properties of ***p***-chloronitrobenzene over polymer-anchored platinum catalysts, Journal of Molecular Catalysis A: Chemical, 2003, 193, 103-108.

22. J. Xiong, J. Chen, J. Zhang, Liquid-phase hydrogenation of o-chloronitrobenzene over supported nickel catalysts, Catalysis Communications, 2007, 8, 345-350.

23. B. Coq, A. Tijani, R. Dutartre, F. Figueras, Influence of support and metallic precursor on the hydrogenation of *p*-chloronitrobenzene over supported platinum catalysts, Journal of Molecular Catalysis, 1993, 79, 253-64.

24. X. X. Han, R. X. Zhou, G. H. Lai, X. M. Zheng, Influence of support and transition metal (Cr, Mn, Fe, Co, Ni and Cu) on the hydrogenation of *p*-chloronitrobenzene over supported platinum catalysts, Catalysis Today, 2004, 93–95, 433-437.

25. X. X. Han, R. X. Zhou, G. H. Lai, B. H. Yue, X. M. Zheng, Effect of transition metal (Cr, Mn, Fe, Co, Ni and Cu) on the hydrogenation properties of chloronitrobenzene over Pt/$TiO_2$ catalysts, Journal of Molecular Catalysis, 2004, 209, 83-87.

26. S. K. Tanielyan, S. R. More, R. L. Augustine, St. R. Schmidt, Continuous liquid phase hydrogenation of 1,4-butynediol to high purity 1,4-butanediol over particulate raney ® nickel catalyst in a fixed bed reactor, *Organic Process Research & Development,* 2017, 21, 327-335.

27. H. Li, Y. Wu, J. Zhang, W. Dai, M. Qiao, Liquid phase acetonitrile hydrogenation to ethylamine over highly active and selective Ni-Co-B amorphous alloy catalyst, Applied Catalysis A: General, 2004, 275, 199-206.

28. S. Liu, F. Hao, P. Liu, H. Luo, H. Liao, Liquid phase hydrogenation of adiponitrile over amorphous alloy nickel catalyst, Research on Chemical Intermediates, 2015, 41, 5879-5887.

29. G. Wowsnick, D. Teschner, M. Armbrüster, I. Kasatkin, F. Girgsdies, Y. Grin, R. Schlögl, M. Behrens, Surface dynamics of the intermetallic catalyst Pd2Ga, Part II–Reactivity and stability in liquid-phase hydrogenation of phenylacetylene, Journal of Catalysis, 2014, 309, 221-230.

30. A. Cross, S. Roslyakov, K. V. Manukyan, S. Rouvimov, A. S. Rogachev, D. Kovalev, E. E. Wolf, A. S. Mukasyan, In situ Preparation of Highly Stable Ni-based Supported Catalysts by Solution Combustion Synthesis, Journal of Physical Chemistry C, 2014, 118, 26191-26198.

31. A. Kumar, A. S. Mukasyan, E. E. Wolf, Combustion Synthesis of Ni, Fe and Cu Multi-component catalysts for hydrogen production from ethanol reforming, Applied Catalysis A: General, 2011, 401, 20−28.

32. A. N. Fatsikostas, X. E. Verykios, Reaction network of steam reforming of ethanol over Ni-based catalysts, Journal of Catalysis, 2004, 225, 439−452.

33. S. M. de Lima, A. M. da Silva, L. O. O. da Costa, J. M. Assaf, L. V. Mattos, R. Sarkari, A. Venugopal, F. B. Noronha, Hydrogen production through oxidative steam reforming of ethanol over Ni-based catalysts derived from $La_{1-x}Ce_xNiO_3$ perovskite-type oxides, Applied Catalysis B: Environmental, 2012, 121–122, 1-9.

34. T. Wang, D. G. Ren, Z. Huo, Z. Song, F. Jin, M. Chen, L. Chen, A nanoporous nickel catalyst for selective hydrogenation of carbonates into formic acid in water, 2016, Green Chemistry, 2017, 19, 716-721.

35. Y. Gao, F. Meng, Y. Cheng, Z. Li, Influence of fuel additives in the urea-nitrates solution combustion synthesis of Ni-$Al_2O_3$ catalyst for slurry phase CO methanation, Applied Catalysis A:General, 2017, 534, 12-21.

36. J. Qi, X. Sun, S. Tang, Y. Sun, C. Xu, X. Li, X. Li, Integrated study on the role of solvent, catalyst and reactant in the hydrodeoxygenation of eugenol over nickel-based catalysts. Applied Catalysis A: General, 2017, 535, 24-31.

37. N. Borchtchoukova, V. Feldman, G. Finkelshtain, S. K. Rakovsky, M. V. Gabrovska, D. A. Nikolova, L. P. Bilyarska, Nickel-based catalyst for fuel cell, USA Patent 20170263942, 2017.

38. S. Liang, Y. Qian, L. Lv, L. Sun, Y. Zheng, T. Wang, J. Wu, F. Cao, Selective nickel based hydrogenation catalysts and the preparation thereof, USA Patent 9597668 B2, 2017.

39. The Handbook of Homogeneous Hydrogenation, Editors: J. G. de Vries, C. J. Elsevier, 2008 ISBN: 9783527311613, WILEY-VCH Verlag GmbH & Co. KGaA.

40. N. Kalyon, K. Hofmann, J. Malter, M. Lucas, P. Claus, B. Albert, Catalytic activity of nanoscale borides: $Co_2B$ and $Ni_7B_3$ in the liquid-phase hydrogenation of citral, Journal of Catalysis, 2017, 352, 436-441.

41. Y. Chen, Chemical preparation and characterization of metal–metalloid ultrafine amorphous alloy particles, Catalysis Today,1998, 44, 3-16.

42. A. Baiker, Metallic glasses in heterogeneous catalysis,F araday Discussions of the Chemical Society, 1989, 87, 239-251.

43. A. Molnar, G.V. Smith, M. Bartok, New catalytic materials from amorphous metal alloys, Advances in Catalysis, 1989, 36, 329-383.

44. J. F. Deng, H. X. Li, W. J. Wang, Progress in design of new amorphous alloy catalysts Catalysis Today, 1999, 51, 113-125.

45. X. Yan, J. Sun, Y. Wang, J. Yang, A Fe-promoted Ni–P amorphous alloy catalyst (Ni–Fe–P) for liquid phase hydrogenation of m- and p-chloronitrobenzene, Journal of Molecular Catalysis A: Chemical, 2006, 252, 17-22.

46. X. Chen, Y. Ma, L. Wang, Z. Yang, S. Jin, L. Zhang, C. Liang, Nikel-aluminium intermetallic compounds as highly selective and stable catalysts for the hydrogenation of naphthaleme to tetralin, ChemCatChem, 2015, 7, 978-983.

47. H. U. Blaser, A. Schnyder, H. Steiner, F. Rössler, P. Baumeister, Handbook of Heterogeneous Catalysis, (Eds.: G. Ertl, H. Knözinger,J. Weitkamp), Wiley-VCH, Weinheim, Germany, 2008, p. 3284.

48. N. V. Semagin, A. V. Bykov, E. M. Sulman, V. G. Matveeva, S. N. Sidorov, L. V. Dubrovina, P. M. Valetsky, O. I. Kiselyova, A. R. Khokhlov, B. Stein, L. M. Bronstein, Selective dehydrolinalool hydrogenation with poly (ethylene oxide)-block-poly-2-vinylpyridine micelles filled with Pd nanoparticles, Journal of Molecular Catalysis A: Chemical, 2004, 208, 273-284.

49. A. F. Trasarti, N. M. Bertero, C. R. Apesteguía, A. J. Marchi, Liquid-phase hydrogenation of acetophenone over silica-supported Ni, Co and Cu catalysts: Influence of metal and solvent, Applied Catalysis A: General, 2014, 475, 282-291.

50. A. Pintar, J. Batista, J. Levec, T. Kajiuchi, Kinetics of the catalytic liquid-phase hydrogenation of aqueous nitrate solutions, Applied Catalysis B: Environmental, 1996, 11, 81-98.

51. P. Weerachawanasak, P. Praserthdam, M.Arai, J. Panpranot, A comparative study of strong metal–support interaction and catalytic behavior of Pd catalysts supported on micron-and nano-sized $TiO_2$ in liquid-phase selective hydrogenation of phenylacetylene, Journal of Molecular Catalysis A: Chemical, 2008, 279, 133-139.

52. U. K. Singh, M. A. Vannice, Kinetics of liquid-phase hydrogenation reactions over supported metal catalysts — a review, Applied Catalysis A: General, 2001, 213, 1-24.

53. Pr. D. Vaidya, V. V. Mahajani, Kinetics of aqueous phase hydrogenation of maleic acid to succinic acid over an $Ru/Al_2O_3$ catalyst, Journal of Chemical Technology & Biotechnology, 2003, 78, 504-511.

54. J. G. Zeikus, M. K. Jain, P. Elanhovan, Biotechnology of succinic acid production and markets for derived industrial products, Applied Microbiology and Biotechnology, 1999, 51, 545-552.

55. S. E. Pedersen, J. G. Jr. Frye, T. G. Attig, J. R. Budge, Catalysts for the hydrogenation of aqueous solutions of maleic acid and its derivatives in to 1,4-butanediol, USA Patent 5698749, 1997.

56. T. G. Attig, A. M. Graham, Preparation of γ-butyrolactone and 1,4-butanediol by catalytic hydrogenation of maleic acid, USA Patent 4827001, 1989.

57. P. Ruiz, M. Crine, A. Germain, G. L' Homme, Influence of the reactional system on the irrigation rate in trickle-bed reactors, ACS Symposium Series, 1984, 237, 15-36.

58. G. Vertes, G. Horanyi, G. Kiss, Effect of a small amount of noble metal additive on the behavior of active and inactive supports in catalytic hydrogenation, Acta chimica Academiae Scientiarum Hungaricae, 1974, 83, 135-149.

59. M. A. Kulagina, P. A. Simonov, E. Yu. Gerasimov, R. I. Kvon, A. V. Romanenko, To the nature of the support effect in palladium-catalyzed aqueous-phase hydrogenation of maleic acid, Colloids and Surfaces A: Physicochemical and Engineering Aspects, 2017, 526, 29-39.

60. C. A. Brown, H. C. Brown The reaction of sodium borohydride with nickel acetate in aqueous solution – a convenient synthesis of an active nickel hydrogenation catalyst of low isomerizing tendency, Journal of the American Chemical Society, 1963, 85, 1003-1005

61. K. C. Patil, S. T. Aruna, S. Ekambaram, Combustion synthesis, Current Opinion in Solid State & Materials Science, 1997, 2, 158-165.

62. K. C. Patil, S. T. Aruna in Redox Methods in SHS Practice in Self-Propagating High Temperature Synthesis of Materials, A. A. Borisov, L. T. De Luca, A. G. Merzhanov, Y. N. Scheck (Eds), Taylor & Francis, New York, USA2002; Collection of 17 articles by experts in the area reflecting the trends in SHS covering theory andpractice of combustion, material synthesis and applications.

63. A. S. Mukasyan, P. Epstein P. Dinka, Solution combustion synthesis of nanomaterials, Proceedings of the Combustustion Institute, 2007, 31, 1789-1795.

64. S. T. Aruna, A. S. Mukasyan, Combustion synthesis and nanomaterials, Current Opinion in Solid State & Materials Science, 2008, 12, 44-50.

65. K. C. Patil, S. T. Aruna, T. Mimani, Combustion synthesis: an update, Current Opinion in Solid State and Materials Science, 2002, 6, 507-512.

66. A. G. Merzhanov, Self-propagating high-temperature synthesis: Twenty years of search and finding. In Combustion and Plasma Synthesis of High-Temperature Materials, Z. A. Munir and J. B. Holt (Eds.), VCH Publ. Inc., New York, 1990.

67. G. Xanthopoulou, G. Vekinis, SHS catalysts: synthesis, properties and applications, Advances in Science and Technology, 2006, 45, 1058-1066.

68. A. Varma, A. S. Mukasyan, A. S. Rogachev, K. V. Manukyan, Solution combustion synthesis of nanoscale materials, Chemical Reviews, 2016, 116, 14493-14586.

69. F. Deganello, A. K. Tyagi, Solution combustion synthesis, energy and environment: Best parameters for better materials, Progress in Crystal Growth and Characterization of Materials, 2018, 64, 23-61.

70. A. E. Danks, S. R. Hall, Z. Schnepp, The evolution of ‘sol – gel’ chemistry as a technique for materials synthesis, Materials Horizons, 2016, 3, 91 – 112.

71. S. R. Jain, K. C. Adiga, V. R. Pai Verneker, A new approach to thermochemical calculations of condensed fuel-oxidizer mixtures, Combustion and Flame, 1981, 40, 71-79.

72. J. J. Kingsley, K. C. Patil, A novel combustion process for the synthesis of fine particle α -alumina and related oxide materials, Materials Letters, 1988, 6, 427- 432.

73. R. Ghose, H. T. Hwang, A. Varma, Oxidative coupling of methane using catalysts synthesized by solution combustion method, Applied Catalysis A: General, 2013, 452, 147-154.

74. K. C. Patil, M. S. Hegde, T. Rattan, S. T. Aruna, Chemistry of Nanocrystalline Oxide Materials: Combustion Synthesis, Properties and Applications, World Scientific, 2008.

75. K. C. Patil, Advanced ceramics: combustion synthesis and properties, Bulletin of Materials Science, 1993, 16, 533- 541.

76. A. Kumar, E. E. Wolf, A. S. Mukasyan, Solution combustion synthesis of metal nanopowders: Nickel—Reaction pathways, AlChE Journal, 2011, 57, 2207-2214.

77. S. Specchia, C. Galletti, V. Specchia, Solution Combustion Synthesis as intriguing technique to quickly produce performing catalysts for specific applications, Studies in Surface Science and Catalysis, 2010, 175, 59-67.

78. A. S. Mukasyan, P. Dinka, Novel Approaches to Solution- Combustion Synthesis of Nanomaterials. International Journal of Self-Propagating High-Temperature Synthesis, 2007, 16, 23-35.

79. R. Ianos, I. Lazău, C. Păcurariu, P. Barvinschi, Fuel Mixture Approach for Solution Combustion Synthesis of $Ca_3Al_2O_6$ Powders, Cement and Concrete Research, 2009, 39 , 566-572.

80. K. Deshpande, A. Mukasyan, A. Varma, Direct synthesis of iron oxide nanopowders by the combustion approach: reaction mechanism and properties, Chemistry of Materials, 2004, 16, 4896-4904.

81. A. S. Mukasyan, C. Costello, K. P. Sherlock, D. Lafarga, A. Varma, Perovskite membranes by aqueous combustion synthesis: synthesis and properties. Separation and Purification Technology, 2001, 25, 117-126.

82. K. V. Manukyan, A. Cross, S. Roslyakov, S. Rouvimov, A. S. Rogachev, E. E. Wolf, A. S. Mukasyan, Solution Combustion Synthesis of Nano-Crystalline Metallic Materials: Mechanistic Studies. Journal of Physical Chemistry C, 2013, 117, 24417-24427.

83. P. Erri, J. Nader, A. Varma, Controlling combustion wave propagation for transition metal/alloy/cermet foam synthesis, Advanced Materilas, 2008, 20 , 1243-1245.

84. M. S. Hegde, G. Madras, K. C. Patil, Noble Metal Ionic Catalysts. Accounts of Chemical Research, 2009, 42, 704-712.

85. S. Roy, D. A. Sharma, S. N. Roy, H. S. Maiti, Synthesis of $YBa_2Cu_3O_{7-x}$ powder by autoignition of citrate-nitrate gel, Journal of Materials Research, 1993, 8, 2761-2766.

86. D. G. Lamas, R. E. Juarez, G. E. Lascalea, N. E. Walsoe de Reca, Synthesis of Compositionally Homogeneous, Nanocrystalline $ZrO_2$ - 35 mol% $CeO_2$ powders by gel-combustion. Journal of Materials Science Letters, 2001, 20, 1447-1449.

87. X. Yu, J. Smith, N. Zhou, L. Zeng, P. Guo, Y. Xia, A. Alvarez, S. Aghion, H. Lin, J. Yu, R. P. C. Chang, M. J. Bedzyk, R. Ferragut, T. J. Marks, A. Facchetti, Spray-Combustion Synthesis: Efficient Solution Route to High-Performance Oxide Transistors, Proceedings of the National Academy of Sciences of the U.S.A., 2015, 112, 3217-3222.

88. S. Biamino, P. Fino, D. Fino, N. Russo, C. Badini, Catalyzed traps for diesel soot abatement: In situ processing and deposition of perovskite catalyst, Applied Catalysis B: Environmental, 2005, 61, 297-305.

89. P. Dinka, A. S. Mukasyan, In situ preparation of oxide-based supported catalysts by solution combustion synthesis, Journal of Physical Chemistry B, 2005, 109, 21627-21633

90. A. Vita, G. Cristiano, C. Italiano, S. Specchia, F. Cipitì, V. Specchia, Methane oxy-steam reforming reaction: performances of Ru/$\gamma$-$Al_2O_3$ catalysts loaded on structured cordierite monoliths, International Journal of Hydrogen Energy, 2014, 9, 18592–18603.

91. A. S. Mukasyan, P. Dinka, Novel method for synthesis of nano-materials: Combustion of active impregnated layers. Advanced Engineering Materials, 2007, 9, 653-657.

92. A. Ashok, A. Kumar, R. R. Bhosale, M. A. H. Saleh, L. J. P. van den Broeke, Cellulose assisted combustion synthesis of porous Cu − Ni nanopowders, RSC Advances, 2015, 5, 28703-28712.

93. K. V. Manukyan, X. Liu, J. K. Furdyna, Y.-S. Chen, A. Orlov, S. Rouvimov, G. H. Bernstein, P. Li, X. Li, W. Porod, S. Dong, S. Roslyakov, A. S. Mukasyan, Ultrasmall $\alpha$ -$Fe_2O_3$ superparamagnetic nanoparticles with high magnetization prepared by template-assisted combustion process, Journal of Physical Chemistry C, 2014, 118, 16264-16271.

94. Y. Yuan, C. Liu, Y. Zhang, X. Shan, Sol − gel auto-combustion synthesis of hydroxyapatite nanotubes array in porous alumina template, Materials Chemistry and Physics, 2008, 112, 275-280.

95. A. A. Voskanyan, K.-Y. Chan, C.-Y. V. Li, Colloidal Solution combustion synthesis: Towards mass production of crystalline uniform mesoporous $CeO_2$ catalyst with tunable porosity, Chemistry of Materials, 2016, 28, 2768-2775.

96. S. Jalota, A. C. Tas, S. B. Bhaduri, Microwave-assisted synthesis of calcium phosphate nanowhiskers, Journal of Materials Research, 2004, 19, 1876-1881.

97. R. Rosa, P. Veronesi, C. Leonelli, A review on combustion synthesis intensification by means of microwave energy, Chemical Engineering and Processing, 2013 , 71,2-18.

98. H. Ajamein, M. Haghighi, On the microwave enhanced combustion synthesis of CuO–ZnO–$Al_2O_3$ nanocatalyst used in methanol steam reforming for fuel cell grade hydrogen production: Effect of microwave irradiation and fuel ratio, Energy Conversion and Management, 2016, 118, 231-242.

99. J. S. Cho, K. Y. Jung, Y. C. Kang, Yolk − shell Structured $Gd_2O_3Eu^{3+}$ phosphor prepared by spray pyrolysis: The effect of preparation conditions on microstructure and luminescence Properties, Physical Chemistry Chemical Physics, 2015, 17, 1325-1331.

100. S. C. Pillai,; J. M. Kelly, R. Ramesh, D. E. McCormack, Advances in the synthesis of ZnO nanomaterials for varistor devices. Journal of Materials Chemistry C, 2013, 1, 3268-3281.

101. G. V. Trusov, A. B. Tarasov, E. A. Goodilin, A. S. Rogachev, S. I. Roslyakov, S. Rouvimov, K. B. Podbolotov, A. S. Mukasyan, Spray solution combustion synthesis of metallic hollow microspheres, Journal of Physical Chemistry C, 2016, 120, 7165-7171.

102. J. W. Jung, C. C. Chueh, A. K. Y. Jen, A low-temperature, solution-processable, Cu-doped nickel oxide hole-transporting layer via the combustion method for high-performance thin-film perovskite solar cells. Advanced Materials, 2015, 27, 7874-7880

103. M.-G. Kim, M. G. Kanatzidis, A. Facchetti, T. J. Marks, Low- temperature fabrication of high-performance metal oxide thin-film electronics via combustion processing, Nature Materials, 2011, 10, 382-388.

104. A. Alves, C. P. Bergmann, F. A. Berutti, Novel synthesis and characterization of nanostructured materials, Engineering Materials, Berlin, Heidelberg: Springer-Verlag, 2013.

105. S. M. Khaliullin, V. D. Zhuravlev, V. G.Bamburov, Solution-combustion synthesis of oxide nanoparticles from nitrate solutions containing glycine and urea: Thermodynamic aspects, International Journal of Self-Propagating High-Temperature Synthesis, 2016, 25, 139–148.

106. P. Ravindranathanan, K. C. Patil, A one-step process for the preparation of γ-$Fe_2O_3$, Journal of Materials Science Letters, 1986, 5, 221-222.

107. S. L. González-Cortés, F. E. Imbert, Fundamentals, properties and applications of solid catalysts prepared by solution combustion synthesis (SCS), Applied Catalysis B: Environmental, 2013,452, 117-131.

108. P. Erri, P. Pranda, A. Varma, Oxidizer − fuel Interactions in aqueous combustion synthesis. 1. Iron(III) nitrate − model fuels, Industrial & Engineering Chemistry Research, 2004, 43, 3092-3096.

109. S. Hadke, M. T. Kalimila, S. Rathkanthiwar, S. Gour, R. Sonkusare, A. Ballal, Role of fuel and fuel-to-oxidizer ratio in combustion synthesis of nano-crystalline nickel oxide powders, Ceramics International, 2015, 41, 14949-14957.

110. H. Fathi, S. M. Masoudpanah, S. Alamolhoda, H. Parnianfar, Effect of fuel type on the microstructure and magnetic properties of solution combusted $Fe_3O_4$ powders, Ceramics International, 2017, 43, 7448-7453.

111. C. Aliotta, L. F. Liotta, V. La Parola, A. Martorana, E.N.S. Muccillo, R. Muccillo, F. Deganello, Ceria-based electrolytes prepared by solution combustion synthesis: The role of fuel on the materials properties, Applied Catalysis B: Environmental, 2016, 197, 14-22.

112. U. Zavyalova, P. Scholz, B. Ondruschka, Influence of cobalt precursor and fuels on the performance of combustion synthesized $Co_3O_4/\gamma\text{-}Al_2O_3$ catalysts for total oxidation of methane, Applied Catalysis A: General, 2007, 323 226-233.

113. T. Striker, J. A. Ruud, Effect of fuel choice on the aqueous combustion synthesis of lanthanum ferrite and lanthanum manganite, Journal of the American Ceramic Society, 2010, 93, 2622-2629.

114. S. Specchia, A. Civera, G. Saracco, In situ combustion synthesis of perovskite catalysts for efficient and clean methane premixed metal burners, Chemical Engineering Science, 2004, 59, 5091-5098.

115. U. Zavyalova, B. Nigrovski, K. Pollok, F. Langenhorst, B. Muller, P. Scholz, B. Ondruschka, Gel-combustion synthesis of nanocrystalline spinel catalysts for VOCs elimination, Applied Catalysis B: Environmental, 2008, 83, 221-228.

116. X. Guo, D. Mao, S. Wang, G. Wu, G. Lu, Combustion synthesis of $CuO–ZnO–ZrO_2$ catalysts for the hydrogenation of carbon dioxide to methanol, Catalysis Communications, 2009, 10, 1661-1664.

117. X. Guo, D. Mao, G. Lu, S. Wang, G. Wu, Glycine–nitrate combustion synthesis of $CuO–ZnO–ZrO_2$ catalysts for methanol synthesis from $CO_2$ hydrogenation, Journal of Catalysis, 2010, 271, 178-185.

118. B. Murugan, A. V. Ramaswamy, D. Srinivas, C. S. Gopinath, V. Ramaswamy, Effect of fuel and its concentration on the nature of Mn in Mn/$CeO_2$ solid solutions prepared by solution combustion synthesis, Acta Materialia, 2008, 56, 1461-1472.

119. Y. Zhang, G. C. Stangle, Preparation of fine multicomponent oxide ceramic powder by a combustion synthesis process, Journal of Materials Research, 1994, 9, 1997-2004.

120. Q. Zhou, Y. Mou, X. Ma, L. Xue, Y. Yan, Effect of fuel-to-oxidizer ratios on combustion mode and microstructure of $Li_2TiO_3$ nanoscale powders, Journal of the European Ceramic Society, 2014, 34, 801-807.

121. S. Balakrishnan, D. S. Kumar, K. Ananthasivan, Gel-combustion synthesis of nanocrystalline cerium oxide and its powder characteristics, Transactions of the Indian Institute of Metals, 2015, 68, S243-S252.

122. T. Pine, X. Lu, R. Daniel, G. Mumm, J. S. Brouwer, Emission of pollutants from glycine – nitrate combustion synthesis processes, Journal of the American Ceramic Society, 2007, 90, 3735-3740.

123. S. Challagulla, S. Roy, The role of fuel to oxidizer ratio in solution combustion synthesis of $TiO_2$ and its influence on photocatalysis, Journal of Materials Research, 2017, 32, 2764-2772.

124. V. Bedekar, R. Shukla, A.K. Tyagi, Nanocrystalline $YCrO_3$ with onion-like structure and unusual magnetic behavior, Nanotechnology, 2007,18, 155706.

125. A. Civera, M. Pavese, G. Saracco, V. Specchia, Combustion synthesis of perovskite-type catalysts for natural gas combustion, Catalysis Today, 2003, 83, 199-211.

126. S. L. Gonzalez-Cortes, T. -C. Xiao, S.M.A. Rodulfo-Baechler, M. L. H. Green, Impact of the urea–matrix combustion method on the HDS performance of Ni-$MoS_2$/γ-$Al_2O_3$ catalysts, Journal of Molecular Catalysis A: Chemical, 2005, 240. 214-225.

127. F. Deganello, G. Marcì, G. Deganello, Citrate–nitrate auto-combustion synthesis of perovskite-type nanopowders: a systematic approach, Journal of the European Ceramic Society, 2009, 29, 439-450.

128. H. S. Potdar, S. B. Deshpande, Y. B. Khollam, A. S. Deshpande, S. K. Date, Synthesis of nanosized $Ce_{0.75}Zr_{0.25}O_2$ porous powders via an autoignition: glycine nitrate process, Materials Letters, 2003, 57, 1066-1071.

129. S. Colussi, A. Gayen, M. Boaro, J. Llorca, A. Trovarelli, Influence of different palladium precursors on the properties of solution-combustion-synthesized palladium/ceria catalysts for methane combustion, ChemCatChem, 2015, 7, 2222-2229.

130. M. Biswas, P. K. Ojha, C. D. Prasad, N. M. Gokhale, S. C. Sharma, Synthesis of fluorite-type nanopowders by citrate-nitrate auto-combustion process: a systematic approach, Materials Sciences and Applications, 2012, 3, 110-115.

131. P. Vijayadarshan, T. Mohan, J. Venkata Viswanath, K.J. Venugopal, N.V. Srinivasa Rao, Amarnath Gupta, A. Venkataraman, Large scale synthesis of nickel oxide (NiO) by self propagated combustion reaction, Material Science Research India, 2017, 14, 37-42.

132. B. Pourgolmohammad, S.M. Masoudpanah, M.R. Aboutalebi, Synthesis of $CoFe_2O_4$ powders with high surface area by solution combustion method: Effect of fuel content and cobalt precursor, Ceramics International, 2017, 43, 3797-3803

133. P. Kaur, S. K. Chawla, S. S. Meena, S. M. Yusuf, S. Bindra Narang, Synthesis of Co-Zr doped nanocrystalline strontium hexaferrites by sol-gel auto-combustion route using sucrose as fuel and study of their structural, magnetic and electrical properties, Ceramics International, 2016, 42, 14475-14489.

134. L. Ortega-San Martín, K. Vidal, B. Roldán-Pozo, Y. Coello, A. Larrañaga, M. I. Arriortua, Synthesis method dependence of the lattice effects in Ln0.5M0.5FeO3 perovskites (Ln=La and (Nd or Gd); M=Ba and (Ca or Sr)), Materials Research Express, 2016, 3, Article 056302

135. O. Burgos-Montes, R. Moreno, M. T. Colomer, J.C. Farinas, Influence of combustion aids on suspension combustion synthesis of mullite powders, Journal of the European Ceramic Society, 2006, 26, 3365-3372.

136. M. A. Gabal, E. A. Al-Harthy, Y. M. Al Angari, M. Abdel Salam, A. M. Asiri, Synthesis, characterization and magnetic properties of MWCNTs decorated with Zn-substituted MnFe2O4 nanoparticles using waste batteries extract, Journal of Magnetism and Magnetic Materials, 2016, 407, 175-181.

137. R. Choudhary, S. Koppala, S. Swamiappan, Bioactivity studies of calcium magnesium silicate prepared from eggshell waste by sol – gel combustion synthesis, Journal of Asian Ceramic Societies, 2015, 3, 173-177.

138. K. Rajeshwar, N. R. de Tacconi, Solution combustion synthesis of oxide semi-conductors for solar energy conversion and environmental remediation, Chemical Society Reviews, 2009, 38, 1984-1998.

139. W. Kang, D.O. Ozgur, A.Varma, Solution combustion synthesis of high surface area $CeO_2$ nanopowders for catalytic applications: reaction mechanism and properties, ACS Applied Nano Materials, 2018, 1, 675-685.

140. J. J. Kingsley, L. R. Pederson, Combustion synthesis of perovskite $LnCrO_3$ powders using ammonium dichromate, Materials Letters, 1993, 18, 89-96.

141. S. Sasikumar, R. Vijayaraghavan, Solution combustion synthesis of bioceramic calcium phosphates by single and mixed fuels — A comparative study, Ceramics International, 2008, 34, 1373-1379.

142. R. A. Adams, V. G. Pol, A. Varma, Tailored solution combustion synthesis of high performance ZnCo2O4 anode materials for lithium-ion batteries, Industrial & Engineering Chemistry Research, 2017, 56, 7173-7183.

143. S. R. Nair, R. D. Purohit, P. K. Sinha, A. K. Tyagi, Sr-doped LaCoO3 through acetate – nitrate combustion: effect of extra oxidant $NH_4NO_3$, Journal of Alloys and Compounds, 2009, 477, 644-647.

144. K. V. Manukyan, A. V. Yeghishyan, C. E. Shuck, D. O. Moskovskikh, S. Rouvimov, E. E. Wolf, A. S. Mukasyan, Mesoporous metal - silica materials: synthesis, catalytic and thermal properties, Microporous Mesoporous Materials, 2018, 257, 175-184.

145. M. Amala Sekar, G. Dhanaraj, H. L. Bhat, K. C. Patil, Synthesis of fine-particle titanates by the pyrolysis of oxalate precursors, Journal of Materials Science: Materials in Electronics, 1992, 3, 237-239.

146. M. G. Chourashiya, A. Urakawa, Solution combustion synthesis of highly dispersible and dispersed iridium oxide as an anode catalyst in PEM water electrolysis, Journal of Materials Chemistry A, 2017, 5, 4774-4778.

147. S. R. Jain, Solid propellants binders, Journal of Scientific and Industrial Research, 2002, 61, 899-911.

148. J. E. Tasca, C. E. Quincoces, A. Lavat, A. M. Alvarez, M. G. González, Preparation and characterization of $CuFe_2O_4$ bulk catalysts, Ceramics International, 2011,37, 803-812.

149. G. Avgouropoulos, J. Papavasiliou, T. Ioannides, Hydrogen production from methanol over combustion-synthesized noble metal/ceria catalysts, Chemical Engineering Journal, 2009, 154, 274-280.

150. A. S. Rogachev, A. S. Mukasyan, Combustion for Material Synthesis, CRC Press, 2014, New York, USA.

151. D. De Sloovere, W. Marchal, F. Ulu, T. Vranken, M. Verheijen, M.K. Van Bael, A. Hardy, Combustion synthesis as a low temperature route to $Li_4Ti_5O_{12}$ based powders for lithium ion battery anodes, RSC Advances, 2017, 7, 18745-18754.

152. L. Junliang, Z. Wei, G. Cuijing, Z. Yanwei, Synthesis and magnetic properties of quasi-single domain M-type barium hexaferrite powders via sol – gel auto-combustion:

Effects of pH and the ratio of citric acid to metal ions (CA/M), Journal of Alloys and Compounds, 2009, 479, 863-869.

153. B. Pourgolmohammad, S. M. Masoudpanah, M. R. Aboutalebi, Effect of starting solution acidity on the characteristics of CoFe powders prepared by solution combustion synthesis, Journal of Magnetism and Magnetic Materials, 2017, 424, 352-358.
154. N. Lwin, R. Othman, A.F.M. Noor, S. Sreekantan, R. Singh, C.-C. Tin, T.C. Yong, Influence of pH on the physical and electromagnetic properties of Mg – Mn ferrite synthesized by a solution combustion method, Mater. Charact. 110 (2015) 109 – 115.
155. P. Jaimeewong, M. Promsawat, S. Jiansirisomboon, A. Watcharapasorn, Influence of pH values on the surface and properties of BCZT nanopowders synthesized via sol-gel auto-combustion method, Surface and Coatings Technology, 2016, 306, 16-20.
156. H.-W. Kim, H.-E. Kim, J.C. Knowles, Improvement hydroxyapatite sol – gel coating on titanium with ammonium hydroxide addition, Journal of the American Ceramic Society, 2005, 88, 154-159.
157. O. V. Komova, V. I. Simagina, S. A. Mukha, O. V. Netskina, G. V. Odegova, O. A. Bulavchenko, A. V. Ishchenko, A. A. Pochtar, A modified glycine – nitrate combustion method for one-step synthesis of $LaFeO_3$ , Advanced Powder Technology, 2016, 27, 496-503.
158. W. Chen, F. Li, J. Yu, L. Liu, A facile and novel route to high surface area ceria-based nanopowders by salt-assisted solution combustion synthesis, Materials Science and Engineering, B, 2006, 133, 151-156.
159. Y. Tong, S. Zhao, X. Wang, L. Lu, Evaluation of simple, easily sintered $La_{0.7}Ca_{0.3}Cr_{0.9}7O_{3-\delta}$ perovskite oxide as novel interconnect material for solid oxide fuel cells Journal of Alloys and Compounds, 2009, 479, 764-768.
160. W. Chen, J. Hong, Y. Li, Facile fabrication of perovskite single-crystalline $LaMnO_3$ nanocubes via a salt-assisted solution combustion process, Journal of Alloys and Compounds, 2009, 484, 846-850.
161. W. Wen, J. M. Wu, Eruption combustion synthesis of NiO/Ni nanocomposites with enhanced properties for dye-absorption and lithium storage, ACS Applied Materials & Interfaces, 2011, 3, 10, 4112-4119.

162. X. Li, A. Dhanabalan, K. Bechtold, C. Wang, Binder-free porous core–shell structured Ni/NiO configuration for application of high performance lithium ion batteries, Electrochemistry Communications, 2010,12, 1222-1225.

163. M. Huang, M. Qin, D. Zhang, Y. Wang, Q. Wan, B. Jia, X. Qu, Q. He, Facile synthesis of sheet-like Fe/C nanocomposites by a combustion-based method, Journal of Alloys and Compounds, 2017, 695, 1870-1877.

164. X. Deng, K. Chen, H. Tüysüz, Protocol for the nanocasting method: preparation of ordered mesoporous metal oxides, Chemistry of Materials, 2017, 29, 40-52.

165. A. H. Lu, F. Schüth, Nanocasting: a versatile strategy for creating nanostructured porous materials, Advanced Materials, 2006, 18, 1793-1805.

166. V. Valtchev, L. Tosheva, Porous nanosized particles: preparation, properties, and applications, Chemical Reviews, 2013, 113, 6734-6760.

167. N. D. Petkovich, A. Stein, Controlling macro- and mesostructures with hierarchical porosity through combined hard and soft templating, Chemical Society Reviews, 2013, 42, 3721-3739.

168. A. Stein, B. E. Wilson, S.G. Rudisill, Design and functionality of colloidal-crystal-templated materials—chemical applications of inverse opals, Chemical Society Reviews, 2013, 42, 2763-2803.

169. W. Wen, J.-M. Wu, Nanomaterials via solution combustion synthesis: a step nearer to controllability, RSC Advances, 2014, 4, 58090-58100.

170. W. Wen, J. M. Wu, Y. D. Wang, Large-size porous ZnO flakes with superior gas-sensing performance, Applied Physics Letters, 2012, 100, 262111.

171. W. Wen, J.M. Wu, M.H. Cao, Facile synthesis of a mesoporous $Co_3O_4$ network for Li-storage via thermal decomposition of an amorphous metal complex, Nanoscale, 2014, 6, 12476-12481.

172. W. Brockner, C. Ehrhardt, M. Gjikaj, Thermal decomposition of nickel nitrate hexahydrate, $Ni(NO_3)_2\cdot 6H_2O$, in comparison to $Co(NO_3)_2\cdot 6H_2O$ and $Ca(NO_3)_2\cdot 4H_2O$, Thermochimica Acta, 2007, 456, 64−68.

173. J. Li, Z. Wang, X. Yang, L. Hu, Y. Liu, C. Wang, Evaluate the Pyrolysis Pathway of Glycine and Glycylglycine by TG−FTIR, Journal of Analytical and Applied Pyrolysis, 2007, 80, 247−253.

174. B. Liu, Y. Zhang, L. Zhang, Characteristics of $Ba_{0.5}Sr_{0.5}Co_{0.8}Fe_{0.2}O_{3-\delta}$–$La_{0.9}Sr_{0.1}Ga_{0.8}Mg_{0.2}O_{3-\delta}$ composite cathode for solid oxide fuel cell, Journal of Power Sources, 2008, 175, 189-195.

175. S. Saha, S. J. Ghanawat, R. D. Purohit, Solution combustion synthesis of nanoparticle $La_{0.9}Sr_{0.1}MnO_3$ powder by a unique oxidant-fuel combination and its characterization, Journal of Materials Science, 2006, 41, 1939-1943.

176. H. Mohebbi, T. Ebadzadeh, F.A. Hesari, Synthesis of nano-crystalline (Ni/NiO)-YSZ by microwave-assisted combustion synthesis method: the influence of pH of precursor solution, Journal of Power Sources, 2008, 178, 64-68.

177. S. R. Nair, R. D. Purohit, A. K. Tyagi, P. K. Sinha, B. P. Sharma, Role of glycine-to-nitrate ratio in influencing the powder characteristics of $La(Ca)CrO_3$, Materials Research Bulletin, 2008, 43, 1572-1582.

178. A. Lan, A. S. Mukasyan, Perovskite-based catalysts for direct methanol fuel, The Journal of Physical Chemistry C, 2007, 111, 9573-9582.

179. C. Agrafiotis, M. Roeb, A. G. Konstandopoulos, L. Nalbandian, V.T. Zaspalis, C. Sattler, et al., Solar water splitting for hydrogen production with monolithic reactors, Solar Energy, 2005, 79, 409-421.

180. M. Jayalakshmi, M. Palaniappan, K. Balasubramanian, Single step solution combustion synthesis of ZnO/carbon composite and its electrochemical characterization for supercapacitor application, International Journal of Electrochemical Science, 2008, 3, 96-10.

181. Y. X. Wen, H. Xiao, Y. L. Gan, H.F. Su, F. Wang, Self-propagating high temperature synthesis of $LiCoO_2$ as cathode material for lithium ion batteries, Journal of Inorganic Materials, 2008, 23, 286-290.

182. C. M. Wang, S. L. Chung, Dye-sensitized solar cell using a $TiO_2$ nanocrystalline film electrode prepared by solution combustion synthesis. In: Technical proceedings of the nanotechnology conference and trade show, Vol. 4, 2007, p. 606–609.

183. R. E. Muenchausen, E. A. McKigney, L. G. Jacobsohn, M. W. Blair, B. L. Bennett, D. W. Cooke, Science and application of oxyorthosilicate nanophosphors, IEEE Transactions on Nuclear Science, 2008, 55, 1532-1535.

184. Z. Qiu, Y. Zhou, M. Lü, A. Zhang, Q. Ma, Combustion synthesis of three-dimensional reticular -structured luminescence $SrAl_2O_4$:Eu, Dy nanocrystals, Solid State Sciences, 2008, 10, 629-633.

185. Y. Jin, W. P. Qin, J. S. Zhang, Y. Wang, C. Y. Cao, Synthesis of $Gd_3PO_7:Eu^{3+}$ nanospheres via a facile combustion method and optical properties, Journal of Solid State Chemistry, 2008, 181, 724-729.

186. X. M. Lou, D. H. Chen, Synthesis of $CaWO_4$: $Eu^{3+}$ phosphor powders via a combustion process and its optical properties, Materials Letters, 2008, 62, 1681-1684.

187. Z. Qiu, Y. Zhou, M. Lu, A. Zhang, Q. Ma, Combustion synthesis of long-persistent luminescent $MAl_2O_4:Eu^{2+}$, $R^{3+}$ (M = Sr, Ba, Ca, R = Dy, Nd and La) nanoparticles and luminescence mechanism research, Acta Materialia, 2007, 55, 2615-2620.

188. R. Krsmanovi´c, V.A. Morozov, O. I. Lebedev, S. Polizzi, A. Speghini, M. Bettinelli, et al., Structural and luminescence investigation on gadolinium gallium garnet nanocrystalline powders prepared by solution combustion synthesis, Nanotechnology, 2007, 18, 325604-325613.

189. L. Xu, B. Wei, Z. Zhang, Z. Lü, H. Gao, Y. Zhang, Synthesis and luminescence of europium doped yttria nanophosphors via a sucrose-templated combustion method, Nanotechnology, 2006, 17, 4327-4331.

190. A. Khort, K. Podbolotov, R. Serrano-García, Y. K. Gun'ko, One-step solution combustion synthesis of pure Ni nanopowders with enhanced coercivity: The fuel effect, Journal of Solid State Chemistry, 2017, 253, 270-276.

191. K. B. Podbolotov, A. A. Khort, A. B. Tarasov, G. V. Trusov, S. I. Roslyakov, A. S. Mukasyan, Solution combustion synthesis of copper nanopowders: The fuel effect, Combustion Science and Technology, 2017, 189, 1878-1890.

192. A. Aguilar-Tapia, L. Delannoy, C. Louis, C. W. Han, V. Ortalan, R. Zanella, Selective hydrogenation of 1, 3-butadiene over bimetallic Au-Ni/$TiO_2$ catalysts prepared by deposition-precipitation with urea, Journal of Catalysis, 2016, 344, 515-523.

193. Y. Bang, S. Park, S. J. Han, J. Yoo, J. H. Song, J. H. Choi, K. H. Kang, I. K. Song, Hydrogen production by steam reforming of liquefied natural gas (LNG) over mesoporous Ni/$Al_2O_3$ catalyst prepared by an EDTA-assisted impregnation method, Applied Catalysis B: Environmental, 2016, 180, 179-188.

194. A. Khaleel, M. Nawaz, The effect of composition and gel treatment conditions on the textural properties, reducibility, and catalytic activity of sol–gel-prepared Fe (III)–Cr (III) bulk mixed oxides, Colloids and Surfaces A: Physicochemical and Engineering Aspects, 2016, 488, 52-57.

195. N. Russo, D. Mescia, D. Fino, G. Saracco, V. Specchia, $N_2O$ decomposition over perovskite catalysts, Industrial & Engineering Chemistry Research, 2007, 46, 4226-4231.

196. N. F. P. Ribeiro, M. M. V. M. Souza, M. Schmal, Combustion synthesis of copper catalysts for selective CO oxidation, Journal of Power Sources, 2008, 179, 329-334.

197. S. Roy, M. S. Hegde, Pd ion substituted $CeO_2$: a superior de-NOx catalyst to Pt or Rh metal ion doped ceria, Catalysis Communications, 2008, 9, 811-815.

198. S. Schuyten, P. Dinka, A. S. Mukasyan, E. Wolf, A novel combustion synthesis preparation of $CuO/ZnO/ZrO_2/Pd$ for oxidative hydrogen production from methanol, Catalysis Letters, 2008, 121, 189-198.

199. Y. Z. Chen, W. Zhou, Z. P. Shao, N. P. Xu, Nickel catalyst prepared via glycine nitrate process for partial oxidation of methane to syngas, Catalysis Communications, 2008, 9, 1418-1425.

200. M. A. Naik, B. G. Mishra, A. Dubey, Combustion synthesized $WO_3$–$ZrO_2$ nanocomposites as catalyst for the solvent-free synthesis of coumarins, Colloids and Surfaces A: Physicochemical and Engineering Aspects, 2008, 317, 234-238.

201. W. Morales, M. Cason, O. Aina, N. R. de Tacconi, K. Rajeshwar, Combustion synthesis and characterization of nanocrystalline $WO_3$, Journal of the American Chemical Society, 2008, 130, 6318-6319.

202. T. Aarthi, G. Madras, Photocatalytic reduction of metals in presence of combustion synthesized nano-$TiO_2$, Catalysis Communications, 2008, 9, 630-634.

203. B. Nagappa, G. T. Chandrappa, Mesoporous nanocrystalline magnesium oxide for environmental remediation, Microporous and Mesoporous Materials, 2007, 106, 212-218.

204. K. Taniguchi, N. Okinaka, T. Akiyama, Preparation and characterization of $La_{1-x}K_xFeO_3$ (x=0-1) by self-propagating high-temperature synthesis for use as soot combustion catalyst, Journal of Alloys and Compounds, 2011, 509, 4084-4088.

205. P. S. Sathiskumar, C. R. Thomas, G. Madras, Solution combustion synthesis of nanosized copper chromite and its use as a burn rate modifier in solid propellants, Industrial & Engineering Chemistry Research, 2012, 51, 10108-10116.

206. C. H. Bartholomew, R. J. Farrauto, Fundamentals of Industrial Catalytic Processes, 2nd ed., Wiley-Interscience, NJ2006.

207. P. Erri, P. Dinka, A. Varma, Novel perovskite-based catalysts for autothermal JP-8 fuel reforming, Chemical Engineering Science, 2006,61, 5328-5333.

208. M. Piumetti, D. Fino, N. Russo, Mesoporous manganese oxides prepared by solution combustion synthesis as catalysts for the total oxidation of VOCs, Applied Catalysis B: Environmental, 2015,163, 277-287.

209. A. Singhania, V. V. Krishnan, A. N. Bhaskarwar, B. Bhargava,D. Parvatalu, S. Banerjee, Hydrogen production from the decomposition of hydrogen iodide over nanosized nickel-oxide-zirconia catalysts prepared by solution-combustion techniques, Catalysis Communications, 2017, 93, 5-9.

210. J. R. Rostrup-Nielsen, Conversion of hydrocarbons and alcohols for fuel cells, Physical Chemistry Chemical Physics, 2001,3, 283-288.

211. N. Iwasa, N. Takezawa, Reforming of Ethanol –Dehydrogenation to Ethyl Acetate and Steam Reforming to Acetic Acid over Copper-Based Catalysts, Bulletin of the Chemical Society of Japan, 1991, 64, 2619-2623.

212. A. Ashok, A. Kumar, R. Bhosale, M. A. Saleh Saad, F. Al Momani, F. Tarlochan, Study of ethanol dehydrogenation reaction mechanism for hydrogen production on combustion synthesized cobalt catalyst, International Journal of Hydrogen Energy, 2017,42, 23464-23473.

213. A. Kumar, A. Ashok, Y. Kuty, R. R. Bhosale, LJP van den Broke, Solution combustion synthesis of active catalysts for hydrogen production from ethanol, Conference: Proceedings of 2014 AIChE Annual Meeting, Atlanta, USA, Volume: ISBN 978-0-8169-1086-1.

214. A. Kumar, A. Cross, K. Manukyan, R.R. Bhosale, L. J. P. van den Broeke, J. T. Miller, A. S. Mukasyan, E. E. Wolf, Combustion synthesis of copper–nickel catalysts for hydrogen production from ethanol, Chemical Engineering Journal, 2015, 278, 46-54.

215. B. Roy, K. Artyushkova, H. N. Pham, L. Li, A. K. Datye, C. A. Leclerc, Effect of Preparation Method on the Performance of the Ni/$Al_2O_3$ Catalysts for Aqueous-Phase Reforming of Ethanol: Part II-Characterization, International Journal of Hydrogen Energy, 2012, 7, 18815−18826.

216. B. Roy, K. Loganathan, H. N. Pham, A. K. Datye, C.A. Leclerc, Surface Modification of Solution Combustion Synthesized Ni/$Al_2O_3$ Catalyst for Aqueous-Phase Reforming of Ethanol, International Journal of Hydrogen Energy, 2010, 35, 11700−11708.

217. B. Roy, U. Martinez, K. Loganathan, A. K. Datye, C.A. Leclerc, Effect of Preparation Methods on the Performance of Ni/$Al_2O_3$ Catalysts for Aqueous-Phase Reforming of Ethanol: Part I-Catalytic Activity, International Journal of Hydrogen Energy 2012, 37, 8143−8153.

218. B. Roy, C. A. Leclerc, Study of Preparation Method and Oxidization/reduction Effect on the Performance of Nickel-Cerium Oxide Catalysts for Aqueous-Phase Reforming of Ethanol, Journal of Power Sources 2015, 299, 114−124.

219. J. Agrell, H. Birgersson, M. Boutonnet, Steam reforming of methanol over a Cu/ZnO/$Al_2O_3$ catalyst: a kinetic analysis and strategies for suppression of CO formation, Journal of Power Sources, 2002, 106, 249-257.

220. M. Turco, G. Bagnasco, C. Cammarano, P. Senese, U. Costantino, M. Sisani, Cu/ZnO/$Al_2O_3$ catalysts for oxidative steam reforming of methanol: the role of Cu and the dispersing oxide matrix, Applied Catalysis B: Environmental, 2007, 77, 46-57.

221. Á. Mastalir, Á. Patzkó, B. Frank, R. Schomäcker, T. Ressler, R. Schlögl, Steam reforming of methanol over Cu/ZnO/$Al_2O_3$ modified with hydrotalcites, Catalysis Communications, 2007, 8, 1684-1690.

222. T. Conant, A. Karim, V. Lebarbier, Y. Wang, F. Girgsdies, R. Schlögl, A. Datye. Stability of bimetallic Pd–Zn catalysts for the steam reforming of methanol, Journal of Catalysis, 2008, 257, 64-70.

223. J. Baneshi, M. Haghighi, N. Jodeiri, M. Abdollahifar, H. Ajamein, Urea–nitrate combustion synthesis of $ZrO_2$ and $CeO_2$ doped CuO/$Al_2O_3$ nanocatalyst used in steam reforming of biomethanol for hydrogen production, Ceramics International, 2014, 40, 9A, 14177-14184.

224. R. Shokrani, M. Haghighi, N. Jodeiri, H. Ajamein, M. Abdollahifar, Fuel cell grade hydrogen production via methanol steam reforming over CuO/ZnO/$Al_2O_3$ nanocatalyst with various oxide ratios synthesized via urea-nitrates combustion method, International Journal of Hydrogen Energy, 2014, 39, 13141-13155.

225. H. Ajamein, M. Haghighi, R. Shokrani, M. Abdollahifar, On the solution combustion synthesis of copper based nanocatalysts for steam methanol reforming: effect of precursor, ultrasound irradiation and urea/nitrate ratio, Journal of Molecular Catalysis A: Chemical, 2016, 421, 222-234.

226. H. Ajamein, M. Haghighi, S. Alaei, S. Minaei, Ammonium nitrate-enhanced microwave solution combustion fabrication of CuO/ZnO/Al2O3 nanocatalyst for fuel cell grade hydrogen supply, Microporous and Mesoporous Materials, 2017, 245, 82-93.

227. H. Ajamein, M. Haghighi, S. Alaei, The role of various fuels on microwave-enhanced combustion synthesis of CuO/ZnO/$Al_2O_3$ nanocatalyst used in hydrogen production via methanol steam reforming, Energy Conversion and Management, 2017, 137, 61-73.

228. H. Ajamein, M. Haghighi, Influence of ambient gas on microwave-assisted combustion synthesis of CuO–ZnO–$Al_2O_3$ nanocatalyst used in fuel cell grade hydrogen production via methanol steam reforming, Ceramics International, 2016, 42, 17978-17989.

229. S. Maiti, J. Llorca, M. Dominguez, S. Colussi, A. Trovarelli, K. R. Priolkar, G. Aquilanti, A. Gayen, Combustion synthesized copper-ion substituted FeAl2O4 ($Cu_{0.1}Fe_{0.9}Al_2O_4$): A superior catalyst for methanol steam reforming compared to its impregnated analogue, Journal of Power Sources, 2016, 304, 319-331.

230. T. Nguyen, G. Postole, S. Loridant, F. Bosselet, L. Burel, M. Aouine, L. Massin, P. Gélin, F. Morfin and L. Piccolo, Ultrastable iridium–ceria nanopowders synthesized in one step by solution combustion for catalytic hydrogen production, Journal of Materials Chemistry A, 2014, 2, 19822-19832.

231. G. Postole, T. Nguyen, M. Aouine, P. Gélin, L. Cardenas, L. Piccolo, Efficient hydrogen production from methane over iridium-doped ceria catalysts synthesized by solution combustion, Applied Catalysis B: Environmental, 2015, 166–167, 580-591.

232. A. Vita, G. Cristiano, C. Italiano, L. Pino, S. Specchia, Syngas production by methane oxysteam reforming on Me/$CeO_2$ (Me=Rh, Pt, Ni) catalyst lined on cordierite monoliths, Applied Catalysis B: Environmental, 2015, 162, 551-563.

233. W. Edelmann Biogas production and usage. In: Kaltschmitt M, Hartmann H (Eds.), Energy from biomass: basic principles, technologies and processes, Springer Leipzig, Germany, 2001.

234. G. Alkanok, B. Demirel, T.T. Onay. Determination of biogas generation potential as a renewable energy source from supermarket wastes, Waste Management 34, 2014, 134-140.

235. I. Wheeldon, C. Caners, K. Karan, Brant Peppleyd, Utilization of biogas generated from Ontario wastewater treatment plants in solid oxide fuel cell systems: A process modeling study, International Journal of Green Energy, 2007, 4, 221-231.

236. J. Xuan, M. K. H. Leung, D. Y. C. Leung, M. Ni, A review of biomass-derived fuel processors for fuel cell systems, Renewable & Sustainable Energy Reviews, 2009, 13, 1301-1313.

237. M. Ashrafi, T. Proll, C. Pfeifer, H. Hofbauer, Experimental study of model biogas catalytic steam reforming: 1. thermodynamic optimization, Energy Fuels, 2008, 22, 4182-4189.

238. A. Vita, M. A. Ashraf, C. Italiano, C. Fabiano, L. Pino, S. Specchia, Syngas Production By Biogas Steam and Oxy Steam Reforming Processes on Rh/$CeO_2$ Catalyst Coated on Ceramics Monolith and Open Foams, 2015 AIChE Annual Meeting, Salt Lake City, United States.

239. C. Italiano, A. Vita, C. Fabiano, M. Laganà, L. Pino, Bio-hydrogen production by oxidative steam reforming of biogas over nanocrystalline Ni/$CeO_2$ catalysts, International Journal of Hydrogen Energy, 2015, 40, 35, 11823-11830.

240. A. Iulianelli, S. Liguori, A. Vita, C. Italiano, C. Fabiano, Y. Huang, A. Basile, The oncoming energy vector: Hydrogen produced in Pd-composite membrane reactor via bioethanol reforming over Ni/$CeO_2$ catalyst, Catalysis Today, 2016, 259, 368-375.

241. A. Vita, C. Italiano, C. Fabiano, M. Laganà, L. Pino, Influence of Ce-precursor and fuel on structure and catalytic activity of combustion synthesized Ni/$CeO_2$ catalysts for biogas oxidative steam reforming, Materials Chemistry and Physics, 2015, 163, 337-347.

242. S. Specchia, G. Ercolino, S. Karimi, C. Italiano, A. Vita, Solution combustion synthesis for preparation of structured catalysts: A mini-review on process intensification for energy applications and pollution control, International Journal of Self-Propagating High-Temperature Synthesis, 2017, 26, 166-186.

243. C. Italiano, R. Balzarotti, A. Vita, S. Latorrata, C. Fabiano, L. Pino, C. Cristiani, Preparation of structured catalysts with Ni and Ni–Rh/$CeO_2$ catalytic layers for syngas production by biogas reforming processes, Catalysis Today, 2016, 273, 3-11.

244. A. Vita, C. Italiano, C. Fabiano, L. Pino, M. Laganà, V. Recupero, Hydrogen-rich gas production by steam reforming of *n*-dodecane: Part I: Catalytic activity of Pt/$CeO_2$ catalysts in optimized bed configuration, Applied Catalysis B: Environmental, 2016, 199, 350-360.

245. K. Liu, A. Wang, T. Zhang, Recent Advances in Preferential Oxidation of CO Reaction over Platinum Group Metal Catalysts, ACS Catalysis, 2012, 2, 1165–1178.

246. P. S. Barbato, S. Colussi, A. Di Benedetto, G. Landi, L. Lisi, J. Llorca, A. Trovarelli, Origin of high activity and selectivity of $CuO/CeO_2$ catalysts prepared by solution combustion synthesis in CO-PROX reaction, *The Journal of Physical Chemistry C*, 2016, 120, 13039-13048.

247. T. S. Nguyen, F. Morfin, M. Aouine, F. Bosselet, J. L. Rousset, L. Piccolo, Trends in the CO oxidation and PROX performances of the platinum-group metals supported on ceria, Catalysis Today, 2015, 253, 106-114.

248. G. Xanthopoulou, V. Novikov, Yu. Knysh, A. Amosov, Nanocatalysts for low-temperature oxidation of CO: Review, Eurasian Chemico-Technological Journal, 2015, 17, 17-32.

249. V. Novikov, G. Xanthopoulou, Yu. Knysh, A. P. Amosov, Solution Combustion Synthesis of nanoscale Cu-Cr-O spinels: Mechanism, properties and catalytic activity in CO oxidation, Ceramics International, 2017, 43, 11733-11742.

250. S. A. Singh, G. Madras, Detailed mechanism and kinetic study of CO oxidation on cobalt oxide surfaces, Applied Catalysis A: General, 2015, 504, 463-475.

251. P. Bera, M. S. Hegde, Noble Metal Ions in $CeO_2$ and $TiO_2$: Synthesis, Structure and Catalytic Properties, RSC Advances, 2015, 5, 94949-94979.

252. I. V. Desyatykh, A. A. Vedyagin, I. V. Mishakovb, Yu. V. Shubin, CO oxidation over fiberglasses with doped Cu-Ce-O catalytic layer prepared by surface combustion synthesis, Applied Surface Science, 2015, 349, 21-26.

253. T. Mitsui, T. Matsui, R. Kikuchi, K. Eguchi, Low-temperature complete oxidation of ethyl acetate over $CeO_2$-supported precious metal catalysts, Topics in Catalysis, 2009, 52, 465-469.

254. L. Pinard, J. Mijoin, P. Magnoux, M. Guisnet, Oxidation of chlorinated hydrocarbons over Pt zeolite catalysts 1-mechanism of dichloromethane transformation over PtNaY catalysts, Journal Catalysis, 2003, 215, 234-244.

255. G. Ertl, H. Knözinger, F. Schüth, J. Weitkamp, Handbook of Heterogeneous Catalysis, 2nd edition, Weinheim, Wiley-VCH, 2008, pp. 2394-2411.

256. B.K. Hodnett, Heterogeneous Catalytic Oxidation, Wiley-VCH, New York, 2000, pp. 189-238.

257. B. Farin, A. H. A. M. Videla, S. Specchia, E. M. Gaigneaux, Bismuth molybdates prepared by solution combustion synthesis for the partial oxidation of propene, Catalysis Today, 2015, 257, Part 1, 11-17.

258. G. Ercolino, G. Grzybek, P. Stelmachowski, S. Specchia, A. Kotarba, V. Specchia, Pd/$Co_3O_4$-based catalysts prepared by solution combustion synthesis for residual methane oxidation in lean conditions, Catalysis Today, 2015, 257, Part 1, 66-71.

259. Q. Wang, Y. Peng, J. Fu, G. Z. Kyzas, S. M. Reduwan Billah, S. An, Synthesis, characterization, and catalytic evaluation of Co3O4/γ-Al2O3 as methane combustion catalysts: Significance of Co species and the redox cycle, Applied Catalysis B: Environmental, 2015, 168–169, 42-50.

260. S. Bensaid, J. C. Caroca, N. Russo, D. Fino, Detailed investigation of non-catalytic DPF regeneration, The Canadian Journal of Chemical Engineering, 2011, 89, 401-407.

261. A. Trovarelli, P. Fornasiero, Catalysis by Ceria and related Materials, 2nd edition, Imperial College Press, London, 2013, pp. 565-621.

262. A. Bueno-López, Diesel Soot combustion ceria catalysts, Applied Catalysis B: Environmental, 2014, 146, 1-11.

263. E. Aneggi, D. Wiater, C. de Leitenburg, J. Llorca, A. Trovarelli, Shape-dependent activity of ceria in soot combustion, ACS Catalysis, 2014, 4, 172-181.

264. M. Piumetti, S. Bensaid, N. Russo, D. Fino, Nanostructured ceria-based catalysts for soot combustion: investigations on the surface sensitivity, Applied Catalysis B: Environmental, 2015, 165, 742-751.

265. M. Piumetti, S. Bensaid, T. Andana, N. Russo, R. Pirone, D. Fino, Cerium-copper oxides prepared by solution combustion synthesis for total oxidation reactions: From powder catalysts to structured reactors, Applied Catalysis B: Environmental, 2017, 205, 455-468.

266. S. E. Allen, R. R. Walvoord, R. Padilla-Salinas, M. C. Kozlowski, Aerobic copper-catalyzed organic reactions, Chemical Reviews, 2013, 113, 6234-6645.

267. G. E. Dobereiner, R. H. Crabtree, Dehydrogenation as a substrate-activating strategy in homogeneous transition-metal catalysis, Chemical Reviews, 2010, 110, 681-703.

268. B. L. Ryland, S. S. Stahl, Practical aerobic oxidations of alcohols and amines with homogeneous copper/TEMPO and related catalyst systems, Angewandte Chemie International Edition, 2014, 53, 8824-8838.

269. M. Trincado, D. Banerjee, H. Grutzmacher, Molecular catalysts for hydrogen production from alcohols, Energy & Environmental Science, 2014, 7, 2464-2503.

270. M. N. Kopylovich, A. P. C. Ribeiro, E. C. B. A. Alegria, N. M. R. Martins, L. M. D. R. S. Martins, A. J. L. Pombeiro, Chapter Three - Catalytic Oxidation of Alcohols: Recent Advances, Advances in Organometallic Chemistry, 2015, 63, 91-174.

271. J. March, Advanced Organic Chemistry: Reactions, Mechanisms, and Structure, 3rd edition, Wiley, New York, 1985, ISBN 0-471-85472-7.

272. C. Ragupathi, J. J. Vijaya, R. T. Kumar, L. J. Kennedy, Selective liquid phase oxidation of benzyl alcohol catalyzed by copper aluminate nanostructures, Journal of Molecular Structure, 2015, 1079, 182-188.

273. C. Ragupathi, J. J. Vijaya, S.Narayanan, S. K. Jesudoss, L. J. Kennedy, Highly selective oxidation of benzyl alcohol to benzaldehyde with hydrogen peroxide by cobalt aluminate catalysis: A comparison of conventional and microwave methods, Ceramics International, 2015, 41, Part A, 2069-2080.

274. C. Ragupathi, J. J. Vijaya, L. J. Kennedy, Preparation, characterization and catalytic properties of nickel aluminate nanoparticles: A comparison between conventional and microwave method, Journal of Saudi Chemical Society, 2017, 21, S231-S239.

275. A. Manikandan, M. Durka, S. Arul Antony, One-pot flash combustion synthesis, structural, morphological and opto-magnetic properties of spinel $Mn_xCo_{1-x}Al_2O_4$ ($x$ = 0, 0.3, and 0.5) nanocatalysts, Journal of Superconductivity and Novel Magnetism, 2015, 28, 209-218.

276. S. Jayasree, A. Manikandan, A. M. U. Mohideen, C. Barathiraja, S. Arul Antony, Comparative study of combustion methods, opto-magnetic and catalytic properties of spinel $CoAl_2O_4$ nano- and microstructures, Advanced Science, Engineering and Medicine, 2015, 7, 672-682.

277. S. Cimino, R. Nigro, U. Weidmann, R. Holzner, Catalytic combustion of methanol over La, Mn-hexaaluminate catalysts, Fuel Processing Technology, 2015,133, 1-7.

278. S. L. Ma, Y. S. Tan, Y. Z. Han, Methanation of syngas over coral reef-like $Ni/Al_2O_3$ catalysts, Journal of Natural Gas Chemistry, 2011, 20, 435-440.

279. F. B. Derekaya, G. Yaşar, The CO methanation over NaY-zeolite supported $Ni/Co_3O_4$, $Ni/ZrO_2$, $Co_3O_4/ZrO_2$ and $Ni/Co_3O_4/ZrO_2$ catalysts

280. W. M. Budzianowski, R. Miller, Superadiabatic lean catalytic combustion in a high-pressure reactor, International Journal of Chemical Reactor Engineering, 2009, 7, Article A20.

281. J. J. Gao, Q. Liu, F. N. Gu, B. Liu, Z.Y. Zhong, F.B. Su, Recent advances in methanation catalysts for the production of synthetic natural gas, RSC Advances, 2015, 5, 22759-22776.

282. D. Y. Tian, Z. H. Liu, D. d. Li, H.L. Shi, W. X. Pan, Y. Cheng, Bimetallic Ni–Fe total-methanation catalyst for the production of substitute natural gas under high pressure, Fuel, 2013, 104, 224-229.

283. P. Sabatier, J. B. Senderens, Hydrogenation of CO over nickel to produce methane, Journal of the Indian Chemical Society, 1902, 21, 504-506.

284. J. Ji, X.Z. Duan, G. Qian, X.G. Zhou, D. Chen, W.K. Yuan, In situ production of Ni catalysts at the tips of carbon nanofibers and application in catalytic ammonia decompositionIndustrial & Engineering Chemistry Research, 2013, 52, 1854-1858.

285. Y Zeng, H Ma, H Zhang, W Ying, D Fang, Ni–Ce–Al composite oxide catalysts synthesized by solution combustion method: Enhanced catalytic activity for CO methanation, Fuel, 2015, 165, 16-22.

286. Z. Zhang, G. Xu, Thermally differential methanation–A novel method to realize highly selective removal of CO from $H_2$-rich reformates, Catalysis Communications, 2007, 8, 1953-1956.

287. K. K. Mohaideen, W. K. Wang, L. Yoon, Highly efficient non-noble metal based nanostructured catalysts for selective CO methanation, Catalysis Communications, 2015, 71, 7-12.

288. A. Zhao, W. Ying, H. Zhang, H. Ma, D. Fang, Ni–$Al_2O_3$ catalysts prepared by solution combustion method for syngas methanation, Catalysis Communications, 2012, 17, 34-38.

289. Y. Zeng, H. Ma, H. Zhang, W. Ying, D. Fang, Highly efficient $NiAl_2O_4$-free Ni/γ-$Al_2O_3$ catalysts prepared by solution combustion method for CO methanation, Fuel, 2014, 137, 155-163.

290. Y. Zeng, H. Ma, H. Zhang, W. Ying, Na promoted $NiAl_2O_3$ catalysts prepared by solution combustion method for syngas methanation, International Journal of Chemical, Molecular, Nuclear, Materials and Metallurgical Engineering, 2014, 8, 649-653.

291. Y. Gao, F. Meng, K. Ji, Y. Song, Z. Li, Slurry phase methanation of carbon monoxide over nanosized Ni–$Al_2O_3$ catalysts prepared by microwave-assisted solution combustion, Applied Catalysis A: General, 2016, 510, 74-83.

292. R. Mistri, J. Llorca, B. C. Ray, A. Gayen, $Pd_{0.01}Ru_{0.01}$ $Ce_{0.98}O_{2-\delta}$: A highly active and selective catalyst for the liquid phase hydrogenation of p-chloronitrobenzene under ambient conditions, Journal of Molecular Catalysis A: Chemical, 2013, 376, 111-119.

293. F. Ren, H. Li, D. Wang, J. Wang, Methanol synthesis from syngas in a slurry reactor, American Chemical Society Division of Fuel Chemistry, 2003, 48, 921-922.

294. L. Shi, K. Tao, R. Yang, F. Meng, C. Xing, N. Tsubaki, Study on the preparation of Cu/ZnO catalyst by sol–gel auto-combustion method and its application for low-temperature methanol synthesis, Applied Catalysis A: General, 2011, 401, 46-55.

295. L. Shi, C. Zeng, Y. Jin, T. Wang, N. Tsubaki, A sol–gel auto-combustion method to prepare Cu/ZnO catalysts for low-temperature methanol synthesis, Catalysis Science & Technology, 2012, 2, 2569-2577.

296. L. Shi, K. Tao, R. Yang, F. Meng, C. Xing, N. Tsubaki, Surface impregnation combustion method to prepare nanostructured metallic catalysts without further reduction: As-burnt Cu–ZnO/$SiO_2$ catalyst for low-temperature methanol synthesis, Catalysis Today, 2012, 185, 54-60.

297. W. Wang, S. Wang, X. Ma, J. Gong, Recent advances in catalytic hydrogenation of carbon dioxide, Chemical Society Reviews, 2011, 40, 3703-3727.

298. M. A. Rauf, S. S. Ashraf, Fundamental principles and application of heterogeneous photocatalytic degradation of dyes in solution, Chemical Engineering Journal, 2009,151, 10-18.

299. V. K. Pandit, S. S. Arbuj, Y. B. Pandit, S. D. Naik, S. B. Rane, U. P.Mulik, S. W. Gosavic, B. B. Kale, Solar light driven dye degradation using novel organo–inorganic (6,13-Pentacenequinone/$TiO_2$) nanocomposite, RSC Advances, 2015, 5, 10326-10331.

300. S. Challagulla, R. Nagarjuna, R. Ganesan, S. Roy, $TiO_2$ synthesized by various routes and its role on environmental remediation and alternate energy production, Nano-structures &Nano-Objects, 2017,12, 147-156.

301. P. D. Bhange, S. V. Awate, R. S. Gholap, G. S. Gokavi, D. S. Bhang, Photocatalytic degradation of methylene blue on Sn-doped titania nanoparticles synthesized by solution combustion route, Materials Research Bulletin, 2016, 76, 264.

302. R. Bakkiyaraj, M. Balakrishnan, Physical, optical and photochemical properties of $CeO_2$ nanoparticles synthesized by solution combustion method, Journal of Advanced Physics, 2017, 6, 41-47.

303. T. N. Ravishankar, T. Ramakrishnappa, G. Nagaraju, H. Rajanaika, Synthesis and characterization of $CeO_2$ nanoparticles via solution combustion method for photocatalytic and antibacterial activity studies, Chemistry Open, 2015, 4, 146-154.

304. P. Kumaran, S. Mohanamurugan, P. Shankar, P. Vijayanand, R. Narayanan, Wash coating of ceramic honeycomb with Ce–Al–Mn mixed oxides for no catalytic reduction in diesel engines, Journal of Engineering and Applied Sciences, 2016, 11, 11112-11116.

305. B. Rahmani, V. M. Haghighi, Urea-nitrate combustion synthesis of MgO/MgAl2O4 nanocatalyst used in biodiesel production from sunflower oil: Influence of fuel ratio on catalytic properties and performance, Energy Conversion and Management, 2016, 126, 362-372.

306. S. Andreoli, F. A. Deorsola, R. Pirone, MnOx-$CeO_2$ catalysts synthesized by solution combustion synthesis for the low-temperature NH3-SCR, Catalysis Today, 2015, 253, 99-206.

307. S. Lee, M. Bae, J. Bae, S. P. Katikaneni, Ni–Me/$Ce_{0.9}Gd_{0.1}O_{2-x}$ (Me: Rh, Pt and Ru) catalysts for diesel pre-reforming, International Journal of Hydrogen Energy, 2015, 40, 3207-3216.

308. T. L. Pfeil, T. L. Pourpoint, L. J. Groven, Effects of crystallinity and morphology of solution combustion synthesized $Co_3O_4$ as a catalyst precursor in hydrolysis of sodium borohydride, International Journal of Hydrogen Energy, 2014, 39, 2149-2159.

309. G. Xanthopoulou, A. Marinou, K. Karanasios, G. Vekinis, Combustion synthesis during flame spraying (“CAFSY”) for the production of catalysts on substrates, Coatings, 2017, 7, 14.

310. D. V. Sokolsky, A. M. Sokolskaya, Metals – Catalysts of hydrogenation, Nauka, Alma – Ata, 1970.

311. G. E. M. Jauncey, The scattering of x-rays and Bragg's law, Proceedings of the National Academy of Sciences, 1924, 10, 57-60.

312. A. L. Patterson, The Scherrer Formula for X-Ray Particle Size Determination, Physical Review, 1939, 56, 978-982.

313. S. Brunauer, P. H. Emmett, E. Teller, Adsorption of Gases in Multimolecular Layers, Journal of the American Chemical Society, 1938, 60, 2, 309–319.

314. K. S. W. Sing, D. H. Everett, R. A. W. Haul, L. Moscou, R. A. Pierotti, J. Rouquerol, T. Siemieniewska, Reporting physisorption data for gas/solid systems with special

reference to the determination of surface area and porosity, Pure and Applied Chemistry, 1985, 57, 603-619.

315. B. Nie, X. Liu, L. Yang, J. Meng, X. Li, Pore structure characterization of different rank coals using gas adsorption and scanning electron microscopy, Fuel, 2015, 158, 908-917.

316. N. A. Katsanos, G. Karaiskakis, Time-resolved inverse gas chromatography and its practical applications, 1st edition, HNB Publishing, New York, 2004, ISBN: 0-9728061-0-5.

317. E. Metaxa, A. Kolliopoulos, T. Agelakopoulou, F. Roubani-Kalantzopoulou, The role of surface heterogeneity and lateral interactions in the adsorption of volatile organic compounds on rutile surface, Applied Surface Science, 2009, 255, 13-14, 6468-6478.

318. I. Arvaniti, V. Netos, V. Siokos, E. Metaxa, F. Roubani-Kalantzopoulou, Relation between adsorption and catalysis in the case of NiO and $Co_3O_4$, Applied Surface Science, 2010, 256, 17, 5559-5565.

319. E. Metaxa, Air pollution and cultural heritage searching for the relation between cause and effect, School of Chemical Engineering, National Technical University of Athens, August 2011, Athens, Greece.

320. A. M. M. Santos, W. L. Vasconcelos, Obtention of nanostructured silica glass by sol-gel process with incorporation of lead compounds, Materials Research, 1999, 2, 3.

321. J.L. Carter, J.A. Cusumano, J.H. Sinfelt, Catalysis over supported metals. V. The effect of crystallite size on the catalytic activity of nickel, The Journal of Physical Chemistry, 1966, 70, 2257-2263.

322. G. Xanthopoulou, O. Thoda, S. Roslyakov, A. Steinman, E. Levashov, D. Kovalev, G. Vekinis, A. Sytschev, A. Chroneos, Solution combustion synthesis of nano-catalysts with a hierarchical structure, Journal of Catalysis, 2018, 364, 112-124.

323. P. Heinrich, Course of Inorganic Chemistry Vol. 2, Akademische Verlagsgesellschaft, Leipzig, Germany, 1961.

324. I. A. Zoubovich, , Inorganic Chemistry, Nauka, Moscow, Russia, 1989.

325. Semenov, N.N., Some Problems in Chemical Kinetics and Reactivity. Parts 1 and 2, London, U. K.: Pergamon Press, 1959.

326. Prokof’ev, V.G. and Smolyakov, V.K., Non-stationary combustion regimes in gasless systems with a low-melting inert component, Combust. Explo. Shock+, 2002, vol. 38, pp. 143.

327. R. N. Ripan, I. Chetyanou, Neorganicheskaya khimiya (Inorganic Chemistry), Mir, vol.2, Moscow, 1972.

328. L. E. Shea, J. McKittrick, O. A. Lopez, Synthesis of red-emitting, small particle size luminescent oxides using an optimized combustion process, Journal of the American Chemical Society, 1996, 79, 3257-3265.

329. E. El-Shereafy, M. M. Abousekkina, A. Mashaly, M. El-Ashry, Mechanism of thermal decomposition and γ-pyrolysis of aluminum nitrate nonahydrate [$Al(NO_3)_3{\cdot}9H_2O$], Journal of Radioanalytical and Nuclear Chemistry, 1998, 237, 183-186.

330. V. D. Zhuravlev, V. G. Vasil'ev, E. V. Vladimirova, V. G. Shevchenko, I. G. Grigorov, V. G. Bamburov, A. R. Beketov, M. V. Baranov, Glycine–nitrate combustion synthesis of finely dispersed alumina, Glass Physics and Chemistry, 2010, 36, 506-512.

331. R. Khanna, M. Ikram-Ul-Haq, S. F. Sadi, V. Sahajwalla, P. S. Mukherjee, S. Seetharaman Reduction reactions in $Al_2O_3$-C-Fe and Al $_2O_3$-$Fe_2O_3$-C systems at 1823K, ISIJ International, 2014, 54, 1485–1490.

332. N. M. Deraz, Synthesis and characterization of nano-sized nickel aluminate spinel crystals, International Journal of Electrochemical Science, 2013, 8, 5203-5212.

333. R. Koirala, S. E. Pratsinis, A. Baiker, Synthesis of catalytic materials in flames: opportunities and challenges, Chemical Society Reviews, 2016, 45, 3053-3068.

334. A. Marinou, O. Thoda, G. Xanthopoulou, G. Vekinis, Ni-based catalytic coatings synthesized by in-flight SCS during flame spraying, XIV International Symposium on Self-Propagating High-Temperature Synthesis, September 25-28, 2017, Tbilisi, Georgia, pp.292-295.

335. S. K. Sharna, F. J. Vastola, P. L. Walker Jr., Reduction of nickel oxide by carbon, Carbon, 1996, 34, 1407-1412.

336. J. H. Krasuk, J. M. Smith, Kinetics of reduction of nickel oxide with CO, AlChe journal, 1972, 18, 506-512.

337. Alkyne Selective Hydrogenation with Mono- and Bimetallic- Anchored Catalysts, in New Advances in Hydrogenation Processes, Editor: Maryam Takht Ravanchi, Cecilia Lederhos, Carolina Betti, Domingo Liprandi, Edgardo Cagnola and Mónica Quiroga, January 2017, Iran, Iran Polymer and Petrochemical Institute, ISBN: 978-953-51-2870-0

338. Liquid Phase Oxidation via Heterogeneous Catalysis: Organic Synthesis and Industrial Applications, Editors: Mario G. Clerici, Oxana A. Kholdeeva, April 2013, New Jersey, USA, John Wiley & Sons, Inc. ISBN:9780470915523.

# Appendix

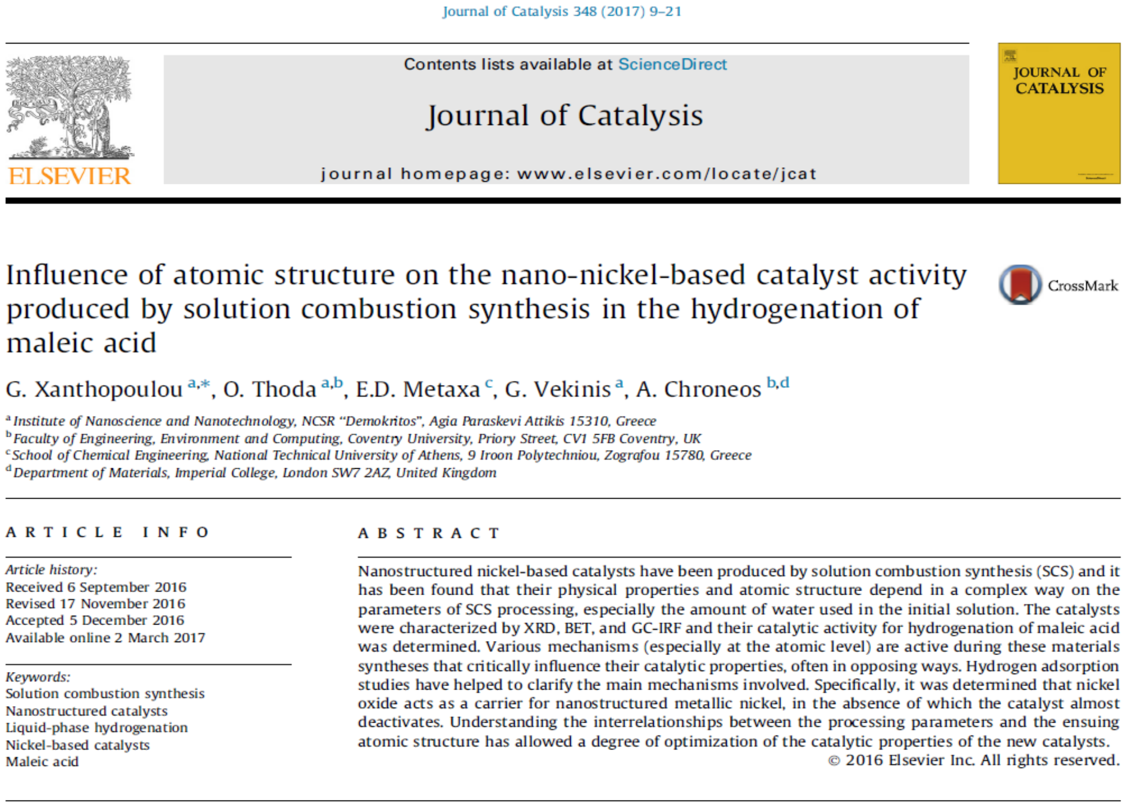

Journal of Catalysis 348 (2017) 9–21

Contents lists available at ScienceDirect

Journal of Catalysis

journal homepage: www.elsevier.com/locate/jcat

## Influence of atomic structure on the nano-nickel-based catalyst activity produced by solution combustion synthesis in the hydrogenation of maleic acid

G. Xanthopoulou [a,*], O. Thoda [a,b], E.D. Metaxa [c], G. Vekinis [a], A. Chroneos [b,d]

[a] *Institute of Nanoscience and Nanotechnology, NCSR "Demokritos", Agia Paraskevi Attikis 15310, Greece*
[b] *Faculty of Engineering, Environment and Computing, Coventry University, Priory Street, CV1 5FB Coventry, UK*
[c] *School of Chemical Engineering, National Technical University of Athens, 9 Iroon Polytechniou, Zografou 15780, Greece*
[d] *Department of Materials, Imperial College, London SW7 2AZ, United Kingdom*

ARTICLE INFO

*Article history:*
Received 6 September 2016
Revised 17 November 2016
Accepted 5 December 2016
Available online 2 March 2017

*Keywords:*
Solution combustion synthesis
Nanostructured catalysts
Liquid-phase hydrogenation
Nickel-based catalysts
Maleic acid

ABSTRACT

Nanostructured nickel-based catalysts have been produced by solution combustion synthesis (SCS) and it has been found that their physical properties and atomic structure depend in a complex way on the parameters of SCS processing, especially the amount of water used in the initial solution. The catalysts were characterized by XRD, BET, and GC-IRF and their catalytic activity for hydrogenation of maleic acid was determined. Various mechanisms (especially at the atomic level) are active during these materials syntheses that critically influence their catalytic properties, often in opposing ways. Hydrogen adsorption studies have helped to clarify the main mechanisms involved. Specifically, it was determined that nickel oxide acts as a carrier for nanostructured metallic nickel, in the absence of which the catalyst almost deactivates. Understanding the interrelationships between the processing parameters and the ensuing atomic structure has allowed a degree of optimization of the catalytic properties of the new catalysts.

Journal of Catalysis 364 (2018) 112–124

Contents lists available at ScienceDirect

Journal of Catalysis

journal homepage: www.elsevier.com/locate/jcat

# Solution combustion synthesis of nano-catalysts with a hierarchical structure

G. Xanthopoulou [a,*], O. Thoda [a,b], S. Roslyakov [c], A. Steinman [c], D. Kovalev [d], E. Levashov [c], G. Vekinis [a], A. Sytschev [d], A. Chroneos [b]

[a] *Institute of Nanoscience and Nanotechnology, NCSR "Demokritos", Agia Paraskevi Attikis 15310, Greece*
[b] *Faculty of Engineering, Environment and Computing, Coventry University, Priory Street, CV1 5FB Coventry, UK*
[c] *National University of Science and Technology "MISIS", Moscow 119049, Russia*
[d] *Institute of Structural Macrokinetics and Materials Science, Russian Academy of Sciences Chernogolovka, Moscow Region, Russia*

ARTICLE INFO

*Article history:*
Received 19 January 2018
Revised 20 March 2018
Accepted 4 April 2018
Available online 31 May 2018

*Keywords:*
Solution combustion synthesis
Nano catalysts
Liquid-phase hydrogenation
Nickel-based catalysts

ABSTRACT

The structure, composition, surface area and catalytic activity of Solution Combustion Synthesis (SCS) catalysts are all influenced by the conditions of preparation and in particular, the glycine concentration in the initial SCS solution. NMR was used to monitor the formation of glycine-nickel nitrate complexes in solution before SCS initiates, IR high speed temperature measurements have allowed to elucidate the mechanism of synthesis during SCS, dynamic X-ray analysis and thermogravimetric analysis have clarified the mechanisms of phase formation during SCS, BET analyses have shown the regularity of pore formation and SEM and TEM studies have indicated the regularities involved during microstructure formation. Regular three-dimensional (3D) flowerlike Ni-NiO hierarchical architectures were synthesized by SCS. The results have revealed a three-dimensional percolation network with hierarchical structure on the basis of nano-structured metal oxides and metals synthesized during SCS. Such hierarchically nanoporous catalysts have versatile structural properties such as increased surface area and large overall pore volume that can alleviate diffusional limitations of conventional nanocatalysts with solely microporous framework. This is important for liquid phase heterogeneous catalysis. These new insights provide a valuable capability for optimizing the selectivity and activity of SCS catalysis and will no doubt be of significant interest to a wide range of researchers working in catalysis and other fields.

# Review of Recent Studies on Solution Combustion Synthesis of Nanostructured Catalysts

*Olga Thoda, Galina Xanthopoulou,* George Vekinis, and Alexandros Chroneos*

**Solution combustion synthesis (SCS) is a relatively new method for synthesizing catalytic materials with many distinct advantages: simplicity of method, short reaction times, and the capability to regulate crystal lattice parameters and thereby the activity and selectivity of catalysts. Over the last years, SCS has been used for the production and study of a multitude of new catalytic materials. This review considers and discusses the recent developments and trends in SCS of nanocatalysts, while special attention is paid to the development and applications of nanostructured catalysts.**

Prof. G. Xanthopoulou, O. Thoda, Dr. G. Vekinis
Institute of Nanoscience and Nanotechnology
NCSR "Demokritos," Agia Paraskevi Attikis
15310, Greece
E-mail: g.xanthopoulou@inn.demokritos.gr

O. Thoda, Prof. A. Chroneos
Faculty of Engineering
Environment and Computing
Coventry University
Priory Street, CV1 5FB, Coventry, UK

The ORCID identification number(s) for the author(s) of this article can be found under https://doi.org/10.1002/adem.201800047.

**DOI: 10.1002/adem.201800047**

Catalysis Letters (2018) 148:764–778
https://doi.org/10.1007/s10562-017-2279-y

# Parametric Optimisation of Solution Combustion Synthesis Catalysts and Their Application for the Aqueous Hydrogenation of Maleic Acid

**O. Thoda**[1,2] · **G. Xanthopoulou**[1] · **G. Vekinis**[1] · **A. Chroneos**[2]

Received: 19 October 2017 / Accepted: 11 December 2017 / Published online: 22 December 2017

## Abstract

Ni-based nano-catalysts were synthesized by solution combustion synthesis. Nickel aluminate spinels and Ni–Al alloys yielded during combustion, although it is difficult to be produced at low temperatures. A multistage mechanism of the Ni–NiAl catalysts formation was identified which indicates that SCS is general and can be utilized for the preparation of many different types of metal–alloys nanostructures.

### Graphical Abstract

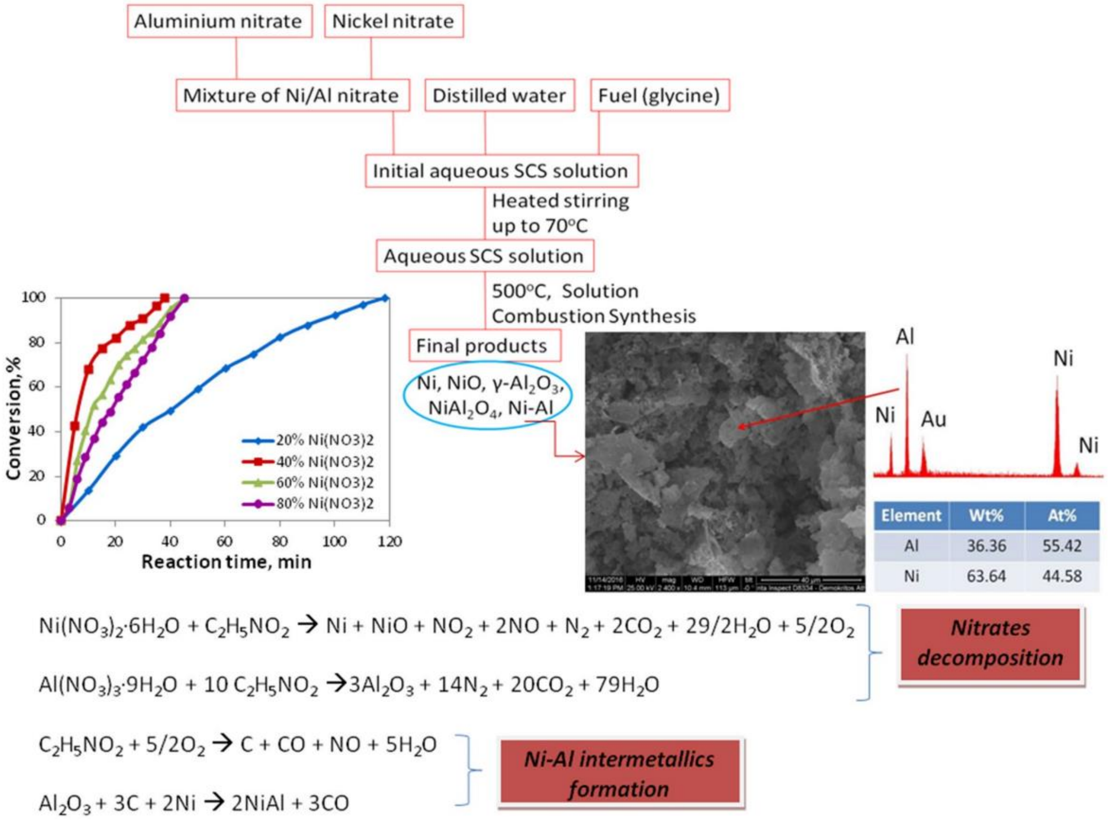

| Element | Wt% | At% |
|---|---|---|
| Al | 36.36 | 55.42 |
| Ni | 63.64 | 44.58 |

$$Ni(NO_3)_2{\cdot}6H_2O + C_2H_5NO_2 \rightarrow Ni + NiO + NO_2 + 2NO + N_2 + 2CO_2 + 29/2H_2O + 5/2O_2$$

$$Al(NO_3)_3{\cdot}9H_2O + 10\ C_2H_5NO_2 \rightarrow 3Al_2O_3 + 14N_2 + 20CO_2 + 79H_2O$$

$$C_2H_5NO_2 + 5/2O_2 \rightarrow C + CO + NO + 5H_2O$$

$$Al_2O_3 + 3C + 2Ni \rightarrow 2NiAl + 3CO$$

ISSN 1061-3862, International Journal of Self-Propagating High-Temperature Synthesis, 2018, Vol. 27, No. 4, pp. 207–215. © Allerton Press, Inc., 2018.

# Influence of Preheating Temperature on Solution Combustion Synthesis of Ni–NiO Nanocomposites: Mathematical Model and Experiment[1]

**O. Thoda[a, b], G. Xanthopoulou[a, c, *], V. Prokof'ev[d, **], S. Roslyakov[e], G. Vekinis[a], and A. Chroneos[b]**
[a] Institute of Nanoscience and Nanotechnology, NCSR Demokritos, Agia Paraskevi Attikis, Greece
[b] Faculty of Engineering, Environment and Computing, Coventry University, London, United Kingdom
[c] Samara National Research University, Samara, Russia
[d] Tomsk State University, Tomsk, Russia
[e] National University of Science and Technology MISiS, Moscow, Russia
*e-mail: g.xanthopoulou@inn.demokritos.gr
**e-mail: pvg@ftf.tsu.ru

Received July 10, 2018

**Abstract**—Solution combustion synthesis (SCS) is a widely recognized method to synthesize nanoscale materials. In this work, an attempt was made to analytically simulate (using the Semenov method) and evaluate the influence of preheating temperature on flame temperature as well as on physicochemical characteristics of SCS products. Preheating was found to affect combustion temperature only slightly. An increase in preheating temperature led to a decrease in the induction period due to enhanced heating rate and an increase in cooling time as a result of additional exothermic reactions taking place at higher temperatures. Variation in cooling time caused changes in composition and microstructure of product. For the first time, a mathematical model of SCS was suggested.

applied sciences

Article

# The Effect of the Precursor Solution's Pretreatment on the Properties and Microstructure of the SCS Final Nanomaterials

**Olga Thoda [1,2], Galina Xanthopoulou [1,3], George Vekinis [1] and Alexander Chroneos [2,*]**

[1] Institute of Nanoscience and Nanotechnology, NCSR "Demokritos", Agia Paraskevi Attikis, Athens 15310, Greece; o.thoda@inn.demokritos.gr (O.T.); g.xanthopoulou@inn.demokritos.gr (G.X.); g.vekinis@inn.demokritos.gr (G.V.)

[2] Faculty of Engineering, Environment and Computing, Coventry University, Priory Street, Coventry CV1 5FB, UK

[3] Laboratory of Catalytic Processes in Gas Turbines, Samara State Aerospace University, Moskovskoye Hwy 34, Samara 443086, Russia

* Correspondence: alexander.chroneos@imperial.ac.uk

Received: 25 January 2019; Accepted: 16 March 2019; Published: 21 March 2019

**Abstract:** Nanostructured nickel-based catalysts were produced by solution combustion synthesis and it was found that their properties and structure depended on the pretreatment of the precursor solution. X-ray diffraction, $N_2$ adsorption, and an infrared high-speed camera were used to follow the various synthesis steps and to characterize the obtained catalysts, while their catalytic activity was determined in the hydrogenation of maleic acid. It was determined that the amount of water used and the heating of the precursor solution under mild stirring up to 70 °C influenced the nickel nitrate–glycine–water complexes that were formed in the precursor solution in the form of dendrites. These play a key role in the solution combustion synthesis (SCS) reaction mechanism and in particular in the formation of nickel-based catalysts. Understanding the interrelationships between the processing parameters and the ensuing powder properties allowed an efficient optimization of the catalytic performance.